Entrainment and mixing in turbulent negatively buoyant jets and fountains

Liam Milton-McGurk

A thesis submitted to fulfil the requirements for
the degree of *Doctor of Philosophy*

THE UNIVERSITY OF
SYDNEY

School of Aerospace, Mechanical and Mechatronic Engineering
The University of Sydney

May 2021

Statement of originality

I hereby declare that to the best of my knowledge, the content of this thesis is my own work and has not been submitted elsewhere for any degree or other purpose. The intellectual content of this thesis is a product of my own work and all assistance received in preparing this thesis and sources have been acknowledged.

Liam Milton-McGurk
Monday 10th May, 2021

Authorship attribution statement

This thesis contains material published in McGurk et al. (2018) and Milton-McGurk et al. (2020b). This can be found in chapter 3, 4 and §5.2. With the guidance of my supervisor, I designed these studies, carried out the experiments, analysed the data and wrote the manuscripts.

The contents of chapter 5, and a portion of chapter 2, have been accepted for publication in Milton-McGurk et al. (2020a). With the guidance of my supervisor, I designed this study, carried out the experiments, analysed the data and wrote the manuscript.

Liam Milton-McGurk
Monday 10$^{\text{th}}$ May, 2021

Acknowledgements

I would like to gratefully acknowledge the guidance and support of my supervisor, Dr Nicholas Williamson. Nick has been a mentor to me since my undergraduate degree, and I thank him for his time, expertise and advice. I am lucky to have got to know him over the last few years.

I would also like to thank Krishna Talluru and Daisy Huang for their help around the lab, and consistent willingness to discuss problems and ideas. I am grateful to the rest of the fluid dynamics research group, led by the inspiring Professor Steve Armfield, for providing valuable feedback along the way. I am also indebted to the mechanical engineering workshop for their essential technical assistance.

Finally, I would like to thank my parents for all their support and encouragement over this long and challenging journey. I would not be where I am today without them.

Abstract

Turbulent negatively buoyant jets occur when the buoyancy of a jet directly opposes its momentum, and will decelerate until its mean momentum is reduced to zero. Here the flow reverses direction and, for an axisymmetric flow originating from a round inlet, returns annularly towards the source, mixing with the opposing fluid and forming a fountain. The initial stage, before the return flow forms, is referred to as the 'negatively buoyant jet' (NBJ) stage. Once the return flow has established, it is referred to as the fully developed 'fountain' (F) stage. This study investigates both the initial and final stages of this flow experimentally, using two-dimensional particle image velocimetry (PIV) and planar laser induced fluorescence (PLIF). Data is obtained at a range of axial locations for source Froude numbers, $10 \leq Fr_o \leq 30$, and Reynolds numbers, $5500 \leq Re \leq 5800$.

Analysing the mean statistics of the NBJ stage reveals several important differences with neutral jets. Although the mean velocity and scalar profiles are found to take similar Gaussian shapes at a wide range of axial locations, the widths of these profiles do not grow at the same rate. This can be seen in the ratio of widths of the scalar and velocity profiles, which is larger than in neutral jets and plumes and increases with axial distance. The turbulence intensity and Reynolds stress do not decrease at the same rate as the mean flow in NBJs, and a new turbulence scale is defined that can collapse these profiles onto approximately a single curve. The entrainment coefficient, α, is estimated for negatively buoyant jets, where it is found to decrease with axial distance, or equivalently, increasingly negative local Richardson number, Ri. Eventually, $\alpha < 0$ for $Ri \lesssim -0.2$, indicating there is a net radial outflow from the NBJ to the environment. Using a linear fit of the α data, an integral model was solved for the NBJ with predictions in reasonable agreement with the present data for $z/D \lesssim 30$.

Fully developed fountains are explored alongside NBJs, allowing the effect of the return flow on the inner core to be investigated. The mean and turbulence profiles in fountains are generally not self-similar along the flow. This is most evident in the outer flow region of the mean velocity and scalar profiles, and across the full width of

the turbulence profiles, such as the Reynolds stress and scalar fluxes. Entrainment between the inner and outer flow of fountains is investigated using two alternative approaches, both finding that radial flow is predominantly from the inner to the outer flow for the majority of the fountains height. An alternative interpretation of entrainment in NBJs and fountains is presented, which decomposes the radial flow into inflow and outflow components. The inflow component can be related to the inner flow velocity scale by an approximately constant entrainment coefficient, similar to the classical description of entrainment in pure jets and plumes developed by Morton et al. (1956). The outflow component can be interpreted as capturing the effect of negative buoyancy on entrainment, in addition to complex interactions with the outer flow in the fountain case. This term varies with local Richardson number along the flow, and is present in both negatively buoyant jets and fountains.

Contents

List of Figures

List of Tables

Nomenclature

Acronyms

AF	Ambient fluid
F	Fountain
IA	Interrogation area
IF	Inner flow
J	Jet
MTT	Morton et al. (1956)
NBJ	Negatively buoyant jet
ODE	Ordinary differential equation
OF	Outer flow
PB	Priestley and Ball (1955)
PIV	Particle image velocimetry
PLIF	Planar laser induced fluorescence
TNTI	Turbulent non-turbulent interface

Symbols

α	Entrainment coefficient
β	Dimensionless momentum flux profile coefficient
δ	Dimensionless turbulence production profile coefficient
γ	Dimensionless axial kinetic energy flux profile coefficient

$\hat{w}$	Characteristic axial velocity
$\hat{u}_e$	Characteristic radial 'entrainment' velocity
Λ	Ratio of initial to steady state heights, z_i/z_{ss}
λ	Ratio of buoyancy to velocity $1/e$ widths, r_b/r_w
ν	Kinematic viscosity
$\overline{x}$	The mean component of x in the Reynolds decomposition $x = \overline{x} + x'$
ρ	Density
ρ_e	Density of the ambient fluid (environment)
θ	Dimensionless buoyancy flux profile coefficient
$\tilde{r}$	Integration limit used in several equation definitions. Typically $\tilde{r} = \infty$ for jets/plumes/NBJs and $\tilde{r} = r_{io}$ for fountains
B	Scaled integral buoyancy
b	Buoyancy (reduced gravity)
b_m	Integral buoyancy scale
c	Scalar concentration
D	Source diameter
F	Scaled buoyancy flux
Fr	Froude number
G	Scaled integral of buoyancy squared
g	Gravitational acceleration ($g = 9.81$ m s^{-2})
g_m	Alternative buoyancy scale
I	PLIF image captured of the region of interest
I_b	Background image
I_p	Image captured of fluid in the laser calibration box
K	Rhodamine 6G concentration

M Scaled axial momentum flux

P Laser power profile

Q Scaled volume flux

r Radial coordinate

r_b Mean buoyancy profile $1/e$ width

r_m Integral length scale (based on velocity profile)

r_w Mean velocity profile $1/e$ width

r_{mb} Integral length scale (based on buoyancy/scalar profile)

Ri Richardson number

u Radial velocity

w Axial velocity

w_m Integral axial velocity scale

x' The fluctuating component of x in the Reynolds decomposition $x = \overline{x} + x'$

z Axial coordinate

z_i Initial rise height of a negatively buoyant jet

z_{ss} Mean quasi-steady state rise height of a fully developed fountain

I_c PLIF reference image of the region of interest

Subscripts

f Turbulence component of a profile coefficient, e.g. δ_f

g Sum of the mean and turbulence components of a profile coefficient, e.g. $\delta_g = \delta_m + \delta_f$

j The 'neutral jet' value, e.g. α_j is the entrainment coefficient of a jet

m Mean component of a profile coefficient, e.g. δ_m

o Quantity corresponds to the value at the source, e.g. Q_o

p The 'pure plume' value, e.g. Ri_p is the Richardson number of a plume

Chapter 1

Introduction

1.1 Background

In typical day-to-day conversation, the word 'fountain' is usually reserved for the decorative water features found in parks or town squares, or to describe naturally occurring phenomena such as geothermal geysers (as in figure 1.1), where water travels upwards from a source below and then falls back down due to gravity. From a fluid mechanics perspective, this can be thought of as a dense fluid (water) entering a less dense ambient (air) in a direction opposing its buoyancy. In this case, the density difference between the source and ambient fluid is very large (orders of magnitude) and so the fluids do not mix. There are many other cases where the density difference is much smaller and mixing between the fountain flow and the ambient fluid is significant, such as when a jet of cold air enters a warm room from below (or hotter air from above), which can be found in many building ventilation systems. Other applications often discussed in literature include brine discharge in desalination plants, stratification of water reservoirs, and natural processes such as magma chambers and explosive volcanic jets (Pincince and List 1973; Larson and Jönsson 1996; Roberts et al. 1997; Campbell and Turner 1989).

Consider a turbulent jet entering a homogeneous environment with buoyancy opposed to its momentum, such as a dense fluid entering lighter ambient vertically from below (or vice versa). This jet is considered 'negatively buoyant', and will continually decelerate upon entry until its mean momentum is reduced to zero, reaching a stagnation point. Here the fluid reverses direction and, for an axisymmetric flow originating from a round inlet, returns annularly towards the source, mixing with the opposing fluid and forming a fountain. Some time after the initial rise of a negatively buoyant jet, the flow reaches a quasi-steady state where it oscillates around a height, z_{ss}, which is typically lower than the maximum height reached during the

Figure 1.1: Strokkur, a natural fountain-type geyser located in southwest Iceland (photograph taken January 23, 2017).

jets initial rise, z_i (Turner 1966; Burridge and Hunt 2012). These locations may be formally defined as where the characteristic axial velocity is equal to zero, which occurs immediately before the flow reverses direction. This quasi-steady state stage of the flow will referred to as the 'fully developed fountain' (F) stage, with a structure consisting of an inner flow (IF) surrounded by an opposing annular outer flow (OF), as illustrated in figures 1.2(c) and (d). Prior to the fully developed fountain forming, during the initial rise to z_i, there is no OF and the flow structure resembles a turbulent jet or plume. This will be referred to as the 'negatively buoyant jet' (NBJ) stage of the flow, and is shown in figures 1.2(a) and (b).

For a round inlet, z_i and z_{ss} are governed by the source Froude or Richardson numbers,

$$Fr_o = \frac{w_o}{(-r_o b_o)^{1/2}} = \frac{1}{(-Ri_o)^{1/2}} \tag{1.1}$$

where w_o and r_o are the initial average axial velocity and source radius, and $b_o = g\Delta\rho_o/\rho_e$ is the source buoyancy (often referred to as the 'reduced gravity'). Here g is the gravitational acceleration and $\Delta\rho_o$ is the difference between the density of the source fluid, ρ_o, and the environment, ρ_e. Flows will be considered negatively buoyant if $\Delta\rho_o < 0$ and hence $b_o < 0$, such as a dense fluid entering a lighter environment from below, where we would define $\Delta\rho_o = \rho_e - \rho_o < 0$. For the reverse case, where light fluid enters a dense ambient from above, the flow is still considered

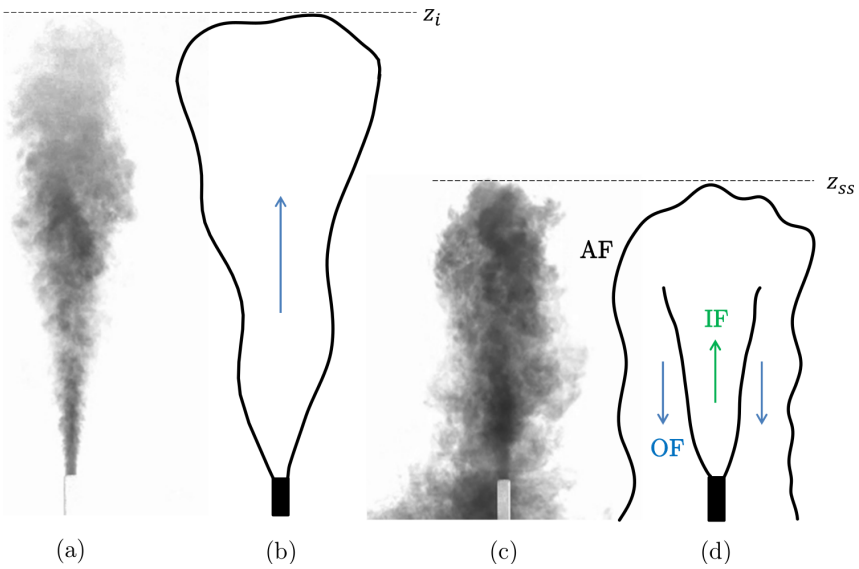

Figure 1.2: Images and illustrations of a negatively buoyant jet and fully developed fountain. Figures (a) and (b) show the initial negatively buoyant jet (NBJ) stage before a return flow has formed, and (c) and (d) show a fountain in a quasi-steady state with an inner flow (IF) surrounded by an opposing outer flow (OF) and ambient fluid (AF). The images have been rotated 180°, and were taken while testing the experiment set-up with food dye added to the source fluid.

'negatively buoyant' since the buoyancy is opposing the initial momentum, but we would instead define $\Delta\rho_o = \rho_o - \rho_e < 0$. For fountains where the density difference is relatively small ($|\Delta\rho_o/\rho_e| \lesssim 0.05$), these two cases of upward and downward fountains are opposite but equivalent, reaching the same z_i and z_{ss} for the same Fr_o (Turner 1966; Burridge and Hunt 2012; Cresswell and Szczepura 1993; Papanicolaou et al. 2008). However, recent research has reported that for large density differences ($|\Delta\rho_o/\rho_e| \gtrsim 0.2$), the rise height scaling is different for upward and downward fountains (Vaux et al. 2019). In the present investigation, the flow will be restricted to the small, $|\Delta\rho_o/\rho_e| \lesssim 0.05$, regime, and measurements are obtained for downward fountains.

The source Froude number is used to classify fountains into different categories, ranging from 'very weak' to 'highly forced', where weaker fountains have a low source momentum flux relative to the opposing buoyancy flux (thus a low Fr_o), and vice versa for forced fountains. Figure 1.3 shows some representative images of fountains from different classes reaching their initial rise height, where the different structures can be seen. There are Froude number relations for different classes to predict the steady state height, such as $z_{ss}/r_o = 2.46Fr_o$ for forced and highly forced fountains ($Fr_o \gtrsim 2.8$) (Turner 1966; Burridge and Hunt 2012). The ratio between the initial and steady-state rise height, while constant for highly forced fountains

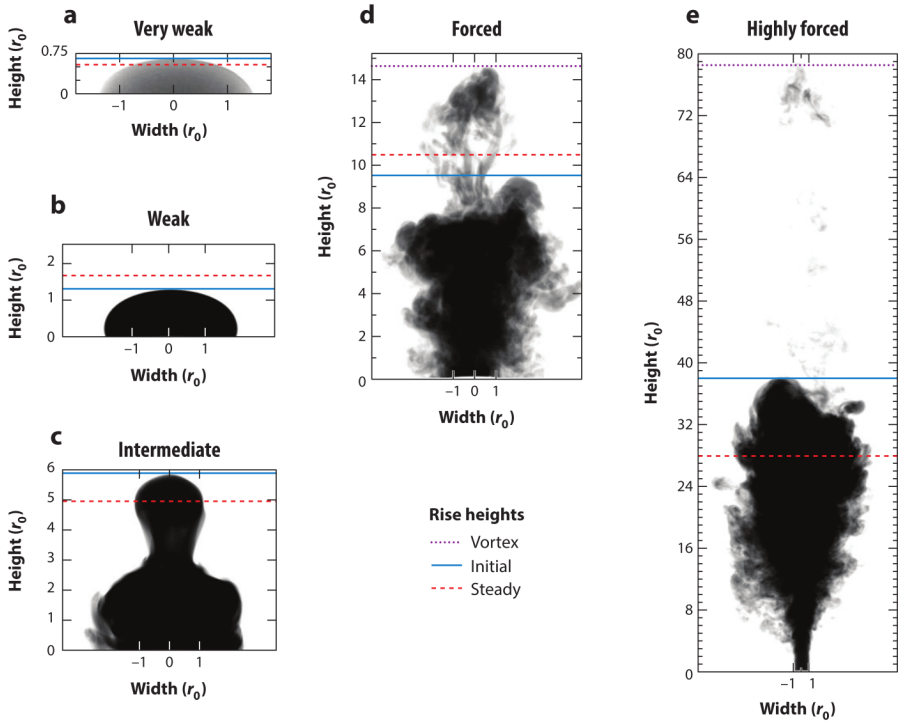

Figure 1.3: Experimentally obtained images of fountains during their initial rise, with superimposed lines indicating the initial and steady state heights, as well as the height that a detaching vortex reaches if present. The images show fountains of increasing Fr_o from (a) to (e). A classification by Burridge & Hunt (2012) has grouped very weak fountains as $Fr_0 \lesssim 1$ up to highly forced $Fr \gtrsim 5.5$. Figure reproduced from Hunt and Burridge (2015) with permission.

($z_i/z_{ss} = 1.45$), has been found to vary in the lower Fr_o classes. For weak fountains, $1.0 \lesssim Fr_o \lesssim 1.7$, the initial rise height is actually lower than the steady state height, $z_i \lesssim z_{ss}$, and a different Fr_o relation is followed (Burridge and Hunt 2012). However, these are not considered in the present investigation, which is primarily focused on the high Fr_o regime.

1.2 Motivation

Despite the relative success of predicting the bulk properties of fountain flow, such as the rise heights, there has been considerably less progress in describing their detailed internal structure, or the entrainment between the different layers (e.g. IF/OF). Many of the existing models are extensions of Morton's (1959) plume theory derived from the governing conservation equations, which assume self-similar flow and come in the form of integral models (McDougall 1981; Bloomfield and Kerr 2000; Hunt and Debugne 2016). Other studies have cast doubt on the validity of some of

these assumptions, such as the direct numerical simulations (DNS) by Williamson et al. (2011), who found that for $Fr_o = 2.1, 4$, and 7, the fountain flow continues to develop over most of its height and is not self-similar. A similar result was also obtained experimentally by Mizushina et al. (1982) and Cresswell and Szczepura (1993). These integral models typically also depend on simple entrainment relations based on the model by Morton et al. (1956), which was originally applied to a simple jet or plume with no return flow. This related the fluid entrained across the edge of a plume/jet to a characteristic vertical velocity at that height by a single (constant) entrainment coefficient, α (Morton et al. 1956). Bloomfield and Kerr (2000) developed a more sophisticated relation specifically for fountains, which included three entrainment coefficients to describe entrainment between the IF, OF, and ambient fluid (AF). They developed four formulations of their model and compared them to existing experimental data, and although they predicted initial rise heights within the error margins observed, none of their models were clearly supported by the results at the steady-state.

Aside from measurements of z_i, there has also been very limited research into the initial negatively buoyant jet stage, before the return flow develops. This case is simpler than the fully developed fountain from a theoretical perspective, since there is no OF and it may be possible to apply the same integral models originally applied to jets and plumes except with the direction of buoyancy reversed. Solutions have been obtained for simplified cases (Morton 1959; Abraham 1967). To the best of the authors knowledge, there has yet been no experimental data published on the internal velocity or buoyancy fields during this initial stage of the flow. Obtaining such data would aid in better understanding the effect of negative buoyancy on these 'jet-like' flows, and particularly the consequences it has for entrainment.

The present research will investigate the validity of some of the underlining assumptions prevalent in existing literature, which are critical to the accuracy of the various integral models. By taking high resolution measurements using particle image velocimetry (PIV) and planar laser induced fluorescence (PLIF), the internal structure of fountains can by studied with more detail and accuracy than previous attempts, and over a larger range of source Froude numbers than DNS can provide. Obtaining a better understanding of the underlining physics of turbulent negatively buoyant jets and fountains will also allow for better predictions of the larger scale flow parameters, such as rise heights or total entrainment, which are important in practical applications such as building ventilation and desalination plants. Furthermore, an improved description of turbulent entrainment in NBJs/fountains will be useful in a range of other areas that involve shear flows, as well answering the more

fundamental question of how entrainment is affected by negative buoyancy.

1.3 Thesis aims and structure

This investigation broadly aims to contribute to an improved understanding of the internal physics of both the initial and quasi-steady stages of high Fr_o fountain flow. A particular focus will be given to how negative buoyancy affects entrainment and the development of the flow more generally, which will be discussed in the context of an integral model framework. Several specific objectives, and the corresponding sections of the thesis where they are pursued, are given below.

(i) Review previous literature on negatively buoyant jets and fountains, and the application of existing integral models to these and other similar flows (chapter 2).

(ii) Design and construct an experimental set-up and procedure capable of obtaining high resolution velocity and density measurements of negatively buoyant jets and fountains (chapters 3-4).

(iii) Examine the effect of negative buoyancy on the internal velocity and scalar fields of negatively buoyant jets, and how they differ to neutral jets (chapter 5).

(iv) Investigate the effect of negative buoyancy on turbulent entrainment in negatively buoyant jets and fountains (chapters 5, 7).

(v) Determine the extent to which negatively buoyant jets and fountains can be considered self-similar (chapters 5-7).

(vi) Investigate the effect of the return flow by identifying key differences between the inner flow of fully developed fountains and the initial negatively buoyant jet stage (chapters 6-7).

Chapter 2

Literature review

2.1 Bulk flow

Turner (1966) used dimensional arguments to derive a linear Fr_o scaling for the steady state rise height of a fountain,

$$\frac{z_{ss}}{r_o} = \text{constant} \times Fr_o, \tag{2.1}$$

and experimentally determined the value of the constant to be 2.46. This value was later supported by Baines et al. (1990). Turner's (1966) experiments also suggested that the ratio between the initial and steady state rise heights of fountains was constant,

$$\Lambda = \frac{z_i}{z_{ss}}, \tag{2.2}$$

with $\Lambda = 1.43$. However, both of these results have since been re-examined, with Kaye and Hunt (2006) showing that (2.1) only holds for large Fr_o, with different, non-linear, z_i scaling relations for lower Fr_o fountains. Burridge and Hunt (2012) additionally found that Λ is only constant for highly forced fountains, where $Fr_o \gtrsim 5.5$ and $\Lambda = 1.45$. A summary of these classifications based on previous literature is given in table 2.1 (Burridge and Hunt 2012; Turner 1966; Kaye and Hunt 2006).

From table 2.1, we see that forced and highly forced fountains follow the same z_{ss}/r_o scaling law, yet have a different Λ behaviour. This difference has been attributed to the behaviour of a vortex that forms at the top of the NBJ during its initial rise (Burridge and Hunt 2012). A series of images taken from the present experimental set-up are given in figure 2.1, showing the initial rise of a $Fr_o \cong 30$ NBJ. This is in the highly forced regime ($Fr_o \gtrsim 5.5$), with the images showing a vortex visibly forming and then detaching in (a)-(d). In forced fountains ($2.8 \lesssim Fr_o \lesssim 5.5$), this vortex is unable to detach from the main jet, which has the effect of reducing its

Class	Fr_o range	Λ variation	Scaling law (z_{ss}/r_o)
Very weak	$0.4 - 1.0$	$1.1 \rightarrow 1.0$	$0.81Fr_o^{2/3}$
Weak	$1.0 - 1.7$	$1.0 \rightarrow 0.5$	$0.86Fr_o^2$
Intermediate	$1.7 - 2.8$	$1.4 \rightarrow 1.0 \rightarrow 1.3$	
Forced	$2.8 - 5.5$	$1.0 \rightarrow 1.45$	$2.46Fr_o$
Highly forced	$\gtrsim 5.5$	1.45	

Table 2.1: Summary of fountain classifications, including rise height scaling and behaviour of the generally non-constant Λ in different Fr_o ranges (Burridge and Hunt 2012; Kaye and Hunt 2006; Turner 1966).

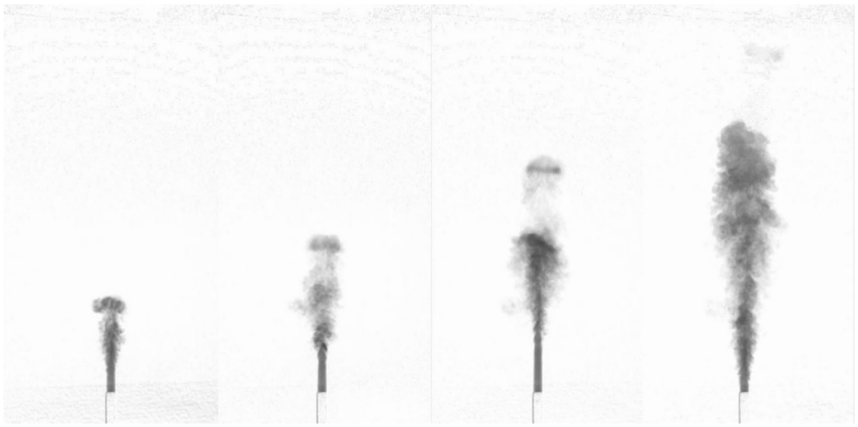

(a) (b) (c) (d)

Figure 2.1: Photographs of the initial rise of an NBJ using the present experimental set up, showing a vortex forming and then detaching from the top of the jet. Images (a)-(d) were captured within the first 3 s of the flow exiting the pipe, and have been rotated 180°.

initial height z_i, although does not noticeably influence the steady state height, z_{ss}. This is the reason for the lower Λ in the forced regime in table 2.1, and serves as the feature that distinguishes forced and highly forced fountains (Burridge and Hunt 2012). The present study focuses on the highly forced regime, with experiments investigating $Fr_o \gtrsim 10$ fountains and negatively buoyant jets.

2.2 Local flow

Studies relying on bulk measurements, such as z_i and z_{ss}, are unable to provide detailed information about the internal structure of negatively buoyant jets/fountains. There have been several studies to have obtained local velocity and density measurements of fully developed fountains, although there is limited data available. For the negatively buoyant jet stage, there does not appear to be any internal veloc-

ity/density data available.

Mizushina et al. (1982) used constant temperature and current anemometry to obtain velocity and temperature measurements inside of high Fr_o fountains, finding temperature profiles similar to a neutral jet, and that the inner velocity profile was similar but wider. Mizushina et al. (1982) also found that the mean velocity and temperature profiles, and the turbulence intensities, were not self-similar. That is, that the profiles measured at different axial locations along the fountain did not collapse onto a single curve when normalised by simple local quantities. The contrasts to neutral jets, for example, which have velocity and scalar profiles that have approximately Gaussian shapes once they are fully developed (Hussein et al. 1994; Papanicolaou and List 1988; Wang and Law 2002).

Cresswell and Szczepura (1993) investigated fully developed fountains with $Fr_o \cong 3.2$ using laser Doppler anemometry (LDA) and thermocouples to obtain velocity and temperature measurements. They reported high shear stresses at the IF/OF boundary and in the cap region, and found that velocity-temperature correlations in the OF were similar to those in pure plumes. They also found that the flow in general could not be described by self-similar profiles. More recently, Williamson et al. (2011) undertook direct numerical simulations (DNS) for $Fr_o = 4$ and 7 fountains, also finding that the profiles were not generally self-similar.

2.3 Entrainment

Entrainment can be described as the process where fluid is transported from a non-turbulent to turbulent region across a turbulent/non-turbulent interface (TNTI), such as from a quiescence ambient into a turbulent jet (Mistry et al. 2016). The term entrainment has also been used to describe fluid transport of between two turbulent regions, such as between coaxial turbulent jets (Morton 1962), or across the IF/OF boundary of a fountain (McDougall 1981; Bloomfield and Kerr 2000; Hunt and Debugne 2016). In a mean description of the flow, this complicated turbulent process can be characterised by the entrainment coefficient, α, and has been used extensively in previous studies into jets and plumes (Morton 1959; Fox 1970; Wang and Law 2002; Ezzamel et al. 2015). The simplest form of this relation was used in the pioneering integral model by Morton et al. (1956),

$$\hat{u}_e = \alpha \hat{w} \tag{2.3}$$

where $\hat{u}_e$ is the radial velocity of entrained fluid and $\hat{w}$ is a characteristic axial velocity of the flow. Morton et al. (1956) originally applied this to self-similar pure

plumes with a constant α at all axial locations. Alternative formulations, such as by Fox (1970) based on the model by Priestley and Ball (1955), have also been developed where α is no longer a constant. Here α may change along the length of the jet/plume subject to local conditions through the *local* Froude or Richardson numbers, Fr and Ri, which are defined in (2.11). More recent studies have extended these further, omitting assumptions about the shape of the profiles and whether they are self-similar (Kaminski et al. 2005; van Reeuwijk and Craske 2015). These models, and their application to negatively buoyant jets are discussed in more detail in §2.4.

2.3.1 Jet-like flows

In general, the assumption of a constant α is suitable for pure jets ($Ri = 0$) and pure plumes (Ri = constant) (Fox 1970; van Reeuwijk and Craske 2015). Despite some scatter in the literature, a robust result is that entertainment is lower in jets ($0.065 \lesssim \alpha_j \lesssim 0.080$) than plumes ($0.10 \lesssim \alpha_p \lesssim 0.16$) (Hussein et al. 1994; Carazzo et al. 2006; Ezzamel et al. 2015; van Reeuwijk et al. 2016). For buoyant jets or 'forced plumes' (positive initial momentum and buoyancy), a non-constant α is more realistic, taking asymptotic values between α_j and α_p (Priestley and Ball 1955; Fox 1970; van Reeuwijk and Craske 2015; Wang and Law 2002; Ezzamel et al. 2015). Theoretical studies, such as by Abraham (1967) and a Lagrangian analysis by Lee and Chu (2012), have predicted that there is a region of 'negative entrainment' ($\alpha < 0$) in the upper region of a negatively buoyant jet without a return flow.

Other than simply comparing model predictions to bulk flow measurements such as rise height, these entrainment relations have not been rigorously assessed against experimental data for negatively buoyant jets. The attempts to estimate α in NBJs by matching z_i observations to model predictions have typically required significantly reducing the value of α below that of a neutral jet (Carazzo et al. 2006; Kaminski et al. 2005; Papanicolaou et al. 2008). The entrainment coefficient is then estimated as the value of α that results in the best model predictions. Kaminski et al. (2005) took a slightly different approach by calculating 'bulk entrainment' in collapsing ethanol and ethylene glycol (EEG) jets, also finding that a reduced value was required ($\alpha = 0.057$). The present investigation will obtain measurements of the internal velocity and buoyancy fields of the flow, allowing the entrainment coefficient to be measured more directly and without some of the assumptions that underline the models, such as that the flow is self-similar. This will also allow local predictions of the integral models to be assessed, rather than relying solely on bulk values such as z_i.

2.3.2 Fountains

Several previous studies have sought to use entrainment coefficients to describe the flow between the IF/OF and OF/AF of fully developed fountains. These models are more complex than the NBJ case since they generally require a set of conservation equations for both the inner and outer flows, with most previous attempts assuming constant entrainment coefficients (McDougall 1981; Bloomfield and Kerr 2000; Hunt and Debugne 2016). Bloomfield and Kerr (2000) produced four different models based on alternative formulations of the buoyancy force and description of entrainment between the IF/OF. They found that all models underestimated the steady state rise height, z_{ss}, reported in previous literature, differing by approximately $15\% - 40\%$ depending on the model choice. They also noted that although their results were not significantly sensitive to the chosen entrainment coefficients between the IF/OF, reducing entrainment between the OF/AF significantly reduced z_{ss} predictions.

Hunt and Debugne (2016) developed a modified version of the model by Bloomfield and Kerr (2000) for the main body of the fountain, but additionally allowed for entrainment into the cap region where the fluid reverses direction. This model slightly underpredicted the z_{ss} reported in the literature, although no attempt was made to adjust the constant entrainment coefficients used to improve predictions. This model assumed constant entrainment from the OF to IF, and from the AF to OF. Although this simple characterisation of the internal dynamics between the IF/OF layers did give a reasonable prediction of z_{ss}, there has been evidence that the radial flow in fountains is actually primarily in the opposite direction, instead moving from the IF to the OF. This includes a direct numerical simulation (DNS) study by Williamson et al. (2011), who found that other than in a short region near the source, fluid is primarily ejected from the inner to the outer flow for $Fr_o = 7$ fountains. As similar observation was also made in experiments by Cresswell and Szczepura (1993), after an axial distance of $1.3r_o$ for a $Fr_o \cong 3.2$ fountain. Obtaining additional detailed measurements of fully developed fountains at larger Fr_o would be useful in better understanding their internal dynamics, and aid the development of models that better represent the true underlying physics.

2.4 Integral models

Existing NBJ and fountain models have predominantly been developed by building on earlier integral models applied to simpler flows such as pure jets and plumes. Early work in this area was pioneered by Morton et al. (1956) and Priestley and

Ball (1955) who derived a system of ordinary differential equations (ODEs) that will be refereed to as the MTT and PB models, respectively. Both models can be derived from equations for the conservation of axial momentum and buoyancy, with the MTT model additionally using the conservation of volume, and the PB model instead using the conservation of mean kinetic energy. Fox (1970) further developed the PB model by invoking the conservation of volume, and showed how it is equivalent to the MTT model under certain situations (e.g. a pure momentum jet). Both models make use of the Boussinesq approximation, which assumes that local variations in density are small compared to the reference (ambient) density (Morton et al. 1956; Priestley and Ball 1955). That is, density differences are ignored other than when they contribute to the fluids buoyancy. Analytical solutions to these models have be obtained by assuming fully self-similar velocity and buoyancy profiles in the flow, where the shape of the profiles are assumed to be Gaussian or 'top-hat' (constant inside the plume/jet, zero outside it) (Morton et al. 1956; Morton 1959; Priestley and Ball 1955).

More recent studies have developed these models further, by omitting assumptions about the shape or self-similarity of the profiles (Kaminski et al. 2005; van Reeuwijk and Craske 2015). In the following sections, the equations will be presented starting in their most general form with minimal assumptions (van Reeuwijk and Craske 2015), followed by a discussion of the key assumptions and simplifications needed to obtain the classical PB and MTT models (Morton et al. 1956; Priestley and Ball 1955). One of the aims of the present investigation is to determine the extent to which these assumptions are valid for negatively buoyant jets, and consider how this integral model approach can be applied to fully developed fountains.

2.4.1 Governing equations

For a high Re_o, axisymmetric flow in a homogeneous environment, and after invoking the Boussinesq approximation and neglecting pressure contributions, the equations for conservation of volume, momentum, buoyancy and kinetic energy may be written

as (van Reeuwijk et al. 2016; Kaminski et al. 2005),

$$\frac{\partial}{\partial r}\left(r\overline{u}\right)+\frac{\partial}{\partial z}\left(r\overline{w}\right)=0, \tag{2.4}$$

$$\frac{\partial}{\partial r}\left(r\overline{u}\,\overline{w}+r\overline{u'w'}\right)+\frac{\partial}{\partial z}\left(r\overline{w}^2+r\overline{w'^2}\right)=r\overline{b}, \tag{2.5}$$

$$\frac{\partial}{\partial r}\left(r\overline{u}\overline{b}+r\overline{u'b'}\right)+\frac{\partial}{\partial z}\left(r\overline{w}\overline{b}+r\overline{w'b'}\right)=0, \tag{2.6}$$

$$\frac{\partial}{\partial r}\left(r\overline{u}\,\overline{w}^2+2r\overline{u'w'}\overline{w}\right)+\frac{\partial}{\partial z}\left(r\overline{w}^3+2r\overline{w'^2}\overline{w}\right)=2r\overline{u'w'}\frac{\partial\overline{w}}{\partial r}+2r\overline{w'^2}\frac{\partial\overline{w}}{\partial z}+2r\overline{w}\overline{b}. \tag{2.7}$$

Here w and u are the axial and radial velocities, corresponding to the vertical and radial coordinates z and r, respectively, and $b = g\Delta\rho/\rho_e$ is the buoyancy. The difference between the local and environment density is given by $\Delta\rho$, where $\Delta\rho < 0$ in the case of negative buoyancy. These are each decomposed into their mean and fluctuating components, $w = \overline{w}+w'$, $u = \overline{u}+u'$ and $b = \overline{b}+b'$. Here the overline, e.g. $\overline{w}$, denotes the ensemble average of the quantity obtained from multiple statistically independent samples. The source Reynolds number is defined as,

$$Re_o = \frac{w_o D}{\nu_o}, \tag{2.8}$$

where ν_o is the kinematic viscosity of the source fluid and $D = 2r_o$ is the inlet diameter.

These equations can be integrated from $r = 0$ to infinity to obtain a set of ordinary differential equations (ODEs) consistent with the MTT and PB models (Morton et al. 1956; Priestley and Ball 1955; van Reeuwijk and Craske 2015; Kaminski et al. 2005). These can be expressed in terms of the fluxes of volume, momentum and buoyancy, Q, M and F, and the integral buoyancy, B,

$$Q = 2\int_0^{\tilde{r}}\overline{w}r\mathrm{d}r, \quad M = 2\int_0^{\tilde{r}}\overline{w}^2 r\mathrm{d}r, \quad F = 2\int_0^{\tilde{r}}\overline{w}\overline{b}r\mathrm{d}r, \quad B = 2\int_0^{\tilde{r}}\overline{b}r\mathrm{d}r, \tag{2.9a-d}$$

where $\tilde{r} = \infty$, and which have been scaled to remove a factor of π, for simplicity. At the source, these would be denoted Q_o, M_o, F_o and B_o, where $F_o > 0$ and $F_o < 0$ correspond to positively and negatively buoyant flows, respectively. These integral quantities can be used to define the following characteristic velocity, radius and buoyancy for the jet,

$$w_m = \frac{M}{Q}, \quad r_m = \frac{Q}{M^{1/2}}, \quad b_m = \frac{BM}{Q^2} = \frac{F}{\theta_m Q}, \tag{2.10a-c}$$

where θ_m is defined in (2.16). These allow local Froude and Richardson numbers to be defined, Fr and Ri, which depend on the local scales at any given z, and so may change along the length of the jet,

$$Fr = \frac{w_m}{(-r_m b_m)^{1/2}} = \frac{1}{(-Ri)^{1/2}}. \tag{2.11}$$

After integrating (2.5)-(2.7) from zero to infinity with respect to r, the following system of ODEs are obtained,

$$\frac{\mathrm{d}Q}{\mathrm{d}z} = 2\alpha M^{1/2}, \tag{2.12}$$

$$\frac{\mathrm{d}}{\mathrm{d}z}\left(\beta_g M\right) = \frac{FQ}{\theta_m M} = B, \tag{2.13}$$

$$\frac{\mathrm{d}}{\mathrm{d}z}\left(\frac{\theta_g}{\theta_m}F\right) = 0, \tag{2.14}$$

$$\frac{\mathrm{d}}{\mathrm{d}z}\left(\gamma_g \frac{M^2}{Q}\right) = \delta_g \frac{M^{5/2}}{Q^2} + 2F. \tag{2.15}$$

where β, γ, δ and θ are the 'profile coefficients' defined in (2.16) (van Reeuwijk and Craske 2015). Here subscripts m and f correspond to the mean and turbulent components respectively, and g indicates the sum of them both,

$$\left.\begin{aligned}
&\beta_m = \frac{M}{w_m^2 r_m^2} = 1, \quad \beta_f = \frac{2}{w_m^2 r_m^2}\int_0^{\tilde{r}} \overline{w'^2} r \mathrm{d}r, \\
&\gamma_m = \frac{2}{w_m^3 r_m^2}\int_0^{\tilde{r}} \overline{w}^3 r \mathrm{d}r, \quad \gamma_f = \frac{4}{w_m^3 r_m^2}\int_0^{\tilde{r}} \overline{w}\,\overline{w'^2} r \mathrm{d}r, \\
&\delta_m = \frac{4}{w_m^3 r_m}\int_0^{\tilde{r}} \overline{w'u'}\frac{\partial \overline{w}}{\partial r} r \mathrm{d}r, \quad \delta_f = \frac{4}{w_m^3 r_m}\int_0^{\tilde{r}} \overline{w'^2}\frac{\partial \overline{w}}{\partial z} r \mathrm{d}r \\
&\theta_m = \frac{F}{w_m b_m r_m^2}, \quad \theta_f = \frac{2}{w_m b_m r_m^2}\int_0^{\tilde{r}} \overline{w'b'} r \mathrm{d}r. \\
&\beta_g = \beta_m + \beta_f, \quad \gamma_g = \gamma_m + \gamma_f, \quad \delta_g = \delta_m + \delta_f, \quad \theta_g = \theta_m + \theta_f,
\end{aligned}\right\} \tag{2.16}$$

where $\tilde{r} = \infty$. By observing the definitions of these profile coefficients, and their role in (2.13)-(2.15), we see that β, γ, δ and θ are the dimensionless momentum flux, mean energy flux, turbulence production and buoyancy flux (van Reeuwijk and Craske 2015).

The entrainment assumption, which relates the radial velocity of entrained fluid to a characteristic vertical velocity at that height by the entrainment coefficient, α, is defined in (2.12) as (Morton et al. 1956; van Reeuwijk and Craske 2015),

$$\left(r\overline{u}\right)_{r=\tilde{r}} = -\alpha r_m w_m. \tag{2.17}$$

where $\tilde{r} = \infty$. The earlier definition of α given in (2.3) is valid for simplified models, such as those that assume top-hat velocity/buoyancy profiles, while (2.17) is the generalised case that is valid for arbitrary profiles. Unless specified otherwise, the generalised definition in (2.17) will be used when referring to α.

By combining (2.12), (2.13) and (2.15), the following expression for the entrainment coefficient may be derived (van Reeuwijk and Craske 2015),

$$\alpha = -\frac{\delta_g}{2\gamma_g} + \left(\frac{1}{\beta_g} - \frac{\theta_m}{\gamma_g}\right) Ri + \frac{Q}{2M^{1/2}} \frac{\mathrm{d}}{\mathrm{d}z}\left(\ln \frac{\gamma_g}{\beta_g^2}\right). \tag{2.18}$$

This makes no additional assumptions about the flow, and can be considered a consistency requirement for the conservation of volume, momentum and mean kinetic energy equations. It is valid for jets/plumes with arbitrary buoyancy, and by invoking certain additional assumption that will be discussed in the following sections, can be shown to describe entrainment in both the MTT and PB model frameworks (Priestley and Ball 1955; Morton et al. 1956; van Reeuwijk and Craske 2015). Discussion of the individual terms and their interpretation is given in §5.5, where a version of this equation is used to estimate entrainment in negatively buoyant jets.

Mean contributions

Both the MTT and PB models consider only the mean contributions to the flow, neglecting second-order turbulence terms in the conservation equations. This is equivalent to assuming that turbulence components of the profile coefficients, subscript f in (2.16), are negligible. This assumption leads to the following simplified version of (2.12)-(2.15),

$$\frac{\mathrm{d}Q}{\mathrm{d}z} = 2\alpha M^{1/2}, \tag{2.19}$$

$$\frac{\mathrm{d}M}{\mathrm{d}z} = B = \frac{FQ}{\theta_m M}, \tag{2.20}$$

$$\frac{\mathrm{d}F}{\mathrm{d}z} = 0, \tag{2.21}$$

$$\frac{\mathrm{d}}{\mathrm{d}z}\left(\gamma_m \frac{M^2}{Q}\right) = \delta_m \frac{M^{5/2}}{Q^2} + 2F. \tag{2.22}$$

and a simplified expression for α (van Reeuwijk and Craske 2015),

$$\alpha = -\frac{\delta_m}{2\gamma_m} + \left(1 - \frac{\theta_m}{\gamma_m}\right) Ri + \frac{Q}{2M^{1/2}} \frac{\mathrm{d}}{\mathrm{d}z}(\ln \gamma_m). \tag{2.23}$$

This is valid for velocity/buoyancy profiles of arbitrary shapes that may vary with z, provided the second order turbulence terms may be neglected.

Self-similarity

Another common assumption made in applying integral models is that the flow is self-similar. This can be initially understood as assuming that the mean profiles, $\overline{w}$ and $\overline{b}$, have similar shapes along z. This can be expressed as,

$$\overline{w}\,(r,z) = \tilde{w}(z) f\,(r,z)\,, \tag{2.24}$$

$$\overline{b}\,(r,z) = \tilde{b}(z) h\,(r,z)\,, \tag{2.25}$$

where $\tilde{w}$ and $\tilde{b}$ are velocity and buoyancy scales, and $f(r,z)$ and $h(r,z)$ are shape functions. If Gaussian profiles are assumed, as is common for neutral/positively buoyant jets and plume analysis (Morton 1959; Hussein et al. 1994; Ezzamel et al. 2015), then we may set,

$$f(r,z) = \exp\left(-r^2/r_w^2\right), \tag{2.26}$$

$$h(r,z) = \exp\left(-r^2/r_b^2\right), \tag{2.27}$$

$$\tag{2.28}$$

where r_w and r_b are the $1/e$ widths of the velocity and buoyancy profiles, respectively. These correspond to the radial locations where $\overline{w}/\overline{w}_c = 1/e$ and $\overline{b}/\overline{b}_c = 1/e$, where $\overline{w}_c$ and $\overline{b}_c$ are the centreline values of the velocity and buoyancy profiles. We would then have, for Gaussian profiles, $\tilde{w} = \overline{w}_c = 2w_m$ and $\tilde{b} = \overline{b}_c = 2b_m/\lambda^2$, where,

$$\lambda = \frac{r_b}{r_w}. \tag{2.29}$$

It also follows from the definitions in (2.16) that $\theta_m = 2/(\lambda^2+1)$ and $\gamma_m = 4/3$ in this case. If 'top-hat' profiles were assumed instead, as was done in the original MTT model, then $\theta_m = \gamma_m = 1$. If λ remains constant with z, as is typically reported in pure jets and plumes, for example (Fischer et al. 1979), then the mean profiles will be regarded as being self-similar. This was the assumption made by Priestley and Ball (1955) in their original model, as well as in an expanded version of the MTT

model in Morton (1959) that assumed Gaussian profiles. Due to the current lack of experimental data, it is an open question whether negatively buoyant jets can be described by Gaussian profiles, and if they can, the value and behaviour of λ. The present study will obtain measurements of the mean velocity and buoyancy profiles in NBJs, allowing this to be investigated.

There is a second important sense in which a flow can be considered self-similar, which is the development of other turbulence profiles, such as the Reynolds stress, $\overline{w'u'}$. If $\overline{w'u'}$ also maintains a similar shape along z, and scales with the mean velocity, we would have,

$$\overline{w'u'}\,(r,z) = \tilde{w}(z)^2 j\,(r,z)\,, \tag{2.30}$$

where $j(r,z)$ is a shape function. In this case, δ_m, the dimensionless turbulent production, is constant with a value dependent on the shape function, j. For self-similar velocity and buoyancy profiles, and a Reynolds stress that scales with the mean flow, the α relation in (2.23) simplifies to,

$$\alpha = -\frac{\delta_m}{2\gamma_m} + \left(1 - \frac{\theta_m}{\gamma_m}\right) Ri, \tag{2.31}$$

where δ_m, γ_m and θ_m are constant.

The Priestley and Ball (1955) model can therefore be expressed as the system of ODEs in (2.19)-(2.22), while using (2.31) to model α. The MTT model, which does not invoke the conservation of mean kinetic energy equation required to derive (2.31), instead assumes that α is constant. For pure neutral jets ($M_o > 0$, $F_o = 0$), $Ri = 0$ in (2.31) and the entrainment coefficient is constant. A constant α is also obtained in the case of pure plumes ($M_o = 0$, $F_o > 0$), which have a constant $Ri = Ri_p$ everywhere (Fischer et al. 1979). In these two limiting cases, the PB and MTT models are therefore equivalent. For buoyant jets, α follows the linear relationship in (2.31), provided the profile coefficients can be assumed constant and turbulent components ignored. Previous studies have supported this, such as van Reeuwijk et al. (2016) who explicitly calculated δ_m, γ_m and θ_m for a buoyant jet from their DNS simulations, finding they were reasonably constant for $0.25 \lesssim Ri/Ri_p \lesssim 0.75$ ($10 \lesssim z/D \lesssim 25$). Wang and Law (2002) also estimated α in saline/freshwater buoyant jets, with their results agreeing with a linear Ri relation. However, close to the source before the flow is fully developed, the assumption of self-similar mean profiles and constant profile coefficients are likely to no longer hold (van Reeuwijk et al. 2016; Ezzamel et al. 2015; Carazzo et al. 2006). For negatively buoyant jets, $Ri < 0$, and there is yet no available data on the value of δ_m and whether it is constant in these flows. This has important consequences for the behaviour of α,

and is a key subject of this investigation.

2.4.2 Morton's (1959) analytical solution

By assuming self-similar Gaussian velocity/buoyancy profiles and a constant α, Morton (1959) derived an analytical solution to (2.19)-(2.21) for a negatively buoyant jet originating from a point source ($F_o < 0$, $M_o > 0$). To interpret the solution, the following new variables are first defined,

$$q = \alpha^{-1/2}\theta_m^{-1/2}\,|F_o|^{1/2}\,|M_o|^{-5/4}\,Q, \tag{2.32}$$

$$m = \frac{M}{|M_o|}, \tag{2.33}$$

$$\zeta = 2\alpha^{1/2}\theta_m^{-1/2}\,|F_o|^{1/2}\,|M_o|^{-3/4}\,z. \tag{2.34}$$

New integral velocity, width and buoyancy scales can then be defined based on these variables (Morton 1959),

$$\hat{w}_m = \frac{m}{q}, \quad \hat{r}_m = \frac{q}{m^{1/2}}, \quad \hat{b}_m = \frac{1}{q}. \tag{2.35$a-c$}$$

These allow new 'scaled' local Froude and Richardson numbers to be defined,

$$\hat{Fr} = \frac{\hat{w}_m}{\left(\hat{r}_m\hat{b}_m\right)^{1/2}} = \frac{1}{\hat{Ri}^{1/2}}. \tag{2.36}$$

The solution to (2.19)-(2.21) for a negatively buoyant jet originating from a point source is plotted against ζ in figures 2.2(a) and (b) in terms of the integral scales defined in (2.35) (Morton 1959). An additional term, $\hat{H}_2 = -\hat{r}_m/(2\hat{w}_m)(\mathrm{d}\hat{w}_m/\mathrm{d}\zeta)$, is plotted in figure 2.2(c) and is discussed in more detail in §5.7. The velocity scale, $\hat{w}_m$, decreases with ζ until it reaches its maximum height at $\zeta_i = 1.454$ where $\hat{w}_m = 0$ and $\hat{Fr} = 0$. Here the width scale, $\hat{r}_m$, approaches infinity and the buoyancy scale decreases to a finite value, $\hat{b}_m = 0.791$. Figure 2.2(b) reveals that $1/\hat{w}_m$, $1/\hat{b}_m$ and $\hat{r}_m$ increase approximately linearly with ζ for $\zeta \lesssim 0.5$ ($\hat{Fr} \gtrsim 2$), implying that the velocity and buoyancy scales are nearly proportional to $\zeta^{-1} \sim z^{-1}$, and radial scale to $\zeta \sim z$, in the lower portion of the jet. Although $\hat{w}_m$, $\hat{b}_m$ and $\hat{r}_m$ all change continuously along the negatively buoyant jet, the flow may still be characterised as consisting of two separate regimes. A 'forced regime' where the scales may be approximated as linear with ζ (for $\zeta \lesssim 0.5$, $\hat{Fr} \gtrsim 2$), and a 'buoyancy dominated' regime where this approximation is no longer suitable. The $\hat{Fr} \lesssim 2$ regime is

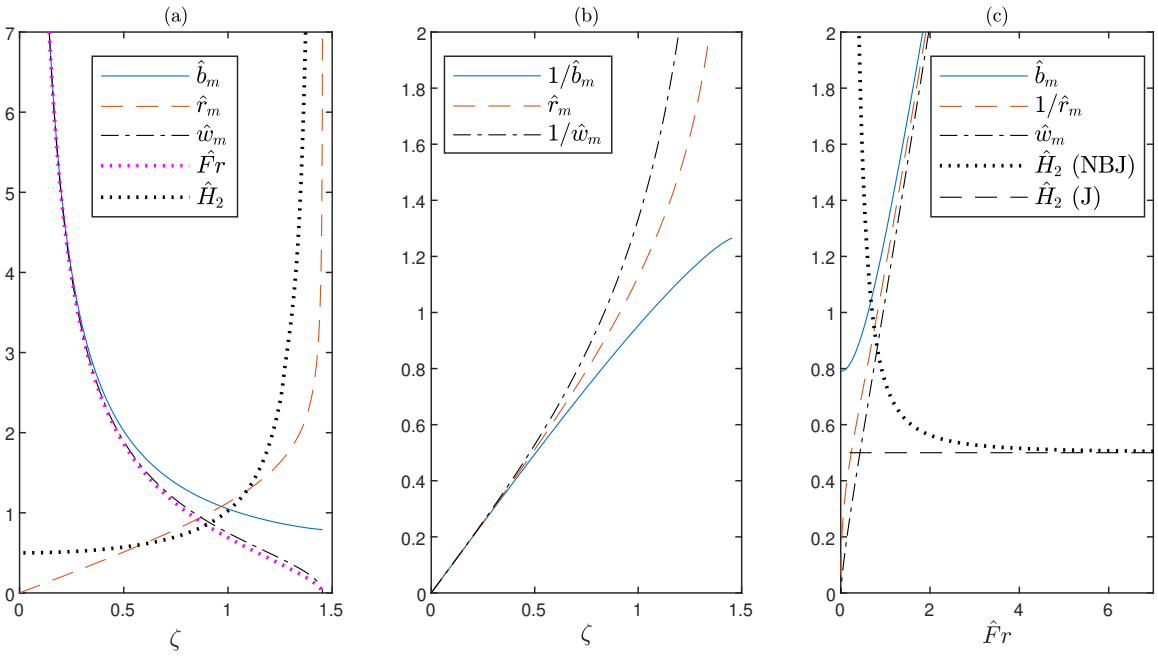

Figure 2.2: The solution to the system of ordinary differential equations in (2.19)-(2.21) for the case when $F_o < 0$ (i.e. a negatively buoyant jet, NBJ). The solution assumes fully self-similar velocity and buoyancy profiles and a constant entrainment coefficient, α, and is presented in terms of the integral buoyancy, velocity and width scales defined in (2.35). Plots of $\hat{b}_m$, $\hat{r}_m$, $\hat{w}_m$, $\hat{F}r$ and $\hat{H}_2 = -\hat{r}_m/(2\hat{w}_m)(\mathrm{d}\hat{w}_m/\mathrm{d}\zeta)$ against ζ are shown in (a). The quantities $1/\hat{b}_m$ and $1/\hat{w}_m$ are additionally plotted in (b), which, for relatively small ζ, are approximately proportional to ζ. The quantities $\hat{b}_m$, $1/\hat{r}_m$, $\hat{w}_m$ and $\hat{H}_2$ are plotted against $\hat{F}r$ in (c). For a neutral jet (J), $\hat{H}_2 = 0.5$ everywhere, which is also plotted in (c) as a horizontal line.

characterised by the strong deceleration of the flow, which is captured by the non-dimensional term $\hat{H}_2$. This is plotted in figure 2.2(c) against $\hat{F}r$ for both a negatively buoyant jet (NBJ) and neutral jet (J). For $\hat{F}r \gtrsim 2$ in the NBJ, $\hat{H}_2$ is small and similar to the neutral jet value of $\hat{H}_2 = 0.5$, corresponding to the 'forced' regime. After this, for $\hat{F}r \lesssim 2$, $\hat{H}_2$ rapidly increases with decreasing $\hat{F}r$ as the flow is strongly decelerated, corresponding to the 'buoyancy dominated' regime.

In the analytical solution for high Re_o self-similar neutral jets, which have $Fr = \infty$, w_m scales with z^{-1} exactly (Fischer et al. 1979), and so it may be expected that the velocity in self-similar, constant α, negatively buoyant jets scales in approximately the same way for sufficiently high local Fr (i.e. in the forced regime). Similarly, the scalar concentration and width scales in a neutral jet are also proportional to z^{-1} and z respectively, just as is approximately true for $\hat{b}_m$ and $\hat{r}_m$ in the forced regime. Figure 2.2(c) also shows how these scales change with $\hat{F}r$, with $\hat{b}_m$, $1/\hat{r}_m$ and $\hat{w}_m$ all scaling approximately linearly for high $\hat{F}r$.

The present investigation will show that, even in the forced regime ($\zeta \lesssim 0.5$, $\hat{F}r \gtrsim$

2), there are significant differences between the behaviour of negatively buoyant jets and what is captured in this simplified model. These include turbulence intensities and shear stress that scale differently to the mean flow, a non-constant entrainment coefficient, and the spreading of the velocity and buoyancy profiles. These are all discussed in chapter 5, which examines, in detail, the negatively buoyant jet stage prior to a return flow forming.

2.5 Summary

The study of negatively buoyant jets and fountains is a natural extension of early investigations into positively buoyant jets and plumes (Morton et al. 1956; Priestley and Ball 1955), where something as simple as the direction of buoyancy has substantial effects on both the transient and steady state flow observed (Turner 1986; Morton 1959). Several studies have sought to build on these models and apply them to NBJs and fountains, with results showing that negative buoyancy can have a significant effect on entrainment (Abraham 1967; Papanicolaou et al. 2008; Kaminski et al. 2005). The development of these integral models have included efforts to model fully developed fountains as an NBJ surrounded by a descending annular plume, and characterising entrainment between the IF, OF and AF with several constant entrainment coefficients (McDougall 1981; Bloomfield and Kerr 2000; Hunt and Debugne 2016). Although these models have had some success in predicting bulk flow properties such as the steady state rise height, it is likely these simplified models are not accurate representations of the underlying physics. For example, they typically assume self similarity and constant entrainment coefficients, while other experimental and numeric studies have shed doubt on these assumptions (Williamson et al. 2011; Cresswell and Szczepura 1993; Mizushina et al. 1982).

The application of integral model approaches to fountains, both for the initial NBJ and fully developed fountain stage, has been hampered by a lack of data of the inner flow structure. If these integral models are to be more successful, a better understanding of the effect of negative buoyancy on turbulent jets (both with and without a return flow) is a necessary and important step. In addition to assessing these models and their assumptions, a key aim of this investigation is to contribute to an improved understanding of how negative buoyancy affects entrainment and the development of these flows more generally.

The present research will undertake simultaneous two-dimensional particle image velocimetry (PIV) and planar laser induced fluorescence (PLIF) measurements of NBJs and fountains to obtain instantaneous velocity and scalar concentration fields.

Full details of the experimental method are discussed in chapter 3, followed by a validation of the set-up on a neutral jet in chapter 4. An in-depth analysis of negatively buoyant jets prior to the return flow forming is presented in chapter 5, followed by the fully developed flow in chapter 6. Mean and turbulence statistics are presented over a range of axial locations for NBJs and fountains, and the variation of the entrainment coefficient, α, is investigated. Several important differences between NBJs and neutral jets are discussed to highlight the effect of negative buoyancy, as well as between NBJs and fountains to reveal the effect of the OF. These include the extent to which the flows can be considered self-similar, and whether there is a Fr_o dependence on certain quantities such as δ_m, both of which have important consequences for theoretical modelling.

Chapter 3

Experimental method

The following chapter details the experimental method designed and implemented in the present investigation to obtain particle image velocimetry (PIV) and planar laser induced fluorescence (PLIF) measurements. The experimental procedure is outlined, including the development of a laser power correction algorithm for the PLIF measurements. This algorithm corrects for spatial variations in the shape of the laser profile, as well as the overall power magnitude, for each instantaneous PLIF image taken of the flow. A portion of the material appearing in this chapter has been adapted from the published manuscript, Milton-McGurk et al. (2020b).

3.1 Experimental rig

The flow was achieved by injecting a mixture of freshwater, ethanol and Rhodamine 6G vertically down into a 1m^3 tank of salt-water through a round pipe. Since the freshwater and ethanol mixture is lighter than the ambient saltwater, the injected fluid descends into the tank until it reaches its maximum penetration depth, and then returns towards the source, mixing with the opposing fluid and forming a fountain. A graphical illustration of the experimental set up is given in figure 3.1, and a schematic of the flow in the tank in figure 3.2. The flow was measured using planar laser-induced fluorescence (PLIF) and particle image velocimetry (PIV), capturing images using four cameras synchronised with a laser pulse using a MotionPro Timing Hub. The specifics of these two measurement techniques will be discussed in §3.3 and §3.4.

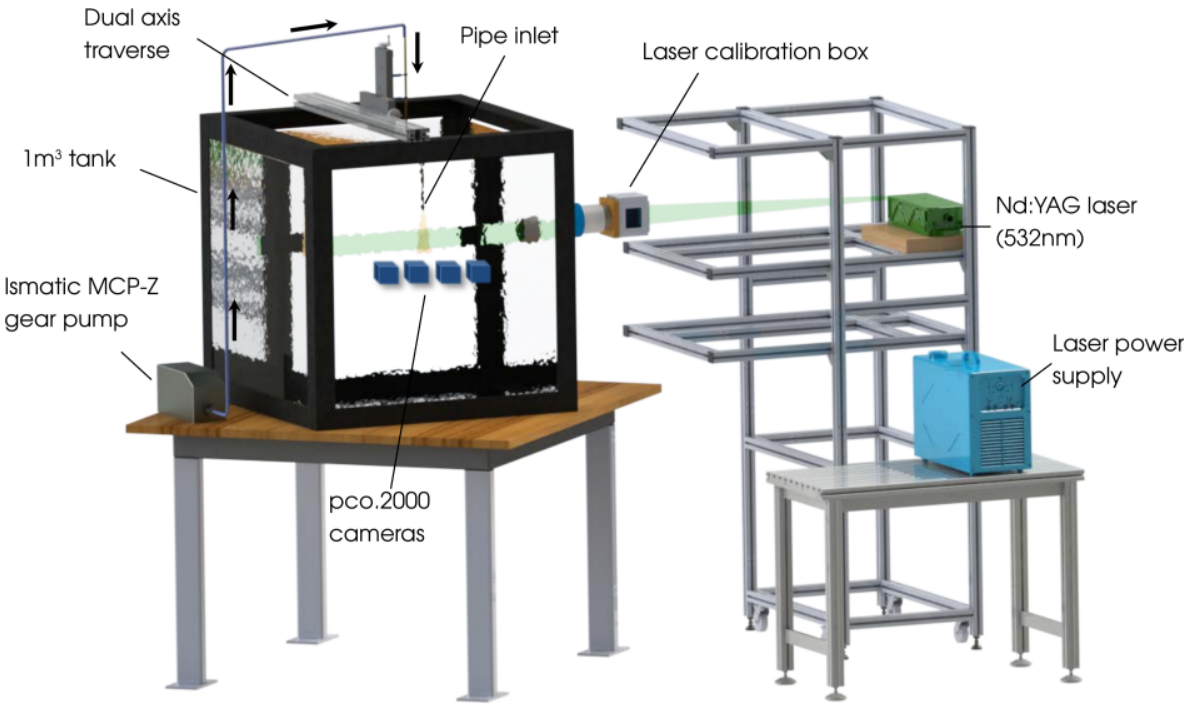

Figure 3.1: Graphical illustration of the present experimental set-up. The path of the laser sheet is indicated by the green shade (optics not shown), which enters the tank from the right and passes in front of the four pco.2000 cameras. The flow enters the tank through the pipe inlet shown above the tank, which is suspended by the dual axis traverse. During experiments, the walls of the tank and the frame holding the laser/optics are covered in black sheets. This reduces the amount ambient light in the tank, and provides an additional level of protection to lab occupants from the laser.

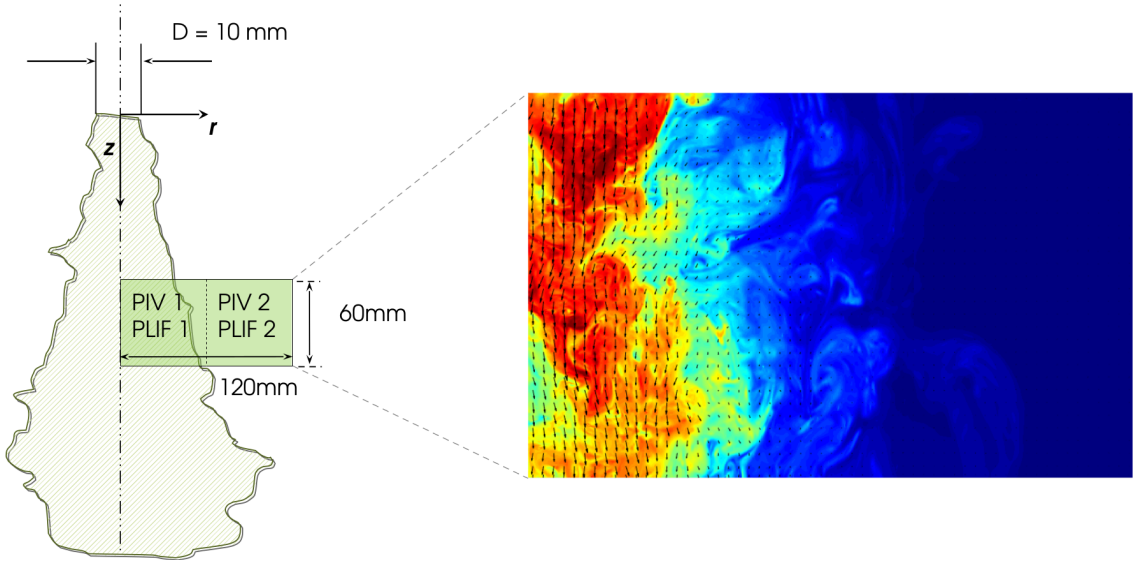

Figure 3.2: Schematic of a negatively buoyant jet prior to the return flow forming. The region of interest is indicated by the green rectangle, and an example of a processed experimental image with the velocity vectors and scalar field is shown. The region of interest is captured by two pairs of PIV and PLIF cameras, with the images stitched together to form a single image like shown.

3.1.1 Support frames

The core experimental apparatus available for the project included a 1 m^3 tank, four pco.2000 CCD cameras, a 145 mJ 532 nm Evergreen Nd:YAG laser, several optical lenses, and an Ismatic MCP-Z gear pump. Two Aluminium frames were designed and constructed using Maytech beams. One to hold the laser and optics, shown in 3.1, and the other to hold the cameras pointing at the region of interest. Both frames were designed so that the height of the platform holding the laser/cameras could be manually adjusted so that the flow could be measured at different axial distances.

3.1.2 Pipe set-up

To suspend the pipe above the rig, an additional beam was attached to the top of the tank with two perpendicular adjustable Velmex sliders which allowed the pipe to be finely adjusted in both the horizontal and vertical planes. Horizontally, so that the pipe could be correctly aligned in the centre of the laser sheet, and vertically so that the location of the flow inlet could be adjusted relative to the cameras, effectively moving the region of interest up and down the flow. The pipe was attached to the sliders using holders originally designed for optics, which steadily held the pipe in place and allowed for it to be easily interchanged with pipes of different diameters.

The present experiments used pipes with diameters from $D = 5$mm to 10mm with entry lengths $\geq 75D$, ensuring that the flow would be fully developed by the time it exits the pipe. By changing the salinity of the ambient fluid, the diameter of the pipe, or the flow rate of the gear pump, a range of Fr_o could be obtained at suitably high Re_o. The present study investigates fountains and NBJs with $10 \lesssim Fr_o \lesssim 30$ and $4500 \lesssim Re_o \lesssim 6000$, at axial locations $18 \lesssim z/D \lesssim 39$.

3.1.3 Laser optics

The Nd:YAG laser emits 532 nm light in the form of a circular, approximately Gaussian, beam with a near-field diameter ≤ 6.35 mm. This beam must be re-shaped into a thin rectangular sheet that will pass into the field of view of the cameras and through the centre-plane of the flow. This is accomplished using a cylindrical and spherical lens pair, separated by the correct distance so that the beam expands to a width of approximately 60 mm (the approximate vertical field of view of the cameras) and then remains at this width, converging to a minimum thickness in the region of interest. In the present case, the required lenses were a 75 mm cylindrical lens and a 750 mm spherical lens (focal lengths). The beam exits the laser, reflects of the mirror and passes through the cylindrical lens where it begins expanding in the vertical direction. Once it expands to a width of approximately 60 mm, it passes through the spherical lens where it maintains its width and begins to thin as it passes through the tank filled with ambient fluid. The thickness of the laser sheet was measured to be less than 1 mm in the region of interest.

3.2 Experimental procedure

This section will detail the experimental procedure used to obtain raw images of the flow for the PIV and PLIF measurements, which would later be processed to obtain velocity and density fields through the algorithms discussed in §3.3 and §3.4.

3.2.1 Fluid preparation

Degassing

Initial testing of the flow set-up indicated that the presence of air bubbles in the fluid could cause problems. Not only are bubbles buoyant and so can affect the flow being measured, but if the laser sheet passes through one then high energy light may reflect out towards the cameras, distorting results and potentially damaging the sensors. An unexpected reflection of the laser sheet out of the tank is also a

safety issue, and so it is essential to minimise the probability of bubbles forming in the flow. In preparing the source and ambient fluids, freshwater was taken from the local water supply and passed through a 'degassing' system consisting of a heat exchanger and hot water urn. The water, sourced from the mains supply, is passed through the heat exchanger and then into the insulated hot water urn. Here the water is heated to approximately 70°C, which then flows out of the urn and back through the heat exchanger (heating the incoming fluid), and then eventually out of the degassing system and into a large storage tank. This process allowed most of the air to escape the water, and was found to reduced the prevalence of bubbles in the fluid. The water was then left to cool in the storage tank before being used in any experiments.

Refractive index matching

The refractive index of a saline solution is affected by its salinity, and so if pure freshwater was used as the source fluid, it would have a different refractive index to the saltwater ambient. When the laser passes through the flow, it will refract and change direction depending on the (varying) local density of the fluid. This will result in the illuminated part of the flow no longer being the centre plane of the NBJ/fountain, or in the focal plane of the cameras, leading to a measurement error (Budwig 1994). To remedy this, ethanol is added to the freshwater solution, which lowers the density of the water and increases its refractive index. Once the correct amount of ethanol is added, the refractive indexes of the source and ambient fluid are 'matched', thus negating the issue of refraction of the laser sheet. Based on fluid property data for aqueous solutions (Haynes 2014), the salinity and ethanol content of the ambient and source fluid required to obtain a desired density difference, while simultaneously having the same refractive index, could be calculated. The required amount of ethanol and salt was then added to freshwater to produce the source and ambient fluids during preparation for a given experiment. A separate testing apparatus, which involved shining a 532 nm laser beam through the two fluids, was used to verify the refractive indexes were indeed the same.

Once matched, the density of the source and ambient fluids were measured using a densitometer to an accuracy of 0.1 kg m^{-3}. This then sets the source buoyancy of the flow, and the desired Fr_o may be achieved by adjusting the gear pump flow rate. At this stage, the required amount of Rhodamine 6G dye needed for the PLIF measurements was also added to the source fluid. This was typically $\lesssim 3$ mL added to $\gtrsim 60$ L, and so had a negligible affect on the refractive index and density of the source fluid. Additional details about the PLIF procedure are given in §3.4.

3.2.2 Laser alignment and target images

Target images

In order to convert between the 'pixel' and 'real world' coordinates in a given image of the flow, it was necessary to take a 'target image' prior to each experiment. This was an image of a checker-board pattern, with squares of known dimensions and a 'reference circle', printed onto an object that was placed into the tank after it was filled with the ambient fluid. Prior to an experiment, the target sheet was carefully placed so that its face was in the plane of the laser sheet and the cameras adjusted so that they are also focused on this plane. At this stage, the vertical location of the pipe may be adjusted up and down using the sliders, effectively moving the region of interest of the cameras relative to the pipe inlet. Images of the target sheet are then taken from each camera, and the real world location of the reference circle relative to the pipe inlet is recorded. An algorithm, written for a previous project in MATLAB (Williamson et al. 2018; Bartos 2012), was used to take these images and generate real world-coordinates based on the inputted location of the reference circle and size of the squares on the checker-board pattern. This process allows lens distortion effects, which would be the same in both images of the target sheet and the flow, to be accounted for.

3.2.3 Data Acquisition

Camera and laser synchronisation

Images of the flow were captured using four pco.2000 CCD cameras synchronised with pulses from the 532 nm Nd:YAG laser using a MotionPro timing tub. Additional images used for a laser power correction algorithm, discussed further in §3.4.2, were obtained from an IDS USB 3.0 uEye camera. The system was capable of capturing pairs of images at a frequency of 7 Hz.

NBJ and fountain runs

Each experiment would be optimised to gather data from either the initial negatively buoyant jet stage of the flow, or the fully developed fountain stage. For the NBJ experiments, there is a much shorter time frame where it is possible to obtain data, and so in a single 'run', images are captured at the maximum frequency of the system (7 Hz) and over a shorter overall time (e.g. 15 s), after which the flow is stopped. This would be repeated several times (e.g. 10 'runs') in order to obtain a sufficient number of images of the flow. Since a fully developed fountain is quasi-steady, these

may be imaged for much longer time periods that are only limited by the memory and data transfer speed of the cameras. These runs were typically imaged at a lower frequency (e.g. 3 Hz) and for longer time period (e.g 100 s), allowing for more images to be captured overall per run.

3.3 Particle image velocimetry (PIV)

Particle image velocimetry (PIV) is an optical measurement technique that measures the instantaneous velocity of fluid in some flow. The general principle involves using pairs of images taken at two close instances in time and detecting the location of visible particles present in the flow. If the flow is moving then the particles will be in slightly different locations in each image, and it is possible to calculate their displacement using various algorithms (Keane and Adrian 1992; Hart 2000; Adrian and Westerweel 2011). If the time between the two images is known, then the velocity of the particles can be estimated, and provided the particles are small enough to follow the fluid motion, then this is an estimate of the fluid velocity. In PIV, groups of particles within a specified 'interrogation area' are detected, rather than individual particles, and the velocities obtained correspond to the average velocity of the particles in each interrogation area (Adrian and Westerweel 2011).

There are several different PIV methods available that are capable of obtaining either two or three dimensional velocity vectors of a flow. Two-dimensional (planar) PIV requires a single camera to capture images of a plane, typically illuminated by a thin light or laser sheet, in some flow. Computing the displacement of particles in each image then allows a two dimensional velocity vector field to be estimated, corresponding to flow in the plane of the illuminated sheet (Keane and Adrian 1992; Westerweel 1994). There are also three-dimensional methods, such as stereographic PIV, which requires a second camera also focused on a thin illuminated sheet, and is capable of obtaining sufficient data to reconstruct the 3D vectors within that plane (Willert 1997; Soloff et al. 1997). By using four cameras and an illuminated volume it is possible to reconstruct the full 3D vector field within that volume, which is referred to as tomographic PIV (Elsinga et al. 2006). This clearly provides the most complete data set for velocity measurements in a three-dimensional flow, but requires a more complex experimental set-up and computationally expensive image processing procedure (Adrian and Westerweel 2011).

Fountains and negatively buoyant jets produced from a round source are statistically axisymmetric flows, and so two-dimensional PIV measurements of a plane through the centreline are sufficient to estimate many of key the radial profiles.

This includes the terms appearing in the Reynolds averaged conservation of mass, momentum, buoyancy and kinetic energy equations in (2.4)-(2.7), such as $\overline{w}$ and $\overline{w'u'}$. The scalar and mass flux terms, such as $\overline{b}$ and $\overline{u'b'}$, similarly require only two-dimensional scalar measurements. The broad aim of the present study is to investigate the development of NBJs and fountains, with a particular focus on entrainment and self-similarity. Measuring the aforementioned mean and turbulent profiles, which may be obtained from planar measurements, allows this to be pursued. The circumferential velocity components could be obtained from stereographic or tomographic PIV measurements, but these do not appear in the most relevant conservation equations due to the axisymmetry, and significant progress towards the present aims can be made without them. Two-dimensional PIV is therefore deemed sufficient for the purposes of this investigation. This is simpler to set-up experimentally and is less computationally intensive than the 3D methods. Another advantage is that the additional cameras required for stereographic and tomographic PIV can instead be used to widen the field of view in a 2D PIV system. Planar PIV will be therefore be the method pursued for obtaining velocity measurements in the present experimental investigation.

3.3.1 PIV algorithm

In the present experimental set-up, the flow was illuminated using a double pulsed laser, which would rapidly fire two pulses separated by a short interval, dt, at a rate set by the laser frequency. Each pulse would be accompanied by one image from the PIV cameras, so if the laser frequency was 7 Hz, then there would be 7 'double pulses' per second, and 14 images per second taken from each PIV camera. The time period, dt, was set so that the typical displacement calculated in a given image pair was of the order of 5 pixels (Adrian and Westerweel 2011). The value of dt would depend on the source velocity and location of the region of interest, but was typically in the range $0.5 \lesssim dt \lesssim 2$ ms. For the present measurements, a cross-correlation based algorithm implemented by the open source MATLAB package, PIVsuite, was used to calculate the particle displacement (Vejražka et al. 2018). This implements a multi-pass, multi-grid interrogation scheme, where the displacement calculated from each 'pass' is used to refine the computation in subsequent passes, as well as reducing the size of the interrogation window. This reduces the amount of spurious vectors arising due to a loss of correlation between images, allowing for a smaller window size to be used in the final pass and hence better spatially resolved measurements to be obtained (Adrian and Westerweel 2011; Westerweel et al. 1997; Westerweel 1994). For the present measurements, a final interrogation area of 24×24 pixels

(0.78mm×0.78mm) with a 75% overlap between adjacent windows was used.

There were many natural impurities in the water supply for the experiments, which were detectable by the PIV cameras and appeared as approximately $3-8$ pixel particles in the images. These natural particles provided sufficient particle density in the PIV images for the cross-correlation algorithm, and additional artificial particles were not needed. This also reduced the possibility of the light scattered off seeded particles distorting the PLIF measurements. A 532 ± 2mm band-pass filter was used on the PIV cameras to filter out ambient light and fluorescence from the PLIF signal, discussed further in §3.4.1, but allowing scattered light from the particles through to the CCD sensor. Although the PIV package used to process the present images has been used in other studies (Williamson et al. 2018; Vejražka et al. 2018; Tan et al. 2015), it was still useful to validate its application to the current experimental set-up and chosen settings. This is discussed in chapter 4.

3.4 Planar laser induced fluorescence (PLIF)

Planar laser induced fluorescence is an optical measurement technique capable of measuring the scalar concentration, or density, of a flow. This is done by adding a fluorescent dye to the source fluid, which, when excited by a laser, fluoresces with an intensity proportional to the dye concentration at that point. Images are taken of the illuminated flow and, with appropriate calibration, the pixel intensity of the fluoresced fluid can be used to determine the dye concentration at that point, which can then be used to infer the density (Crimaldi 2008; Shan et al. 2004; Ferrier et al. 1993). As with PIV, three dimensional laser induced fluorescence methods have also been developed that can measure the scalar concentration in a volume (Medford et al. 2011; Wu et al. 2015), but as previously mentioned, obtaining planar measurements is sufficient for the present investigation given the axisymmetry of the flow. The full calibration and image processing procedure for the present PLIF measurements is discussed in the following sections.

3.4.1 Fluorescent dye

Rhodamine 6G was chosen as the fluorescent dye to act as a scalar tracer in the PLIF measurements. This has a high absorption near the laser wavelength of 532 nm and peak emission at approximately 560 nm (Zehentbauer et al. 2014). Since the concentration of Rhodamine 6G used in the present experiments was so low, a diluted solution of 0.5 g/mL of Rhodamine 6G in water was first made. This diluted solution could then be added to the source fluid using a syringe, rather

than directly adding pure Rhodamine 6G. The diluted Rhodamine 6G solution was made by carefully placing the required amount of Rhodamine 6G (in the form of a fine powder) in a container, and measuring its weight using an digital scale to the accuracy of ±0.001 g. The required amount of water, measured using a volumetric flask accurate to ±0.4 mL is then added to produce the diluted solution.

The Rhodamine 6G concentrations used in the sourced mixture were in the range 20 ppb $\lesssim K_0 \lesssim$ 160 ppb, with the higher concentrations corresponding to experiments where the region of interest was further downstream from the inlet, after the jet had undergone considerable mixing/diluting. The concentration in the region of interest was typically $K \lesssim 10$ ppb, well within the linear excitation range reported by Zehentbauer et al. (2014), and confirmed by our own measurements. A B+W Orange MRC 040M filter was used on the PLIF cameras to cut off light below approximately 550 nm, allowing the fluorescence from the dye, but not the scattered light from the particles, through to the CCD sensor.

3.4.2 Laser power correction

Although the present Nd:YAG laser is capable of operating at high frequency and power, the power output and profile shape of the beam can vary up to 5% between individual pulses. To account for this variation, the 'laser camera' (IDS USB 3.0 uEye camera) was used to capture the fluorescence of a uniform water and Rhodamine 6G mixture before it reaches the region of interest. The mixture sits inside the 'laser calibration box', shown in figure 3.3, which is fitted with anti-reflective coated optical glass and placed in the path of the laser sheet outside of the main tank. The box was made from acrylic, painted black to minimise reflections, and designed so that the anti-reflective glass could be removed and cleaned as required.

The captured image from the laser camera of the fluoresced fluid is then a measurement of the laser power profile of that pulse. Images captured of the fluid in the laser calibration box will be denoted I_p, while images of the region of interest denoted I. The box contained approximately 1L of the water with a typical Rhodamine concentration of 15 ppb. It was observed that the pixel intensities in I_p would gradually decrease after several hundred images/laser pulses, which was attributed to some percentage of the dye particles in the box photobleaching and losing their fluorescence, thus reducing the overall signal. This effect was negligible within the maximum number of images of a single run ($\lesssim 400$), but could be detected after several runs (e.g. $\gtrsim 1200$ images). To prevent this effect, and thus maintain reliable power measurements, the box was re-filled with a fresh (unbleached) Rho-

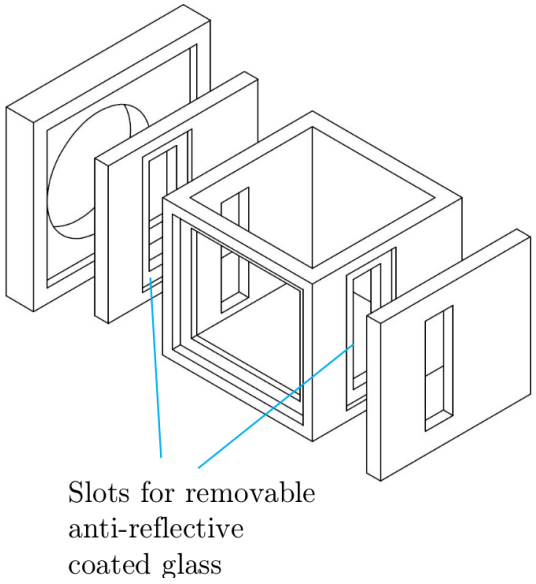

Figure 3.3: Exploded schematic diagram of the 'laser calibration box'

damine 6G mixture after each run. With a measurement of the power profile of the laser sheet for any individual pulse, the corresponding PLIF images in the region of interest could be corrected so that differences in the profile (in both magnitude and shape) between pulses were accounted for. After this correction, the PLIF images were filtered using a wavelet based denoising algorithm designed for CCD cameras (Weinkauff et al. 2015).

3.4.3 Image processing algorithm

The PLIF image processing procedure can be summarised by (3.1)-(3.3), where c is a measurement of the scalar concentration field corresponding to a given image. Equation (3.3) corresponds to the final processing method used, and (3.1) and (3.2) are methods that were tested for validation purposes.

(i) Standard method.

$$c = \frac{I - I_b}{\hat{I}_c} \tag{3.1}$$

(ii) Power profile corrected.

$$c = \frac{(I - I_b)/P}{\tilde{I}_c} \tag{3.2}$$

(iii) Power profile corrected and images denoised with wavelet filter.

$$c = \frac{\mathcal{D}\{(I - I_b)/P\}}{\mathcal{D}\{\tilde{I}_c\}} \tag{3.3}$$

Here I corresponds to the raw PLIF image of the region of interest taken during an experiment, I_b is a background image capturing any ambient light present, and $\hat{I}_c$ and $\tilde{I}_c$ are reference images corresponding to the maximum possible Rhodamine concentration in the tank. Images I_b, $\hat{I}_c$ and $\tilde{I}_c$, and the procedures for generating them, are discussed further in §3.4.4-3.4.5. These images can be used to calculate the scalar concentration, c, in the region of interest through (3.1) (Shan et al. 2004; Crimaldi 2008), which assumes variations in the laser power profile are negligible between pulses. Equation (3.2) omits this assumption by including the laser power profile, P, which corresponds to the PLIF images I. The third method, using (3.3), additionally includes applying the wavelet-based denoising filter (Weinkauff et al. 2015), denoted here by $\mathcal{D}\{\cdot\}$. All three methods rely on weak absorption (valid for low dye concentrations), and assume that light attenuation along the laser path is similar in I, $\hat{I}_c$ and $\tilde{I}_c$ (Shan et al. 2004), which is discussed further in §3.4.5. It additionally assumes that lens vignetting effects are the same in I, $\hat{I}$ and I_b (Ferrier et al. 1993).

In order to obtain the one-dimensional power profile, P, the image taken of the laser calibration box fluid, I_p, needed to be mapped to a one-dimensional vector with matching vertical world-coordinates to the main PLIF image, I. Any small misalignment of the laser optics could cause the laser sheet to widen/contract or shift vertically between the laser calibration box and the region of interest in the tank, which could result in I and P being vertically misaligned. This effect is negligible within the region of interest of I (width $\lesssim$ 120mm), but may not be in the distance between the region of interest and the laser calibration box (approximately 800mm). To account for this, and to ensure P is correctly aligned with I, an additional set of reference images were taken where a small vertical section of the laser sheet was temporarily deliberately obstructed by a cable. The location of the intensity dip in I_p and I was then matched so that the one-dimensional power profile extracted from I_p could be interpolated to exactly match the world-coordinates of the laser sheet appearing in I. This procedure allows the laser power profile, P, to be calculated from (3.4),

$$P = \mathcal{M}\left\{\overline{I_p}\right\}, \tag{3.4}$$

where $\overline{I_p}$ denotes the mean column in image I_p, and $\mathcal{M}\{\cdot\}$ represents mapping the world-coordinates to ensure P and I are correctly aligned.

Validation

This PLIF processing procedure was validated by taking 100 images of the tank containing fluid of a known concentration (defining this as $C = 1$), and running it

through the three processing methods given in (3.1)-(3.3) to compute the concentration field. The difference between the calculated concentration and the actual concentration is then the error. The results of this validation are presented in figure 3.4, which shows the mean spectra of the error in a single column of the images. This was computed by taking the Fourier transform of the error in this column in every image, and then calculating the mean. The ∘ and △ markers in figure 3.4 show that the error at low to medium frequencies is reduced when the power correction is applied (method (ii) versus (i)), but that there is little effect at high frequencies. This corresponds to reducing the error due to variations in both the mean power and the profile shape between pulses, without having a significant effect on the high frequency noise. Conversely, when the denoising filter is applied, it does not significantly affect the lower frequencies but reduces the error in the high frequency noise. Method (iii), applying both the power profile correction and denoising filter, was therefore used in calculating the concentration field from the PLIF measurements.

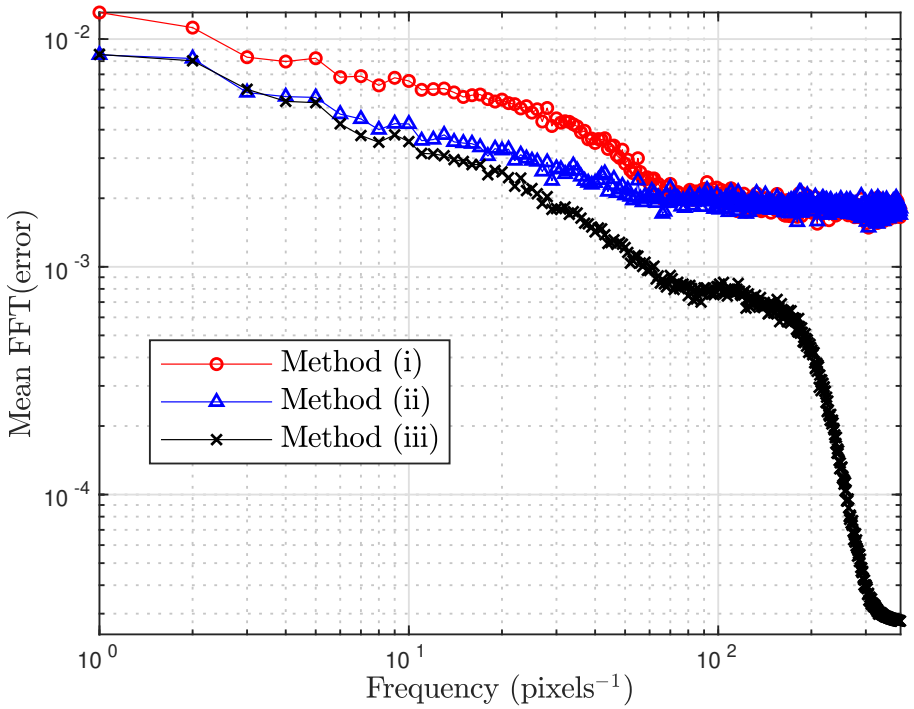

Figure 3.4: The spectra of the error in scalar concentration measurements produced from the three different PLIF processing methods described in (3.1)-(3.3). The ∘ markers correspond to the 'standard' method (i) without any laser profile correction or denoising, the △ to when only the profile correction is applied (ii), and the × for when both the profile correction and denoiser is applied (iii).

3.4.4 Background image

To account for the camera's black level and any ambient background light present in the experiments, a background image, I_b, without any flow present was taken so that it could be subtracted from the experimental images, I. However, due to the experimental procedure used in the present study, two background images were taken, $I_{b,0}$ and $I_{b,end}$ (one before the experiment and one at the end). This is because in order to capture a sufficient number of images to obtain statistical convergence, each experiment consisted of multiple 'runs' that would linearly increase the background signal. Each run involved operating the pump for a fixed length of time (typically between 15 to 130 s) using the pump's timing mode. This would add a known volume of source fluid to the tank each run, slightly changing the ambient fluid's density and Rhodamine 6G concentration. Because of the short experimental time and large tank volume relative to source fluid, after stirring around the tank the ambient fluid density would change by $\lesssim 0.008\%$ and Rhodamine concentration by $\lesssim 0.4$ ppb each run. The change in density has a negligible effect on the source Froude and Reynolds numbers, and so is assumed to have a negligible effect on the flow dynamics. However, the increasing concentration of Rhodamine 6G dye in the ambient can be detected as a linearly increasing background signal in the PLIF images. This effect is accounted for by linearly interpolating between $I_{b,0}$ and $I_{b,end}$ to create an image, I_b, for each run in the experiment. This procedure was validated during an experiment in which background images were taken prior to each run so that the growing pixel intensity could be recorded and confirmed to be linear. Figure 3.5 shows the value of both a single pixel and the mean of all the pixels in these background images with each run, with a second axis also indicating the Rhodamine 6G concentration in the tank at the time. The trend is linear, and thus it was considered sufficient to take background images only at the start and end of the experiment, $I_{b,0}$ and $I_{b,end}$, and interpolate between them to obtain I_b for each run.

3.4.5 Calibration reference image

The PLIF algorithm described by (3.1)-(3.3) requires the reference images, $\hat{I}_c$ and $\tilde{I}_c$, which are obtained by taking 100 images of the tank filled with fluid with a constant Rhodamine 6G concentration, typically $K_c \cong 5$ ppb, and applying (3.5) and (3.6),

$$\hat{I}_c = \langle I_c - I_{b,0} \rangle \frac{K_0}{K_c}, \tag{3.5}$$

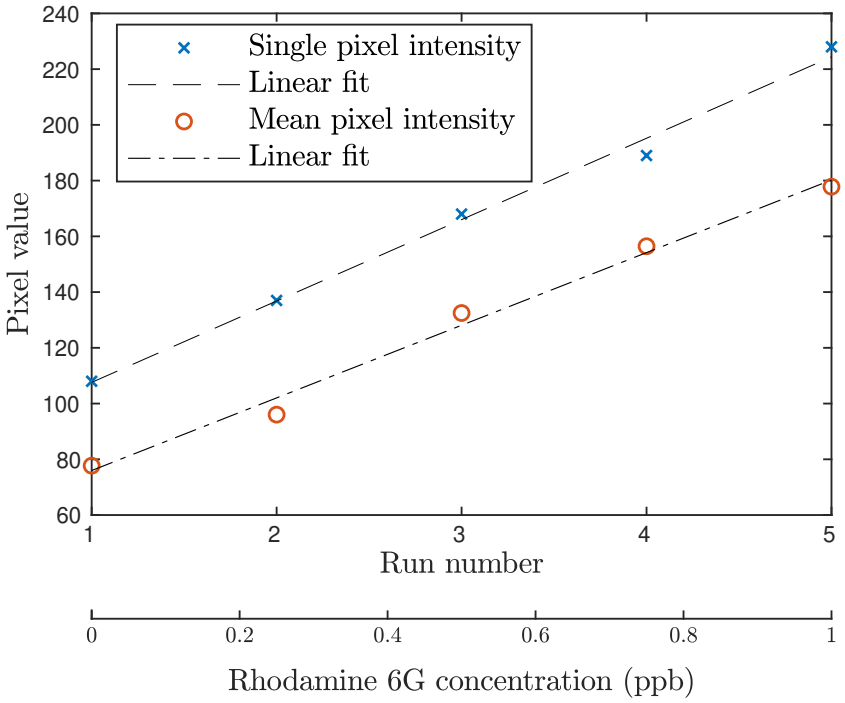

Figure 3.5: The intensity value (count) of a single pixel, and mean of all the pixels, in several background images taken prior to each run during an experiment. A small, fixed, amount of Rhodamine 6G is added to the ambient during each run, and so the background signal grows linearly.

$$\tilde{I}_c = \langle (I_c - I_{b,0})/P_c \rangle \frac{K_0}{K_c}. \tag{3.6}$$

Here I_c is a single image of the tank containing fluid with uniform Rhodamine concentration K_c, the corresponding laser profile is P_c, and the angle brackets denote averaging over all 100 images. The Rhodamine 6G concentration of the source mixture, typically between 40 and 160 ppb, is denoted by K_0. Images $\hat{I}_c$ and $\tilde{I}_c$ are then reference images that correspond to a maximum scalar concentration of $c = 1$, where $\tilde{I}_c$ employs the laser profile correction on each image in the ensemble and $\hat{I}_c$ does not.

During experiments, the PLIF cameras are focused near the centre of the 1 m^3 tank where the flow is, meaning the laser sheet travels through approximately 500 mm of ambient fluid before it enters the region of interest. There will be some light attenuation of the laser sheet along this path, so there will be less laser light in the region of interest than in the laser calibration box. There will also be slightly less laser light available in the left side of the images than than the right side as the sheet attenuates light within the region of interest. This light attenuation in the laser path is accounted for in the reference images, $\hat{I}_c$ and $\tilde{I}_c$, as they will be subject

to a similar attenuation effect as the PLIF images, I. The attenuation will not be exactly the same since in $\hat{I}_c$ and $\tilde{I}_c$ the laser sheet travels through the ambient with a uniform Rhodamine concentration of $K_c \cong 5$ ppb, while during experiments the Rhodamine concentration will not be uniform (it will be highest along the jet centreline and low further from the jet). The difference in attenuation in these two cases is assumed to be negligible, and so when the experimental images are divided by $\tilde{I}_c$ or $\hat{I}_c$ in (3.1)-(3.3), the intensity differences as a result of light attenuation approximately cancel out (Crimaldi 2008; Shan et al. 2004).

Figure 3.6 shows the pixel count of a single horizontal row in two images, normalised by the mean pixel count in that row and a reference image. The images correspond to the mean of 100 images taken while the laser was firing into the tank full of freshwater, with and without Rhodamine 6G added. Since they have been divided by a reference image, where the tank contained an intermediate level of Rhodamine (approximately 2 ppb), the effect of lens vignetting is accounted for (Ferrier et al. 1993). If the light attenuation in the tank was strongly affected by the Rhodamine concentration, then the overall shape of these two lines would be notably different. For example, if the presence of Rhodamine increased the attenuation then this would become increasingly prevalent from the right to left of the region of interest as the laser passed through more Rhodamine solution. In this case, we would expect the 5 ppb line in figure 3.6 to be significantly lower than the 0 ppb line on the left hand side of the image. This is not observed, and instead both curves are approximately horizontal. We therefore do not see a significant difference in attenuation in this low Rhodamine concentration range ($0 \lesssim K \lesssim 5$ ppb), which is similar to the range in the region of interest during the experiments. This supports the assumption that attenuation in the reference images, $\tilde{I}_c$ and $\hat{I}_c$, will be similar to the experimental images, I, and so the effect will approximately 'cancel out' when computing c using (3.1)-(3.3).

3.5 Further data processing

The present experiments involved obtaining images from two 'pairs' of PIV and PLIF cameras. Each pair consists of one PIV and one PLIF camera with overlapping regions of interest, so that velocity and scalar concentration fields corresponding to the same region in space are obtained. The two camera pairs are adjacent to each other (with a small overlap) so that a wider field of view of the flow is obtained. Each pair of PIV/PLIF images are interpolated onto a common grid and then 'stitched' together by matching the world-coordinates of the small overlapping region. An

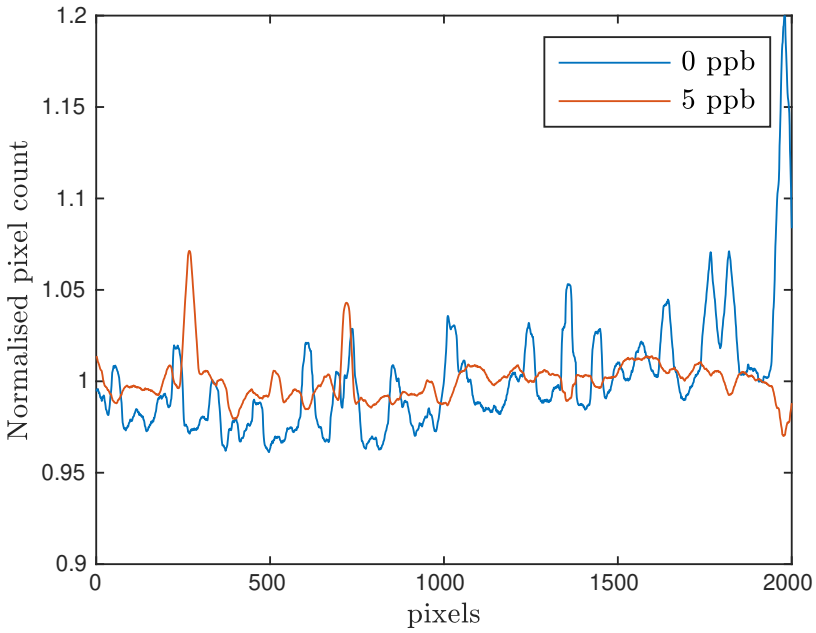

Figure 3.6: The pixel counts along a single horizontal row in two images that correspond to the tank filled with freshwater with and without Rhodamine 6G solution added. The images have been normalised by the mean pixel value in that row and a reference image of the tank containing approximately 2 ppb of Rhodamine 6G (to account for lens vignetting).

example of a pair of PLIF fields before interpolation/stitching, and after, is shown in figure 3.7. A stitched image overlaid with velocity vectors was also shown in figure 3.2.

3.6 Summary

An experimental set-up has been designed and constructed that allows for simultaneous PIV and PLIF measurement to be obtained for vertically aligned negatively buoyant jets and fountains entering a tank from above. The same rig can also be used to take measurements of neutral jets by simply using the same fluid as the source and ambient, and ommiting the 'refractive index matching' stage discussed in §3.2.1.

Figure 3.8 shows a flow chart of the experimental procedure. The 'Fluid preparation' and 'Laser alignment and target images' were discussed in §3.2.1-3.2.2. The 'Pre-experimental PLIF calibration images' stage corresponds to capturing images for $I_{b,0}$, while 'Post-experimental PLIF calibration images' corresponds to capturing images for $I_{b,end}$ and I_c. These are needed to obtain a measurement of scalar concentration from the raw PLIF images, as was discussed in §3.4.3-3.4.5. The 'Data

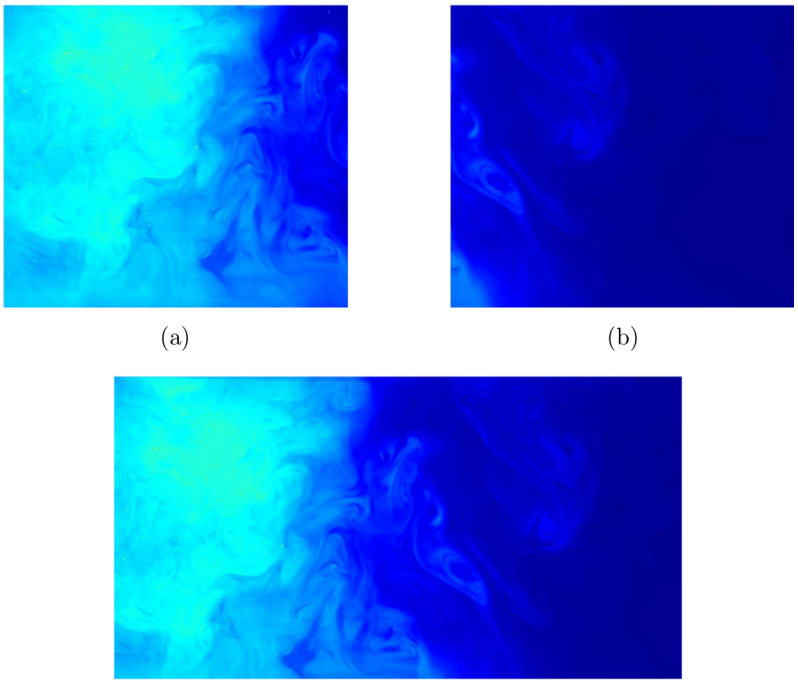

(a) (b)

(c)

Figure 3.7: Processed scalar concentration fields images taken from the left PLIF camera (a), the right PLIF camera, (b), and after interpolating onto a common grid and stitched together, (c).

acquisition (experimental runs)' stage is when the flow is actually produced and images captured.

The last stage in the figure 3.8 flow chart is the 'PIV+PLIF image processing', which is broken down into more specific stages in figure 3.9. This figure indicates the order required for processing the raw PIV and PLIF images to obtain velocity and scalar concentration measurements. As indicated in the chart, the first stage is to process the target images in order to obtain real world-coordinates for the PIV and PLIF images. Using the world-coordinate data the PLIF calibration images, such as $\hat{I}_c$, may be calculated, as discussed in §3.4.5. With the necessary calibration images obtained, all PIV and PLIF images may be processed using the algorithms discussed in §3.3-3.4 to obtain instantaneous velocity and concentration fields corresponding to each image. Once this is complete the fields are interpolated onto a common grid and then stitched together using the world-coordinate data, and the processing is complete.

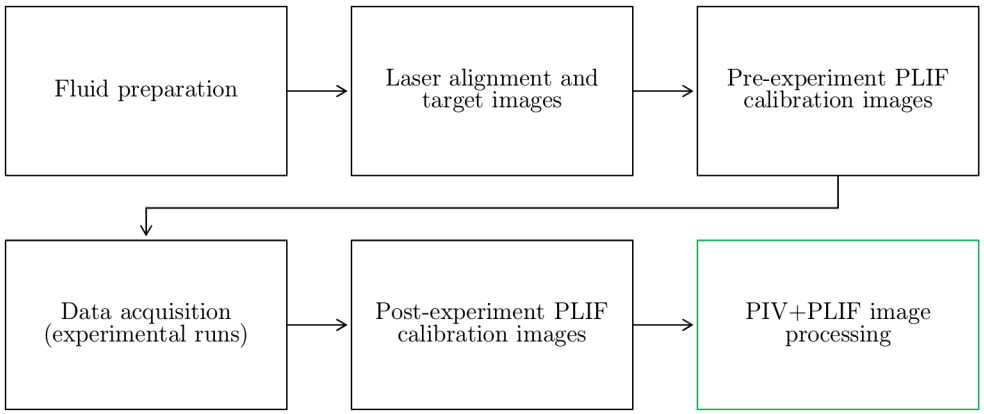

Figure 3.8: Flow chart summarising the steps required in the experimental procedure to obtain velocity and scalar concentration measurements.

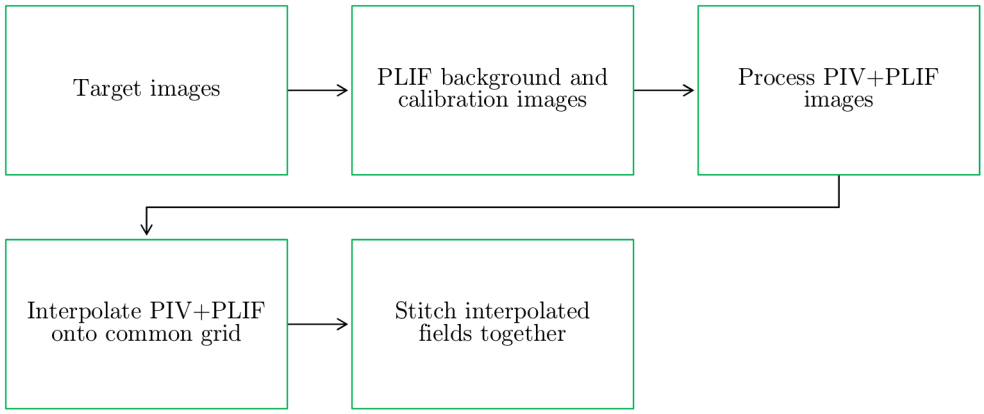

Figure 3.9: Flow chart detailing the order of steps in the image processing procedure to obtain velocity and scalar fields from raw PIV and PLIF images.

Chapter 4

Validation

The following chapter will detail the validation undertaken for the experimental method discussed in chapter 3. This is done by using the present experimental set-up to obtain measurements of a neutrally buoyant turbulent jet originating from a round source, a well understood flow with an abundance of data available from previous studies. Several key elements of the image processing procedure are examined, including the PIV interrogation and the world-coordinate grid interpolation. The neutral jet results obtained from both the PIV and PLIF measurements are found to be consistent with existing literature. A portion of the material appearing in this chapter has been adapted from the published manuscript, Milton-McGurk et al. (2020b).

4.1 PIV algorithm

4.1.1 Interrogation area

A key parameter in the PIV algorithm is the size of the interrogation area (IA), the square window measured in pixels (px^2) that the cross-correlation algorithm uses to detect the displacement of particles in an image pair. The smaller the IA, the higher the spatial resolution of the velocity field obtained from each image pair. However, if the area is too small then there may be insufficient particles in a given window for the cross-correlation algorithm to detect, resulting in spurious, invalid vectors that must be discarded and/or replaced (e.g. by interpolation) (Westerweel 1994; Adrian and Westerweel 2011). Spurious vectors may also arise due to a out-of-plane motion, where a particle moves outside of the plane of the laser sheet after the first image, and so cannot be detected in the second. To determine the most appropriate

IA to use with the present experimental set-up, the same set of PIV images taken of a neutral jet was processed using different sized IAs. Additionally, the number of passes in the multi-pass interrogation, and the percentage overlap between adjacent windows, was also adjusted.

Table 4.1 summarises the results from these PIV processing tests, listing the settings used and the overall percentage of valid vectors detected. The highest percentage of valid vectors corresponds to the largest IA, 96% with a size of 32×32 px^2, while the lowest detection rate had the smallest IA, 80% with an 16×16 px^2 area. It was also found that increasing the percentage overlap between adjacent windows from 50% to 75% increased the percentage of valid vectors, while using 2 passes rather than 4 did not have a significant effect. It was found that with 2 passes, a 75% overlap and a final IA size of 24×24 px^2, an acceptable detection rate of 94% valid vectors is obtained (Keane and Adrian 1992; Westerweel 1994; Adrian and Westerweel 2011). This is only slightly lower than the 32×32 px^2 IA but results in higher spatially resolved measurements, and was therefore used to process the PIV images in the present experiments.

Settings #	Final IA (px^2)	% overlap	No. passes	% valid vectors	F_{PL}
1	32×32	50	4	96	0.27
2	24×24	50	4	91	0.27
3	24×24	50	2	91	0.28
4	24×24	75	2	94	0.28
5	16×16	50	4	80	0.26

Table 4.1: The summarised results of a PIV processing test, where the same PIV images (taken of a neutral jet) were processed using different settings.

4.1.2 Pixel locking

In addition to obtaining a sufficient number of valid vectors from the PIV images, it is also important to minimise the possibility of other bias affecting the measurements. One such issue is referred to as 'pixel locking', which occurs if the size of the particles are too small relative to the pixel size in a given image (e.g. $1 - 2$ pixels in diameter). This results in computed displacements being biased towards integer values (Overmars et al. 2010; Adrian and Westerweel 2011). Overmars et al. (2010) proposed a method of quantifying the extent of pixel locking in given a set of displacement vectors. This involves truncating the integer part of the displacements so that only the fractional part remains (i.e. a value between -0.5 and $+0.5$ pixels), and considering a histogram of the result. If there is no pixel locking, then the histogram should be relatively flat as the fractional displacements should be

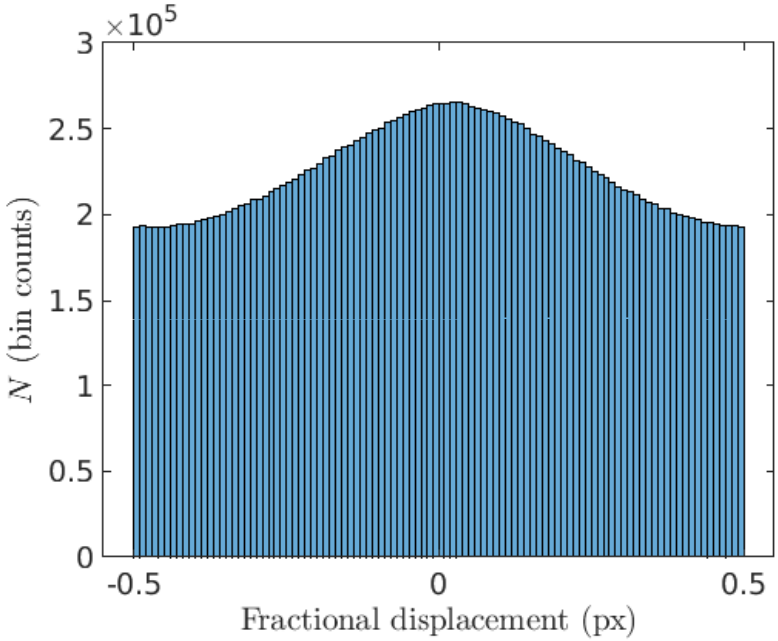

Figure 4.1: Histogram of the fractional displacements obtained from PIV images of a neutral jet. The images were processed using settings no. 4 in table 4.1.

randomly distributed. The more 'peaked' the histogram is at 0 px, the more biased the displacements are to integer values and the more significant the effect of pixel locking. This may be quantified by a 'pixel locking factor', F_{PL},

$$F_{PL} = 1 - \frac{N_{\min}}{N_{\max}}, \tag{4.1}$$

where $N_{\min}$ and $N_{\max}$ are the minimum and maximum number of counts in the histogram. If the histogram was approximately flat then $N_{\min} \cong N_{\max}$ and $F_{PL} \cong 0$, indicating no pixel locking (Overmars et al. 2010).

A histogram of the fractional displacements obtained from the present data (processed using settings #4 in table 4.1) is given in figure 4.1. This has a pixel locking factor of $F_{PL} = 0.28$, which lies within the acceptable 'mild' range proposed by Overmars et al. (2010) of $0.2 < F_{PL} < 0.4$. They consider $0.4 < F_{PL} < 0.6$ and $F_{PL} > 0.6$ as 'strong' and 'severe' pixel locking. The pixel locking factor was also calculated for displacements obtained using the other settings in table 4.1, and did not show significant variation between them.

4.2 Grid interpolation

As discussed in §3.5, physical limitation mean that the PIV and PLIF cameras do not have identical fields of view. Therefore, if combined velocity and scalar statistics are to be obtained, it is necessary to interpolate the images from each camera onto a common grid.

To validate that the interpolation scheme did not produce any unexpected effects or biases in the data, mean statistics for a neutral jet were calculated both before and after the interpolation. These are shown in figures 4.2(a)-(d), where profiles for $\overline{w}$, $\sqrt{\overline{w'^2}}$, $\overline{c}$ and $\sqrt{\overline{c'^2}}$ are given at an axial location of $z/D \cong 20$. All profiles are very similar for both the original and interpolated data, implying that the interpolation is not having any unexpected effects on the data. The $\overline{w}$ and $\sqrt{\overline{w'^2}}$ profiles calculated from the interpolated data are slightly less noisy than the originals, although their overall shapes and magnitudes are very similar. This is because the spurious vectors were discarded when calculating the mean statistics from the original velocity data, but were replaced and included in the calculation for the interpolated case. Since the percentage of valid vectors in a given image is sufficiently high, as discussed in §4.1, the interpolated vectors can be considered reasonable estimates of the true vectors at those locations (Adrian and Westerweel 2011). For this reason, and given that the difference between the original and interpolated profiles is still very subtle, the present interpolation scheme is considered an appropriate method for replacing spurious vectors and mapping the velocity and scalar fields onto a common grid.

4.3 Uncertainty

Errors in PIV measurements can be broadly separated into two categories, 'bias' and 'random' errors (Wilson and Smith 2013a,b; Adrian and Westerweel 2011). Bias errors can arise due to pixel locking, for example, and dominates the error when the particle size is small ($\lesssim$ 1 pixel) (Adrian and Westerweel 2011). As was discussed in the §4.1.2, pixel locking is sufficiently low in the present study (particle size $\gtrsim$ 3 pixels) and so the bias error is assumed to be negligible. Random error can arise in the sub-pixel interpolation step of the PIV algorithm, which in the present case involves using a three-point Gaussian fit (Adrian and Westerweel 2011). Several studies have investigated this random error in PIV measurements, such as the theoretic analysis by Westerweel (1993), who showed it depends on the second and fourth order moments of the intensity probability density function. Another study by Wilson and Smith (2013b) used Monte-Carlo simulations and a Taylor series method to estimate time-varying bias and random errors. Typically,

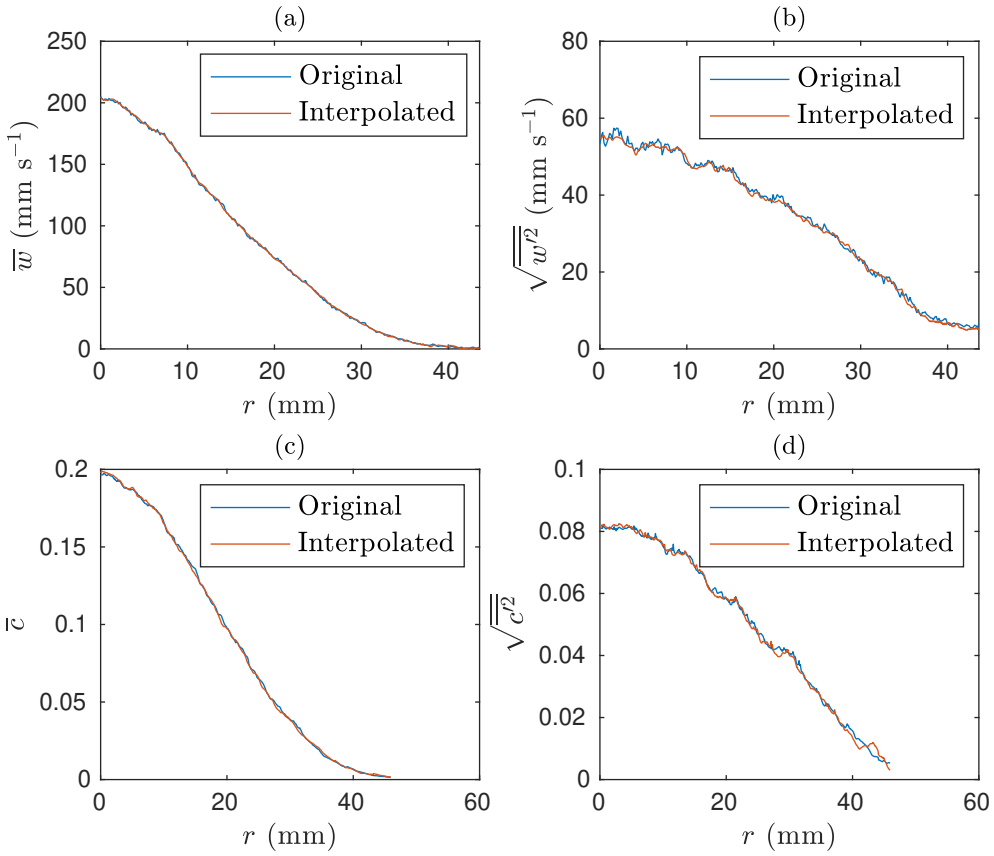

Figure 4.2: Mean and turbulence profiles for a neutral jet, showing both the original and interpolated data. The mean velocity is shown in (a), axial velocity fluctuations in (b), mean scalar concentration in (c), and scalar fluctuations in (d).

the random error in a given PIV displacement measurement is $\hat{r}_e \cong 0.1 - 0.2$ pixels (Adrian and Westerweel 2011; Westerweel 1993).

In addition to the error from the PIV measurement itself, there is also a precision uncertainty when an average is taken from a finite number of samples (i.e. images). The uncertainty in the mean axial velocity, $\overline{w}$, as obtained from PIV measurements, is given by (Wilson and Smith 2013a,b),

$$U_{\overline{w}} = \sqrt{\langle b_{w_i} \rangle^2 + p_{\overline{w}}^2}. \tag{4.2}$$

Here $\langle b_{w_i} \rangle$ is the average bias error and $p_{\overline{w}}$ is the precision uncertainty,

$$p_{\overline{w}} = \pm k \frac{s_w}{\sqrt{N}}, \tag{4.3}$$

where s_w is the standard deviation from the number of samples, N, and k is a constant that determines the confidence interval. For a 95% confidence interval assuming a normally distributed error, $k = 1.96$ (Wilson and Smith 2013a,b; Coleman

and Steele 2018). Based on data from the present experiments, the precision uncertainty in estimated as $p_{\overline{w}} \cong 1.9\%$. By assuming a negligible bias error the overall uncertainty in the mean velocity measurement is then $U_{\overline{w}} \cong \pm 1.9\%$.

Wilson and Smith (2013b) derived an equation for the uncertainty of the fluctuating quantities, such as the turbulence axial velocity fluctuations, $\overline{w'^2}$. For the case of negligible bias error and normally distributed random error, this can be expressed as,

$$U_{\overline{w'^2}} = \sqrt{\hat{r}_e^2 + p_{\overline{w'^2}}^2}, \tag{4.4}$$

where $p_{\overline{w'^2}}$ is the precision uncertain of $\overline{w'^2}$ and is given by,

$$p_{\overline{w'^2}} = k\sqrt{2}\frac{s_w^2}{\sqrt{N}}. \tag{4.5}$$

From the present experimental data, the uncertainty in the fluctuating quantity, $\overline{w'^2}$, is estimated from (4.4) as $U_{\overline{w'^2}} \cong \pm 6.8\%$.

4.4 Neutral jet statistics

With appropriate processing procedures for the PIV and PLIF, the mean flow statistics obtained from neutral jet measurements can be compared to the existing literature. This section will consider mean and turbulence profiles of the velocity and scalar concentration, as well how the mean centreline values change with axial location. The mean statistics were calculated from an ensemble average of images taken from multiple experimental runs, and the profiles shown have been spatially averaged over a vertical distance of half a diameter. Approximately 900 images were taken to obtain the following statistics for the neutral jet, which was considered sufficient for the purposes of comparing with existing literature. When obtaining data for negatively buoyant jets and fountains, the main focus of this investigation, a larger number of images where taken (up to 2400).

4.4.1 Mean profiles

Figure 4.3(a) shows the time-averaged axial velocity profile of a turbulent neutral jet, $\overline{w}$, normalised by the centreline velocity, $\overline{w}_c$, and half-width, $r_{1/2,w}$. Here $r_{1/2,w}$ is defined as the radial location where $\overline{w}/\overline{w}_c = 0.5$. The $z/D = 19$ profile was obtained from a jet with $Re_o \cong 5900$ using a $D = 10$ mm pipe, while the $z/D = 75$ case had $Re_o \cong 10000$ from a $D = 5$ mm pipe. The profiles at both locations take the expected Gaussian shape (Fischer et al. 1979; Hussein et al. 1994), and agree well

with the data from experimental studies by Wang and Law (2002) and Darisse et al. (2015). Similarly to the present experiments, Wang and Law (2002) used PIV+PLIF measurements with freshwater to produce the flow, obtaining jets with $Re_o = 6000$ from a $D = 9.5$ mm inlet, and $Re_o = 12700$ from a $D = 4.5$ mm inlet. Darisse et al. (2015) used a different approach, measuring air jets with $Re_o = 1.4 \times 10^5$ using laser Doppler velocimetry (LDV), as well as cold-wire thermometry and a thermistor probe.

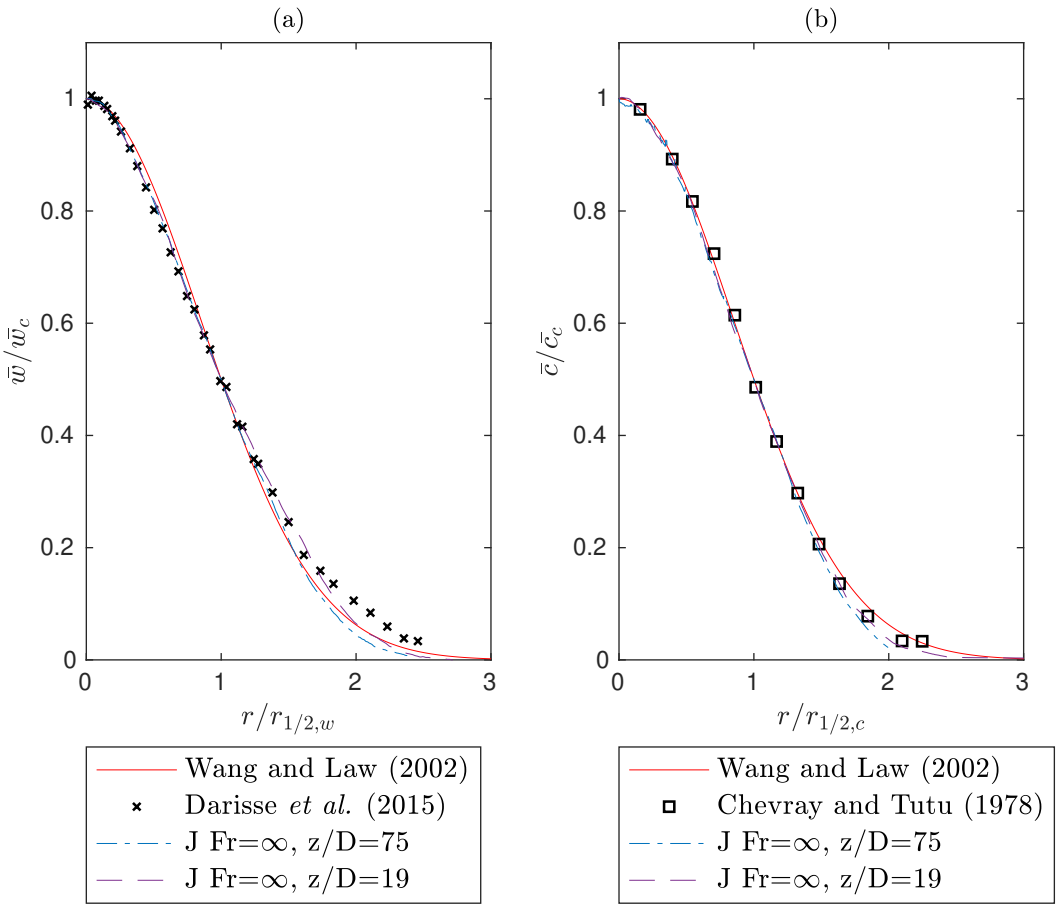

Figure 4.3: Mean axial velocity profile, (a), and scalar concentration profile, (b), normalised by their centreline values and respective half-widths for a turbulent neutral jet obtained from the current experimental set-up. Present measurements are shown alongside shown alongside data obtained from several previous studies (Wang and Law 2002; Darisse et al. 2015; Chevray and Tutu 1978).

The scalar concentration profiles of the present flow are given in figure 4.3(b), normalised by the centreline value $\overline{c}_c$, as well as the 'concentration half-width', $r_{1/2,c}$, defined as the radially location where $\overline{c}/\overline{c}_c = 0.5$. These are plotted with the data from Wang and Law (2002), as well as hot-wire based air jet measurements from Chevray and Tutu (1978) ($Re_o \cong 3.7 \times 10^5$). Just as with the velocity measurements, the scalar profiles take Gaussian shapes and are in good agreement with the

existing literature for both z/D locations shown.

4.4.2 Turbulence profiles

Normalised profiles for the axial and radial turbulence intensities, $\overline{w'^2}/\overline{w}_c^2$ and $\overline{u'^2}/\overline{w}_c^2$, and Reynolds stress, $\overline{w'u'}/\overline{w}_c^2$, are shown in figure 4.4 for a neutral jet. The $z/D = 75$ profiles from the present experiments are in good agreement with both Darisse et al. (2015) and Wang and Law (2002) for the axial fluctuations and Reynolds stress, shown in 4.4(a) and (c). The $z/D = 75$ radial fluctuations, shown in (b), are also in close agreement with Darisse et al. (2015), although the Wang and Law (2002) data is somewhat lower. The $z/D = 19$ data from the present experiments is lower than the other profiles in all three plots, which is likely due to the jet having not fully developed at this axial distance.

The scalar fluctuations, $\sqrt{c'^2}/\overline{c}_c$, and axial/radial fluxes, $\overline{w'c'}/\overline{w}_c\overline{c}_c$ and $\overline{u'c'}/\overline{w}_c\overline{c}_c$, are given in figure 4.5. For $\sqrt{c'^2}/\overline{c}_c$ and $\overline{w'c'}/\overline{w}_c\overline{c}_c$, there is good agreement between the present measurements and data from Wang and Law (2002) and Darisse et al. (2015). There is some variation in the literature for the $\overline{u'c'}/\overline{w}_c\overline{c}_c$ profiles, with the present $z/D = 75$ data lying between them. Again the $z/D = 19$ profile from the current data is slightly slower here, likely due to still being relatively close to the source compared to the $z/D = 75$ case.

4.4.3 Centreline decay

It is well documented that both the centreline velocity and scalar concentration in turbulent neutral jets scale with z^{-1}, so that $1/\overline{w}_c \sim z$ and $1/\overline{c}_c \sim z$. This property can be derived from the conservation equations by assuming self-similar velocity/scalar profiles and a constant entrainment coefficient. The relationship can be expressed using the following linear equations,

$$\frac{w_o}{\overline{w}_c} = K_w \left(\frac{z}{D} - \frac{z_{o,w}}{D} \right), \tag{4.6}$$

$$\frac{c_o}{\overline{c}_c} = K_c \left(\frac{z}{D} - \frac{z_{o,c}}{D} \right), \tag{4.7}$$

where K_w and K_c are constants, $z_{o,w}$ and $z_{o,c}$ are virtual origins unique to a particular experimental set-up, and c_o is the scalar concentration at the source (defined as unity in the present experiments). Previous studies have estimated values for the constants in the ranges $0.14 \lesssim K_w \lesssim 0.16$ and $0.18 \lesssim K_c \lesssim 0.20$ (Kiser 1963; Becker et al. 1967; Fischer et al. 1979; Birch et al. 1978; Grandmaison et al. 1982; Papanicolaou and List 1988; Webster et al. 2001).

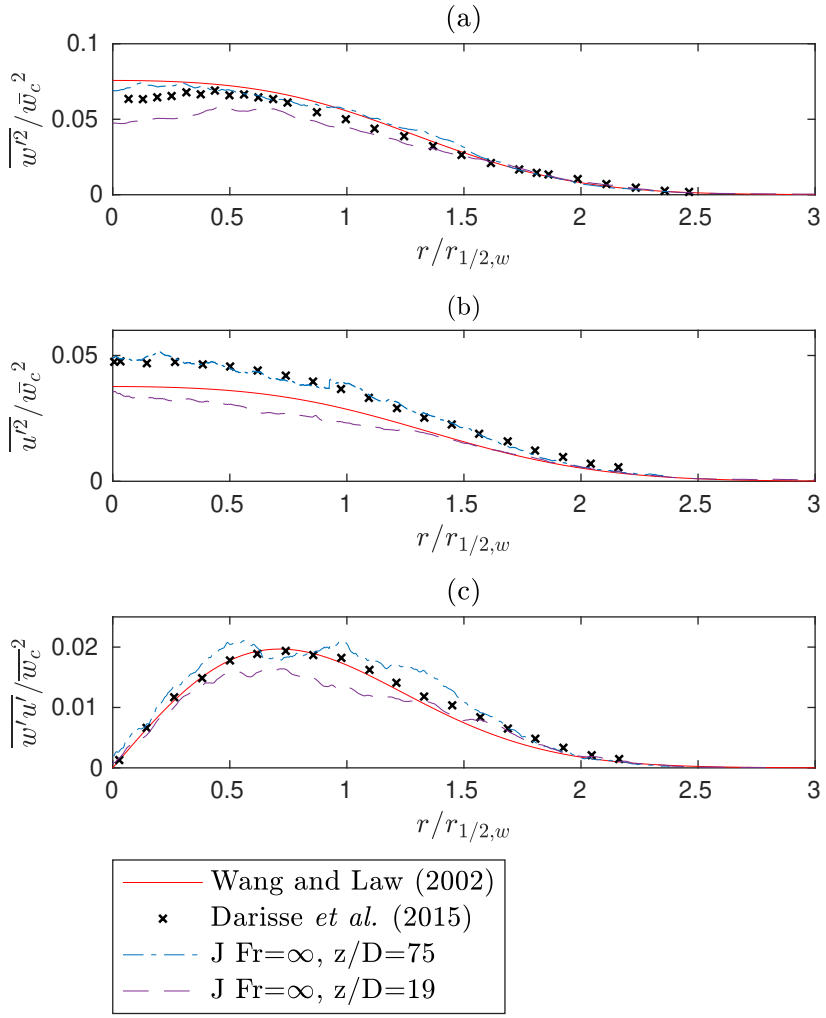

Figure 4.4: Profiles for the axial and radial turbulence intensities, $\overline{w'^2}/\overline{w}_c^2$ and $\overline{u'^2}/\overline{w}_c^2$, and the Reynolds stress, $\overline{w'u'}/\overline{w}_c^2$, for a neutral jet. Measurements obtained using the present experimental set-up are shown alongside data obtained from previous studies by Wang and Law (2002) and Darisse et al. (2015).

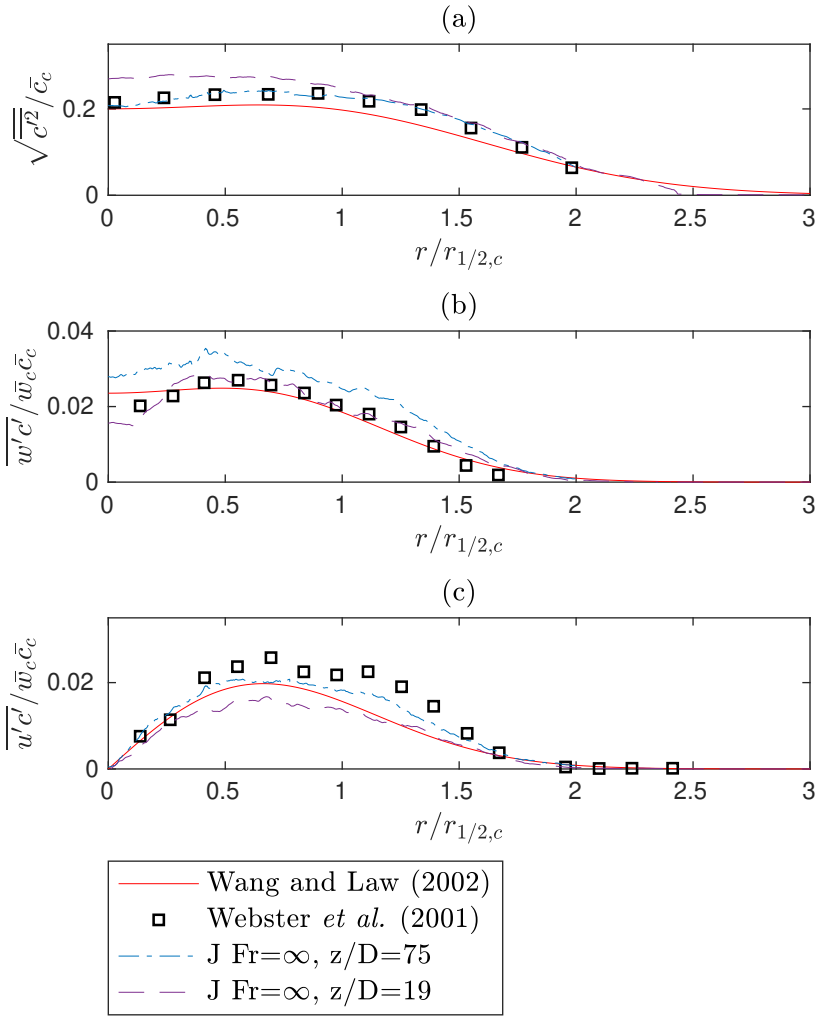

Figure 4.5: Profiles of the turbulent scalar fluctuations, $\sqrt{\overline{c'^2}}/\overline{c}_c$, and the axial and radial fluxes, $\overline{w'c'}/\overline{w}_c\overline{c_c}$ and $\overline{u'c'}/\overline{w}_c\overline{c_c}$, for a neutral jet. Measurements obtained using the present experimental set-up are shown alongside data obtained from previous studies by Wang and Law (2002) and Darisse et al. (2015).

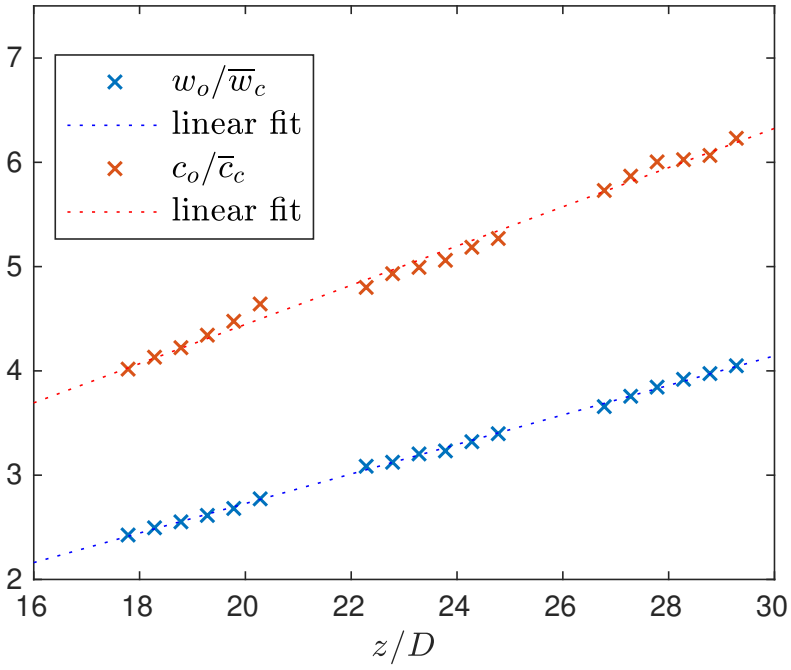

Figure 4.6: Centreline quantities, $w_o/\overline{w}_c$ and $c_o/\overline{c}_c$, plotted with z/D for a neutral jet obtained using the present experimental set-up.

Figure 4.6 shows both $w_o/\overline{w}_c$ and $c_o/\overline{c}_c$ plotted with z/D for a neutral jet obtained with the present experimental set-up. Both quantities are linear with axial distance, with fits of the data also shown. These imply $K_w = 0.14$ and $K_c = 0.19$, which both lie within the range of previously obtained values in the literature, and virtual origins of $z_{o,w}/D = 0.7$ and $z_{o,c}/D = -3.6$. Although the location of the virtual origins depend on the experimental set-up, they are typically $\lesssim 5D$ from the source and may be either positive or negative (downstream or upstream of the source) (Becker et al. 1967; Grandmaison et al. 1982; Papanicolaou and List 1988).

4.5 Summary

The purpose of this chapter has been to validate the experimental procedure designed for this study, which will be used to investigate turbulent negatively buoyant jets and fountains. Before applying the method to such flows, a series of experiments into neutrally buoyant axisymmetric turbulent jets were conducted using the present experimental set-up, with the results obtained using the current image processing procedure.

Suitable parameters for the PIV algorithm have been determined that result in a valid vector detection rate of 94%, while maintaining an appropriate spatial resolution. The effect of pixel locking, which is largely determined by the size of

the particles in the flow (in pixels) as seen by the cameras, has been investigated and found to lie within the acceptable 'mild' range (Overmars et al. 2010). Mean and turbulence statistics are computed for the neutral jet and compared to several previous studies, with the present measurements in good agreement with the existing literature. The present experimental method is therefore considered suitable for this investigation, and will be used to obtain velocity and scalar measurements in negatively buoyant jets and fountains that will be discussed in the remaining chapters.

Chapter 5

Negatively buoyant jets

The following chapter investigates the initial 'negatively buoyant jet' (NBJ) stage of fountain flow, using data obtained experimentally using two-dimensional particle image velocimetry (PIV) and planar laser induced fluorescence (PLIF). The development of the mean and turbulence profiles with local Fr are investigated, and it is found that, unlike neutral jets and plumes, the turbulence intensity in negatively buoyant jets does not scale with the mean flow. Additionally, the ratio of widths of the buoyancy and velocity profiles, λ, increases along the jet. The entrainment coefficient, α, was estimated for a negatively buoyant jet, and was found to decrease with local Fr, eventually becoming negative, indicating fluid is being ejected from the jet. These observations differ to neutral or buoyant jets and plumes, which approach a constant λ and α in the far field. This different behaviour in negatively buoyant jets is a natural consequence of the strongly decelerating mean flow as a result of opposing buoyancy, which is demonstrated in the context of the integral model framework developed by Morton et al. (1956). The contents of this chapter have been adapted from an article accepted for publication in the Journal of Fluid Mechanics, Milton-McGurk et al. (2020a).

5.1 Introduction

A turbulent jet is negatively buoyant when its buoyancy directly opposes its momentum. It will continually decelerate until its mean momentum is reduced to zero and the fluid reverses direction, returning towards the source while mixing with the opposing fluid. The initial stage of the flow, during its initial rise to z_i and before the return flow forms, is referred to as the 'negatively buoyant jet' (NBJ) stage. The

quasi-steady stage consisting of an inner flow/outer flow structure (IF/OF) oscillating around its steady-state height, z_{ss}, is referred to as the 'fully developed fountain' (F) stage. This chapter is focused on the NBJ stage of the flow, where there is no OF present and the flow resembles a neutral or positively buoyant jet/plume.

Many previous studies into NBJs/fountains have involved taking bulk measurements of the flow, such as rise heights, z_i and z_{ss}, to classify fountains and produce Fr_o scaling relations (Turner 1966; Kaye and Hunt 2006; Burridge and Hunt 2012). Other studies have obtained local measurements of the internal velocity/buoyancy fields, although these have primarily been of the fully developed fountain stage (Williamson et al. 2011; Mizushina et al. 1982; Cresswell and Szczepura 1993). There is presently a lack of detailed experimental data available on the initial rise of an NBJ prior to the return flow forming. Attempts to model NBJs have therefore been evaluated primarily on their z_i prediction, rather than the development of the velocity, width and buoyancy scales (McDougall 1981; Bloomfield and Kerr 2000; Papanicolaou et al. 2008; Hunt and Debugne 2016). There is also the open question of whether NBJs can be assumed to be self-similar, and how α differs to that in neutral or positively buoyant jets.

The current chapter used PIV and PLIF measurements to investigate negatively buoyant jets prior to a return flow forming in an effort to tackle these questions. The process for defining this initial stage based on the present experimental data is described in §5.2. Mean statistics are presented in §5.3-5.4, including a discussion regarding the scaling of the mean and turbulence profiles with axial distance. Entrainment along the negatively buoyant jet is investigated in §5.5, followed by integral model predictions in §2.4. The spreading rate of the velocity and buoyancy profiles is discussed in §5.7.

5.2 Defining the NBJ stage

A turbulent negatively buoyant jet entering a homogeneous environment has an initial temporal development, referred to as the negatively buoyant jet stage (NBJ), where decelerating fluid moves towards its initial height, z_i, before it reverses direction and forms a return flow. The return flow then continues to develop, interacting with the inner flow, until it reaches a quasi-steady state when it can be considered a fully developed fountain (F), with its maximum height oscillating around z_{ss}. In order to define the negatively buoyant jet stage of this inherently transient flow, an ensemble average is taken across multiple experimental runs. These are each produced with the same source conditions and are run for the same amount of time.

For example, a $Fr_o = 30$ negatively buoyant jet may be imaged for 133.33s at 3Hz (400 images) in a single run, which would then be repeated 6 times (2400 images in total). An ensemble average for each time step would then be taken across the 6 runs so that there are 400 reasonably smooth 'averaged images' in time. This allows for the transient development of the negatively buoyant jet into a fully developed fountain to be investigated.

Since the region of interest of the cameras was relatively small compared to the height of the jet/fountain ($z_i \cong 535$ mm), the different stages of flow development were determined using velocity measurements of the inner structure. This involved observing how the volume flux in the inner flow (Q_{IF}) and outer flow (Q_{OF}) regions of the NBJ changed in time. These are defined as,

$$Q_{IF} = 2\int_0^{r_{io}} \tilde{w} r \mathrm{d}r, \quad Q_{OF} = 2\int_{r_{io}}^{\infty} \tilde{w} r \mathrm{d}r, \qquad (5.1a-b)$$

where r_{io} is the 'boundary' between the inner and outer flow and $\tilde{w}$ is the instantaneous axial velocity profile of the 'averaged image'. Although the instantaneous boundary is likely to change in time, for the purposes of calculating Q_{IF} and Q_{OF}, r_{io} is taken as constant and defined as the first radial location where the mean velocity (calculated using all the instantaneous velocity profiles) is equal to zero. This IF/OF boundary is a local scale that may vary at different heights as the OF develops, and so may not be well defined at the top where the velocity goes to zero. However, for the purposes of the present investigation it is sufficient to compute Q_{IF} and Q_{OF} prior to this region.

The ratio $-Q_{OF}/Q_{IF}$ is plotted with time in figure 5.1 for a $Fr_o = 30$ negatively buoyant jet at $z/D \cong 19$. There are three distinct regions in figure 5.1, the first where $-Q_{OF}/Q_{IF} \cong 0$ and is approximately constant (since $Q_{OF} \ll Q_{IF}$), then a second, when the ratio rapidly increases then decreases, and a third region where it oscillates around a value $-Q_{OF}/Q_{IF} \cong 2$. The start/end of these regions, which indicate the defined NBJ and fountain stages, are shown as vertical lines on the figure. Images showing the velocity vectors and scalar concentration fields from these stages are given in figures 5.2(a)-(c). The first stage, shown in (a), corresponds to the initial rise of the jet before the return flow has developed, and thus the velocity vectors are primarily orientated downwards (the positive z direction) inside the jet, and have vertical components of approximately zero outside of it. The second stage, shown in (b), corresponds to the intermediate transient period after the NBJ has reached its maximum height as it begins collapsing back onto itself, but before it reaches the quasi-steady state of a fully developed fountain. Here the axial velocity of the

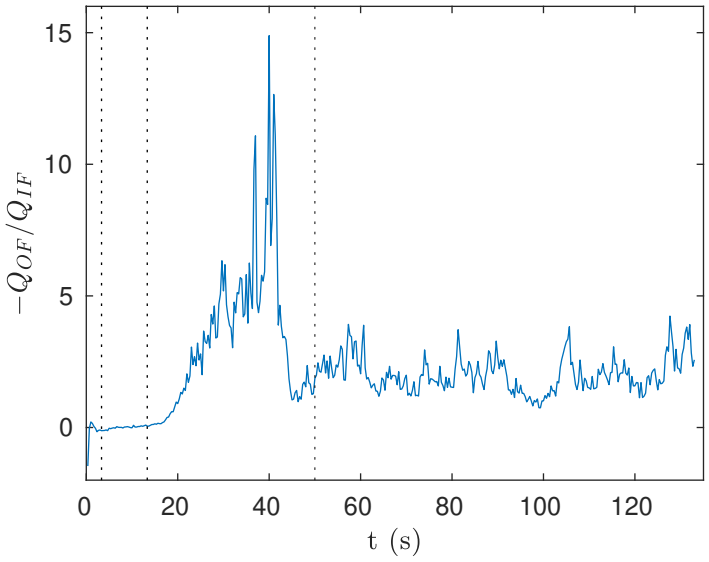

Figure 5.1: The ratio $-Q_{OF}/Q_{IF}$, defined using (5.1), is plotted against time, t (s). The ratio is a measure of the instantaneous volume flux in the inner and outer flow regions of a negatively buoyant jet/fountain, and is used to define the initial negatively buoyant jet stage where $Q_{OF} \ll Q_{IF}$ and is approximately constant. Vertical lines indicating the different flow stages are also shown.

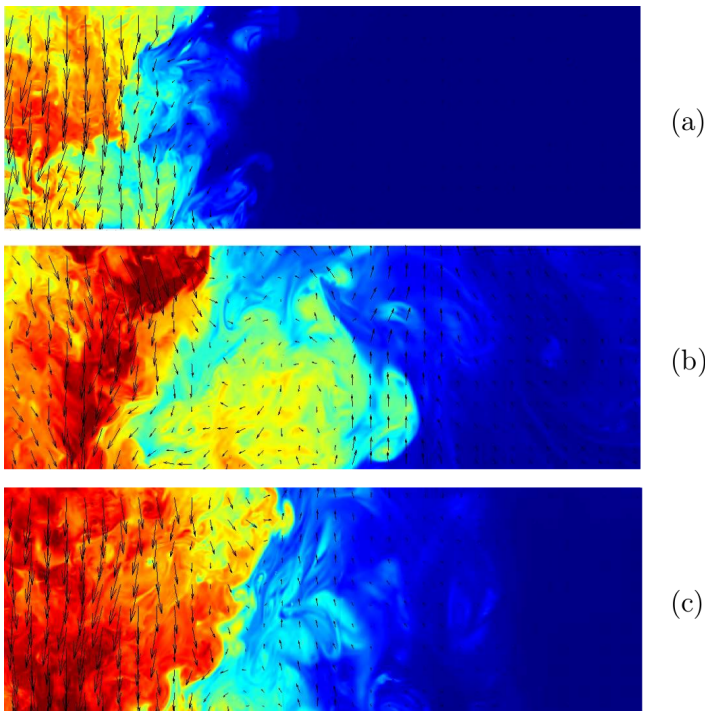

Figure 5.2: Three images showing the instantaneous velocity vectors and scalar concentration field of a negatively buoyant jet as it developing into a fountain. With respect to figure 5.1, image (a) was taken at approximately 5 s, (b) at 32 s and (c) at 106 s. These images correspond to the axial location range $17 \lesssim z/D \lesssim 20$ where $z_i \cong 54D$, and are orientated such that that the jet core is flowing downwards (the positive z direction).

IF reduces and a significant return flow begins to form, evident from the velocity vectors pointing towards the source (upwards in this figure) in the OF, where it was previously a nearly quiescent environment in (a). The fully developed fountain stage, shown in (c), does not look categorically different from the transient stage in the instantaneous images observed, with both images showing downward and upward flowing regions. However, as is shown in the $-Q_{OF}/Q_{IF}$ plot in figure 5.1, the volume flux in the inner and outer flow regions is much more steady in time during the fully developed stage. The shape of this plot, and the location of the three regions, are insensitive to the value of r_{io} used in (5.1). For example, a similar plot is obtained if the velocity profile half-width, defined as the radial location where $\overline{w}/w_c = 0.5$, is used. In the first region, where $-Q_{OF}/Q_{IF}$ is approximately constant, time-averaged profiles were computed and were found not to vary systematically in time, as will be discussed in §5.2.1. The flow could therefore be considered quasi-steady in this range, and so this was used to define the negatively buoyant jet stage for each experiment. All NBJ statistics discussed in the following sections correspond to this initial stage.

The procedure of obtaining a plot of $-Q_{OF}/Q_{IF}$ with time was repeated for NBJ experiments at various different axial locations. Some of these experiments were run at a higher frequency (7Hz) and for a shorter time period (45s), and so ended before the quasi-steady stage was reached. Although this meant that the third region of figure 5.1 was not always visible, the initial approximately steady region was always present. This always preceded a sudden increase in $-Q_{OF}/Q_{IF}$ as the flow started to collapsed, and so was sufficient to define the NBJ region.

5.2.1 Mean profiles in time

After taking the ensemble average across multiple runs of the $Fr_o = 30$ negatively buoyant jet (same as that shown in figure 5.1), time-averaged profiles over several short time intervals (3.67s or 11 'images') were calculated for both the velocity and scalar measurements. These profiles are presented in figures 5.3(a) and (b) to illustrate the initially steady and then transient behaviour of the negatively buoyant jet as it develops into a fountain. The first three curves show averages taken over images $N = 10-20$, $20-30$ and $30-40$, which are all within the defined negatively buoyant jet range. The velocity and scalar profiles are all very si

milar here, with no clear systematic trend in time. There is no significant $\overline{w} < 0$ region in this range, indicating there is no return flow present. Extensive sensitivity testing was carried out for all other results within the defined NBJ range, which similarly found no significant differences or systematic trends. Beyond this point,

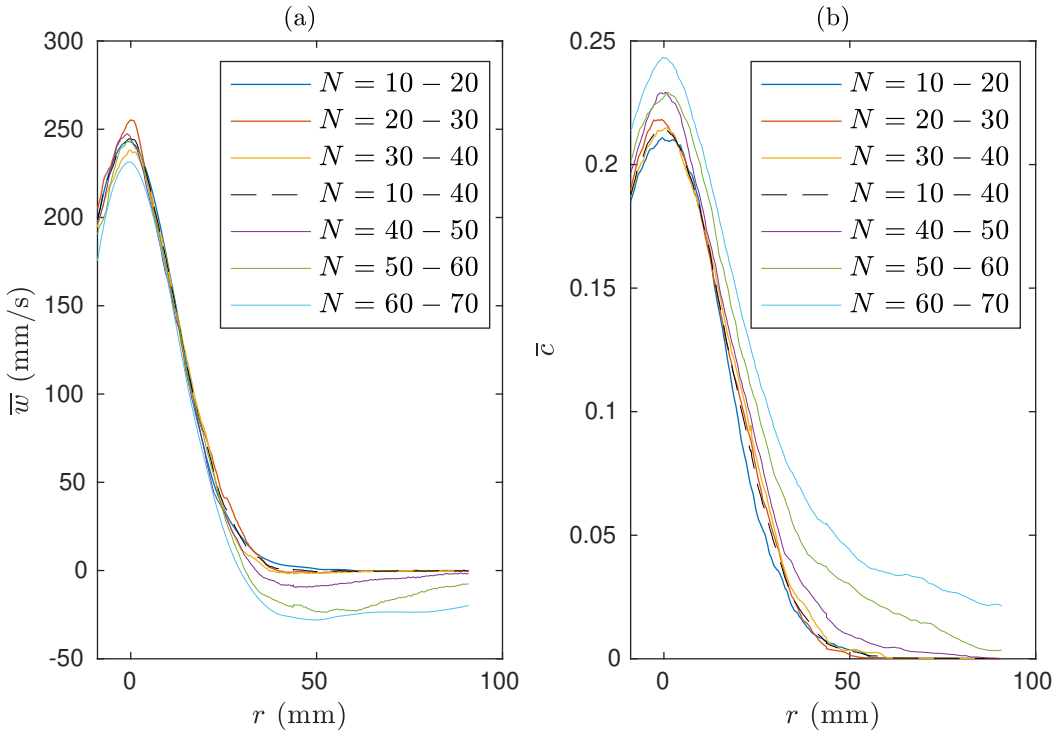

Figure 5.3: Mean axial velocity, (a), and scalar concentration profiles, (b), of a negatively buoyant jet/fountain at various stages in time. The temporal time averages are taken over 3.67 s increments (corresponding to 11 'images' in time), in order to show how the profiles change in time as the negatively buoyant jet develops into a fountain.

for the profiles corresponding to images in the range $N = 40-70$, noticeable transient effects are observed in both the velocity and scalar profiles. In the velocity profiles, larger negative velocities are observed at the tail of the profile indicating a return flow starting to form. The scalar profiles are also changing strongly with time in this range, with an increasing peak concentration at the centreline, as well as higher values at the tails.

5.3 Statistical description of the flow

5.3.1 Centreline decay

For a self-similar neutral jet with constant α, the decay of the centreline velocity along the jet axis follows the scaling $\overline{w}_c^{-1} \sim z$. This was discussed in §4.4.3, where the present experimental procedure was validated on a neutral jet. Figure 5.4 shows $w_o/\overline{w}_c$ plotted against z/D for neutral and negatively buoyant jets where, just as in figure 4.6, linear scaling for the neutral jet is observed. For the negatively buoyant jet, the decay is not linear over the z/D range shown, and can be seen diverging

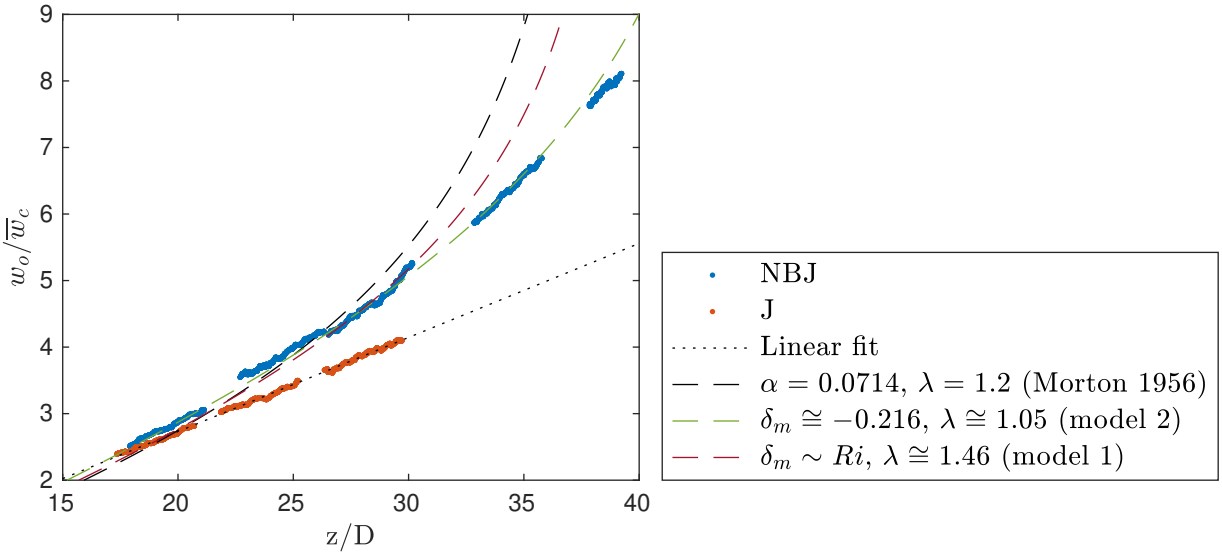

Figure 5.4: The quantity $w_o/\overline{w}_c$ plotted against axial distance z/D, showing the decay of the centreline velocity for a neutral and negatively buoyant jet. Each cluster of points was obtained from a separate experiment with the same source Froude number ($Fr_o = 30$ for the NBJ) and similar Reynolds numbers ($5500 \lesssim Re_o \lesssim 5900$). The prediction of Morton's (1959) model for a constant $\alpha = 0.0714$ and $\lambda = 1.2$ is shown, as well as 'model 2', a linear model for α with Ri using coefficients based on values found by Kaminski et al. (2005). Additionally, 'model 1', which assumes a linear relationship for δ_m with Ri, is also shown. These models are discussed further in §5.5.

from the neutral jet results for $z/D \gtrsim 18$. Figure 5.4 also shows the predictions of three integral models for the NBJ, which will be discussed in §5.5-5.6.

As z/D increases in an NBJ, the local Fr decreases towards zero (and Ri asymptotes to negative infinity) since the velocity approaches zero at the top. This may be interpreted as negative buoyancy playing an increasingly important role in decelerating the flow. Despite the non-linear velocity decay, for the points closest to the source, e.g. for $z/D \lesssim 26$ ($Fr \gtrsim 3.0$, $Ri \gtrsim -0.11$), $w_o/\overline{w}_c$ could be approximated as linear with z, although with a different slope to a neutral jet. This may be considered the 'forced' regime where the flow is more similar to a neutral jet, and is consistent with the arguments made in §2.4.2 regarding the solution to Morton's (1959) simplified model. Although this is a local regime based on local Fr, it may be compared to the classification of fountains by source Froude number, Fr_o, such as those suggested by Burridge and Hunt (2012). They classified $2.8 \lesssim Fr_o \lesssim 5.5$ and $Fr_o \gtrsim 5.5$ as 'forced' and 'highly forced' fountains, which is consistent with the presently suggested local 'forced' regime of $Fr \gtrsim 3.0$.

5.3.2 Velocity and buoyancy profiles

Time-averaged profiles for axial velocity, $\overline{w}$, and scalar concentration, $\overline{c}$, are given in figures 5.5(a) and (b), normalised by their centreline values and respective half-widths. Dimensionless concentration ($0 \leq c \leq 1$) and buoyancy (mm s^{-2}) are related by a constant such that $b = c(\rho_o - \rho_e)g/\rho_e$. All negatively buoyant jets profiles are close to Gaussian for the full range of local Fr investigated, $1.85 \lesssim Fr \lesssim 5.91$, and are similar to the profiles for neutral jets. This is despite the considerable deceleration of the mean flow in the negatively buoyant jet compared to the neutral jet, as demonstrated in figure 5.4, showing that the profiles maintain a Gaussian shape even outside of the forced regime ($Fr \lesssim 3.0$).

The ratio of widths between the buoyancy/scalar and velocity profiles is given by λ, which was defined in (2.29) in terms of the $1/e$ widths. For neutral jets, estimates for λ in the literature typically lie in the range $1.15 \lesssim \lambda \lesssim 1.30$ (Fischer et al. 1979; Wang and Law 2002; Ezzamel et al. 2015), and is assumed to be constant in the far field where the flow is self-similar. As pointed out by Ezzamel et al. (2015), discrepancies in the literature may be attributed to the distance from the source where the profiles were measured (e.g. if the jet has not fully developed), and that it is likely that source conditions play a role.

Figures 5.6(a) and (b) show λ plotted with axial distance and local Ri for both the neutral and negatively buoyant jets from the present experiments. The values for the neutral jet are reasonably constant, and have an average value of $\lambda = 1.181$, in good agreement with $\lambda_j = 1.189$ from Fischer et al. (1979). The slight decreasing trend may be attributed to the jet still developing at this axial distance. For the negatively buoyant jet, λ is higher than the neutral jet and increases with axial distance over the range shown. From figure 5.6(b), λ can been seen increasing almost immediately from $Ri \cong -0.04$ ($Fr \cong 5.0$) with more negative Ri, which is within the previously suggested 'forced' regime of $Ri \gtrsim -0.11$ ($Fr \gtrsim 3.0$). So even for relatively high local Fr, the velocity and buoyancy/scalar profile widths grow at different rates compared to a neutral jet.

A varying λ can be interpreted as a type of 'similarity drift' of the velocity and buoyancy profiles, which has also been reported in jets and plumes that have not yet reached a state of full self-similarity (Carazzo et al. 2006; Kaminski et al. 2005; Ezzamel et al. 2015). The mechanism causing the increasing λ with z for negatively buoyant jets is discussed in §5.7.

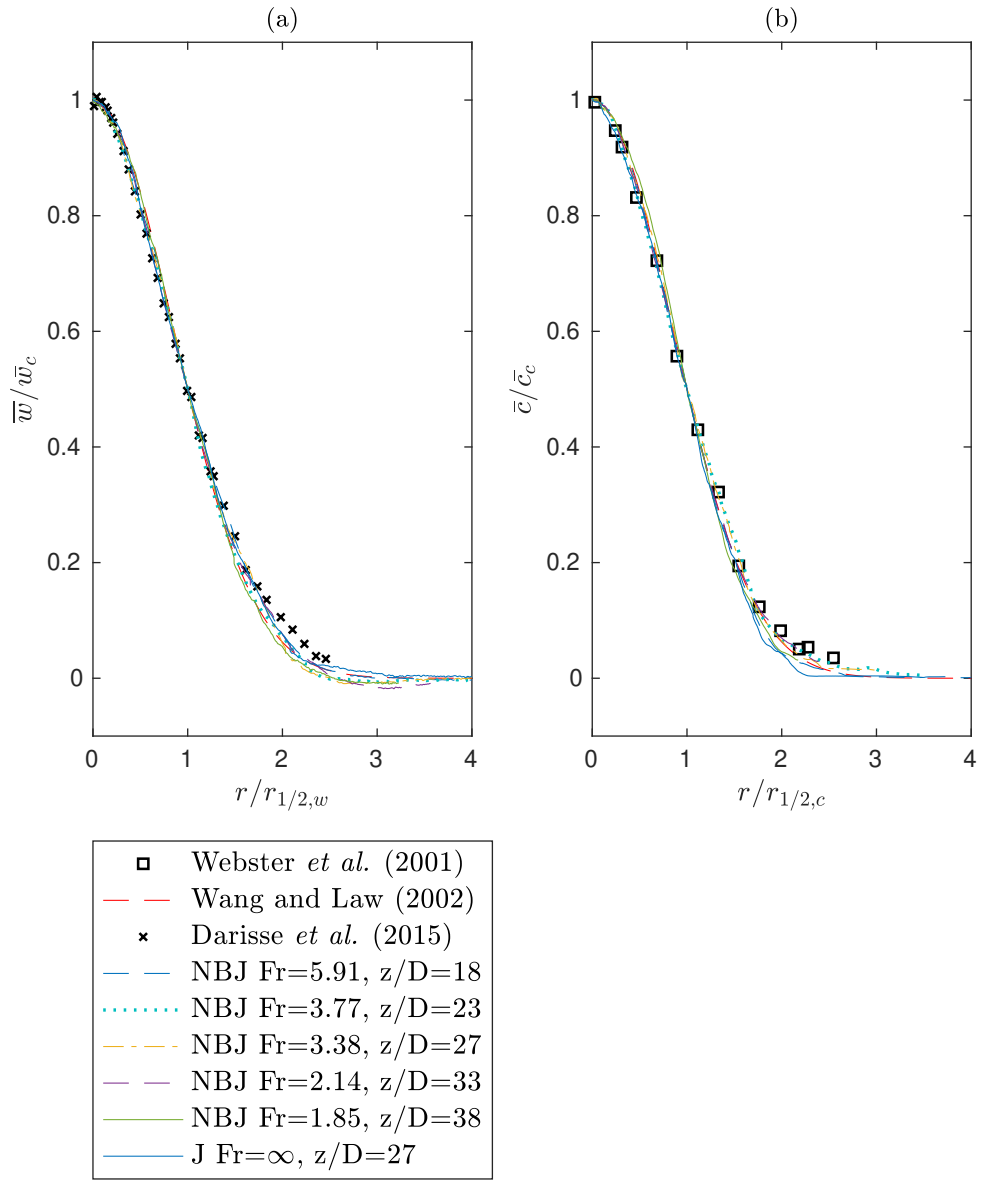

Figure 5.5: Time-averaged axial velocity and scalar concentration profiles, in (a) and (b) respectively, of a negatively buoyant jet (NBJ) with different local Froude numbers. Neutral jet (J) data from the present experimental set-up is also shown ($Re_o = 5900$), as well as by Webster et al. (2001), Wang and Law (2002) and Darisse et al. (2015). The NBJ profiles were obtained using data from multiple experiments using the same pipe, $D = 10$ mm, at the same source Froude number, $Fr_o = 30$, and similar Reynolds number $5500 \lesssim Re_o \lesssim 5900$, while varying the location of the region of interest relative to the source. All velocity and scalar concentration points have been normalised by their respective centreline values, $\overline{w}_c$ and $\overline{c}_c$, and half-widths, $r_{1/2,w}$ and $r_{1/2,c}$.

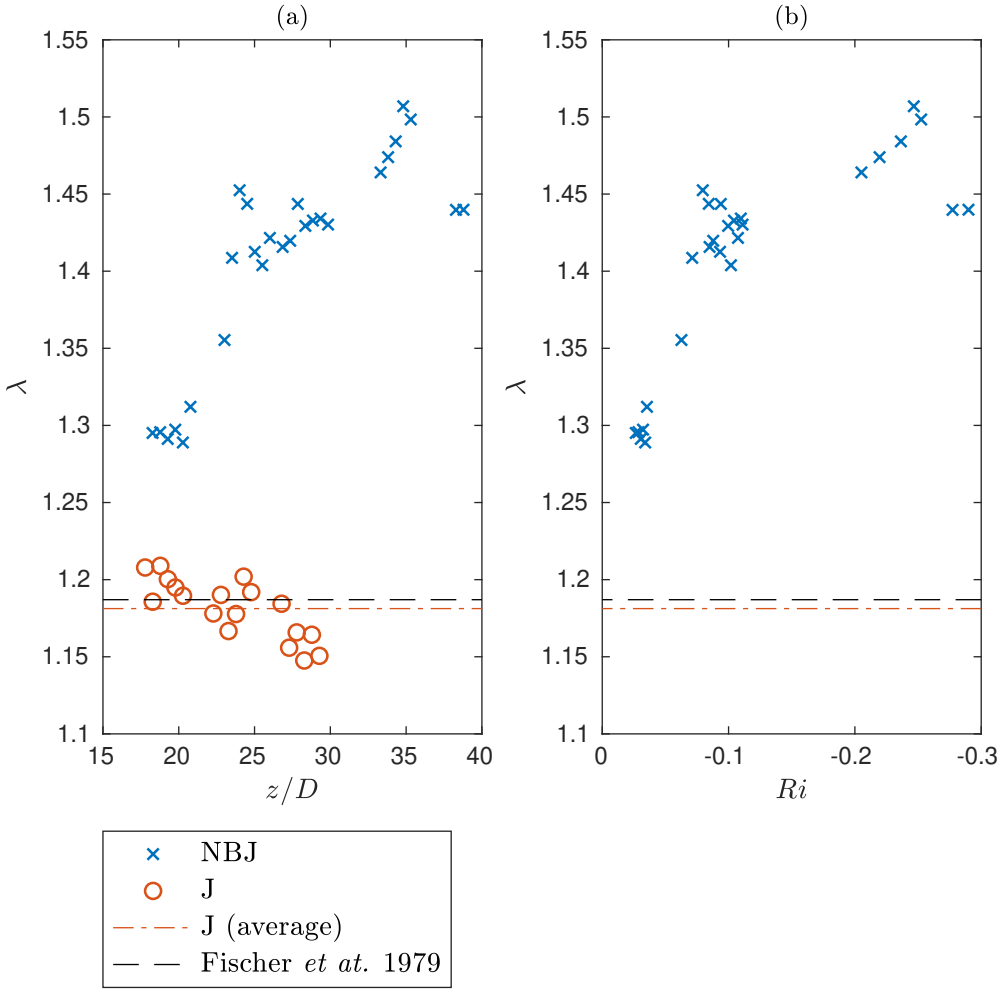

Figure 5.6: The $1/e$ width ratio between the buoyancy (or scalar) and velocity profiles, $\lambda = r_b/r_w$, for a negatively buoyant jet (NBJ) and neutral jet (J). The data is plotted against axial distance normalised by source diameter, z/D, in (a), and against the local Ri in (b). At the source, $Fr_o = 30$ ($Ri_o = -0.0011$), which decreases towards $Fr = 0$ ($Ri \to -\infty$) at the top of the NBJ. In (b), the values for a neutral jet, which have $Ri = 0$ everywhere, are shown as horizontal lines for clarity.

5.3.3 Turbulence statistics

Figures 5.7 and 5.8 show the profiles of the axial turbulence intensity, $\overline{w'^2}/\overline{w}_c^2$, and the normalised Reynolds stress, $\overline{w'u'}/\overline{w}_c^2$. The profiles at $z/D = 73$ for the neutral jet in figures 5.7(a) and (b) are in good agreement with both the best fit curve from Wang and Law (2002) and data from Darisse et al. (2015). This experiment used a smaller, $D = 5$ mm, pipe so that measurements could be taken at a larger downstream distance relative to the source diameter, and a high $Re_o = 10700$ could be achieved. The flow in this experiment could therefore be expected to be fully developed and self-similar and so could be compared to similar experiments in the

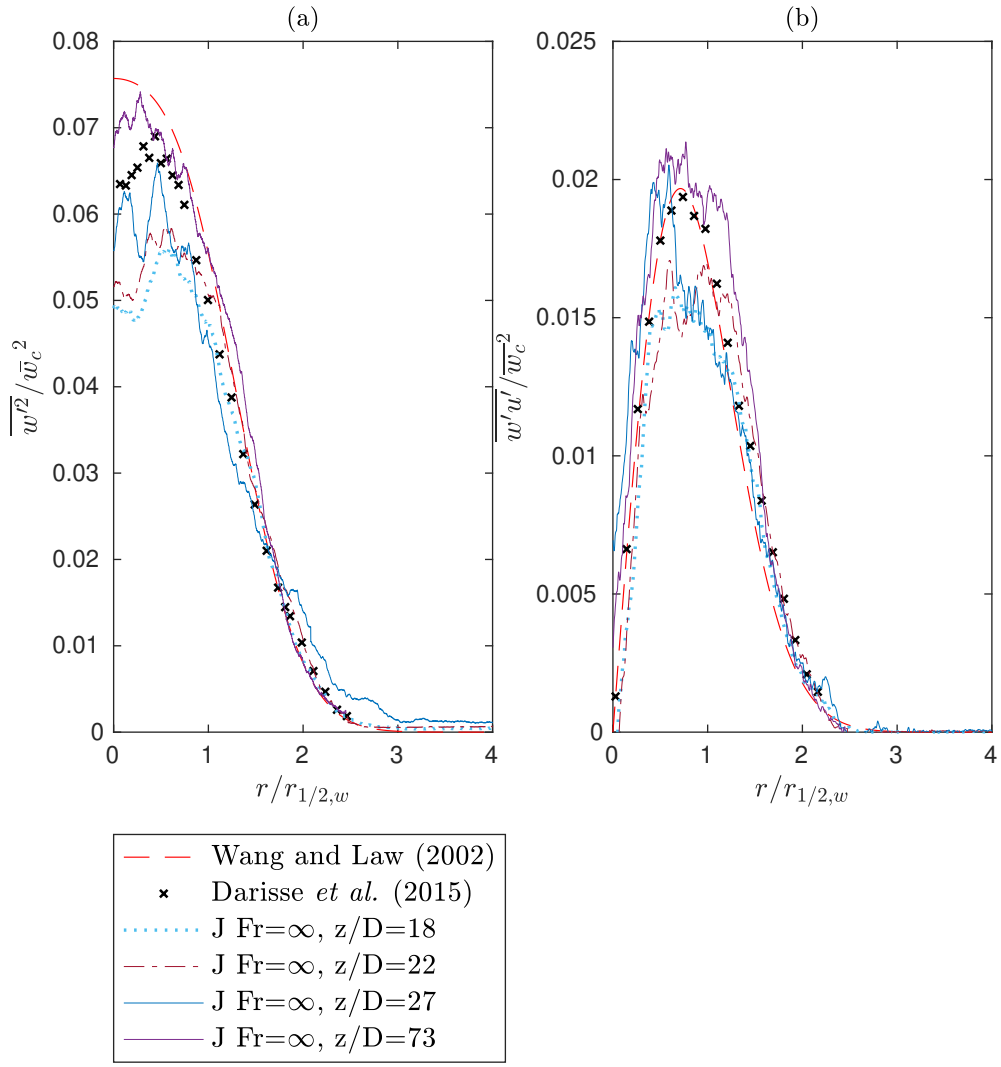

Figure 5.7: Mean turbulent axial velocity fluctuations, (a), and Reynolds stress, (b), for the neutral jet (J) at three different axial locations, normalised by the local mean centreline velocity, $\overline{w}_c^2$. The $z/D = 18$, 23 and 27 profiles correspond to an experiment with $D = 10$ mm and $Re_o = 5900$. The $z/D = 73$ profiles were obtained used $D = 5$ mm and $Re_o = 10700$. The best fit curve from Wang and Law (2002) ($40 < z/D < 80$) and the data from Darisse et al. (2015) ($z/D = 30$) for a neutral jet is also shown.

literature, such as Wang and Law (2002) who had $Re_o = 12700$ and $40 \leq z/D \leq 80$. The remaining J profiles in figure 5.7 correspond to experiments using a $D = 10$ mm pipe and have $Re_o = 5900$ in order to closely match the source conditions of the negatively buoyant jet experiments. These $18 \leq z/D \leq 27$ profiles are generally a little lower than the $z/D = 73$ case since they may not be completely developed at this distance, but are nevertheless reasonably close and can be compared to a negatively buoyant jet at the same axial location.

Figure 5.8(a) and (b) shows the normalised $\overline{w'^2}$ and $\overline{w'u'}$ profiles of a negatively

buoyant jet at some of the same axial distances as the neutral jet in figure 5.7, as well as two additional further downstream locations. Despite some scatter in the data, there is a clear upwards trend for both the axial turbulence intensity and Reynolds stress relative to the centreline velocity with increasing axial distance, or equivalently, decreasing local Fr. This is most evident for the $Fr \lesssim 3.38$ profiles as the flow exits the 'forced' regime, and is particularly strong in the $\overline{w'^2}/\overline{w}_c^2$ plot shown in (a). This does not imply that the magnitude of $\overline{w'^2}$ or $\overline{w'u'}$ is increasing with distance, but is instead revealing that $\overline{w'^2}$ and $\overline{w'u'}$ do not decrease at the same rate as the mean flow. This is consistent with the qualitative description of a negatively buoyant jet, where the mean velocity is reduced to zero at the top of the jet, z_i, but where we can still expect non-zero turbulence.

Cresswell and Szczepura (1993) also obtained $\overline{w'^2}$ and $\overline{w'u'}$ profiles, but for a fully developed fountain with $Fr_o \cong 3.2$. When their data (originally presented normalised by source conditions) is normalised by the centreline velocity, the peak values also increase with axial distance from the source as the mean flow decelerates. Near to the source, $0.03 \lesssim z/D \lesssim 1.7$, their peak values for the inner flow cover the range $0.05 \lesssim \overline{w'^2}/\overline{w}_c^2 \lesssim 0.2$ and $0.01 \lesssim \overline{w'u'}/\overline{w}_c^2 \lesssim 0.03$, which are broadly similar to the present values. However, the flow of Cresswell and Szczepura (1993) was at a much lower $Fr_o \cong 3.2$ and also included a return flow, and so is notably different to the present case of $Fr_o = 30$ negatively buoyant jets. The phenomenon of increasing turbulence intensities in a decelerating mean flow is not exclusive to negatively buoyant jets/fountains. In a flow through a conical diffuser, for example, increasing turbulence fluctuations and shear stresses, relative to the local centreline velocity, can be seen with increasing axial distance as the flow expands and decelerates (Okwuobi and Azad 1973; Singh and Azad 1995). Although such a flow is significantly different to the present case, since the evolution of turbulence with axial distance is affected by the velocity shear near the wall (even at the centreline (Singh and Azad 1995)), a decelerating mean flow will still work to increase the turbulence intensity if it is normalised in this way.

Figures 5.9 and 5.10 show the turbulent scalar fluctuation and axial and radial fluxes, $\sqrt{\overline{c'^2}}$, $\overline{w'c'}$ and $\overline{u'c'}$, normalised by the centreline values and scalar half-widths for the neutral and negatively buoyant jet at different axial distances. The neutral jet profiles in figure 5.9 generally all agree with Wang and Law (2002) and Webster et al. (2001). The $\sqrt{\overline{c'^2}}/\overline{c}_c$ data for $z/D \geq 23$ is in very close agreement with Webster et al. (2001), although the shortest axial location $z/D = 18$ is slightly higher near the centreline. The $\sqrt{\overline{c'^2}}/\overline{c}_c$ centreline value of the best fit by Wang and Law (2002) ($Re_o = 12700$, $40 < z/D < 80$) is slightly lower than the present

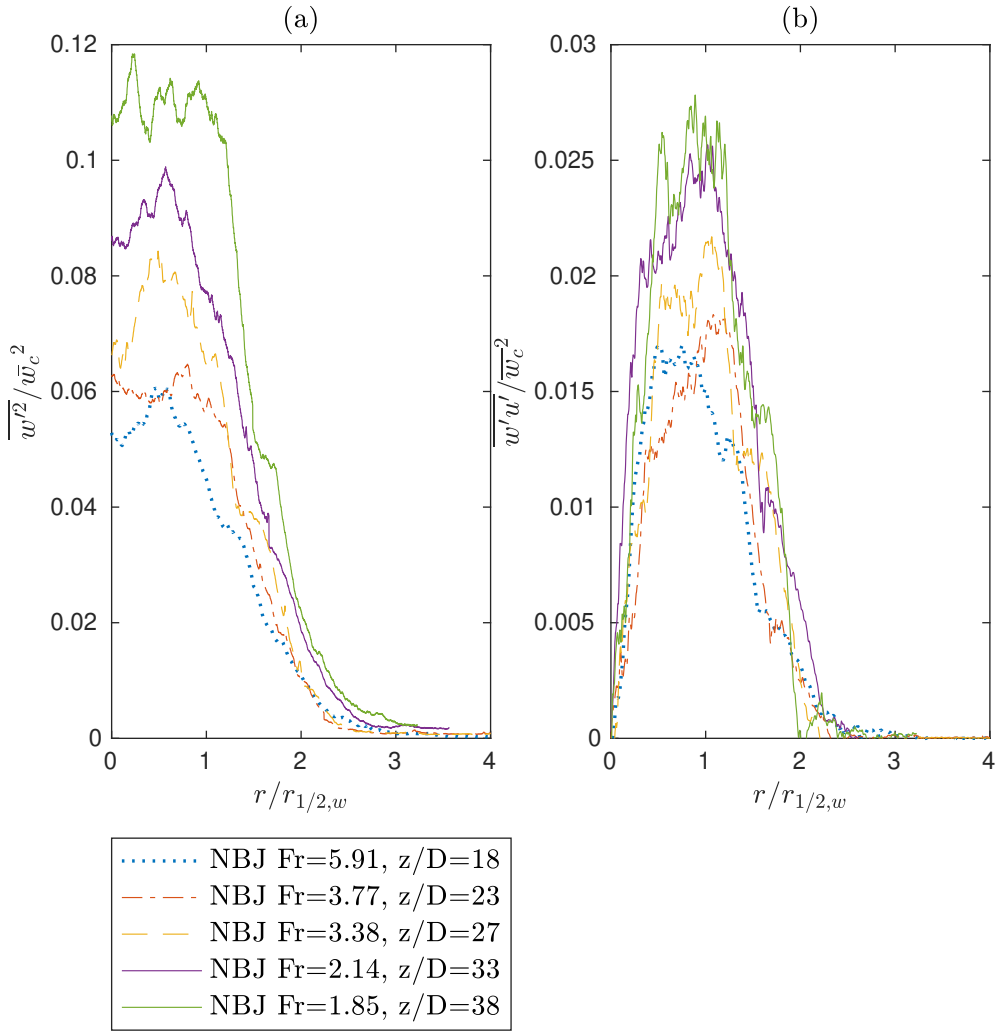

Figure 5.8: Mean turbulent axial velocity fluctuations, (a), and Reynolds stress, (b), for a negatively buoyant jet (NBJ) at several axial locations, normalised by the local mean centreline velocity, $\overline{w}_c^2$. The source conditions were $Fr_o = 30$ and $5500 \lesssim Re_o \lesssim 5900$ using $D = 10$ mm, with data gathered across multiple experiments.

jet data ($Re_o \cong 5700$, $18 < z/D < 27$). However this difference is small ($\lesssim 0.5\%$) when compared to the furthest jet experiment ($Re_o = 10700$, $z/D = 73$), and so the difference may be attributed to the larger z/D and Re_o in the Wang and Law (2002) experiments. The present axial flux data, $\overline{w'c'}/\overline{w}_c\overline{c}_c$, is close to both Wang and Law (2002) and Webster et al. (2001) for $18 \leq z/D \leq 27$ in the neutral jet, but here the $z/D = 73$ profile is a little higher. The radial flux, $\overline{u'c'}/\overline{w}_c\overline{c}_c$, is in reasonable agreement with both studies at all locations. The negatively buoyant profiles, given in figure 5.10, are of similar shape and order to the neutral jet data in figure 5.9, with no discernible trend with axial location evident. Although one might expect to see an increasing trend in $\overline{w'c'}/\overline{w}_c\overline{c}_c$ or $\overline{u'c'}/\overline{w}_c\overline{c}_c$ with axial distance, due to the decelerating mean flow, $\overline{w}_c$, this effect is not noticeable within the experimental

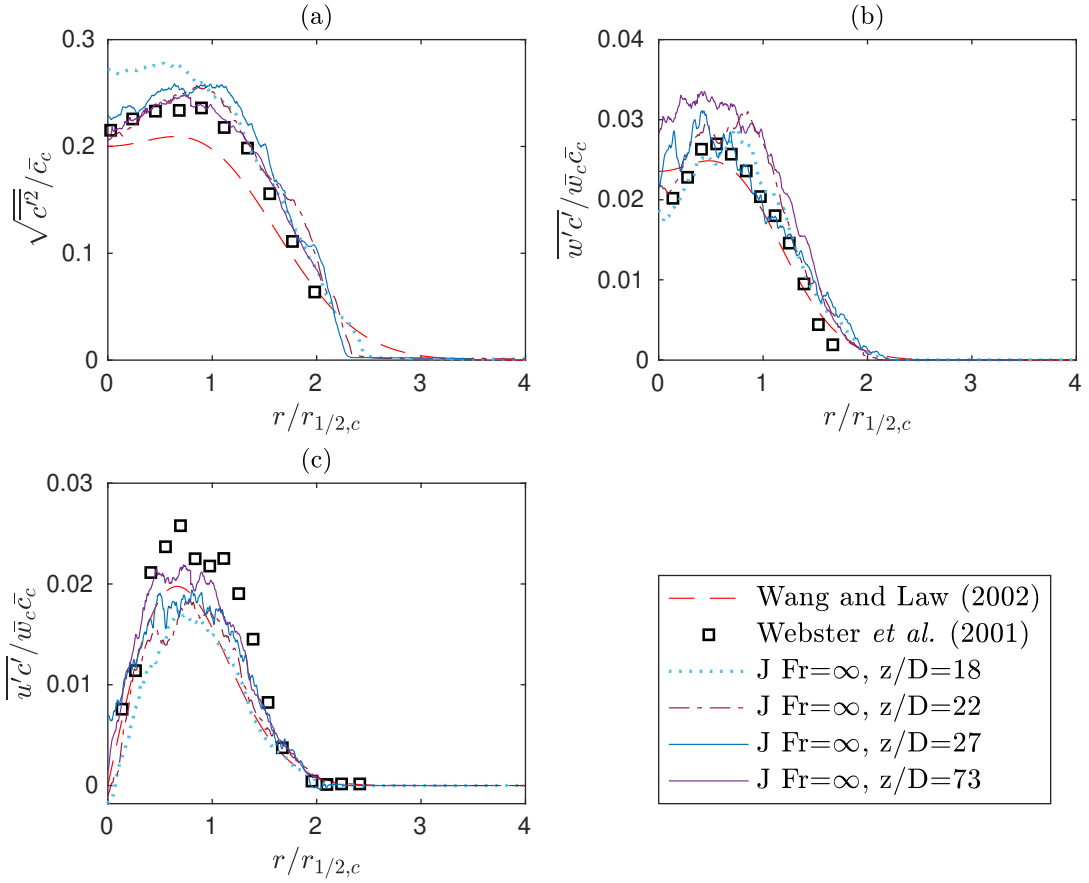

Figure 5.9: The turbulent scalar fluctuations and axial/radial flux profiles, $\sqrt{\overline{c'^2}}$, $\overline{w'c'}$ and $\overline{u'c'}$ are given in (a), (b) and (c), respectively, normalised by the centreline values, $\overline{w}_c$ and $\overline{c}_c$, and scalar half-width, $r_{1/2,c}$ for a neutral jet at various axial locations. The data was obtained from the same experiments as figure 5.7. The best fit curve from Wang and Law (2002) ($30 < z/D < 80$) and data from Webster et al. (2001) ($50 < z/D < 90$) is also shown.

scatter. This is likely due to the fact that, unlike with the velocity fluctuations, there is no clear relative increase of the scalar fluctuations compared to $\overline{c}_c$ (which does not go to zero at the top of the jet), and so the effect of a decreasing $\overline{w}_c$ is less significant. Cresswell and Szczepura (1993) also obtained these quantities for their $Fr_o = 3.2$ fountain using temperature measurements. When normalised by centreline quantities, and treating temperature as a passive scalar, their peak values in the inner flow for $0.3 \lesssim z/D \lesssim 2.3$ covered the range $0.12 \lesssim \sqrt{\overline{c'^2}}/\overline{c}_c \lesssim 0.3$, $0.01 \lesssim \overline{w'c'}/\overline{w}_c\overline{c}_c \lesssim 0.02$, and $0.004 \lesssim \overline{u'c'}/\overline{w}_c\overline{c}_c \lesssim 0.02$. As with the turbulent velocity fluctuations, these are broadly similar to the present range of negatively buoyant jet values, despite the differences in the flow.

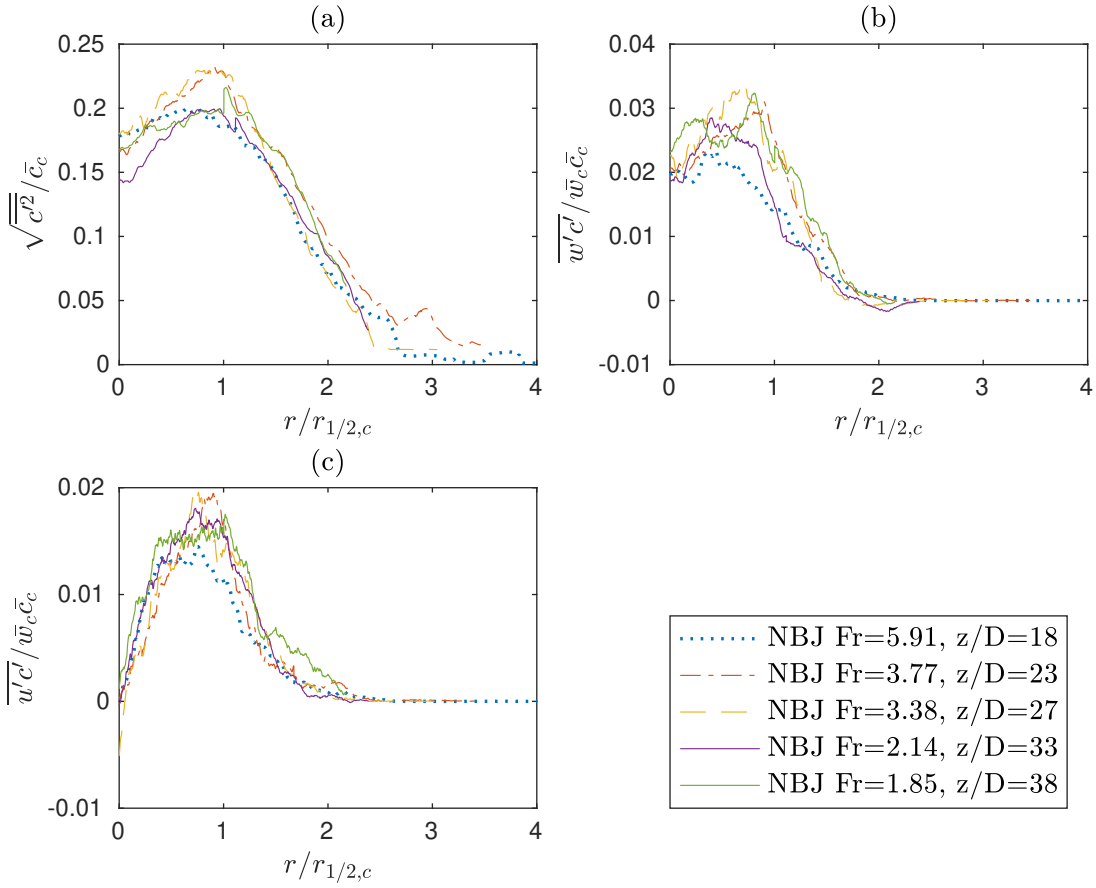

Figure 5.10: The normalised turbulent scalar fluctuations and axial/radial flux profiles, $\sqrt{\overline{c'^2}}$, $\overline{w'c'}$ and $\overline{u'c'}$ are given in in (a), (b) and (c), respectively, for a negatively buoyant jet at different axial locations. The data was obtained from the same experiments as figure 5.8.

5.4 Integral description of the flow

Figures 5.5(b) and 5.10(a)-(c) showed the development of the mean scalar concentration, $\overline{c}$, and the turbulent quantities, $\sqrt{\overline{c'^2}}$, $\overline{w'c'}$ and $\overline{u'c'}$, all scaling well with the centreline, $\overline{c}_c$, for a negatively buoyant jet. Since b and c are related by a constant such that $b = c(\rho_o - \rho_e)g/\rho_e$, this also shows that $\overline{b}$, $\sqrt{\overline{b'^2}}$, $\overline{w'b'}$ and $\overline{u'b'}$ scale with $\overline{b}_c$. However, this does not necessarily imply that they scale with b_m, the integral buoyancy scale. If the mean velocity and buoyancy profiles are assumed to be Gaussian, as is reasonably demonstrated by figure 5.5, then at any given axial location they may be expressed as $\overline{w} = \overline{w}_c \exp(-r^2/r_w^2)$ and $\overline{b} = \overline{b}_c \exp(-r^2/r_b^2)$. By evaluating ($2.10a-c$), the integral scales become $w_m = \overline{w}_c/2$, $r_m = \sqrt{2}r_w$ and $b_m = \overline{b}_c\lambda^2/2$. Note that for all definitions involving the integration limit $\tilde{r}$ in this chapter, we set $\tilde{r} = \infty$. We then see that $\overline{w}$ scales with w_m, but $\overline{b}$ only scales with b_m if λ is constant (i.e. the flow is self-similar). From figure 5.6 we see that λ is not constant in negatively buoyant jets, and instead increases with distance from the source. In light of this, new integral quantities may be defined that scale with $\overline{b}$ independent of the behaviour of λ,

$$G = 2\int_0^{\tilde{r}} \overline{b}^2 r \mathrm{d}r, \quad g_m = \frac{G}{B}, \quad r_{mb} = \mathrm{sgn}(B_o)\frac{B}{G^{1/2}}. \qquad (5.2a-c)$$

where G is the integral of the mean buoyancy squared and is analogous to M, and g_m and r_{mb} are buoyancy and buoyancy-width scales. The sign function, $\mathrm{sgn}(\cdot)$, is used in the definition of r_{mb} so that $\mathrm{sgn}(B_o) = 1$ or -1 for positively and negatively buoyant jets, respectively, ensuring that $r_{mb} > 0$ and the length scale is physically realistic. For neutral jets, B and G may be defined in terms of the scalar concentration, $\overline{c}$, instead of $\overline{b}$. With these definitions we have, for Gaussian $\overline{w}$ and $\overline{b}$ profiles,

$$g_m = \frac{\overline{b}_c}{2}, \quad r_{mb} = \sqrt{2}r_b, \quad \lambda = \frac{r_{mb}}{r_m}. \qquad (5.3a-c)$$

That is, we have an integral quantity, g_m, that scales with $\overline{b}$ without assuming a constant λ. The $\overline{b}$ profiles normalised by b_m, g_m and the buoyancy profile half-width, $r_{b,1/2}$, for the negatively buoyant jet are shown in figure 5.11(a) and (b), respectively. Figure 5.11(a) shows $\overline{b}/b_m$ decreasing with increasing distance from the source, while the $\overline{b}/g_m$ profiles in (b) collapse reasonably well with no systematic trend with Fr. This is a consequence of the increasing λ, which causes b_m to grow faster than $\overline{b}_c$, since $b_m \sim \overline{b}_c\lambda^2$ in Gaussian profiles. The $\overline{b}/g_m$ profiles, however, collapse reasonably well since $g_m \sim \overline{b}_c$ independent of λ.

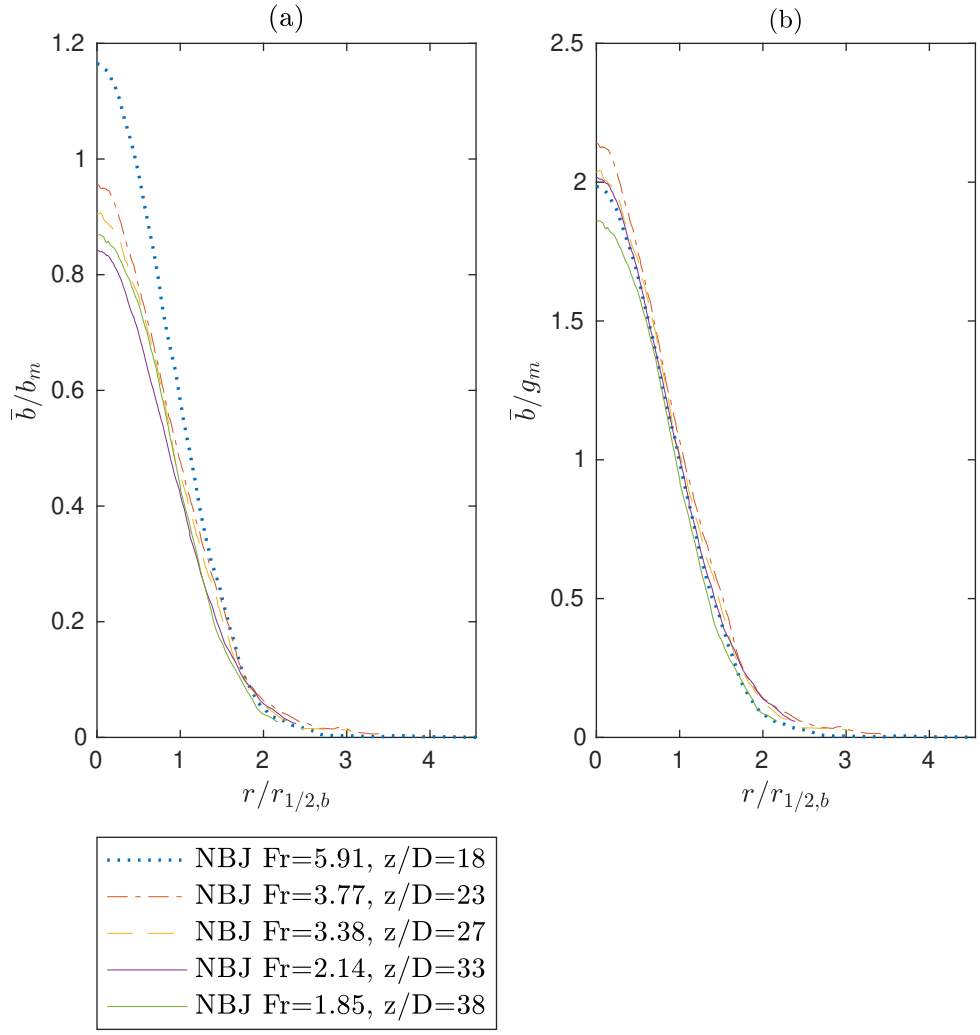

Figure 5.11: Mean buoyancy profiles of a negatively buoyant jet at different local Fr, with the vertical axis normalised by the integral quantities, b_m, (a), and g_m, (b), and the horizontal axis by the buoyancy half-width, $r_{b,1/2}$. The same data is plotted here as in figure 5.5(b), but normalised differently.

We have also observed that the turbulence quantities $\overline{w'^2}$ and $\overline{w'u'}$ increase relative to axial centreline velocity, and thus w_m, in negatively buoyant jets from figure 5.8. It is therefore useful to define a new 'turbulence velocity scale', w_f, that will scale with these quantities since w_m is no longer appropriate. This is defined in terms of the 'turbulent momentum flux', M_f,

$$M_f = 2\int_0^{\tilde{r}} \overline{w'^2} r \mathrm{d}r = r_m^2 w_f^2, \tag{5.4}$$

which is analogous to the 'mean' momentum flux, $M = r_m^2 w_m^2$. It also follows from this definition that $\beta_f = M_f/M$, relating it to the profile coefficient defined in (2.16).

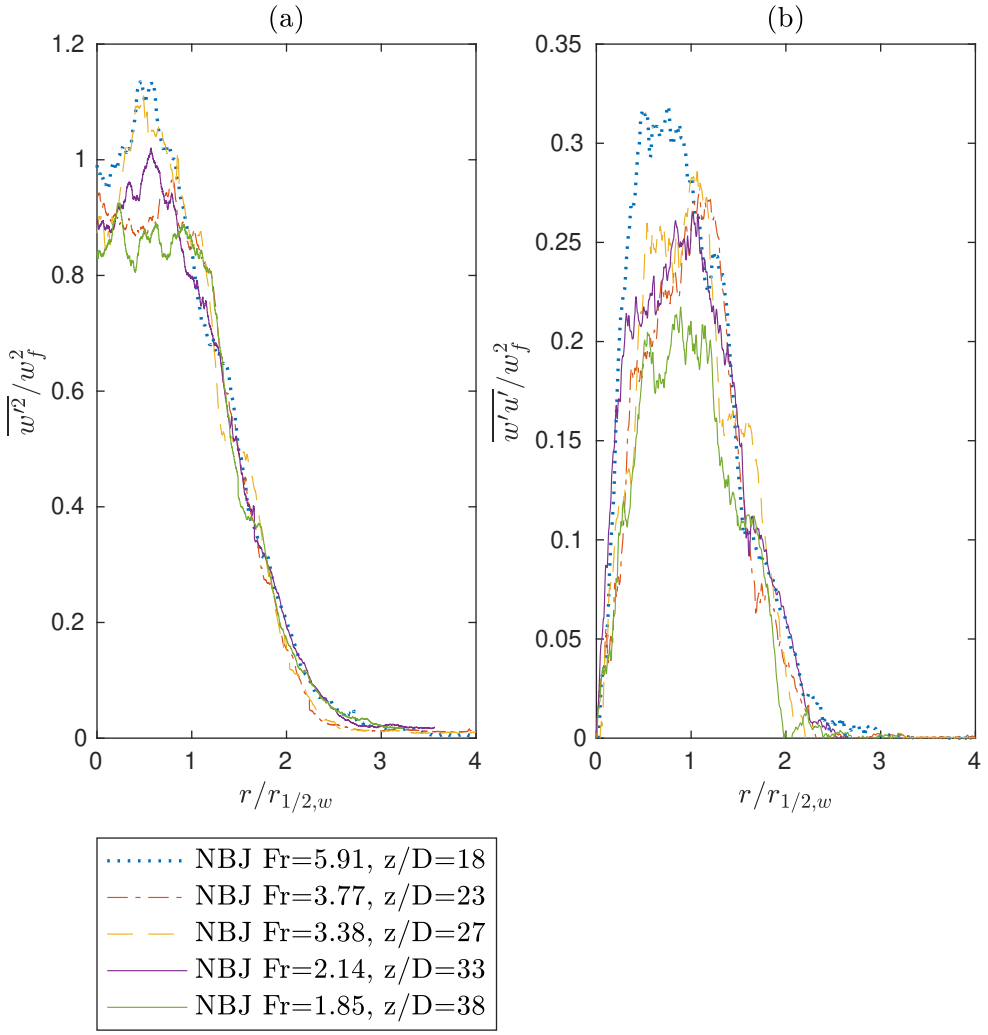

Figure 5.12: Mean turbulent axial velocity fluctuations, (a), and Reynolds stress, (b), for a negatively buoyant jet (NBJ), normalised by the 'turbulence velocity scale', w_f^2, defined in (5.4). The same data is plotted here as in figure 5.8, but normalised differently.

Figure 5.12 shows the $\overline{w'^2}$ and $\overline{w'u'}$ profiles normalised by w_f^2 at several axial distances, which can be compared to figure 5.8 where the same profiles are normalised by $w_c^2 = (2w_m)^2$ (for Gaussian $\overline{w}$ profiles). While figure 5.8 shows a clear increasing trend for both $\overline{w'^2}$ and $\overline{w'u'}$ relative to w_m^2, in figure 5.12 the profiles collapse within some experimental scatter, showing no systematic trend. The horizontal axis in figure 5.12 is $r_{1/2,w} \sim r_m$, showing that although the new turbulence velocity scale is required for the magnitude of turbulence profiles, the same length scale as the mean profiles may be used. The analysis in the following sections will assume that M_f is small compared to M, or equivalently, that the profile coefficient β_f is small. This is reasonable in the high Fr region of the negatively buoyant jet where M is sufficiently large, although may no longer be valid near the top where $M \to 0$. Future

work may seek to take into account M_f in this region, and a conservation equation for M_f, derived from the $\overline{w'^2}$ budget, may be required in addition to (2.12)-(2.15).

5.5 Entrainment

5.5.1 Estimating α

An analytical expression for the entrainment coefficient, α, derived from the conservation of mass, momentum and mean kinetic energy was introduced in §2.4.1. This is given again below, with the turbulence components of the profile coefficients neglected (van Reeuwijk and Craske 2015),

$$\alpha_M = -\frac{\delta_m}{2\gamma_m} + \left(1 - \frac{\theta_m}{\gamma_m}\right) Ri + \frac{Q}{2M^{1/2}} \frac{\mathrm{d}}{\mathrm{d}z}(\ln \gamma_m). \tag{5.5}$$

The first term, $-\delta_m/2\gamma_m$, is the ratio of turbulence production to mean energy flux, and is the only non-zero term in a self-similar neutral jet where it is constant. The second term shows the effect of buoyancy on entrainment through the local Richardson number, and provides a mechanism for buoyancy-driven entrainment associated with the mean flow, rather than by directly affecting turbulence (van Reeuwijk and Craske 2015). The third term reflects how the profile coefficients γ_g and β_g change along the jet, and is zero if the flow is fully self-similar.

By assuming self-similar profiles, (5.5) becomes,

$$\alpha_{MS} = -\frac{\delta_m}{2\gamma_m} + \left(1 - \frac{\theta_m}{\gamma_m}\right) Ri, \tag{5.6}$$

which, for constant δ_m, is equivalent to the PB model. Priestley and Ball (1955) additionally assumed Gaussian profiles with $\lambda = 1$ when first solving their model for positively buoyant jets/plumes. For the case of negatively buoyant jets, although we have shown that an assumption of Gaussian profiles is realistic over the Fr range observed, the non-constant λ indicates that the full self-similarity assumption is not. It is therefore useful to invoke the assumption of Gaussian velocity and buoyancy profiles, yet allowing for a variable λ, to (5.5). The resulting expression is,

$$\alpha_{MG} = \underbrace{-\frac{3}{8}\delta_m}_{A_1} + \underbrace{\left(1 - \frac{3}{2(1+\lambda^2)}\right) Ri}_{A_2}, \tag{5.7}$$

where $\theta_m = 2/(\lambda^2 + 1)$, and the third term from (5.5) vanishes since $\gamma_m = 4/3$ is

constant, for Gaussian profiles.

To calculate δ_m from (2.16), the derivative $\partial\overline{w}/\partial r$ must be estimated from the experimental data. To avoid scatter in the derivative due to the spatially discrete velocity data, a two-dimensional Gaussian filter of width 100 pixels (approximately 4 times the width of a PIV interrogation window) was first applied to $\overline{w}$, and then the derivative estimated using a second order accurate finite difference stencil. A similar procedure was used to calculate the other derivatives present in the profile coefficient definitions. In calculating δ_m, as well as other quantities such as Q, it is also necessary to approximate an integral defined from $r = 0$ to infinity using data from a finite region. In obtaining Q for the NBJ, for example, the integral was first calculated using the trapezoidal rule over the full r range captured in the region of interest. This was compared to the values obtained if the integral was calculated only up to the point where the mean axial velocity first equals zero. The latter gives Q typically around 3% lower than using the full range, since there are small $\overline{w} \lesssim 0$ values in the outer region. This difference is considered negligible, and given these negative velocities are much lower than inside the jet ($\lesssim 0.01\overline{w}_c$), this region is regarded as part of an approximately quiescent ambient. Integrating from $r = 0$ to the edge of the region of interest was therefore used in computing all integral quantities.

5.5.2 The entrainment coefficient in NBJs

Figure 5.13 shows the average value of $\alpha_{MG} = A_1 = 0.0714$ as a horizontal line calculated from the present neutral jet data, assuming self-similar Gaussian profiles. This is in reasonable agreement with the 'mean self-similar' value calculated in van Reeuwijk and Craske (2015) of $\alpha = 0.073$, and their direct estimate (from the conservation of volume (2.12)) of $\alpha = 0.069$.

For the negatively buoyant jet, neither term in (5.7) is necessarily constant, and both are plotted against local Ri in figure 5.13. We see that the first term, A_1, which corresponds to the ratio $-\delta_m/2\gamma_m$, increases with more negative Ri. This is a consequence of the profile coefficient δ_m, which increases in magnitude with axial distance primarily due to $\overline{w'u'}$ remaining high relative to w_m, as discussed in §5.3.3 and §5.4. However, the overall value of α_{MG} decreases for more negative Ri due to the second term, A_2, which reflects the effect of negative buoyancy on entrainment through the factor of Ri. This can also be seen by considering linear fits with Ri of

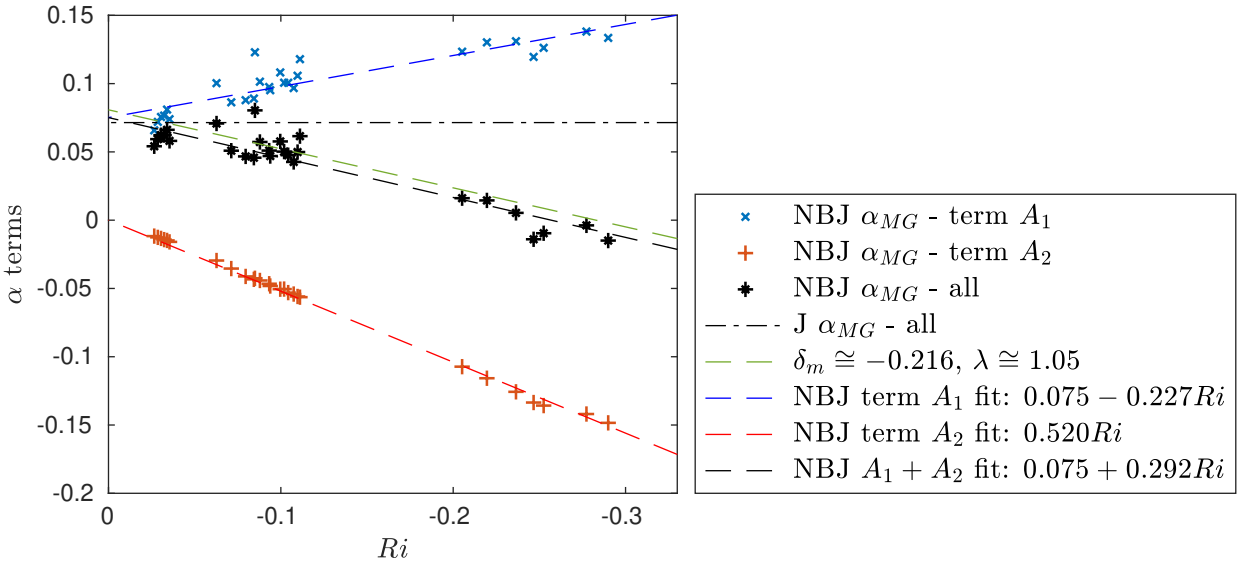

Figure 5.13: The entrainment coefficient in the neutral and negatively buoyant jets from the present experiments, as calculated from (5.7), which assumes Gaussian velocity and buoyancy profiles, and for the NBJ case, allows for non-constant λ. For the neutral jet, which has $Ri = 0$ everywhere, α is shown as a horizontal line for clarity. The prediction of α from (5.7), using the constant values $\delta_m = -0.216$ and $\lambda = 1.05$ obtained from Kaminski et al. (2005), is also shown, as well as linear fits of the terms A_1, A_2, and $A_1 + A_2$.

the terms A_1, A_2, and their summation to give α,

$$\left.\begin{aligned} A_1 &= 0.075 - 0.227Ri \\ A_2 &= 0.520Ri \\ \alpha &= 0.075 + 0.292Ri. \end{aligned}\right\} \tag{5.8}$$

This empirical α relation can be expressed as,

$$\alpha = -\frac{\delta_j}{2\gamma_m} + \left(1 - \frac{\theta_m}{\gamma_m} - \frac{\tilde{\delta}}{2\gamma_m}\right) Ri, \tag{5.9}$$

which is equivalent to (5.6) with $\delta_m = \delta_j + \tilde{\delta}Ri$. The coefficients of the empirical fits of A_1 and A_2 in (5.8) imply $\delta_j \cong -0.200$, $\tilde{\delta} \cong 0.604$ and a constant $\theta_m \cong 0.640$ ($\lambda \cong 1.46$ for Gaussian profiles). The value for δ_j can be interpreted as the 'neutral jet value' implied by the model, which agrees with the jet values reported in van Reeuwijk and Craske (2015) of $0.19 \lesssim -\delta_m \lesssim 0.21$ (Panchapakesan and Lumley 1993; Wang and Law 2002; Ezzamel et al. 2015). The entrainment relation in (5.7) is derived from the conservation equations (2.12), (2.13) and (2.15). In (5.9), we make the ad hoc addition of the $\tilde{\delta}$ term motivated by the approximately linear δ_m

trend observed from the data in figure 5.13. The inclusion of $\tilde{\delta}$ is ad hoc since there has not yet been an analysis of the governing equations to show the necessity of this term. Nevertheless, its inclusion is supported by the data in figure 5.13, which raises the open question for potential future research to explain the apparent need for it. The linear α relation in (5.9) is then a semi-empirical description of the flow based on fits of the present experimental data, rather than a direct derivation from the conservation equations, and will be henceforth referred to as 'model 1'.

The α relation given in (5.8) has a similar form to the linear relationship for positively buoyant jets/plumes, which have $Ri > 0$ (Priestley and Ball 1955; Fox 1970). However, (5.8) is only proposed valid for $Ri < 0$, where we have observed the linear relationship between δ_m and Ri. It is not intended as a universal relation for both positively and negatively buoyant jets. In the far field, buoyant jets approach a state of self-similarity where they become indistinguishable from pure plumes, approaching a constant $Ri = Ri_p > 0$ (Fischer et al. 1979; Papanicolaou and List 1988). For these self-preserving flows, δ_m is constant and hence the linear α relation with Ri in the form of (5.7), where A_1 is constant, is obtained. It has been reported that δ_m is approximately the same pure jets ($Ri = 0$) and plumes ($Ri = Ri_p$) (van Reeuwijk and Craske 2015; Wang and Law 2002; Ezzamel et al. 2015; van Reeuwijk et al. 2016), and an approximately constant δ_m has been reported in buoyant jets for $0.25 \lesssim Ri/Ri_p \lesssim 0.75$ (van Reeuwijk et al. 2016). However, this buoyant jet value was slightly lower than the jet and plume values, and also varied near the source before the flow had developed (van Reeuwijk et al. 2016).

Kaminski et al. (2005) derived an equation for α equivalent to (5.5), but in terms of the coefficients $\tilde{A}$ and $\tilde{C}$ (denoted A and C in their equation (3.33)). These can be related to the profile coefficients in (5.5) by (Kaminski et al. 2005; van Reeuwijk and Craske 2015),

$$\tilde{C} = -\delta_m/(\sqrt{2}\theta_m\gamma_m), \quad \tilde{A} = \gamma_m/\theta_m. \tag{5.10a - b}$$

In this formulation, $\tilde{C}$ is related to the ratio of turbulent production to the mean energy flux, but is also influenced by the shape of $\overline{w}$ and $\overline{b}$ through θ_m. The parameter $\tilde{A}$ is related to the mean energy flux and is also influenced by the shape of the mean profiles. Using (5.10), (5.6) may then be written in terms of these parameters,

$$\alpha_{MS} = \frac{\gamma_m \tilde{C}\sqrt{2}}{2\tilde{A}} + \left(1 - \frac{1}{\tilde{A}}\right) Ri. \tag{5.11}$$

Kaminski et al. (2005) calculated these parameters based on literature for positively buoyant jets/plumes (see their table 3), with average values of $\tilde{C} = 0.12$ and $\tilde{A} = 1.4$. Although limited data was available, Carazzo et al. (2008) later found similar values

in negatively buoyant jets. Using (5.10), these correspond to $\delta_m \cong -0.216$ and $\lambda \cong 1.05$ ($\theta_m \cong 0.952$) for Gaussian velocity/buoyancy profiles. When substituted into (5.7), these give the linear relationship,

$$\alpha = 0.081 + 0.286Ri. \tag{5.12}$$

This relationship will be referred to as 'model 2', and is a reformulation of the linear entrainment relation derived by Fox (1970) based on the work by Priestley and Ball (1955), and uses constants based on values reported in Kaminski et al. (2005). This is very similar to model 1 given in (5.8) and based on empirical fits for an NBJ, which can been seen in figure 5.13 where both models are shown.

Model 2 gives good predictions of α in negatively buoyant jets, but assumes a constant $\delta_m \cong -0.216$ and $\lambda \cong 1.05$ that are not consistent with the increasing A_1 and λ observed in figures 5.13 and 5.6, respectively. Model 2 can also be described by (5.9), but where $\delta_j = \delta_m \cong -0.216$ and $\tilde{\delta} = 0$. It can then be seen that the similarity between the models is partly due to the $\delta_j \cong -0.200$ assumed by model 1 being similar to $\delta_j \cong -0.216$ in model 2 (i.e. the 'neutral jet value'), which results in the first term of the linear α relations in (5.8) and (5.12) being similar. The second term (the Ri coefficient) of the relations are also similar, but for different reasons. In model 2, the value is determined by $\lambda \cong 1.01$ ($\theta_m \cong 0.952$) only, since $\tilde{\delta} = 0$ (and $\gamma_m = 4/3$) with respect to (5.9). For model 1, we have $\tilde{\delta} \cong 0.604$ and $\lambda \cong 1.46$ ($\theta_m \cong 0.640$), which give a similar Ri coefficient when inserted into (5.9). Model 1 appears to provide a representation of α in an NBJs that is more consistent with the observed δ_m and λ in the present data.

5.5.3 Mean radial outflow

For $Ri \gtrsim -0.11$ ($Fr \gtrsim 3.0$), in the forced regime, α_{MG} in the NBJ is positive but generally lower than it is for the neutral jet. For $Ri \lesssim -0.25$ ($Fr \lesssim 2.0$), α_{MG} becomes negative, implying there is a mean radial outflow of fluid from the jet to the ambient. This phenomenon has also been reported in the literature on fully developed fountains, where a mean outflow is observed from the IF to OF (Cresswell and Szczepura 1993; Williamson et al. 2011). In a general sense, entrainment may be considered the process where fluid is transported from a non-turbulent to turbulent region across some interface (e.g. Mistry et al. (2016)). The α given by (5.5), however, is simply a consistency requirement for the conservation of mass, momentum, buoyancy and mean kinetic energy equations. This expression, and subsequent simplifications such as (5.7), are therefore not necessarily describing entrainment in

this general sense, but instead reflecting what the radial mean flow must be in order to satisfy the conservation equations. An NBJ with a mean radial outflow could still be subject to instantaneous 'entrainment' (flow from a non-turbulent to turbulent region) at some times, while ejecting fluid into the ambient at others. The $\alpha < 0$ observed in the present NBJ indicates this net radial outflow, and means that on average there is more fluid ejected outwards than flowing into the jet in this region. This can be observed directly by examining the mean radial velocity profiles across the jet, where the net outflow of fluid corresponds to $\overline{u} > 0$ outside of the jet. This can be seen on the left axis of figure 5.14, which shows $\overline{u}/\overline{w}_c$ plotted for the negatively buoyant jet at $Fr = 3.00$ ($Ri = -0.11$) and $Fr = 1.86$ ($Ri = -0.29$), within the $\alpha > 0$ and $\alpha < 0$ regions respectively. The right axis shows the axial velocity profiles, $\overline{w}/\overline{w}_c$, at the same locations as a reference. The $Fr = 3.00$ curve has $\overline{u}/\overline{w}_c < 0$ for $r/r_{w,1/2} \gtrsim 1.2$, indicating net entrainment of fluid into the edge of the jet where $\overline{w}/\overline{w}_c \to 0$. The $Fr = 1.86$ curve, however, has $\overline{u}/\overline{w}_c > 0$ in this region, indicating there is a net radial outflow of fluid into the ambient.

Although this mean radial outflow does not typically occur in neutral or positively buoyant jets and plumes, which have $\alpha > 0$ everywhere, in negatively buoyant jets, a negative α towards the top of the jet is a natural consequence of (5.7), rather than any fundamentally different physics. This comes from the negative buoyancy and a decelerating mean flow resulting in $Ri \to -\infty$ at the top of the jet. This causes the second term, A_2, to become increasingly negative, dominating (5.7) until $\alpha < 0$ and there is a net radial outflow of fluid from the jet.

In chapter 6 we will seek to incorporate the traditional notion of entrainment (an inflow across a turbulent/non-turbulent interface), into the description of an NBJ with a net outflow. This is pursued by splitting up the mean radial velocity into 'entrainment' and 'outflow' components, where only the inflowing fluid is assumed to be proportional to the mean flow by an entrainment coefficient. This description will provide an alternative notion of 'entrainment' that is conceptually similar to that used in the traditional integral models (Morton et al. 1956; Morton 1959), and that can occur simultaneously with a mean outflow.

5.6 Integral model predictions

In §2.10, the system of ODEs describing positively or negatively buoyant turbulent jet in homogeneous environment, neglecting second order turbulence contributions, were discussed. These are given in (2.19)-(2.21), and are now solved numerically using models 1 and 2 discussed in §5.5.2. Model 1 corresponds to using the α

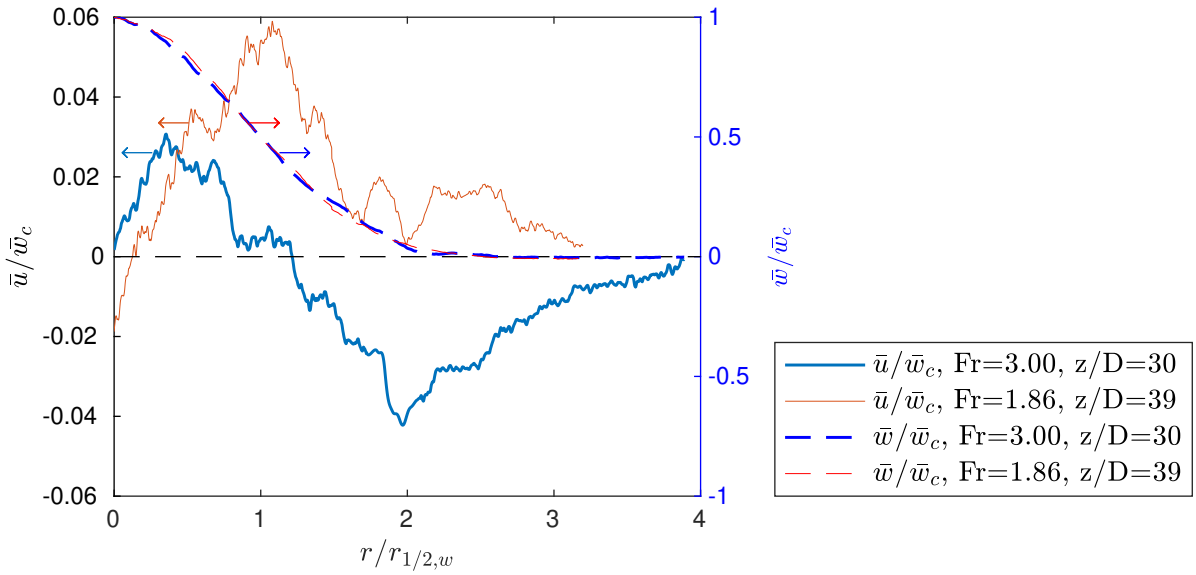

Figure 5.14: The left axis and solid lines show the normalised radial velocity profiles, $\overline{u}/\overline{w}_c$ of a negatively buoyant jet at two different axial locations. The right axis and dashed lines show the corresponding axial velocity profiles, $\overline{w}/\overline{w}_c$. The right and left arrows are shown to indicate the axis each profile corresponds to.

relation defined in (5.8), which assumes a linear δ_m relationship with Ri and constant $\lambda \cong 1.46$. Although we observed from figure 5.6 that λ is not constant in NBJs, $\lambda \cong 1.46$ lies within the range of observed values and so, when solving (2.19)-(2.21), we take it to be constant to simplify the model. When solving model 2, the α relation in (5.12) is used, which assumes a constant $\delta_m \cong -0.216$ and $\lambda \cong 1.05$ (Kaminski et al. 2005; Carazzo et al. 2008). By assuming a constant δ_m, model 2 is simply a reformulation of the PB model (Priestley and Ball 1955; Fox 1970), and although these δ_m and λ values are not consistent with those observed from our NBJ data, this model provides a useful reference case for comparison. The system of equations is also solved using the Morton (1959) model (constant $\alpha = 0.0714$ and $\lambda = 1.2$) as an additional comparison.

The predictions for $w_o/\overline{w}_c$ obtained by solving (2.19)-(2.21) with these models have been presented in figure 5.4 alongside the experimental data. The Morton (1959) model gives similar predictions to both model 1 and 2 for $z/D \lesssim 27$, where there is also reasonably good agreement with our NBJ data. Models 1 and 2 continue to agree with each other and the NBJ data until $z/D \cong 30$. For $30 \lesssim z/D \lesssim 38$, model 2 actually gives better predictions than model 1 based on the empirical data, despite assuming values for δ_m and λ that are not consistent with the present NBJ results. Part of the reason that two similar α models can give significantly different predictions for $\overline{w}_c$ is due to λ. Firstly, this is due to the fact that in addition to the α relation, λ appears in the momentum equation (2.20) through θ_m. Additionally,

λ appears in the definition of Ri through θ_m, which further complicates its influence on the flow.

Neither model 1 or 2 accurately predict the flow over the full Ri range observed while simultaneously maintaining consistency with the present δ_m and λ observations. This suggests that neither model is complete. The $\lambda \cong 1.46$ used in model 1 is closer to the observed experimental data in figure 5.6 than model 2, although has poorer agreement for $z/D \gtrsim 27$. Although the $w_o/\overline{w}_c$ agreement of model 2 is very good, it is not consistent with the observed λ and δ_m in the present data, and we leave this apparent discrepancy as an open question.

Mizushina et al. (1982) found in their experimental study of fully developed fountains ($3 \lesssim Fr_o \lesssim 258$), that the radius of the fountain was approximately constant and given by $r_f/D \cong 0.26 Fr_o$. If the cap region of the fountain was hemispherical, then this would also be equal to the radius and vertical thickness of the cap. The cap region would then extend from $z = z_{ss} - r_f$ to the top of the fountain, $z = z_{ss}$. If the top of a negatively buoyant jet resembles the cap of a fully developed fountain, then this region would not be well described by the present integral model, which was derived for jet-like flows. The present $Fr_o = 30$ negatively buoyant jet, which has $z_i/D \cong 53.5$, would have $r_f/D \cong 7.8$. The end of the 'jet-like' region where the models are applicable would then occur at $z/D \cong 45.7$. This is somewhat further than $z/D \cong 30$ where model 1 departs from the data, possibly due to the limitations of the model discussed above, but is nevertheless broadly consistent.

5.7 Velocity and buoyancy spreading rates

To investigate the mechanism behind the increasing λ observed in figure 5.6, we consider an expression for $\mathrm{d}r_m/\mathrm{d}z$, the spreading rate of the velocity width, based on the conservation of volume, momentum, and kinetic energy equations (van Reeuwijk and Craske 2015),

$$\frac{\mathrm{d}r_m}{\mathrm{d}z} = -\frac{\delta_g}{\gamma_g} + \frac{3}{2}\left(\frac{1}{\beta_g} - \frac{4}{3}\frac{\theta_m}{\gamma_g}\right) Ri + r_m \frac{\mathrm{d}}{\mathrm{d}z}\left(\ln \frac{\gamma_g}{\beta_g^{3/2}}\right), \tag{5.13}$$

and neglecting the turbulence transport by omitting the turbulence components of the profile coefficients,

$$\frac{\mathrm{d}r_m}{\mathrm{d}z} = -\frac{\delta_m}{\gamma_m} + \frac{3}{2}\left(1 - \frac{4}{3}\frac{\theta_m}{\gamma_m}\right) Ri + r_m \frac{\mathrm{d}}{\mathrm{d}z}\left(\ln \gamma_m\right). \tag{5.14}$$

The first term, $-\delta_m/\gamma_m$, corresponds to the ratio of dimensionless turbulent production to dimensionless energy flux, and the second term reflects the effect of buoyancy on the spreading rate through Ri (van Reeuwijk and Craske 2015). We now consider the case where $\overline{w}$ and $\overline{b}$ take Gaussian profiles, but allowing for a variable λ. If only the mean components of the profile coefficients are considered, the resulting expression is,

$$\frac{\mathrm{d}r_m}{\mathrm{d}z} = \underbrace{-\frac{3}{4}\delta_m}_{T_1} + \underbrace{\frac{3}{2}\left(1 - \frac{2}{1+\lambda^2}\right) Ri}_{T_2}, \tag{5.15}$$

where, similarly to (5.7), the third term from (5.14) vanishes since $\gamma_m = 4/3$ is constant for Gaussian profiles. For a self-similar neutral jet, $Ri = 0$ and δ_m is constant, and so $\mathrm{d}r_m/\mathrm{d}z$ is constant. For a negatively buoyant jet with variable λ and $Ri < 0$, $\mathrm{d}r_m/\mathrm{d}z$ need not be constant.

To examine the behaviour of the ratio λ, it is useful to also consider the spreading rate of the buoyancy width, r_{mb} defined in (5.2), since we have $\lambda = r_{mb}/r_m$ for Gaussian profiles. In this case we consider the conservation of buoyancy and an equation for 'squared mean buoyancy', with the second order turbulence terms neglected (Craske et al. 2017),

$$\frac{\partial}{\partial r}\left(r\overline{u}\overline{b} + r\overline{u'b'}\right) + \frac{\partial}{\partial z}\left(r\overline{w}\overline{b}\right) = 0, \tag{5.16}$$

$$\frac{\partial}{\partial r}\left(r\overline{u}\overline{b}^2 + 2r\overline{u'b'}\,\overline{b}\right) + \frac{\partial}{\partial z}\left(\overline{w}\overline{b}^2\right) + = 2r\overline{u'b'}\frac{\partial \overline{b}}{\partial r}. \tag{5.17}$$

These equations may then be integrated from zero to infinity with respect to r, and by defining additional non-dimensional profile coefficients, can be expressed as a pair of ODEs,

$$\frac{\mathrm{d}}{\mathrm{d}z}\left(\hat{\theta}_b \frac{MB}{Q}\right) = 0, \tag{5.18}$$

$$\frac{\mathrm{d}}{\mathrm{d}z}\left(\hat{\gamma}_b \frac{MG}{Q}\right) = \mathrm{sgn}(B_o)\frac{MG^{3/2}}{QB}\hat{\delta}_b, \tag{5.19}$$

where (5.18) and (5.19) correspond to the conservation of buoyancy and mean squared buoyancy, respectively. The profile coefficients are defined as,

$$\left.\begin{aligned}\hat{\theta}_b &= \frac{2}{w_m g_m r_{mb}^2}\int_0^{\tilde{r}} \overline{w}\overline{b} r \mathrm{d}r, \\ \hat{\gamma}_b &= \frac{2}{w_m g_m^2 r_{mb}^2}\int_0^{\tilde{r}} \overline{w}\overline{b}^2 r \mathrm{d}r, \\ \hat{\delta}_b &= \frac{4}{w_m g_m^2 r_{mb}}\int_0^{\tilde{r}} \overline{u'b'}\frac{\partial \overline{b}}{\partial r} r \mathrm{d}r,\end{aligned}\right\} \tag{5.20}$$

where $\hat{\gamma}_b$ is the dimensionless flux of mean squared buoyancy, $\hat{\delta}_b$ is the dimensionless production of buoyancy variance, and $\hat{\theta}_b$ is an alternative expression of the dimensionless buoyancy flux, θ_m. These are similar to the ODEs and profile coefficients used by Craske et al. (2017), who defined them in terms of r_m and b_m, however, in the present case they are defined in terms of r_{mb} and g_m. By applying the product rule to (5.18) and (5.19), and using the definition of r_{mb} from (5.2), the following may be derived,

$$\frac{\mathrm{d}B}{\mathrm{d}z} = -\frac{BQ}{M}\frac{\mathrm{d}}{\mathrm{d}z}\left(\frac{M}{Q}\right) - B\frac{\mathrm{d}}{\mathrm{d}z}\left(\ln\hat{\theta}_b\right), \tag{5.21}$$

$$\frac{\mathrm{d}G}{\mathrm{d}z} = \mathrm{sgn}(B_o)\frac{\hat{\delta}_b}{\hat{\gamma}_b}\frac{G^{3/2}}{B} - \frac{GQ}{M}\frac{\mathrm{d}}{\mathrm{d}z}\left(\frac{M}{Q}\right) - G\frac{\mathrm{d}}{\mathrm{d}z}\left(\ln\hat{\gamma}_b\right), \tag{5.22}$$

$$\begin{aligned}\frac{\mathrm{d}r_{mb}}{\mathrm{d}z} &= \mathrm{sgn}(B_o)\frac{1}{G^{1/2}}\frac{\mathrm{d}B}{\mathrm{d}z} - \mathrm{sgn}(B_o)\frac{B}{2G^{3/2}}\frac{\mathrm{d}G}{\mathrm{d}z} \\ &= -\frac{\hat{\delta}_b}{2\hat{\gamma}_b} - \frac{r_{mb}}{2w_m}\frac{\mathrm{d}w_m}{\mathrm{d}z} + r_{mb}\frac{\mathrm{d}}{\mathrm{d}z}\left(\ln\frac{\hat{\gamma}_b^{1/2}}{\hat{\theta}_b}\right),\end{aligned} \tag{5.23}$$

which provides an analytical expression for the spreading rate of the buoyancy width, r_{mb}, consistent with the conservation of volume, buoyancy, and squared mean buoyancy equations. The first term of (5.23), $-\hat{\delta}_b/(2\hat{\gamma}_b)$, is the ratio of dimensionless production of buoyancy variance to the dimensionless flux of squared mean buoyancy, and is a scalar analogue of the first term of (5.14). The second term relates the behaviour of the velocity scale, w_m, and buoyancy width, r_{mb}, to the spreading rate. The third is related to any similarity drift, and is zero if the flow is fully self-similar. Invoking the assumption of Gaussian mean velocity and buoyancy profiles, but allowing for a non-constant λ, the expression can be written as,

$$\frac{\mathrm{d}r_{mb}}{\mathrm{d}z} = \underbrace{-\frac{\hat{\delta}_b}{8}(2+\lambda^2)}_{H_1}\underbrace{-\frac{r_{mb}}{2w_m}\frac{\mathrm{d}w_m}{\mathrm{d}z}}_{H_2} + \underbrace{r_{mb}\frac{\mathrm{d}}{\mathrm{d}z}\left(\ln\left(\frac{\lambda^2+1}{\sqrt{\lambda^2+2}}\right)\right)}_{H_3}, \tag{5.24}$$

since we have, for Gaussian profiles, $\hat{\theta}_b = \theta_m = 2/(\lambda^2+1)$ and $\hat{\gamma}_b = 4/(\lambda^2+2)$. Here we clearly see that the third term, related to similarity drift, is zero if λ is constant.

For self-similar neutral jets $w_m \sim z^{-1}$ and, since λ is constant, $r_{mb} \sim r_m \sim z$ (Fischer et al. 1979). If assumed to originate from a point source, then these scales may be expressed as power laws of the form $r_{mb} = a_b z$ and $w_m = kz^{-1}$, where a_b and k are constants. From this, the second term of (5.24) becomes $H_2 = a_b/2$ and is constant. Since H_1 is also constant for self-similar jets, and $H_3 = 0$, we obtain the expected result that $\mathrm{d}r_{mb}/\mathrm{d}z$ is constant.

Figure 5.15(a) and (b) show the terms of the velocity and scalar spreading rate equations from (5.15) and (5.24), respectively. The two terms of $\mathrm{d}r_{mb}/\mathrm{d}z$ are similar with mean values of $H_1 \cong 0.081$ and $H_2 \cong 0.084$, giving a combined total of $\mathrm{d}r_{mb}/\mathrm{d}z \cong 0.165$, for the neutral jet assuming self-similar Gaussian profiles. The velocity spreading rate has only one non-zero term in this case, and is $\mathrm{d}r_m/\mathrm{d}z = T_1 \cong 0.151$. If the r_m and r_{mb} power laws from above are assumed to hold, then it follows that,

$$\lambda = \frac{r_{mb}}{r_m} = \frac{(\mathrm{d}r_{mb}/\mathrm{d}z)}{(\mathrm{d}r_m/\mathrm{d}z)}, \tag{5.25}$$

for a neutral jet, which gives $\lambda \cong 1.10$ using these values for $\mathrm{d}r_{mb}/\mathrm{d}z$ and $\mathrm{d}r_m/\mathrm{d}z$. This is in reasonable agreement with the mean value of λ from figure 5.6 of $\lambda \cong 1.18$, obtained by directly measuring the $1/e$ width of the buoyancy and scalar profiles.

For negatively buoyant jets with Gaussian velocity/buoyancy profiles and variable λ, all the terms of (5.15) and (5.24) may be non-zero and vary with distance from the source (or more negative Ri). Figure 5.15(a) shows the first term of $\mathrm{d}r_m/\mathrm{d}z$, T_1, slightly increasing with decreasing Ri. That is, an increasing $-\delta_m/\gamma_m$, the ratio of dimensionless turbulence production to the dimensionless mean energy flux. The second term, T_2, however, strongly increases in magnitude (with the opposite sign) as Ri becomes more negative, reducing the overall magnitude of $\mathrm{d}r_m/\mathrm{d}z$. The effect of negative buoyancy, captured by $Ri < 0$, thus reduces the overall spreading rate of the velocity width.

Conversely, figure 5.15(b) shows that the overall spreading rate of the buoyancy width increases with decreasing Ri, which is driven primarily by the growth of the second term of $\mathrm{d}r_{mb}/\mathrm{d}z$, H_2. This term captures the effect of the decelerating mean flow on the spreading rate, and may be explained by considering the solution by Morton (1959), plotted in figure 2.2, for the simplified case of a self-similar negatively buoyant jet with constant α. Here we see that the gradient of the velocity scale, $\mathrm{d}w_m/\mathrm{d}z$, approaches negative infinity at the top of the jet (where $Ri \to -\infty$),

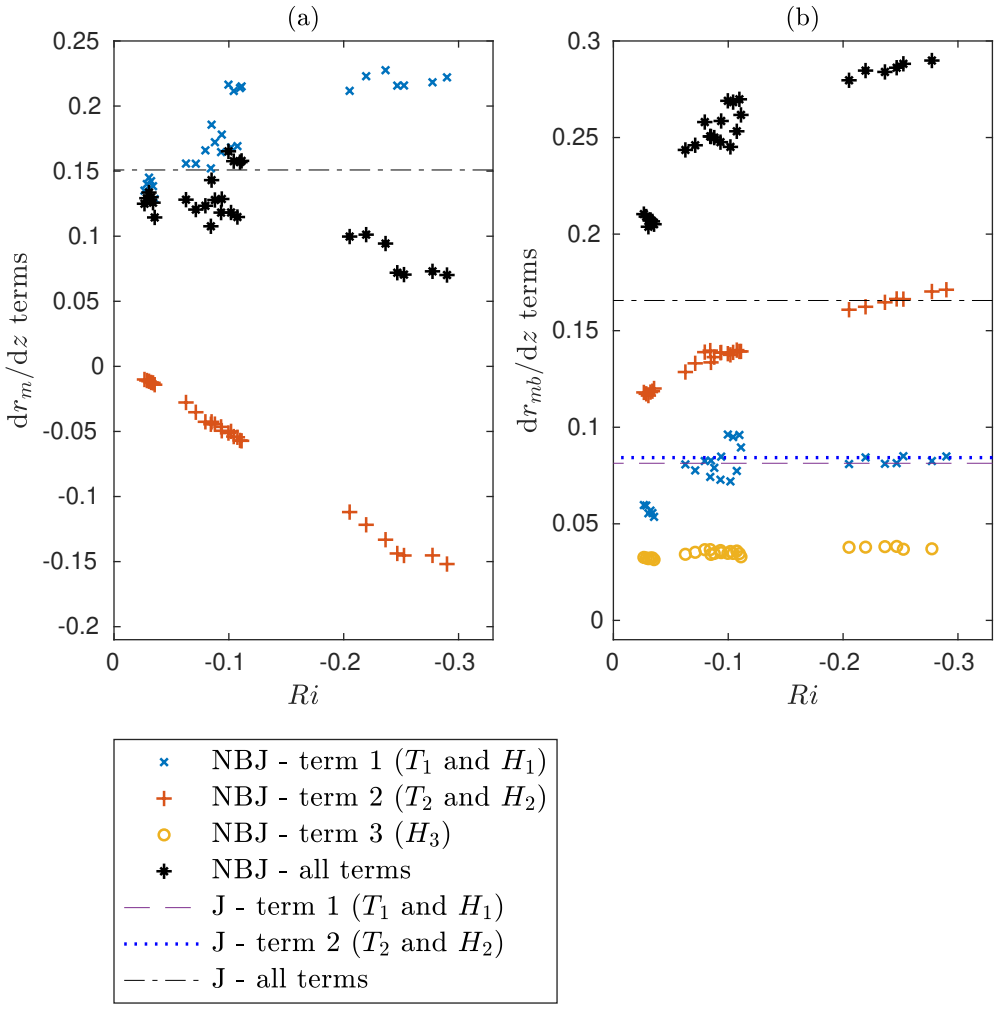

Figure 5.15: The individual terms (and the sum of them) of the velocity, (a), and buoyancy/scalar, (b), spreading rate equations as defined in (5.15) and (5.24) respectively. These assume Gaussian profiles and include only the mean components of the profile coefficients, and are plotted against Ri for the negatively buoyant jet. For the neutral jet, which has $Ri = 0$ and approximately constant terms, the mean values are shown as horizontal lines for clarity.

the width scale approaches positive infinity, and the velocity scale approaches zero. This can also be seen in the plots of $\hat{H}_2$ in figures 2.2(a) and (c), where the term is relatively small and increases slowly with decreasing $\hat{Fr}$ for $\hat{Fr} \gtrsim 2$ ($\hat{Ri} \gtrsim -0.25$), but grows rapidly towards infinity as $\hat{Fr}$ reduces to zero. This may be interpreted as the 'forced' and 'buoyancy dominated' regimes, respectively. It is clear from this that the term $H_2 = -(r_{mb}/2w_m)\mathrm{d}w_m/\mathrm{d}z$ increases as $Ri \to -\infty$ in this simplified model, as is observed in the present flow. However, the model predicts two distinct regimes where H_2 increases slowly and then rapidly further from the source, which is not as clear from figure 5.15(b). The first term of $\mathrm{d}r_{mb}/\mathrm{d}z$, H_1, increases slightly at the start of the jet, but after this remains reasonably constant and similar to the

value of the neutral jet. The third term, H_3, which is non-zero due to the varying λ, is nevertheless relatively small and constant with an average value of $H_3 \cong 0.035$. The net effect of all the terms in both equations is therefore to increase $\mathrm{d}r_{mb}/\mathrm{d}z$ and decrease $\mathrm{d}r_m/\mathrm{d}z$ with decreasing Ri (or increasing z).

In the case of negatively buoyant jets, the right most side of (5.25) does not hold, since r_m and r_{mb} evolve differently and do not scale linearly with z. However, if r_m and r_{mb} could be approximated as power laws of the form $r_m \cong a_w z^m$ and $r_{mb} \cong a_b z^n$, with constants a_w, a_b, n and m, then it follows that,

$$\lambda = \frac{r_{mb}}{r_m} \cong \frac{m}{n}\frac{(\mathrm{d}r_{mb}/\mathrm{d}z)}{(\mathrm{d}r_m/\mathrm{d}z)} \tag{5.26}$$

From this, it can be seen how the increasing $\mathrm{d}r_{mb}/\mathrm{d}z$ and decreasing $\mathrm{d}r_m/\mathrm{d}z$, shown in figure 5.15, can contribute to the increasing λ observed in figure 5.6.

Neutral and positively buoyant jets and plumes all tend towards a state of full self-similarity in the far field (Fischer et al. 1979; Papanicolaou and List 1988). For negatively buoyant jets, however, the mean velocity and buoyancy profiles continue to grow at different rates with increasing axial distance or decreasing Ri. This occurs over the entire range of Ri observed, including the 'forced' regime ($Ri \gtrsim -0.11$). This behaviour can be explained by (5.15) and (5.24), which describe the velocity and buoyancy spreading rates as derived from the conservation equations, rather than any fundamental differences in the physics governing the flow. The lack of self-similarity in negatively buoyant jets, which may be characterised by the increasing λ, is largely driven by the second term in both spreading rate equations, T_2 and H_2. This is a natural consequence of the jets negative buoyancy reducing the mean momentum to zero at the top of the jet, resulting in $Ri \to -\infty$ and a flow regime dominated by negative buoyancy rather than momentum.

When using integral models to describe a negatively buoyant jet, such as (2.12)-(2.14), it is reasonable to assume Gaussian velocity and buoyancy profiles and consider only the mean components of the profile coefficients. From figure 5.4 we have seen that assuming a linear α relation with Ri, given by (5.8) based on a constant $\lambda \cong 1.46$ and linear δ_m relation, gives good predictions of $\overline{w}_c$ up to $z/D \cong 30$. However, it is not accurate over the full z/D range, nor does it take into account the variable λ observed in figure 5.6. For a more complete model, the variation of λ should be taken into account. One approach would be to integrate (5.13) to obtain r_{mb}, and then calculate λ from (2.29). This would require approximating the terms H_1 and H_2, which themselves both contain λ. However, these are not the dominant terms in (5.13), and as was seen in figure 5.15(b), H_2 is reasonably small

and constant with the mean value $H_3 \cong 0.035$. The term H_1 increases slightly over the range $0.03 \lesssim -Ri \lesssim 0.06$, but remains reasonably constant after this. As a first approximation, this term may be assumed constant, taking the mean value from the present data of $H_1 \cong 0.077$. With a value for λ, (5.7) can then be used to model α, and the integral model may be solved.

5.8 Conclusions

Negatively buoyant jets have been investigated experimentally using combined PIV and PLIF measurements. This has allowed for mean velocity and buoyancy profiles, as well as turbulence profiles, to be obtained for a range of local Fr. Although there are differences between a neutral and negatively buoyant jet across the whole range of Fr investigated, a 'forced' regime for $Fr \gtrsim 3.0$ ($Ri \gtrsim -0.11$) was identified, where the flows are more similar. It has been shown that the velocity and buoyancy profiles take Gaussian shapes over a wide range of Fr, and scale with the local centreline values, $\overline{w}_c$ and $\overline{b}_c$, just as in a neutral jet, even outside of the forced regime. However, the velocity fluctuations, $\overline{w'^2}$ and $\overline{w'u'}$, increase relative to $\overline{w}_c^2$, due to the strongly decelerating mean flow, which is more significant for lower Fr. An integral 'turbulence velocity scale', w_f^2, is therefore required to collapse the turbulence fluctuation profiles onto a single curve, where as in a neutral jet $\overline{w}_c^2$ or w_m^2 is sufficient.

The mean velocity and buoyancy profiles have been shown to develop with different length scales across the full Fr range observed, and so the ratio of widths, λ, varies with axial distance. New integral quantities, g_m and r_{mb}, were therefore introduced that scale with $\overline{b}_c$ and r_b independent of λ. We have shown via a derived expression for $\mathrm{d}r_{mb}/\mathrm{d}z$, given in (5.24) and plotted in figure 5.15, some of the factors contributing to why the velocity and buoyancy profiles spread at different rates. The dominant term of the $\mathrm{d}r_{mb}/\mathrm{d}z$ expression is the second term, $H_2 = -(r_{mb}/2w_m)\mathrm{d}w_m/\mathrm{d}z$, which captures the decelerating mean flow of the jet. This term grows for more negative Ri, causing $\mathrm{d}r_{mb}/\mathrm{d}z$ to increase. This is consistent with the broad behaviour of the simplified model of a negatively buoyant jet described by Morton (1959). Conversely, $\mathrm{d}r_m/\mathrm{d}z$ decreases along the jet as Ri becomes more negative, due to the factor of Ri present in the second term, T_2, of (5.15). The increasing $\mathrm{d}r_{mb}/\mathrm{d}z$ and decreasing $\mathrm{d}r_m/\mathrm{d}z$ contributes to the increasing λ observed.

Entrainment in negatively buoyant jets was also investigated by building on the expressions derived by van Reeuwijk and Craske (2015), and applying them

to flows with Gaussian profiles, but without assuming a constant λ. It was found that entrainment is generally lower in the negatively buoyant jet than the neutral jet in the forced regime near the source ($Fr \gtrsim 3.0$, $Ri \gtrsim -0.11$), with α in the NBJ decreasing with more negative Ri. The finding that entrainment is lower in negatively buoyant jets than neutral jets is consistent with several previous studies (Papanicolaou et al. 2008; Kaminski et al. 2005). Further from the source, for $Fr \lesssim 2.0$ ($Ri \lesssim -0.25$), $\alpha < 0$ and there is a net radial outflow fluid from the jet to the ambient. This can be explained by (5.7), the expression for α_{MG}, which becomes negative for sufficiently large and negative Ri. This phenomenon has also been observed by Williamson et al. (2011) and Cresswell and Szczepura (1993) for the inner flow of a fully developed fountain, where fluid was found to move from the inner to the outer flow after some distance from the source.

The present investigation has provided evidence of several differences between neutral and negatively buoyant jets, including the scaling of the turbulent velocity profiles, the buoyancy and velocity spreading rates, a lower entrainment coefficient and the eventual net ejection of fluid near the top of the NBJ. It is possible for an integral model approach to be applied to negatively buoyant jets, and we have seen that reasonable $\overline{w}_c$ agreement can be achieved for $z/D \lesssim 30$ by assuming a linear α relationship with Ri, based on empirical fits of the present data. However, the model is not accurate over the full z/D range observed and thus is likely incomplete. The expression for $\mathrm{d}r_{mb}/\mathrm{d}z$ derived in (5.24) may be of use in further improving predictions by modelling a non-constant λ, although further research is required. Future research may also seek to understand the origins behind the increasing $-\delta_m$ observed in NBJs, which motivated the inclusion of the $\tilde{\delta}$ term in (5.9), the empirical α relation. A detailed analysis of the governing equations, specifically applied to negatively buoyant jets, may provide insight here.

Chapter 6

Fully developed fountains

The following chapter investigates the quasi-steady fully developed stage of fountain flow (F), occurring after the initial rise of a negatively buoyant jet (NBJ), where the flow consists of an inner/outer flow (IF/OF) structure. Fountains and negatively buoyant jets with $Fr_o = 30$ are compared alongside each other, allowing the effect of the return flow to be identified. Unlike NBJs, the mean velocity and buoyancy profiles in fountains do not take similar Gaussian shapes along the flow. The changing shape of these profiles is most evident in the outer flow region, while there is a degree of similarity in the inner flow. Fountains with different source Froude number, Fr_o, are investigated, finding that mean velocity/buoyancy profiles in the IF are similar in $Fr_o = 15$ and 30 fountains at locations where the local Fr is similar. The Reynolds stress and axial turbulence intensity profiles, however, are significantly affected by the return flow and differ for the two Fr_o cases in both the inner and outer flow regions.

6.1 Introduction

The present chapter will now consider the fully developed fountain stage of the flow, which occurs after a negatively buoyant jet has collapsed back onto itself and a quasi-steady state is reached. Forced fountains, $Fr_o \gtrsim 5.5$ (Burridge and Hunt 2012), oscillate around a steady-state height lower than the initial rise reached by the NBJ, $z_{ss} < z_i$, and consist of a two layer, inner flow/outer flow structure such as what was shown in figure 1.2(d).

Several previous investigations into fully developed fountains have involved taking bulk flow measurements, such as of z_i and z_{ss}, to obtain Fr_o scaling relations

for the rise heights (Turner 1966; Kaye and Hunt 2006; Burridge and Hunt 2012). These have aided the classification of distinct fountain regimes by Fr_o, ranging from very weak fountains ($Fr_o \lesssim 1.0$) to highly forced ($Fr_o \gtrsim 5.5$), the latter being the primary focus of the present investigation. Other studies have sought to investigate overall entrainment and dilution in fountains, such as Burridge and Hunt (2016) who proposed scaling relations for the entrained volume flux for the different fountain classes.

Although fewer attempts have been made, there have been some investigations involving local measurements of the internal velocity/scalar fields in fountains. Experimental studies by Mizushina et al. (1982) and Cresswell and Szczepura (1993), and a DNS study by Williamson et al. (2011), all found that the profiles inside fountains were not self-similar. The assumption of self-similarity is common in attempts to model fountains. These typically treat the inner flow as an NBJ surrounded by an opposing outer flow, assume self-similarity, and use constant entrainment coefficients to describe mixing between the IF/OF layers and the ambient fluid (McDougall 1981; Bloomfield and Kerr 2000; Hunt and Debugne 2016).

The present investigation will use combined PIV and PLIF measurements of the velocity/scalar fields in fountains. A key focus will be on differences between the development of NBJs and fountains, thus revealing the effect of the return flow, as well as between fountains with different Fr_o. Time-averaged statistics for a fully developed fountain are presented alongside those for an NBJ in §6.2, including a discussion of the effect of Fr_o on these profiles. The radial expansion of the inner flow of fountains is discussed in §6.5, where a scaling for the overall fountain width is found that is consistent with previous literature (Mizushina et al. 1982).

6.2 Statistics

6.2.1 Velocity and buoyancy profiles

In section 5.3, it was shown that the mean velocity and scalar concentration (buoyancy) profiles of a negatively buoyant jet are Gaussian over a wide range of local Fr. For the fountain, Fr here is defined based on inner flow quantities only, with the integrals in (2.9) being computed up to the IF/OF boundary, $\tilde{r} = r_{io}$, rather than infinity. This is expressed below, where r_{io} is defined as the location where the

mean axial velocity is first equal to zero, $\overline{w}(r = r_{io}) = 0$.

$$Q = 2\int_0^{r_{io}} \overline{w} r \mathrm{d}r, \quad M = 2\int_0^{r_{io}} \overline{w}^2 r \mathrm{d}r, \quad F = 2\int_0^{r_{io}} \overline{w}\overline{b} r \mathrm{d}r, \quad B = 2\int_0^{r_{io}} \overline{b} r \mathrm{d}r. \tag{6.1a-d}$$

With the same definitions for the velocity, length and buoyancy scales, which now apply to the IF only,

$$w_m = \frac{M}{Q}, \quad r_m = \frac{Q}{M^{1/2}}, \quad b_m = \frac{BM}{Q^2}. \tag{6.2a-c}$$

and using the same definition of the local Froude and Richardson numbers,

$$Fr = \frac{w_m}{(-r_m b_m)^{1/2}} = \frac{1}{(-Ri)^{1/2}}. \tag{6.3}$$

When normalised by the centreline quantities, $\overline{w}_c$ and $\overline{c}_c$, and respective half-widths, $r_{1/2,w}$ and $r_{1/2,c}$, the velocity and buoyancy profiles for an NBJ collapse onto a single curve. Although the widths of these profiles grow at different rates along the jet, evident from the non-constant λ shown in figure 5.6, the profiles still maintain a similar Gaussian shape. These normalised velocity profiles, $\overline{w}/\overline{w}_c$, and scalar profiles, $\overline{c}/\overline{c}_c$, are shown in figures 6.1(b) and 6.2(b) for a $Fr_o = 30$ NBJ at a range of locations, along with the best fit profile for a neutral jet by Wang and Law (2002) as a reference.

The profiles for a fully developed fountain, also with $Fr_o = 30$, are shown in figures 6.1(a) and 6.2(a), where it is immediately clear that the profiles do not collapse in the same way as the NBJ. Although the velocity and scalar profiles are reasonably similar for $r/r_{1/2,w} \lesssim 1$ and $r/r_{1/2,c} \lesssim 1$, respectively, they diverge for radial locations beyond this. For the velocity profile, this is particularly evident in the OF where $\overline{w} < 0$. The minimum (most negative) value of the velocity profile will be denoted $\overline{w}_d$, with the radial location of this point denoted r_d. Figure 6.1(a) shows that $\overline{w}_d/\overline{w}_c$ becomes increasingly negative with increasing axial distance, while the location of the local minima, $r_d/r_{1/2,w}$, moves towards the centre. This is primarily a consequence of the normalisation, where $\overline{w}_c$ strongly decreases as the IF is decelerated under negative buoyancy, increasing the magnitude of $\overline{w}_d/\overline{w}_c$. The velocity half-width, $r_{1/2,w}$, also increases relative to r_d, reducing the value of $r_d/r_{1/2,w}$. The actual magnitude of $\overline{w}_d$ is found to decrease towards zero at the top of the fountain, and r_d moves outwards as the IF expands. This can be seen in figure 6.1(c), which shows $\overline{w}$ normalised by the source velocity, w_o, with the radial coordinate normalised by the source radius, r_o. Since w_o and r_o are constant in a given experiment, these

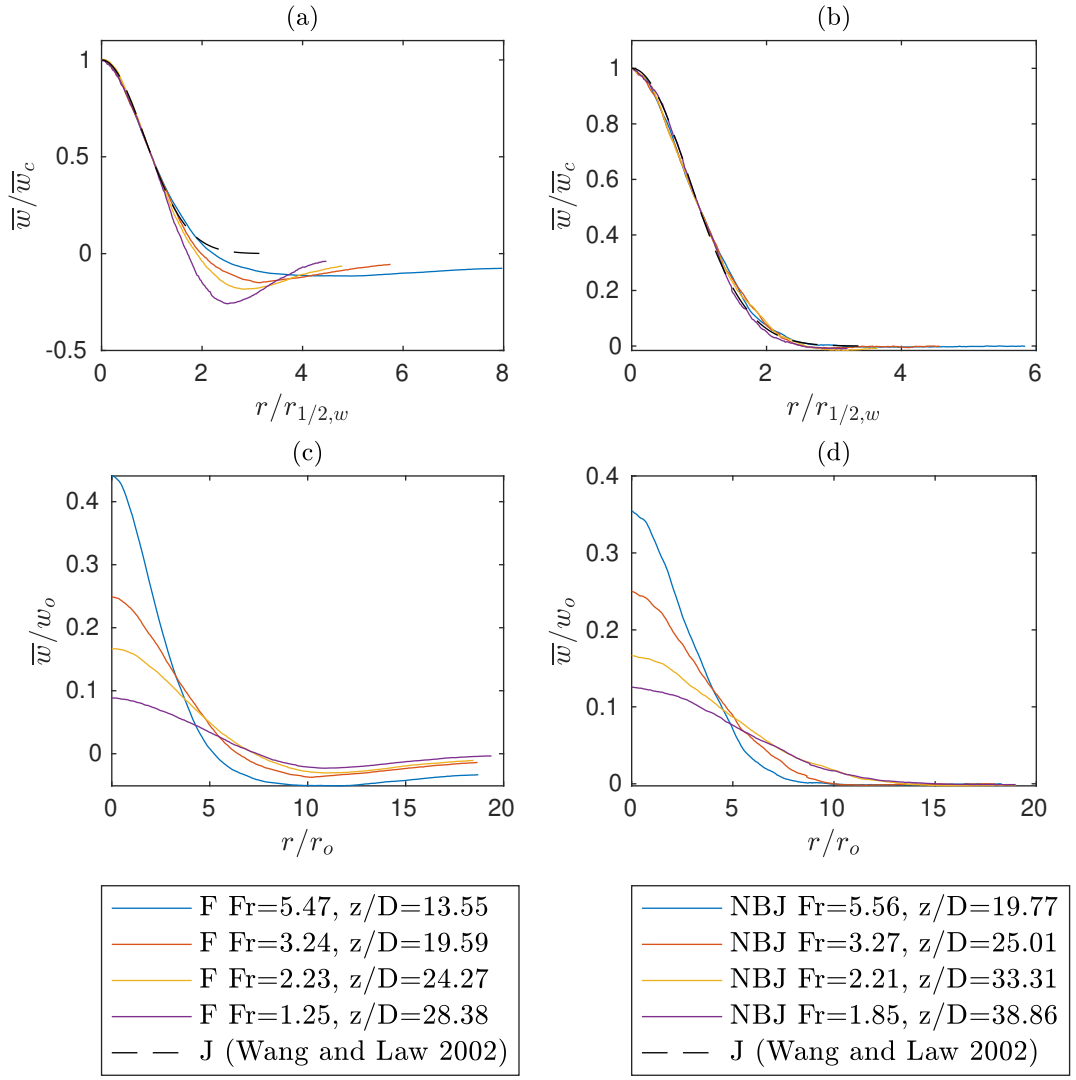

Figure 6.1: Mean velocity profiles, $\overline{w}$, for a fully developed fountain, (a) and (c), and negatively buoyant jet, (b) and (d), both with $Fr_o = 30$ at a range of axial locations. The profiles are normalised by the local centreline value, $\overline{w}_c$, and half-width, $r_{1/2,w}$, in (a) and (b), and by source velocity, w_o, and radius, r_o, in (c) and (d). The best fit profile for a neutral jet by Wang and Law (2002) is also shown as a reference.

profiles directly reflect the magnitude and shape of $\overline{w}$ at a particular location.

The scalar profiles, normalised by both local and source quantities, are given in figures 6.2(a)-(d) for the fountain and NBJ. Unlike the NBJ profiles in (b), the fountain profiles in (a) do not collapse onto the same curve for the full radial width, although they are reasonably similar in the inner-profile for $r/r_{1/2,c} \lesssim 1$. This means that, particularly in the outer-profile ($r/r_{1/2,c} \gtrsim 1$), they are no longer well described by a similar Gaussian shape along the flow, appearing to get narrower with axial distance. Figure 6.2(c), however, reveals that the narrowing is again a

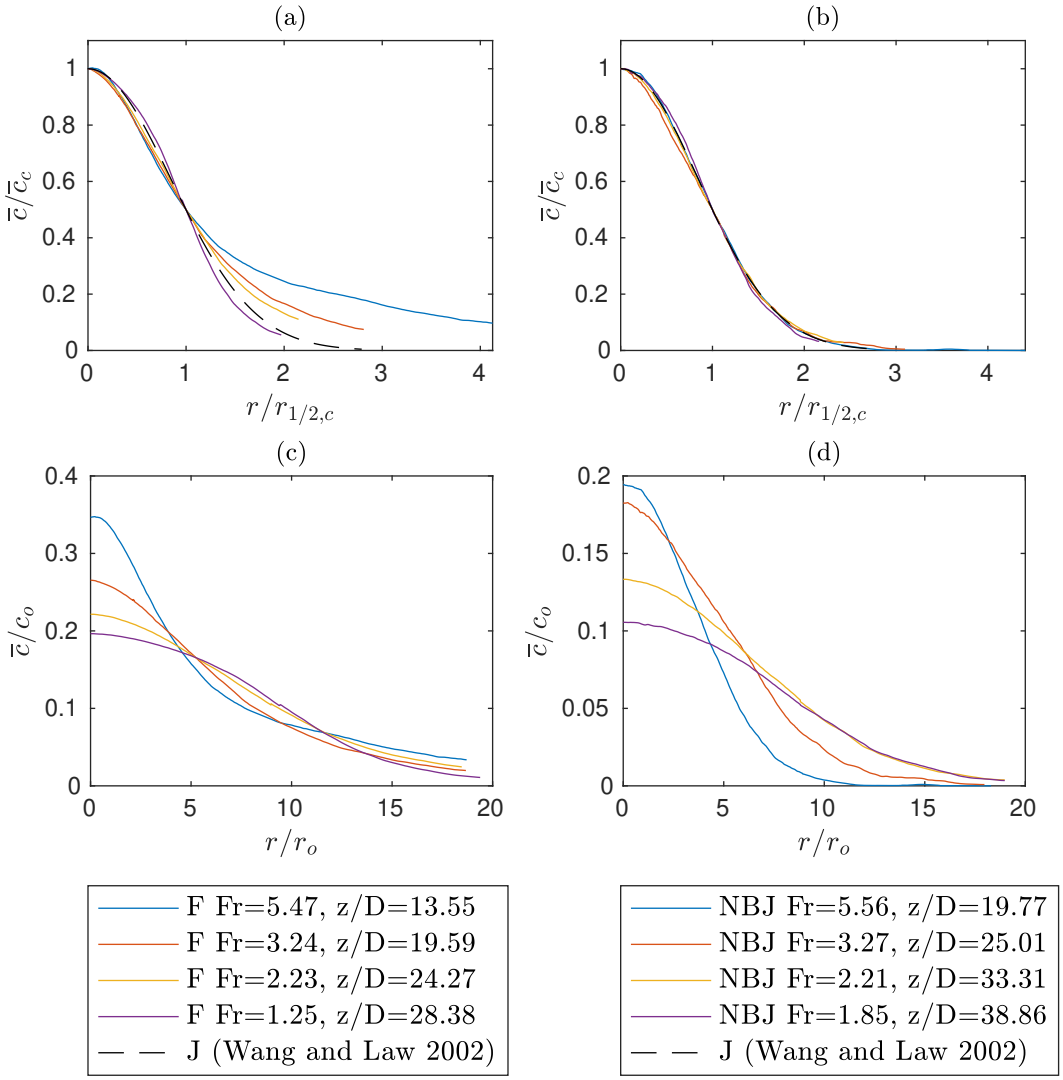

Figure 6.2: Mean scalar profiles, $\overline{c}$, for a fully developed fountain, (a) and (c), and negatively buoyant jet, (b) and (d), both with $Fr_o = 30$ at a range of axial locations. The profiles are normalised by the local centreline value, $\overline{c}_c$, and half-width, $r_{1/2,c}$, in (a) and (b), and by source concentration, c_o, and radius, r_o, in (c) and (d). The best fit profile for a neutral jet by Wang and Law (2002) is also shown as a reference.

consequence of the normalisation by a growing $r_{1/2,c}$. The $\overline{c}/c_o$ profiles show how the shape changes with increasing axial distance, narrowing in the middle section ($5 \lesssim r/r_o \lesssim 12$), but wider at the tails ($r/r_o \gtrsim 15$). Neither the velocity nor scalar (buoyancy) profiles in a fully developed fountain can therefore be considered self-similar in the sense that they have similar shapes along the fountain. Despite this, the most significant shape-change of the profiles occurs in the outer region, with the inner profiles approximately collapsing when normalised by their centreline values and respective half-widths.

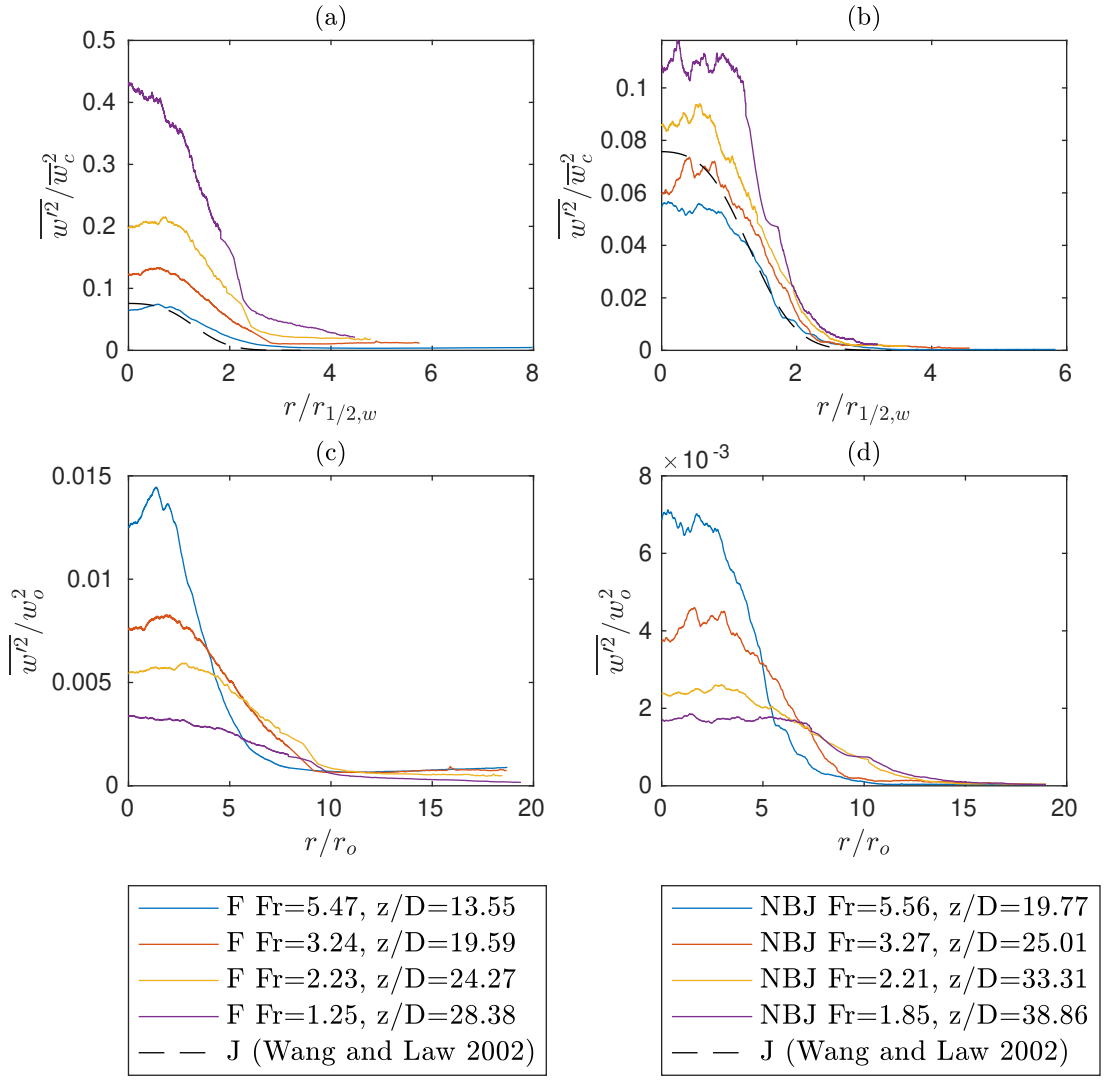

Figure 6.3: Profiles of the mean axial turbulence fluctuations, $\overline{w'^2}$, for a fully developed fountain, (a) and (c), and negatively buoyant jet, (b) and (d), both with $Fr_o = 30$. The profiles are normalised by the local centreline value, $\overline{w}_c^2$, and half-width, $r_{1/2,w}$, in (a) and (b), and by source velocity, w_o^2, and radius, r_o, in (c) and (d). The best fit profile for a neutral jet by Wang and Law (2002) is also shown as a reference.

6.2.2 Turbulence statistics

Profiles for the axial turbulence fluctuations and Reynolds stress, $\overline{w'^2}$ and $\overline{w'u'}$, are given in figures 6.3 and 6.4, normalised by both local and source quantities. The development of these turbulence profiles in an NBJ were discussed in §5.3, where they were found to increase with axial distance due to the strongly decelerating mean flow, characterised here by $\overline{w}_c$. This differs to neutral jets and plumes, where $\overline{w'^2}$ and $\overline{w'u'}$ decrease at the same rate as the mean flow, and so the normalised profiles, $\overline{w'^2}/\overline{w}_c^2$ and $\overline{w'u'}/\overline{w}_c^2$, are approximately constant along the flow (at least in

the fully developed, self-similar region) (Panchapakesan and Lumley 1993; Hussein et al. 1994; Wang and Law 2002).

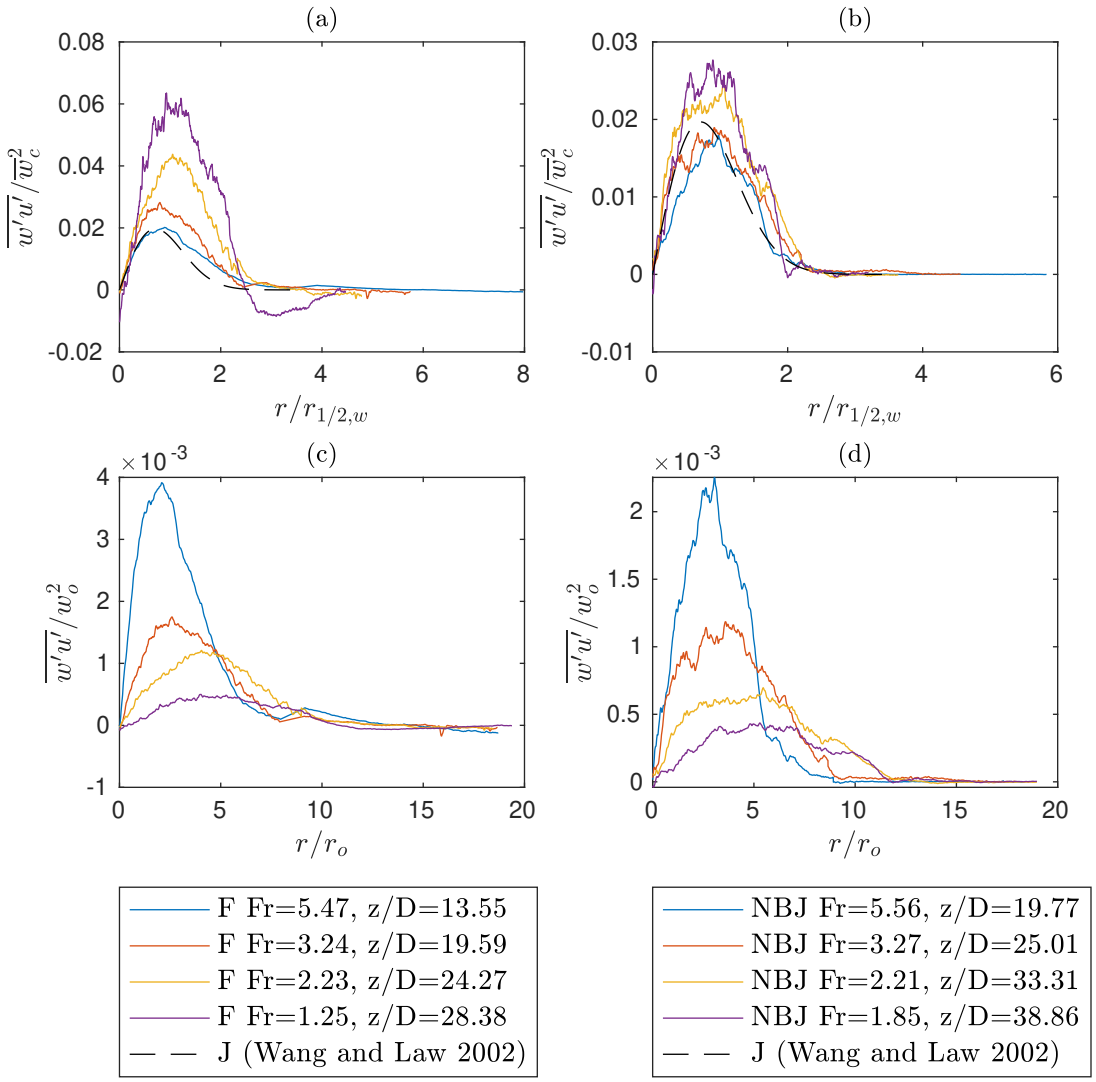

Figure 6.4: Profiles of the mean Reynolds stress, $\overline{w'u'}$, for a fully developed fountain, (a) and (c), and negatively buoyant jet, (b) and (d), both with $Fr_o = 30$. The profiles are normalised by the local centreline value, $\overline{w}_c^2$, and half-width, $r_{1/2,w}$, in (a) and (b), and by source velocity, w_o^2, and radius, r_o, in (c) and (d). The best fit profile for a neutral jet by Wang and Law (2002) is also shown as a reference.

For the fully developed fountain, the behavior of $\overline{w'^2}$ and $\overline{w'u'}$ remaining high relative to $\overline{w}_c^2$ is more prominent than in the NBJ. The locally normalised profiles in figures 6.3(a)-(b) and 6.4(a)-(b) increase more rapidly in the fountain than NBJ, with large peak values of $\overline{w'^2}/\overline{w}_c^2 \cong 0.2$ and $\overline{w'u'}/\overline{w}_c^2 \cong 0.04$ for the $Fr = 2.23$ profile. These are considerably higher than the NBJ peaks at a similar $Fr = 2.21$ of $\overline{w'^2}/\overline{w}_c^2 \cong 0.09$ and $\overline{w'u'}/\overline{w}_c^2 \cong 0.02$. Figures 6.3$(c)$-$(d)$ and 6.4(c)-(d), show the $\overline{w'^2}$ and $\overline{w'u'}$ profiles instead normalised by source conditions. These profiles decrease

with axial distance, showing that the turbulence is actually decreasing along the flow. This illustrates the fact that the increasing turbulence intensities observed in figures 6.3(a)-(b) and 6.4(a)-(b) are primarily driven by the decreasing $\overline{w}_c$, rather than an increase in turbulence production. From these it is clear that $\overline{w'^2}$ and $\overline{w'u'}$ decrease with axial distance for both the NBJ and fountain, and is higher in the fountain than the NBJ at similar local Fr. This is particularly true of the $\overline{w'^2}/w_o^2$ profile, where the peak values in the fountain profiles are approximately twice that of the NBJ at similar Fr. This is likely due to interactions between the IF/OF that result in increased turbulence in the IF, and so also contributes to the greater $\overline{w'^2}/\overline{w}_c^2$ and $\overline{w'u'}/\overline{w}_c^2$ observed in the fountain.

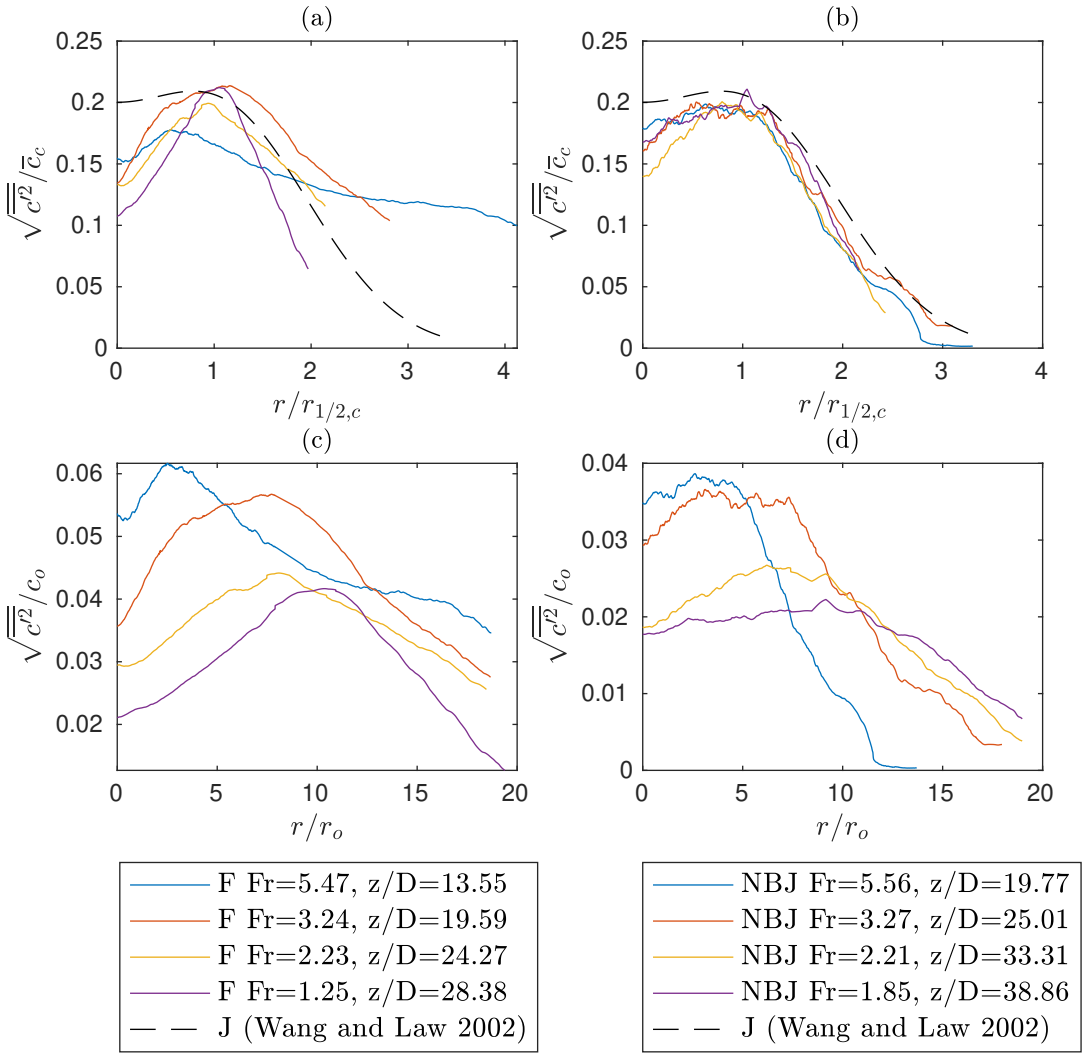

Figure 6.5: Profiles of the mean scalar fluctuations, $\sqrt{\overline{c'^2}}$, for a fully developed fountain, (a) and (c), and negatively buoyant jet, (b) and (d), both with $Fr_o = 30$. The profiles are normalised by the local centreline value, $\overline{c}_c$, and half-width, $r_{1/2,c}$, in (a) and (b), and by source concentration, c_o^2, and radius, r_o, in (c) and (d). The best fit profile for a neutral jet by Wang and Law (2002) is also shown as a reference.

Figure 6.5(a)-(d) shows profiles of the mean turbulence scalar fluctuations, $\sqrt{\overline{c'^2}}$, normalised by both local and source quantities. The $\sqrt{\overline{c'^2}}/\overline{c}_c$ profiles for the NBJ, shown in (b), are reasonably well collapsed with no discernible trend with axial location, as was discussed in §5.3. The fountain profiles however, are not self-similar, and do not appear to follow a clear increasing or decreasing trend with axial distance.

Profiles of the axial and radial fluxes, $\overline{w'c'}$ and $\overline{u'c'}$, for the fountain and NBJ are given in figures 6.6(a)-(c) and 6.7(a)-(c). When normalised by local quantities, as in 6.6(a) and 6.7(a), the profiles clearly increase with axial distance. A moderate increase can also be observed between the NBJ profiles nearest and furthest from the source ($z/D = 19.77$ and $z/D = 38.86$), although the trend is less significant and there is some scatter in the profiles between these locations. This increase may also be attributable to the NBJ still developing over this z/D range. As with the velocity fluctuations, the growth in the turbulent scalar profiles for the fountain is primarily a result of normalising by the decreasing $\overline{w}_c$, rather than an increase in axial/radial scalar transport. This can be seen in figures 6.6(c) and 6.7(c) where the profiles, when normalised by source parameters, are shown to decrease in magnitude with axial distance. It is also notable that the $\overline{w'c'}$ profiles for the fountain drop considerably below zero in the outer profile. This corresponds to the OF region where the direction of axial mean flow is reversed, and so a sign reversal of the axial scalar flux is expected.

Neither the mean velocity/scalar profiles, nor the turbulence fluctuations, scale well with the centreline values in fully developed fountains across the full width of the flow. Another potential scaling option would be to include the OF velocity, which could be characterised by the velocity at the location of 'maximum outer-flow', $\overline{w}(r = r_d) = \overline{w}_d$. The mean velocity profile could then be normalised by a characteristic relative IF/OF velocity, $\overline{w}_c - \overline{w}_d$. However, since $\overline{w}_c >> |\overline{w}_d|$ for the majority of the fountain height, this gives similar results to the $\overline{w}_c$ normalisation, and the profiles do not collapse across the full fountain width. This velocity scale is, however, relevant when considering entrainment between these two regions, and is discussed in §7.3.2. Another approach would be to consider the quantity, $(\overline{w} - \overline{w}_d)/(\overline{w}_c - \overline{w}_d)$, which is the fountain velocity relative to the moving reference frame of the OF. This is always positive and has a centreline value of 1. Although this could potentially be useful from a modelling point of view, it was also not sufficient to collapse the profiles.

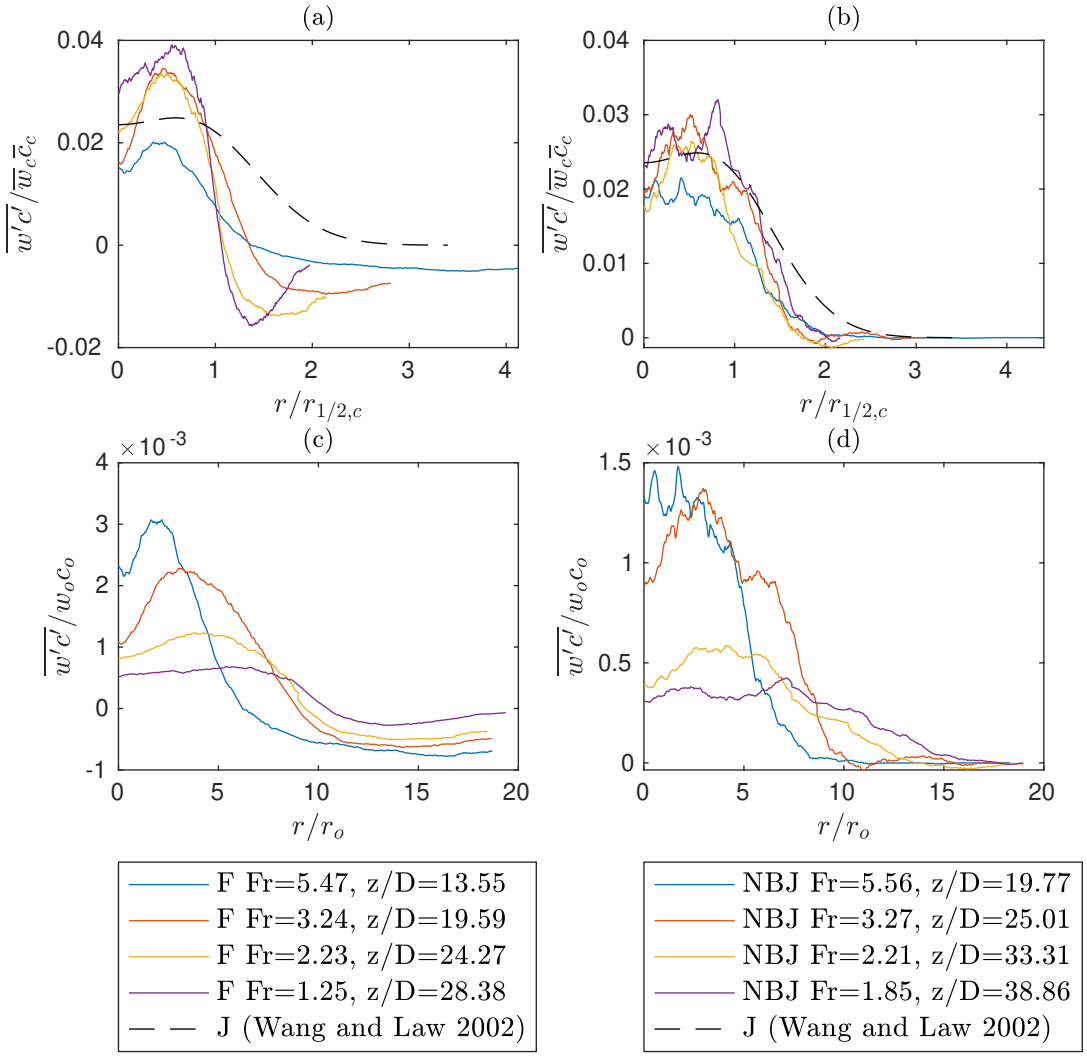

Figure 6.6: Profiles of the mean axial turbulent flux, $\overline{w'c'}$, for a fully developed fountain, (a) and (c), and negatively buoyant jet, (b) and (d), both with $Fr_o = 30$. The profiles are normalised by the local product, $\overline{w}_c\overline{c}_c$, and half-width, $r_{1/2,c}$, in (a) and (b), and by source quantity, w_oc_o, and radius, r_o, in (c) and (d). The best fit profile for a neutral jet by Wang and Law (2002) is also shown as a reference.

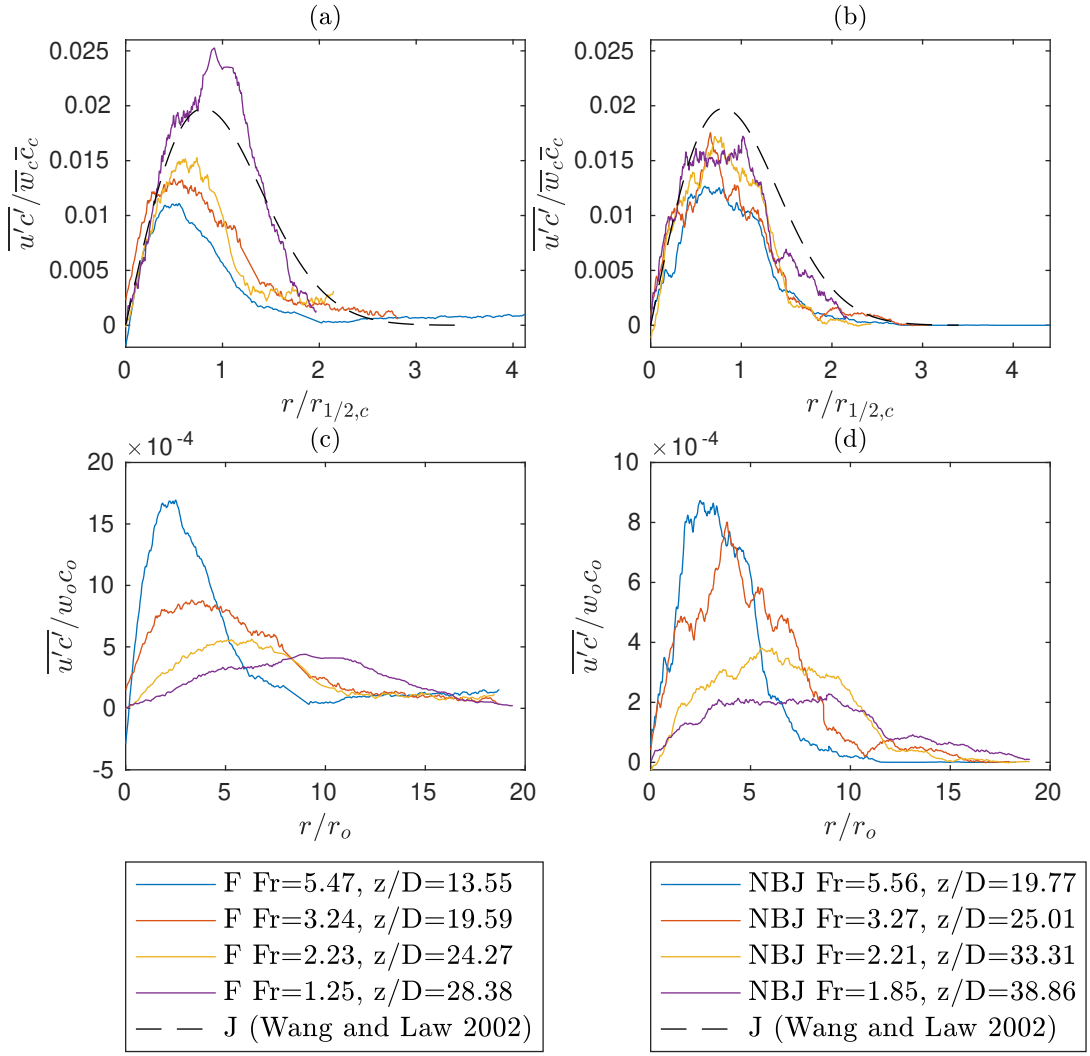

Figure 6.7: Profiles of the mean radial turbulent flux, $\overline{u'c'}$, for a fully developed fountain, (a) and (c), and negatively buoyant jet, (b) and (d), both with $Fr_o = 30$. The profiles are normalised by the local product, $\overline{w}_c\bar{c}_c$, and half-width, $r_{1/2,c}$, in (a) and (b), and by source quantity, w_oc_o, and radius, r_o, in (c) and (d). The best fit profile for a neutral jet by Wang and Law (2002) is also shown as a reference.

6.3 Fr_o dependence

In §6.2.1-6.2.2, mean and turbulence statistics were presented for a fountain and negatively buoyant jet, both with $Fr_o = 30$, at axial locations where they had a similar local Fr. Now, statistics for two fountains with different source Froude numbers, $Fr_o = 30$ and 15, will be presented also for similar Fr. Figure 6.8(a)-(d) shows $\overline{w}/\overline{w}_c$ and $\overline{c}/\overline{c}_c$ profiles for both these fountains at $Fr = 3.1$ and $Fr = 1.3$. The velocity profiles in (a) and (c) are very similar for $0 \lesssim r \lesssim r_d$ at both Fr locations. That is, up to approximately the radial the location of 'maximum return flow'. The profiles with $Fr = 3.1$ are similar even beyond this point, over the full r range obtained, although this is not the case at all Fr locations. The scalar profiles in (b) and (d) are also similar in this r range, where they agree up to near the $\times$ markers that correspond to r_d, while differing somewhat in the outer profile.

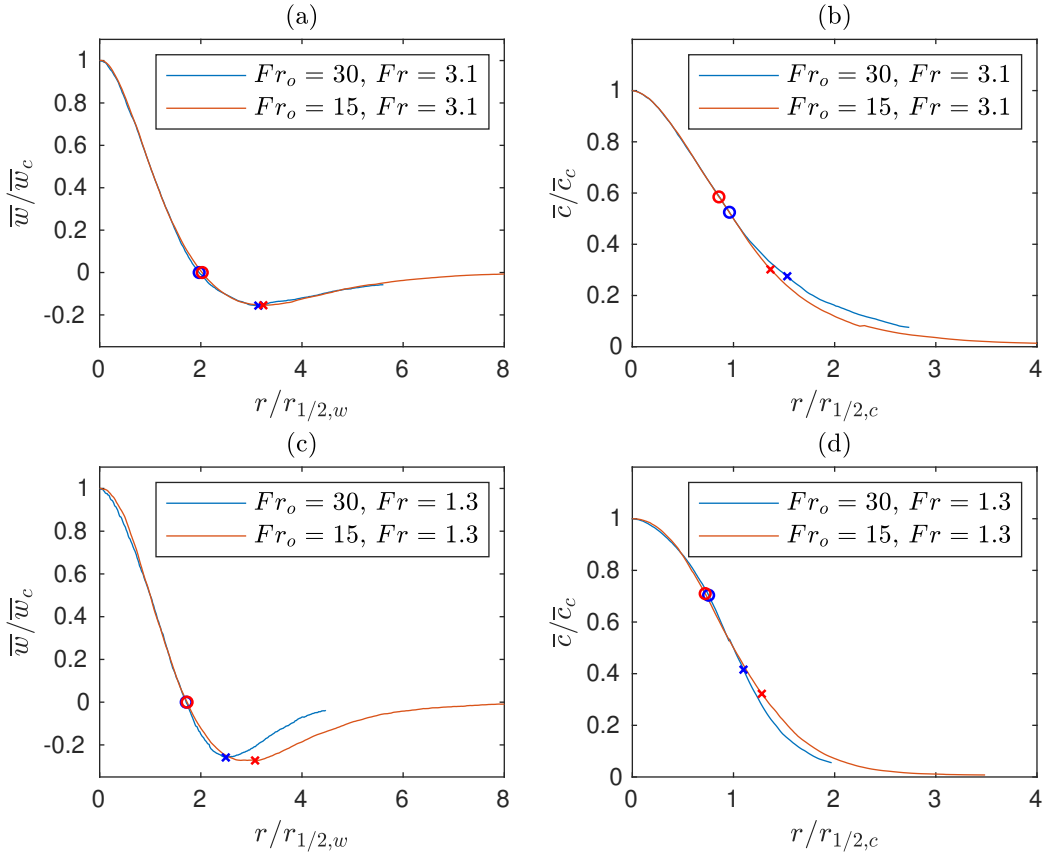

Figure 6.8: Normalised $\overline{w}$ and $\overline{c}$ profiles in $Fr_o = 30$ and 15 fountains. The profiles correspond to axial locations where the local Fr in both flows are approximately equal. Additionally, $\circ$ markers corresponding to radial location, r_{io}, and $\times$ markers corresponding to r_d, are also shown on each profile.

The agreement of these profiles between the two Fr_o fountains at similar Fr is better than those in figures 6.1(a) and 6.2(a), which showed profiles at differ-

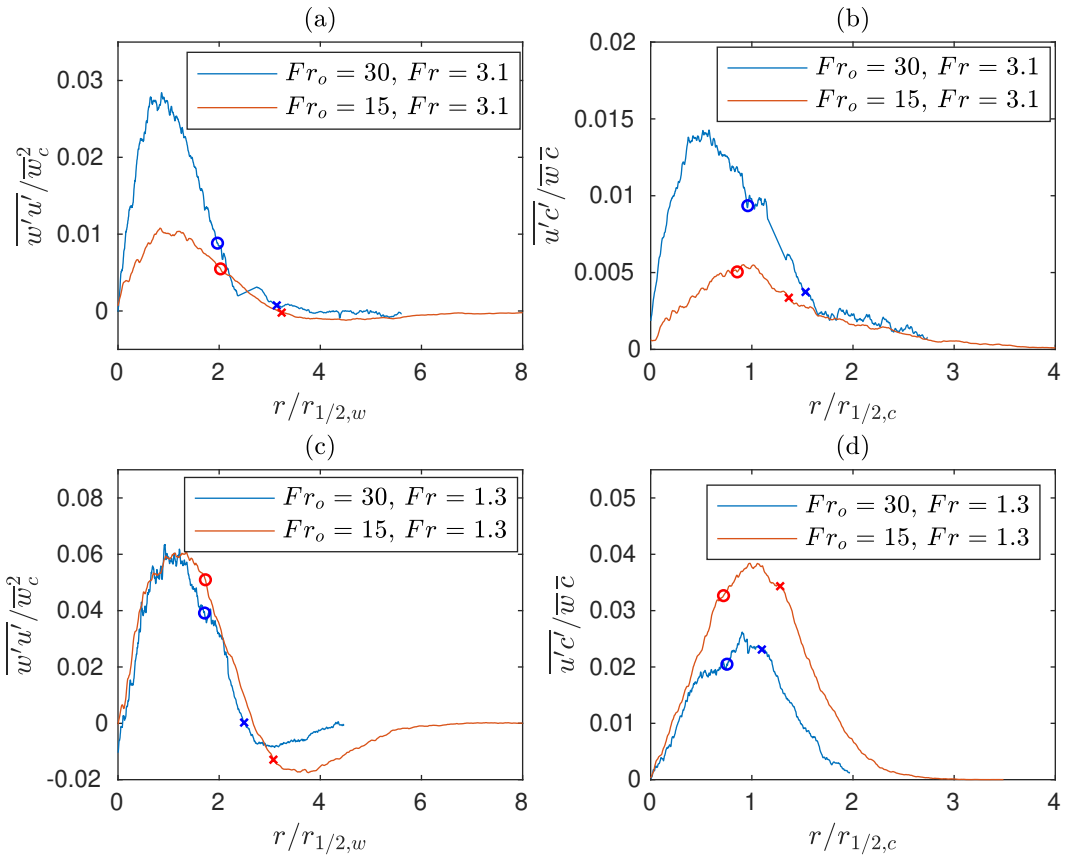

Figure 6.9: Normalised $\overline{w'u'}$ and $\overline{u'c'}$ profiles in $Fr_o = 30$ and 15 fountains. The profiles correspond to axial locations where the local Fr in both flows are approximately equal. Additionally, $\circ$ markers corresponding to radial location, r_{io}, and $\times$ markers corresponding to r_d, are also shown on each profile.

ent Fr locations for the same $Fr_o = 30$ fountain. The latter $\overline{w}/\overline{w}_c$ profiles only agreed up until $r/r_{1/2,w} \lesssim 1$, which is prior to the IF/OF boundary, r_{io}. The $\overline{c}/\overline{c}_c$ profiles in figure 6.2(a) only approximately agree for $r/r_{1/2,w} \lesssim 1$, and are significantly different beyond this. In figure 6.8(b) and (d) the agreement between the $Fr_o = 30$ and 15 profiles is closer over the full profiles shown, but particularly for $r/r_{1/2,c} \lesssim 1$. Together, figures 6.1, 6.2 and 6.8 show that despite the locally normalised velocity/scalar profiles not being generally self-similar within an individual fountain, their shape for $r \lesssim r_d$ does not depend significantly on Fr_o and is instead controlled by Fr. That is, at a given local Fr, these profiles in different Fr_o fountains are similar up to the location of maximum return flow, r_d, with the closest agreement up to the IF/OF boundary, r_{io}. It should be noted that both these fountains have Fr_o in the 'highly forced' regime ($Fr_o \gtrsim 5.5$), and this may not hold in lower Fr_o fountains, particularly those in the the 'intermediate' regime and below ($Fr_o \lesssim 2.8$) (Burridge and Hunt 2012).

Figure 6.9 shows $\overline{w'u'}/\overline{w}_c^2$ and $\overline{u'c'}/\overline{w}_c\,\overline{c}_c$ for both $Fr_o = 30$ and 15 fountains at similar Fr locations. In contrast to the mean velocity/scalar profiles in figure 6.8, these turbulence quantities clearly have both a Fr and Fr_o dependence and are not generally similar in the two fountains at the same Fr. This difference is likely due to interactions with the outer flow having an effect on the turbulence production in the inner flow, since the OF at a given Fr location will be different in a $Fr_o = 30$ and 15 fountain. Although differences in the OF may also affect the mean profiles, $\overline{w}$ and $\overline{c}$ in the IF, this is largely captured by $\overline{w}_c$ and $\overline{c}_c$ in the normalisation. A Fr_o dependence in $\overline{w'u'}/\overline{w}_c^2$ and $\overline{u'c'}/\overline{w}_c\,\overline{c}_c$ at similar Fr locations is not seen in negatively buoyant jets, which do not have an OF present. This can be seen in figures 6.10(a)-(c), which show the profiles for $Fr_o = 30$ and 10 negatively buoyant jets at locations corresponding to $Fr \cong 3.5$ and $Fr \cong 3.1$. Although these are somewhat noisier than in the fountain, both the $\overline{w'u'}/\overline{w}_c^2$ and $\overline{u'c'}/\overline{w}_c\,\overline{c}_c$ profiles are similar shapes and magnitudes at the two Fr locations. This supports the conjecture that the Fr_o dependence observed in figure 6.9 for the fountain is primarily a result of the return flow, which is not present in the NBJ.

6.4 Centreline velocity decay

Figure 6.11 shows the decay of the centreline velocity, characterised by $w_o/\overline{w}_c$, for $10 \leq Fr_o \leq 30$ fountains and negatively buoyant jets plotted with z/D. Data for a neutral jet, which has $Fr = \infty$, is also shown as a reference. As discussed in §5.3.1, in neutral jets this corresponds to a $\overline{w}_c^{-1} \sim z$ scaling. In NBJs, this deceleration is stronger and the relationship between $\overline{w}_c^{-1}$ and z is generally non-linear. Near the source, however, where the local Fr is high and the flow is momentum dominated, NBJs are more similar to neutral jets and $w_o/\overline{w}_c$ could be approximated as linear. This region was referred to as the 'forced' regime in chapter 5, and corresponded to $z/D \lesssim 26$ ($Fr \gtrsim 3.0$) for the $Fr_o = 30$ NBJ.

At similar z/D locations, the $Fr_o = 10$, 20 and 30 fountains all decelerate more rapidly than the corresponding negatively buoyant jet with the same Fr_o. This is most evident in the $Fr_o = 30$ case, where data has been gathered over a larger z/D range, and reveals the significance of the return flow on the development of $\overline{w}_c$. The $Fr_o = 10$ NBJ data, which is close to the source and in the 'forced' regime, almost coincides with the linear fit of the jet data. It is possible that all NBJs with sufficiently high Fr_o approach this 'neutral jet line' near the source where the flow is increasingly momentum dominated, although additional research is required to affirm this. For fountains, $w_o/\overline{w}_c$ may never closely resemble this jet-like state, since

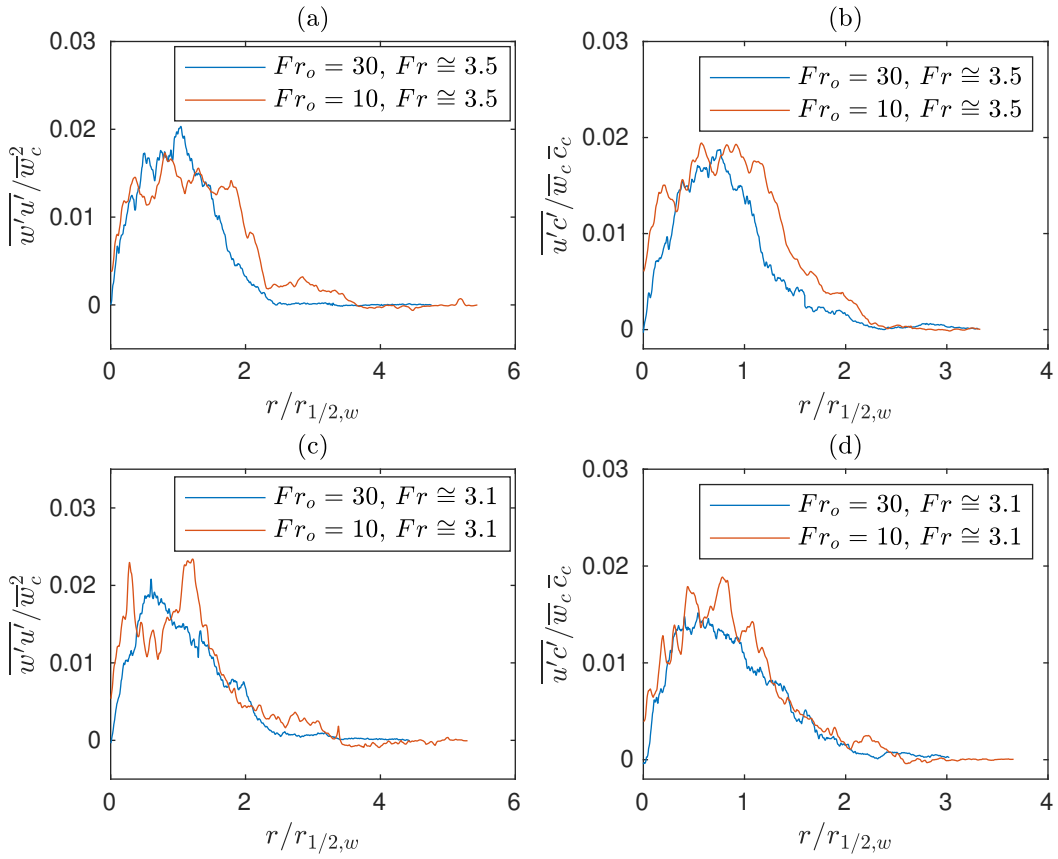

Figure 6.10: Normalised $\overline{w'u'}$ and $\overline{u'c'}$ profiles in $Fr_o = 30$ and 10 negatively buoyant jets. The profiles correspond to axial locations where the local Fr in both flows are approximately equal.

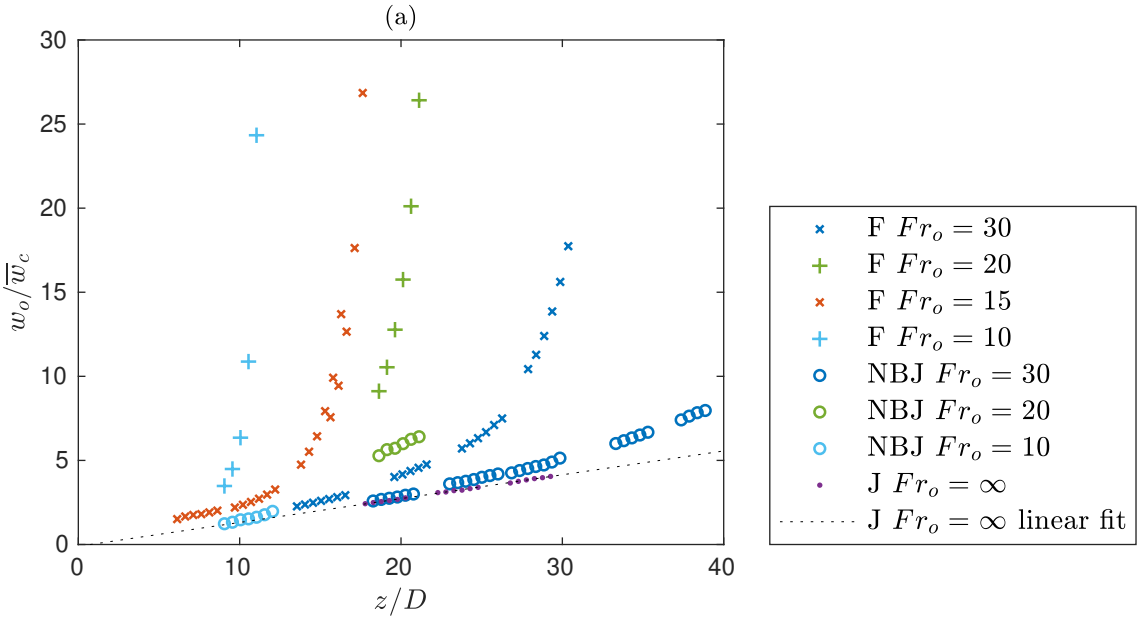

Figure 6.11: The decay of the mean centreline velocity, $\overline{w}_c/w_o$, plotted with z/D for fountains and negatively buoyant jets with $10 \leq Fr_o \leq 30$, and a neutral jet.

the presence of the return flow will continue to affect the IF even at the source.

6.5 Radial expansion and fountain width

The radial expansion of a fountains inner flow may may be characterised by the radial location of the IF/OF boundary, r_{io}, or by other measures of the inner flow velocity profile, such as the half-width, $r_{1/2,w}$. Figure 6.12(a) shows $r_{1/2,w}/D$ with axial distance, z/D, for $Fr_o = 30$ and 15 fountains, a $Fr_o = 30$ NBJ and a neutral jet. For the fountains, r_{io}/D, is also shown. For a large portion of their height, the neutral jet, $Fr_o = 30$ fountain and NBJ, all have similar $r_{1/2,w}/D$ at similar axial locations. This does not mean that the velocity profiles are similar at these locations, as it was shown in figure 6.11(a) that $\overline{w}_c$ is very different in these flows at the same z/D. The $r_{1/2,w}$ agreement may be a result of the fact that these flows had similar source conditions, $0.58 \lesssim w_o \lesssim 0.67$ m s^{-1} and $D = 10$ mm, and were obtained using the same experimental set up. It is not expected that all fountains and NBJs with arbitrary Fr_o and source conditions will have similar $r_{1/2,w}/D$ to a neutral jet at the same z/D locations.

In the fountains, $r_{1/2,w}$ and r_{io} increases with z/D for the majority of their height, followed by a sharp decrease after some critical point. Since the overall width of a fountain decreases in the cap region, the IF width scales could also be expected to decrease in the cap. The location where r_{io} and $r_{1/2,w}$ start to decline may therefore

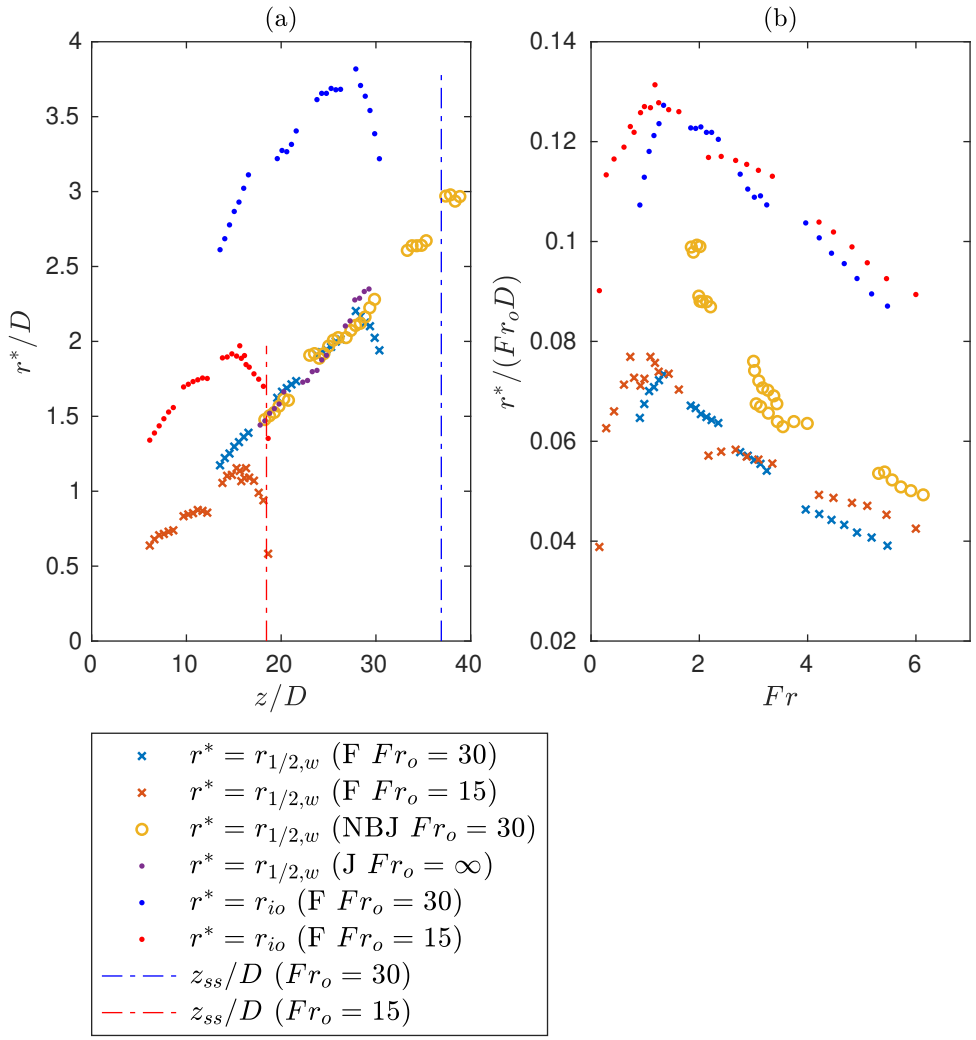

Figure 6.12: The velocity half-width, $r_{1/2,w}$, for $Fr_o = 30$ and 15 fountains, a $Fr_o = 30$ NBJ, and a neutral jet. The radial location of the IF/OF boundary, r_{io}, is also shown for the fountains. In (a), $r_{1/2,w}/D$ and r_{io}/D is plotted against z/D, with vertical lines showing the location of the steady state rise height, z_{ss}/D, of the two fountains. In (b), an alternative normalisation is used, $r_{1/2,w}/(Fr_oD)$ and $r_{io}/(Fr_oD)$, and is plotted with Fr.

reflect the beginning of the cap region, which will be denoted z_c. This occurs at $z_c/D \cong 15$ for the $Fr_o = 15$ case and $z_c/D \cong 28$ for the $Fr_o = 30$ case. The same values are obtained using either the location of maximum $r_{1/2,w}$ or r_{io}, and is approximately $z_c/D \cong Fr_o$ for both fountains. Vertical lines are also shown in figure 6.12(a) to indicate the predicted steady state rise height of the fountains based on the high Fr_o scaling relation, $z_{ss}/r_o = 2.46Fr_o$ (Turner 1966; Kaye and Hunt 2006). If the cap region was assumed hemispherical, then the thickness of the cap would be an approximation of the overall fountain radius, r_f. If, additionally, $z_c/D = Fr_o$ was presumed to be a universal scaling for the start of the cap region, then by using

the aforementioned z_{ss} relation we obtain,

$$\frac{r_f}{D} = \frac{z_{ss}}{D} - \frac{z_c}{D} = 0.23 Fr_o. \tag{6.4}$$

This is in good agreement with proposed relation by Mizushina et al. (1982) of $r_f/D = 0.26 Fr_o$, who directly measured the width of fountains with $3 \lesssim Fr_o \lesssim 258$. The agreement supports the earlier assumption that the location of maximum r_{io} and $r_{1/2,w}$ can be used to estimate the start of the cap region.

Figure 6.12(b) shows the radial expansion of the IF normalised by Fr_o, with $r_{1/2,w}/(Fr_o D)$ and $r_{io}/(Fr_o D)$ plotted against Fr. The start of the cap region occurs at very similar Fr for both fountains, $Fr = 1.1$ for the $Fr_o = 15$ case and $Fr = 1.3$ for $Fr_o = 30$. These are similar to the value proposed by Shrinivas and Hunt (2014) of $Fr = 1.4$, and used by Hunt and Debugne (2016) in their theoretical model of a fountain. Although there is some discrepancy between the two fountains for $Fr \gtrsim 4$ in figure 6.12(b), possibly due to their profiles still developing, the values for both Fr_o are are in reasonable agreement at similar Fr. This suggests that not only does the overall fountain width scale with Fr_o, as was reported by Mizushina et al. (1982) and implied by (6.4), but so does the IF velocity profile at a given Fr. This implies that, for a given local Fr, the width of the the IF is a fixed fraction of the overall width across different Fr_o fountains. This fraction, however, varies along the height of a particular fountain and depends on the local Fr. This is consistent with the arguments made in §6.3 with regard to figure 6.8(a) and (b), where the shape of the velocity profiles in the inner flow are not significantly affected by Fr_o, and are instead governed by Fr.

6.6 Conclusions

Fully developed fountains, with an established IF/OF structure, have been investigated using velocity and buoyancy measurements obtained from combined PIV and PLIF experiments. This data has been compared to negatively buoyant jets, which do not have an OF, that were investigated using the same experimental set-up. Mean and turbulence profiles for fountains and NBJs at similar local Fr were presented in §6.2.1-6.2.2, revealing the effect that a return flow has on the IF of a fountain. Unlike NBJs, the mean $\overline{w}$ and $\overline{c}$ profiles do not collapse when normalised by their local centreline value and respective half-width, and so are not self-similar in this sense. This is consistent with previous studies that have also obtained data on the internal velocity/scalar fields (Williamson et al. 2011; Cresswell and Szczepura 1993; Mizushina et al. 1982). Despite this, there is a degree of similarity for the inner flow

of the fountain, with the $\overline{w}/\overline{w}_c$ and $\overline{c}/\overline{c}_c$ profiles being reasonably similar for $r \lesssim r_{io}$ over the range of axial locations investigated.

Fountains with different source Froude numbers were also investigated, with figure 6.8 showing that the normalised mean velocity and scalar profiles of $Fr_o = 15$ and 30 fountains at similar local Fr locations were similar for $0 \lesssim r \lesssim r_d$. This was not the case for the turbulence quantities, such as $\overline{w'u'}/\overline{w}_c^2$ and $\overline{u'c'}/\overline{w}\,\overline{c}$ in figure 6.9, where there is a clear Fr_o dependence. This can be attributed to differences in the OF at a particular local Fr location in the two fountains, which affects the profiles in both the inner and outer flow regions.

The growth of the inner flow was presented for $Fr_o = 15$ and 30 fountains in figure 6.12, where both the velocity half-width, $r_{1/2,w}$, and IF/OF boundary, r_{io}, were plotted with axial distance and local Fr. These were shown to increase along the fountain as the inner flow expands until they reach some maximum value, after which they rapidly decrease towards zero. This critical location where the IF has reached its maximum thickness was interpreted as the start of the cap region, and was used to estimate the overall fountain width. This could be expressed through (6.4) and is consistent with the relation proposed by Mizushina et al. (1982), who directly measured the width of fountains using flow visualisation.

Chapter 7

Entrainment in fountains and negatively buoyant jets

The following chapter considers the integral models first introduced in chapter 2 and applied to a negatively buoyant jet in chapter 5, and extends them to fully developed fountains. A focus is placed on characterising entrainment between the inner and outer flow regions of fountains, which is then compared to entrainment in negatively buoyant jets. In fountains, entrainment between the IF/OF is shown to depend on the local Richardson number, Ri, through a derived expression for the entrainment coefficient, α. Fountains are found to have $\alpha < 0$ for the majority of their height, implying a net radial outflow of fluid from the IF to the OF. An alternative description of entrainment is considered, the 'decomposed top-hat' model, where the radial flow is separated into inflow and outflow components that are then estimated using the present experimental data. The radial inflow is found to be proportional to the axial IF velocity, which is similar to the classical description of entrainment in pure jets/plumes, while the outflow depends on the local Ri.

7.1 Introduction

Entrainment in negatively buoyant jets was explored in chapter 5 using integral models originally derived to describe neutral/positively buoyant jets and plumes (Morton et al. 1956; Priestley and Ball 1955; van Reeuwijk and Craske 2015). This could be pursued since NBJs do not have a return flow and hence have a structure that resembles these jet-like flows. Fully developed fountains, however, have an inner/outer flow structure that could be described as an NBJ surrounded by an

opposing shear flow. The inner flow of a fountain is then affected by interactions with the return flow, and the previously discussed integral models, which are valid for homogeneous quiescence environments, cannot be directly applied in their current form. Additionally, the lack of full self-similarity in fountains poses a limit to the potentially applicability of integral models. However, since we have that velocity and scalar profiles approximately collapse in the IF, as was discussed in §6.2.1, there is still a degree of self-similarity in the IF that makes these models useful to consider.

McDougall (1981) attempted to model a fountain by considering this IF/OF structure, assuming self-similar profiles, and using constant entrainment coefficients to describe mixing between the IF/OF regions and between the OF/ambient fluid. Bloomfield and Kerr (2000) built upon this model and assessed alternate entrainment formulations, including relating entrainment into the IF to the relative velocity difference of the IF/OF (as assumed by McDougall (1981)), as well as to the IF velocity only. Both formulations under-predicted the steady state rise height, z_{ss}, with the latter approach giving predictions closer to experiments. Hunt and Debugne (2016) developed a similar integral model, but additionally accounted for entrainment into the cap region. They assumed a constant entrainment coefficient that described radial flow from the OF to the IF, and obtained predictions for rise height, IF width and velocity that were in good agreement with experiments. Other experimental and numerical studies, however, have reported that the radial flow of fluid is primarily in the opposite direction, from the IF to the OF (Williamson et al. 2011; Cresswell and Szczepura 1993). In reality, the complex mixing process that occurs between the IF/OF is unlikely to be fully captured by a simple constant entrainment coefficient, and additional research would be useful here. Differences between entrainment in negatively buoyant jets without a return flow, and in the fully developed fountain with the IF/OF structure, has also not been given much attention (Hunt and Debugne 2016).

An aim of the present chapter is to extend the integral model approach applied to NBJs in chapter 5 to study fully developed fountains. A particular focus will be placed on the inner flow, with the aim of characterising mixing between the IF/OF regions. While previous modelling attempts have assumed constant entrainment coefficients to describe radial flow between the layers (McDougall 1981; Bloomfield and Kerr 2000; Hunt and Debugne 2016), this study will utilise the present experimental data to explore alternative entrainment formulations without the need for these assumptions. Entrainment between the IF/OF of fountains is discussed in §7.2 in the context of an integral model framework, where it is found to be primarily from the IF to the OF for the majority of its height. An alternative description of

entrainment that may be applied to both fountains and NBJs is proposed in §7.3, where it is decomposed into an approximately constant inflow component and a locally varying outflow component in the context of a 'decomposed top-hat' model.

7.2 Integral models

As was discussed in §2.4, it is possible to derive an integral model to describe jets and plumes with arbitrary buoyancy in a homogeneous environment from the conservation of volume, momentum, buoyancy and axial kinetic energy given in (2.4)-(2.7) (Morton et al. 1956; Priestley and Ball 1955). By integrating these equations from $r = 0$ to infinity, and neglecting second-order turbulence contributions, the system of ODEs in (2.19)-(2.22) was obtained. These were written in terms of the local volume, momentum and buoyancy fluxes, Q, M and F defined in (2.9), several profile coefficients in (2.16), and the entrainment coefficient, α in (2.17). There were all defined in terms of an integration limit $\tilde{r}$, which was set to $\tilde{r} = \infty$ throughout §2.4 and chapter 5.

Since (2.4)-(2.7) are valid for any axisymmetric flow in a homogeneous environment under the Boussinesq assumption, they may also be applied to a fully developed fountain. A system of ODEs similar to (2.19)-(2.22) may then be derived for the inner flow of a fountain by integrating (2.4)-(2.7) from $r = 0$ to r_{io}, the IF/OF boundary, instead of infinity. In this case, we let $\tilde{r} = r_{io}$ in (2.9)-(2.17), and all integral quantities and profile coefficients correspond to the inner flow,

$$\frac{\mathrm{d}Q}{\mathrm{d}z} = 2\alpha M^{1/2} \tag{7.1}$$

$$\frac{\mathrm{d}M}{\mathrm{d}z} = \frac{FQ}{\theta_m M} - 2\left(r\overline{u'w'}\right)_{r=r_{io}} \tag{7.2}$$

$$\frac{\mathrm{d}F}{\mathrm{d}z} = -2\left(r\overline{u}\overline{b}\right)_{r=r_{io}} - 2\left(r\overline{u'b'}\right)_{r=r_{io}} \tag{7.3}$$

$$\frac{\mathrm{d}}{\mathrm{d}z}\left(\gamma_m \frac{M^2}{Q}\right) = \delta_m \frac{M^{5/2}}{Q^2} + 2F. \tag{7.4}$$

The higher order turbulence terms, i.e. turbulence components of the profile coefficients, have been neglected here. The continuity and kinetic energy equations, (7.1) and (7.4), are in the same form as (2.12) and (2.15) since $\overline{w}(r = r_{io}) = 0$, but the momentum and buoyancy equations have non-zero boundary conditions arising because $\overline{u'w'}$, $\overline{u'b'}$ and $\overline{b}$ do not go to zero at r_{io}. In the present formulation, α is related to the integral scales of the IF only, and describes the exchange of fluid between the IF and OF, where $\alpha > 0$ corresponds to fluid moving from the OF to the

IF. An alternative approach may be to define the velocity scale in the definition of α in (2.17) so that it includes information about the outer flow velocity. However, since no assumptions are being made regarding the value or behaviour of α, any substitution here can be made valid provided it is consistent with the conservation equations.

Similarly to the derivation or (2.23), an expression for α for the inner flow of a fountain may be derived using (7.1), (7.2) and (7.4) (van Reeuwijk and Craske 2015),

$$\alpha = -\frac{\delta_m}{2\gamma_m} + \left(1 - \frac{\theta_m}{\gamma_m}\right) Ri + \frac{Q}{2M^{1/2}} \frac{\mathrm{d}}{\mathrm{d}z}(\ln \gamma_m) - \frac{2Q}{M^{3/2}} \left(r\overline{u'w'}\right)_{r=r_{io}}. \tag{7.5}$$

This expression is almost identical to (2.23), except it includes a non-zero shear stress term at the boundary, and all integral quantities and profile coefficients are defined up to r_{io}.

Carazzo et al. (2010) derived a similar set of equations to (7.1)-(7.4) for the IF of a fountain, but went on to construct additional conservation equations for $\overline{w}^3$ and $\overline{w}\overline{b}$ in order to replace the boundary conditions with integral profiles, and obtained a 'confined top-hat' model for the flow. For the purposes of the present investigation, it is sufficient to derive only the $\overline{w}^3$ equation, obtained by multiplying the momentum equation, (2.5), by $3\overline{w}^2$,

$$\frac{\partial}{\partial r}\left(r\overline{u}\,\overline{w}^3 + 3r\overline{u'w'}\overline{w}^2\right) + \frac{\partial}{\partial z}\left(r\overline{w}^4\right) = 3r\overline{w}^2\overline{b} + 6r\overline{w}\overline{u'w'}\frac{\partial \overline{w}}{\partial r}. \tag{7.6}$$

This may then be integrated with respect to r from 0 to r_{io} giving,

$$\frac{\mathrm{d}}{\mathrm{d}z}\left(\Gamma_m \frac{M^3}{Q^2}\right) = 6\Delta_m \frac{M^{7/2}}{Q^3} + 3\mu_m \frac{MF}{\theta_m Q}, \tag{7.7}$$

which is written in terms of the new profile coefficients,

$$\left.\begin{aligned} \mu_m &= \frac{1}{w_m^2 b_m r_m^2}\int_0^{\tilde{r}} \overline{w}^2\overline{b} r \mathrm{d}r, \\ \Gamma_m &= \frac{1}{w_m^4 r_m^2}\int_0^{\tilde{r}} \overline{w}^4 r \mathrm{d}r, \\ \Delta_m &= \frac{1}{w_m^4 r_m}\int_0^{\tilde{r}} \overline{w}\,\overline{w'u'}\frac{\partial \overline{w}}{\partial r} r \mathrm{d}r, \end{aligned}\right\} \tag{7.9}$$

with $\tilde{r} = r_{io}$. Note that this approach may also be applied to jets and plumes in a homogeneous environment by setting $\tilde{r} = \infty$ in the profile coefficient definitions, and

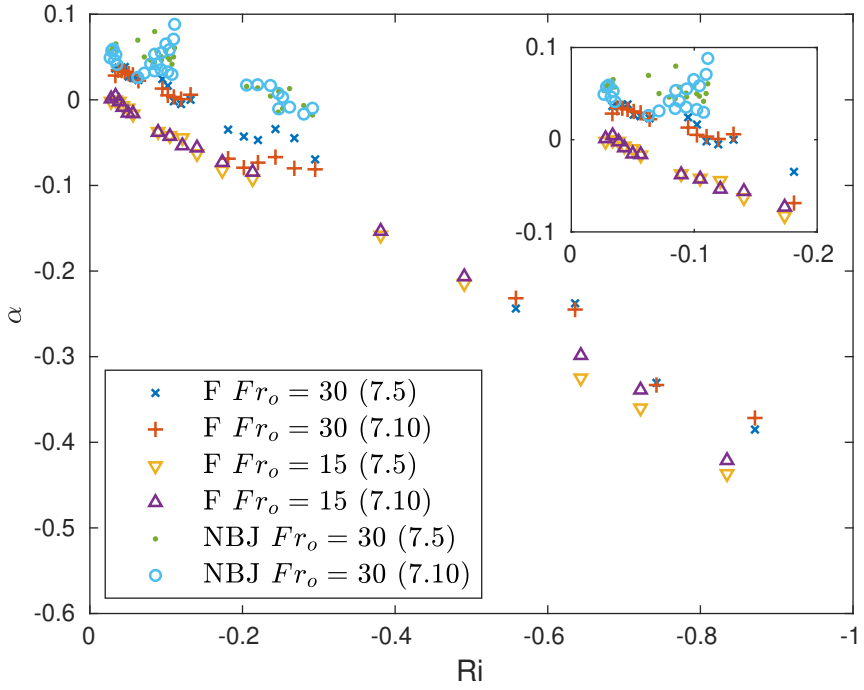

Figure 7.1: The entrainment coefficient, α, plotted with local Ri for the inner flow of a $Fr_o = 30$ and $Fr_o = 15$ fountain (F), and of a $Fr_o = 30$ negatively buoyant jet (NBJ), as calculated using (7.5) and (7.10).

integrating the conservation equations to infinity. In this case, the same expression as (7.7) is obtained.

By applying the product rule to (7.7), and using (7.1) and (7.4), a new expression for α without any boundary conditions may be derived,

$$\alpha = \frac{3}{2}\left(\frac{\delta_m}{\gamma_m} - \frac{4\Delta_m}{\Gamma_m}\right) + 3\left(\frac{\theta_m}{\gamma_m} - \frac{\mu_m}{\Gamma_m}\right) Ri + \frac{Q}{M^{1/2}}\frac{\mathrm{d}}{\mathrm{d}z}\left(\ln\frac{\Gamma_m}{\gamma_m^{3/2}}\right), \tag{7.10}$$

which is valid for arbitrary velocity and buoyancy profiles and does not make any assumptions about the self-similarity of the flow. By setting $\tilde{r} = r_{io}$ in the profile coefficient and α definition, this describes entrainment between the inner and outer flow of a fully developed fountain. As with (7.9), it may also be applied to jets of arbitrary buoyancy in a homogeneous environment by setting $\tilde{r} = \infty$. This is somewhat similar to the expression for α in Carazzo et al. (2010) (their equation (4.38)), which is valid for self-similar profiles and corresponds to entrainment in their top-hat model of the flow. Although both formulations are equally valid with respect to their given framework, (7.10) may be immediately applied to both the IF of a fountain or a negatively buoyant jet with arbitrary profiles, using the classical integral velocity, width and buoyancy scales defined in (2.10).

Both (7.5) and (7.10) are valid expressions for the entrainment coefficient of

the inner flow of a fountain ($\tilde{r} = r_{io}$), as well for a negatively buoyant jet ($\tilde{r} = \infty$). Using data from the present experiments, it is possible to calculate each of the profile coefficients present in these expressions, as well as directly measure the boundary condition, $\left(r\overline{u'w'}\right)_{r=r_{io}}$ in (7.5). Figure 7.1 shows α calculated using both (7.5) and (7.10), for two fully developed fountains with $Fr_o = 30$ and $Fr_o = 15$, as well as for a negatively buoyant jet with $Fr_o = 30$. As in §5.5, Gaussian velocity/buoyancy profiles were assumed for the NBJ, which results in $\gamma_m = 4/3$, $\Gamma_m = 1$, and the third term in (7.5) and (7.10) equalling zero. For the fountain, Gaussian profiles were not assumed, though the third terms in these two equations were found to be negligible and so have been neglected.

As discussed in §5.5 for the negatively buoyant jet, $\alpha < 0$ for $Ri \lesssim -0.25$ in figure 7.1, indicating there is a mean radial outflow of fluid from the jet. For the $Fr_o = 30$ fountain, α becomes negative near $Ri \cong -0.13$, reflecting a mean outflow of fluid from the IF to the OF. For the $Fr_o = 15$ fountain, $\alpha < 0$ for $Ri \lesssim -0.04$, and is close to zero for $Ri \gtrsim -0.04$. This is consistent with studies by Williamson et al. (2011) ($Fr_o = 7$) and Cresswell and Szczepura (1993) ($Fr_o \cong 3.2$), who predominately observed a mean radial flow from the IF to OF, other than in a small region near the source. More generally, figure 7.1 shows good agreement between the α estimated from (7.5), which uses a direct measurement of the IF/OF boundary condition, and (7.10), which uses the new profile coefficients defined in (7.9). This provides a reasonable validation of the approach taken by Carazzo et al. (2010) and here, of replacing the IF/OF boundary conditions by integral profiles obtained from the additional conservation equation.

7.3 Decomposing entrainment

Turbulent entrainment is generally considered the process where fluid is transported from a non-turbulent to turbulent region across a turbulent/non-turbulent interface (TNTI) (e.g. Mistry et al. (2016)). For the negatively buoyant jet, $\alpha < 0$ in figure 7.1 indicates there is a mean radial outflow of fluid from the turbulent jet to the quiescent ambient. For the fully developed fountains, the size and sign of α indicates the direction and magnitude of mean radial flow between the IF and OF. In these contexts, α is simply a parameter constrained by the conservation equations, and is therefore not necessarily a measure of 'turbulent entrainment' in the traditional sense. A negatively buoyant jet with $\alpha < 0$ could undergo instantaneous 'entrainment' (i.e. flow from the ambient across the TNTI into the jet) at some times, while expelling fluid at others. For a fountain, although the IF/OF boundary is between

two turbulent regions rather than a TNTI, there can still be instantaneous fluid transport across this boundary in either direction, separate from the mean flow. Such exchange of fluid across a turbulent shear layer is still often regarded as 'entrainment' (Morton 1962; McDougall 1981), and we will also take this interpretation in the context of fountains.

As discussed in §5.5, the $\alpha < 0$ in the NBJ is a natural consequence of the conservation equations, being primarily driven by the Ri term in (2.23). This term becomes increasingly negative as $Ri \to -\infty$ as the mean flow decelerates and $w_m \to 0$. For a fountain, although α is additionally affected by the return flow, we would still expect $\alpha < 0$ for sufficiently negative Ri as the inner flow velocity approaches zero. This section will explore an alternative approach to characterising entrainment in NBJs and fountains, where it will be separated into an inflowing 'turbulent entrainment' contribution occurring simultaneously with a mean outflow of fluid.

7.3.1 Decomposed top-hat model

Consider a control volume of a thin horizontal slice of an axisymmetric fully developed fountain, such as one taken from the fountain schematic shown in figure 7.2. The slice should be taken before the cap, $z < z_c$, where there are distinct IF and OF regions (e.g. $Ri \geq -0.5$) (Shrinivas and Hunt 2014; Hunt and Debugne 2016). For simplicity, the fountain is presumed to be orientated vertically upwards with a denser IF than OF (the opposite but equivalent case to the present experiments), and have top-hat vertical velocity and buoyancy profiles. Here we have, for the inner and outer flows, $\hat{w}_{if}$ and $\hat{w}_{of}$ denoting the vertical velocities, $\hat{r}_{if}$ and $\hat{r}_{of}$ the widths, and $\hat{g}_{if} = g(\rho_e - \hat{\rho}_{if})/\rho_e$ and $\hat{g}_{of} = g(\rho_e - \hat{\rho}_{of})/\rho_e$ the buoyancies. Here $\hat{\rho}_{if}$, $\hat{\rho}_{of}$ and ρ_e are the densities of the IF, OF and ambient, and so we have $\hat{g}_{if} < 0$ and $\hat{g}_{of} < 0$. There is also a radial exchange of fluid between the inner and outer flow that is presumed to go in both directions simultaneously. The velocity of fluid 'entrained' into the IF from the OF is denoted by $\hat{u}_e$, while velocity of outflowing fluid from the IF to the OF is $\hat{u}_{out}$. Fluid entrained into the OF from the ambient has a radial velocity $\hat{u}_a$. The equations for conservation of volume, momentum and buoyancy flux for the inner flow of this system are then,

$$\frac{\mathrm{d}\hat{Q}_{if}}{\mathrm{d}z} = 2\hat{r}_{if}\hat{u}_e - 2\hat{r}_{if}\hat{u}_{out} \tag{7.11}$$

$$\frac{\mathrm{d}\hat{M}_{if}}{\mathrm{d}z} = -2\hat{r}_{if}\hat{u}_e\hat{w}_{of} - 2\hat{r}_{if}\hat{u}_{out}\hat{w}_{if} + \hat{r}_{if}^2\hat{g}_{if} \tag{7.12}$$

$$\frac{\mathrm{d}\hat{F}_{if}}{\mathrm{d}z} = 2\hat{r}_{if}\hat{u}_e\hat{g}_{of} - 2\hat{r}_{if}\hat{u}_{out}\hat{g}_{if}, \tag{7.13}$$

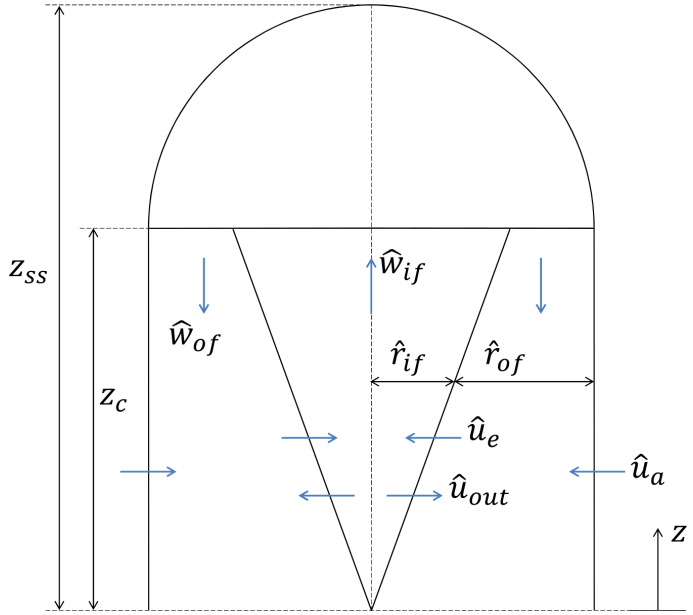

Figure 7.2: Schematic diagram of a fully developed fountain.

where $\hat{Q}_{if} = \hat{r}_{if}^2 \hat{w}_{if}$, $\hat{M}_{if} = \hat{r}_{if}^2 \hat{w}_{if}^2$ and $\hat{F}_{if} = \hat{r}_{if}^2 \hat{w}_{if} \hat{g}_{if}$ are the (scaled) volume, momentum and buoyancy fluxes.

In a fully developed fountain, the mean radial velocity is from the IF to the OF for the majority of its height. A mean radial outflow is also seen in negatively buoyant jets that do not have a return flow, where it is driven by the decelerating mean flow as characterised by $Ri \to -\infty$. Despite this, there may still be instantaneous 'entrainment' from the OF to the IF of a fountain across the IF/OF interface (or from the ambient to the jet in the case of an NBJ). The present analysis will treat $\hat{u}_e$ as the 'entrainment velocity', and assume that it is proportional to the velocity of the IF by an entrainment coefficient, α_e,

$$\hat{u}_e = \alpha_e \hat{w}_{if}. \tag{7.14}$$

Other options for this entrainment relation, such as replacing $\hat{w}_{if}$ with $\hat{w}_{if} - \hat{w}_{of}$, the relative difference between the IF/OF, are explored in §7.3.2. No assumptions will be made about the velocity of the outflowing fluid, $\hat{u}_{out}$, which in practice is likely dependent on both the inner and outer flow. In this formulation, even if $\hat{w}_{of} = 0$ and $\hat{g}_{of} = 0$ and the flow is effectively a negatively buoyant jet without a return flow, there may still be a radial outflow of fluid occurring simultaneously to entrainment (i.e. $\hat{u}_e > 0$ and $\hat{u}_{out} > 0$). This is a key difference when compared to previously proposed fountain models, such as by McDougall (1981) or Bloomfield and Kerr (2000), who treated flow from the IF to OF as proportional to $\hat{w}_{of}$, and

related them by second entrainment coefficient. The conservation equations for the present system may then be written as,

$$\frac{\mathrm{d}\hat{Q}_{if}}{\mathrm{d}z} = 2\alpha_e \hat{r}_{if}\hat{w}_{if} - 2\hat{r}_{if}\hat{u}_{out} \tag{7.15}$$

$$\frac{\mathrm{d}\hat{M}_{if}}{\mathrm{d}z} = -2\alpha_e \hat{r}_{if}\hat{w}_{if}\hat{w}_{of} - 2\hat{r}_{if}\hat{u}_{out}\hat{w}_{if} + \hat{r}_{if}^2\hat{g}_{if} \tag{7.16}$$

$$\frac{\mathrm{d}\hat{F}_{if}}{\mathrm{d}z} = 2\alpha_e \hat{r}_{if}\hat{w}_{if}\hat{g}_{of} - 2\hat{r}_{if}\hat{u}_{out}\hat{g}_{if}, \tag{7.17}$$

This system of equations will be referred to as the 'decomposed top-hat' model, and may also be applied to negatively buoyant jets by setting $\hat{w}_{of} = \hat{g}_{of} = 0$.

If the top-hat variables in (7.15)-(7.17) are replaced with integral quantities calculated from the experimental data, then the only unknowns in the volume and momentum flux equations are α_e and $\hat{u}_{out}$. For the inner flow velocity and radius, we set $\hat{w}_{if} = w_m$ and $\hat{r}_{if} = r_m$ as defined using (2.9) and (2.10*a*-*b*) with $\tilde{r} = r_{io}$ for a fountain and $\tilde{r} = \infty$ for an NBJ. We will define the outer flow velocity, $\hat{w}_{of}$, similarly to w_m except the integrals in (2.9) are evaluated from r_{io} to infinity. For the inner flow buoyancy scale, we take $\hat{g}_{if} = g_m$ as defined in (5.2), again using $\tilde{r} = r_{io}$ for fountains and $\tilde{r} = \infty$ for NBJs. The outer flow buoyancy, $\hat{g}_{of}$, may be similarly defined except with the integration limits set from $r = r_{io}$ to infinity. The derivatives, $\mathrm{d}\hat{Q}_{if}/\mathrm{d}z$ and $\mathrm{d}\hat{M}_{if}/\mathrm{d}z$, are estimated using a second order accurate finite difference stencil. When referring exclusively to negatively buoyant jets, which do not have an outer flow, the subscript 'if' is omitted from the notation.

With all top-hat variables in (7.15) and (7.16) defined based on local integral scales, the pair of equations may then be solved simultaneously to obtain estimates for α_e and $\hat{u}_{out}$ along the fountain and NBJ. Figure 7.3 shows α_e plotted with local Ri for $Fr_o = 30$ and $Fr_o = 15$ fountains, and a $Fr_o = 30$ NBJ. Here only results prior to the cap region are shown, since this is where the present top-hat model is expected to be valid. The entrainment coefficient for a neutral jet, which has $\hat{u}_{out} = 0$, is also shown as a horizontal line as a reference. This corresponds to $\alpha = 0.071$, as calculated in §5.5. For the fully developed fountains, we have a slightly higher α_e in the $Fr_o = 30$ than $Fr_o = 15$ case, with average values of $\alpha_e = 0.062$ and $\alpha_e = 0.050$, respectively. Both fountains have $\alpha_e > 0$ over the full range shown, which contrasts to the original definition of α discussed in §7.2 and shown in figure 7.1. This had $\alpha < 0$ for the majority of the Ri range shown ($Ri \lesssim -0.13$ for $Fr_o = 30$, and $Ri \lesssim -0.011$ for $Fr_o = 15$), and also had α generally lower in the $Fr_o = 15$ case. This previous formulation of α, which was expressed by (7.5) and (7.10), will henceforth referred to as the 'full model'.

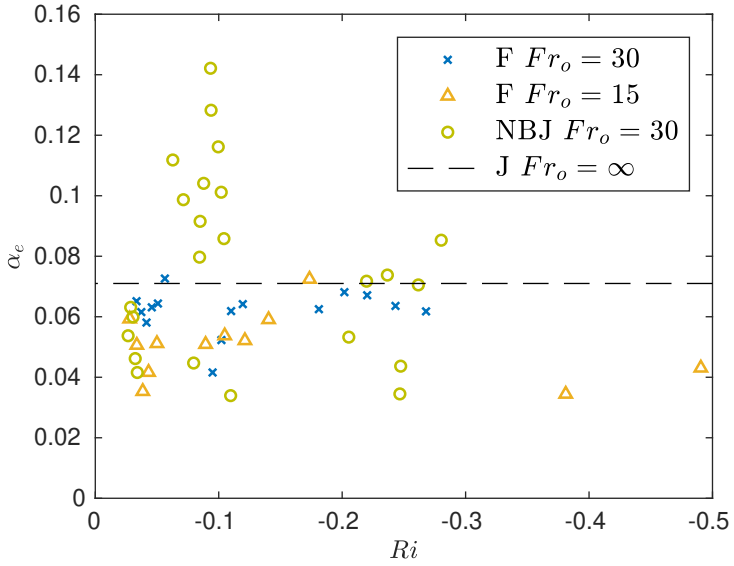

Figure 7.3: The entrainment coefficient, α_e, plotted with local Ri for the inner flow of a $Fr_o = 30$ and $Fr_o = 15$ fountain (F), and of a $Fr_o = 30$ negatively buoyant jet (NBJ). Here $\alpha_e = \hat{u}_e/\hat{w}_{if}$, and corresponds to the 'decomposed top-hat model' described by (7.15)-(7.17). The entrainment coefficient for neutral jet (J), as estimated in §5.5, is also shown as a reference. For neutral jets, $Ri = 0$ everywhere and so α is shown as a horizontal line for clarity.

The results in figure 7.3 for the 'decomposed model' are more scattered in the NBJ since there is less data available, but we clearly have $\alpha_e > 0$ over the Ri range shown (with an average value of $\alpha_e = 0.077$). This again contrasts to the full model in figure 7.1, where $\alpha < 0$ for $Ri \lesssim -0.25$. Since there is no clear systematic trend for α_e with Ri in the NBJ or fountains, α_e could be approximated by taking the average value as constant. We would then have α_e in the NBJ similar to α in a neutral jet, and fountain values somewhat lower.

In the decomposed formulation, α_e can be interpreted as a measure of the rate of 'turbulent entrainment' in the flow. For fountains, this represents 'entrainment' from the OF to IF across the IF/OF interface, and in NBJs it is entrainment from the ambient into the jet across the TNTI. This contrasts to α in the full model shown in figure 7.1, which simply reflects the direction and magnitude of the mean radial velocity.

Solving (7.15) and (7.16) simultaneously also provides values for $\hat{u}_{out}$, the outflow velocity. Figure 7.4 shows $\hat{u}_{out}/\hat{w}_{if}$ plotted with Ri for the $Fr_o = 30$ and $Fr_o = 15$ fountains, and $Fr_o = 30$ NBJ. We see that, for all three flows, $\hat{u}_{out}$ increases with $-Ri$, and that $\hat{u}_{out} > 0$ for all $Ri < 0$. Near the source, where the IF is much stronger than the outer flow, $\hat{u}_{out}/\hat{w}_{if} \to 0$ and $Ri \to 0$. This is consistent with the neutral jet case, which has $Ri = 0$ and does not have a mean outflow. Regions where

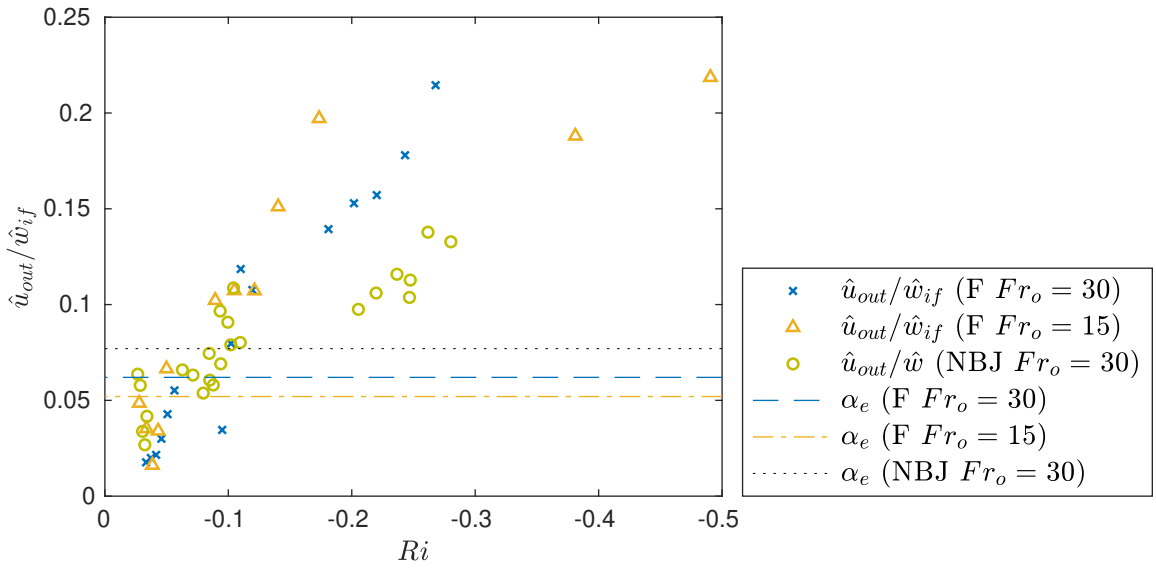

Figure 7.4: The normalised radial outflow velocity, $\hat{u}_{out}/\hat{w}_{if}$, with respect to the 'decomposed top-hat' model for $Fr_o = 30$ and $Fr_o = 15$ fountains, and a $Fr_o = 30$ NBJ. Horizontal lines indicating average values of α_e from figure 7.3 are also shown.

there is a net radial outflow of fluid from the IF correspond to where $\hat{u}_{out} > \hat{u}_e$. Since $\alpha_e = \hat{u}_e/\hat{w}_{if}$ from (7.14), this is equivalent to where $\hat{u}_{out}/\hat{w}_{if} > \alpha_e$. Horizontal lines showing average values of α_e for the fountains and NBJ are also shown in figure 7.4, which therefore indicate the start of the region where there is a net radial outflow of fluid from the IF. Figure 7.4 therefore implies that the IF of both Fr_o fountains and the NBJ have a net radial outflow of fluid for a large portion of their height, with the local Ri at the start of this region broadly consistent with figure 7.1. That is, where $\alpha < 0$ in the original formulation given by (7.5) and (7.10).

The decomposed formulation separates radial flow between the IF/OF of a fountain into two components that are constrained by both the conservation of mass and momentum. The inflow term is described by the approximately constant α_e, which represents 'turbulent entrainment' from the OF to the IF. The outflow term, $\hat{u}_{out}/\hat{w}_{if}$, represents fluid ejected from the IF to the OF and depends on the local Ri. This term approaches zero as $Ri \to 0$ where the IF is much stronger than the OF, and increases for more negative Ri.

7.3.2 Alternative entrainment and body-force formulations

The decomposed model presented in §7.3.1 describes radial flow from the OF to IF as proportional to the IF velocity, as implied by the definition of α_e in (7.14). This was the entrainment formulation used by Hunt and Debugne (2016) and also considered by Bloomfield and Kerr (2000) in their theoretical models of a fountain, and will

be referred to as E1. McDougall (1981) used an alternative formulation, which was also considered by Bloomfield and Kerr (2000), where $\hat{u}_e$ is instead proportional to the relative velocity difference between the IF and OF. In this case, the entrainment coefficient in (7.14) would be defined using the substitution,

$$\hat{u}_e = \alpha_e \left(\hat{w}_{if} + \hat{w}_{of} \right), \tag{7.18}$$

which will be referred to as E2, the second entrainment formulation.

Another way in which the fountain model could be modified is to consider alternative body-force formulations. McDougall (1981) considered two formulations, the first was that the buoyancy force acting on the IF depends on the density difference between the IF and the ambient fluid. This follows from the assumption that the pressure is hydrostatic everywhere and that lines of constant pressure are horizontal. This will be referred to as, B1, and was the formulation used in §7.3.1 in the momentum equations (7.12) and (7.16). The second body-force formulation considered by McDougall (1981), and also by Bloomfield and Kerr (2000) and Hunt and Debugne (2016), is to treat the OF as an effective 'ambient' with respect to the IF. The buoyancy force acting on the IF would then be related the the density difference between the IF and OF. This body-force formulation will be denoted B2, and results in an alternative momentum equation for the IF that would replace (7.12) (McDougall 1981; Bloomfield and Kerr 2000; Hunt and Debugne 2016),

$$\frac{\mathrm{d}\hat{M}_{if}}{\mathrm{d}z} = -2\hat{r}_{if}\hat{u}_e\hat{w}_{of} - 2\hat{r}_{if}\hat{u}_{out}\hat{w}_{if} + \hat{r}_{if}^2 \left(\hat{g}_{if} - \hat{g}_{of} + \hat{w}_{of}\frac{\mathrm{d}\hat{w}_{of}}{\mathrm{d}z} \right), \tag{7.19}$$

where the third term in the parentheses, $\hat{w}_{of}\mathrm{d}\hat{w}_{of}/\mathrm{d}z$, arises due to the accelerating reference frame (i.e. the OF) (McDougall 1981).

There are then four combinations of entrainment and body force formulations, each of which were considered by Bloomfield and Kerr (2000), and which can be expressed as B1E1, B1E2, B2E1 and B2E2. Bloomfield and Kerr (2000) also used entrainment relations to describe radial flow from the IF to OF, and from the ambient to the IF, and assumed constant entrainment coefficients. By combining these with a system of equations similar to (7.11)-(7.13) but for the OF, they solved their fountain model for the four formulations. In the present study, we have instead used experimental data to estimate the inflow entrainment coefficient, α_e, and outflow component $\hat{u}_{out}$, without making any further assumptions. Figures (7.3) and (7.4), and the discussion in §7.3.1, correspond to this approach applied to formulation B1E1.

The same procedure is now applied to the remaining three entrainment/body-

force formulations, B1E2, B2E1 and B2E2. That is, simultaneously solving conservation equations (7.11) and either (7.12) or (7.19), while using either entrainment relation for $\hat{u}_e$, to calculate α_e and $\hat{u}_{out}$ at a range of axial locations along the fountain. The value of α_e for these formulations is plotted with Ri in figure 7.5(a)-(c). Similarly to figure 7.3 corresponding to B1E1, α_e is reasonably constant in each formulation with no significant trend with Ri. The mean α_e value for each case is summarised in table 7.1, which shows the largest values in B2E1, and consistently higher values in the $Fr_o = 30$ than $Fr_o = 15$ fountain.

	B1E1	B1E2	B2E1	B2E2
α_e ($Fr_o = 15$)	0.050	0.042	0.061	0.051
α_e ($Fr_o = 30$)	0.062	0.051	0.073	0.059

Table 7.1: Mean values of α_e for $Fr_o = 15$ and 30 fountains in the decomposed top-hat model for the alternative body-force and entrainment formulations, as estimated from the present experimental data.

While the value of the outflow component, $\hat{u}_{out}$, is affected by the body force formulation, it is independent of the choice of α_e substitution when simultaneously solving the conservation of volume and momentum equations using the present data. This can be seen if the conservation equations are solved simultaneously for $\hat{u}_e$ and $\hat{u}_{out}$ *before* substituting in the chosen entrainment relation, resulting in the same value of $\hat{u}_{out}$ for E1 and E2. However, when comparing with α_e, it is useful to normalise $\hat{u}_{out}$ in a way consistent with the definition of α_e. For example, in B1E2, $\alpha_e = \hat{u}_e/(\hat{w}_{if} + \hat{w}_{of})$, and so it is useful to consider $\hat{u}_{out}/(\hat{w}_{if} + \hat{w}_{of})$. The normalised outflow component is presented in figure 7.6 for B1E2, B2E1 and B2E2, along with horizontal lines corresponding to the mean α_e value to indicate the start of the region where there is a net radial outflow from the IF to OF. Similarly to figure 7.4, all cases show that the normalised outflow component is strongly dependent on Ri. The precise values differ slightly for each entrainment/body-force formulation, but are nevertheless broadly similar.

McDougall (1981) and Bloomfield and Kerr (2000) both assumed that the radial outflow component was proportional to the OF velocity when solving their fountain models. In the present case, it was desirable to formulate a 'fountain' model that could also be applied to NBJs, which have $\hat{w}_{of} = \hat{g}_{of} = 0$ but can also be subject to a net radial outflow as demonstrated in §5.5. In this case, such an entrainment relation is not well defined and so has not been considered until now. Despite this, we now briefly consider $\hat{u}_{out}/\hat{w}_{of}$ for the two body-force formulations in the $Fr_o = 15$ and 30 fountains, shown in figure 7.7, recalling that the value of $\hat{u}_{out}$ is the same in both entrainment formulations. Figure 7.7 shows a strong Ri dependence on

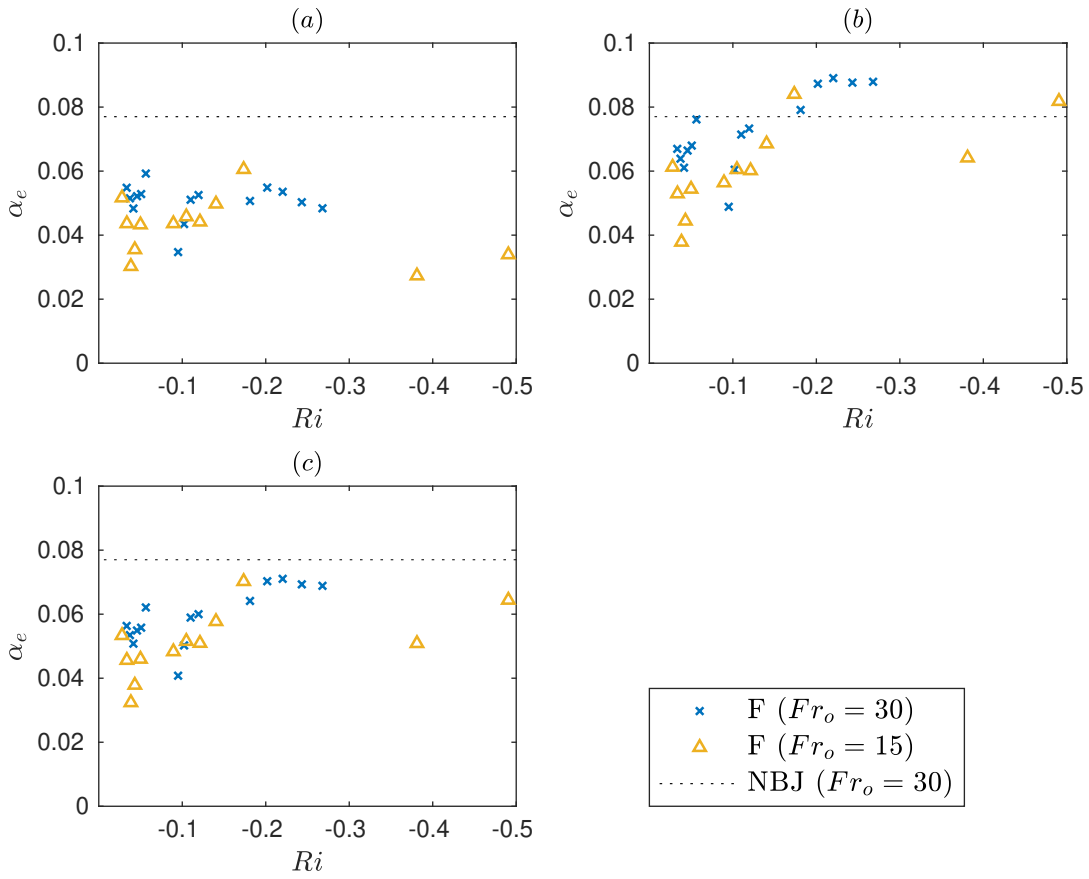

Figure 7.5: The entrainment coefficient, α_e, for (a) B1E2, (b) B2E1 and (c) B2E2, for $Fr_o = 15$ and 30 fountains under the decomposed top-hat model, as estimated from the present experimental data. The mean NBJ value, which is the same in all formulations, is shown as a horizontal line as a reference.

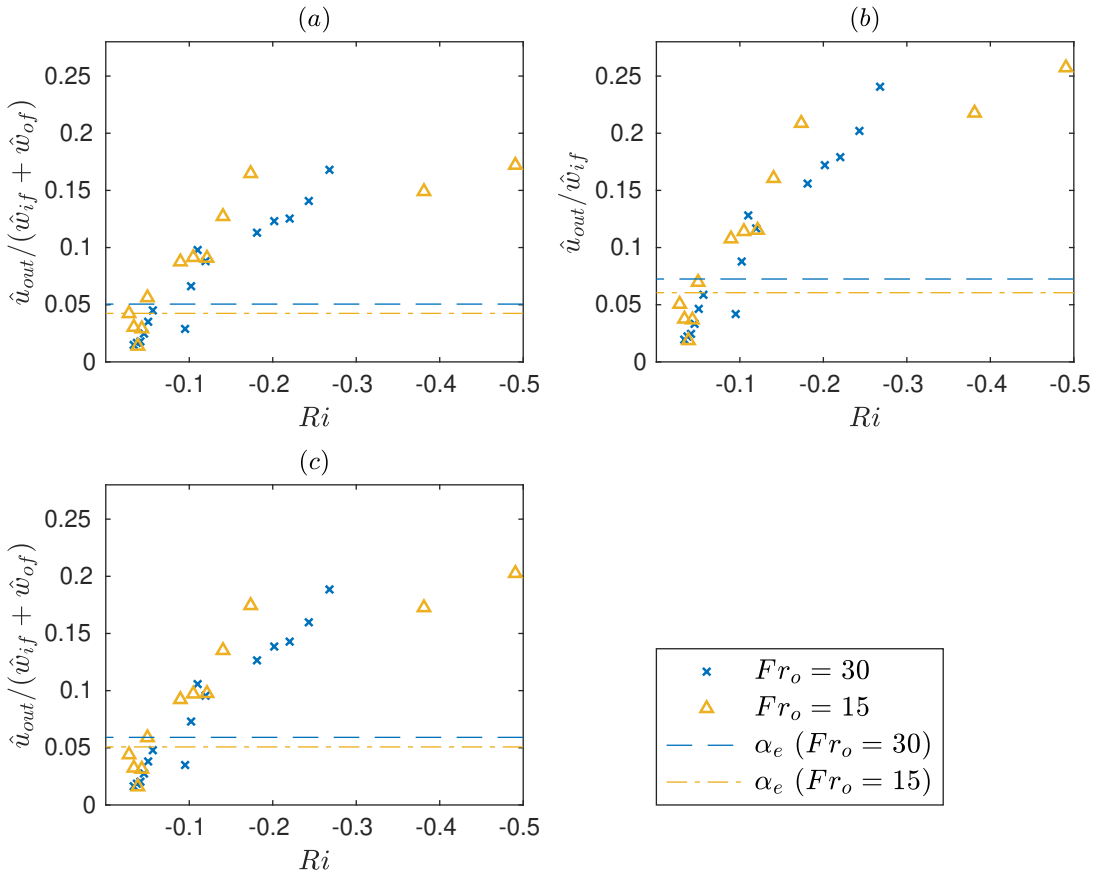

Figure 7.6: The radial velocity outflow component, $\hat{u}_{out}$, for (a) B1E2, (b) B2E1 and (c) B2E2, for $Fr_o = 15$ and 30 fountains under the decomposed top-hat model, as estimated from the present experimental data. In each case, $\hat{u}_{out}$ is normalised so that it is consistent with the definition of α_e.

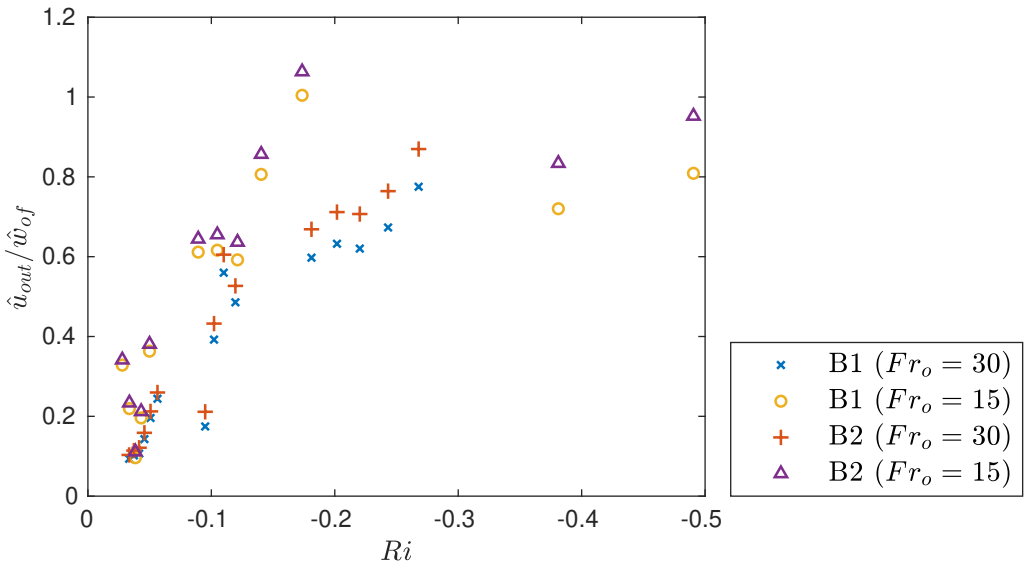

Figure 7.7: The radial velocity outflow component, $\hat{u}_{out}$, normalised by the outer flow velocity, $\hat{w}_{of}$, for $Fr_o = 15$ and 30 fountains under the decomposed top-hat model.

$\hat{u}_{out}/\hat{w}_{of}$, with broadly similar values for both body-force formulations for each Fr_o fountain. Bloomfield and Kerr (2000) assumed that this quantity was a constant equal to $\hat{u}_{out}/\hat{w}_{of} = 0.147$, which is similar to the present values near $Ri \cong -0.05$, but lower than those further along the fountain.

Although the precise values of α_e are affected by the choice of body-force and entrainment formulations, and $\hat{u}_{out}$ by the choice of body-force formulation only, the overall trends for both quantities are very similar. That is, the Ri-dependence of the outflow component shown in figure 7.6-7.7, and the approximately constant α_e in figure 7.5 and table 7.1. The arguments put forward in §7.3.1 corresponding to B1E1 may therefore also be applied to the other formulations. Namely, that the approximately constant α_e can be interpreted as representing 'turbulent entrainment' from the OF to IF, similar to the classical description of entrainment in pure jets and plumes (Morton et al. 1956). The outflow component then represents the fluid ejected from the IF to the OF as a result of the decelerating and expanding IF, as well as capturing other complex interactions with the OF. Although all four formulations are similar in this way, the B1E1 formulation most closely resembles the 'full model' discussed in §7.2, which relates α to IF quantities only. The following section will seek to compare the decomposed formulation to the full model, and so we will now primarily consider B1E1. All further references to the 'decomposed top-hat' model correspond to this formulation unless specified otherwise.

7.3.3 Connection to the full model

Figures 7.3 and 7.4 show that, in the present decomposed top-hat formulation, the radial flow across the IF/OF boundary of a fountain (or between an NBJ and the ambient) can be described by an approximately constant turbulent entrainment coefficient, α_e, and a local Ri-dependent outflow component, $\hat{u}_{out}/\hat{w}_{if}$. If the net radial flow from the IF to OF is denoted $\hat{u}$, so that $\hat{u} = \hat{u}_{out} - \hat{u}_e$, then the ratio $\hat{\alpha} = -\hat{u}/\hat{w}_{if}$ is a non-dimensional measure of the direction and magnitude of the mean radial flow at a given height. Using (7.14), this may then be written as,

$$\hat{\alpha} = \alpha_e - \frac{\hat{u}_{out}}{\hat{w}_{if}}, \tag{7.20}$$

which expresses $\hat{\alpha}$ as the sum of a constant and Ri-dependent component, α_e and $-\hat{u}_{out}/\hat{w}_{if}$, respectively. This is then the present top-hat model's equivalent to α in the full model, defined by (2.23) or (7.10), which is also a measure of the mean radial velocity relative to the IF velocity scale. If the profile coefficients in (7.10) were assumed constant, then this may be written as,

$$\alpha = \frac{3}{2}\left(\frac{\delta_m}{\gamma_m} - \frac{4\Delta_m}{\Gamma_m}\right) + 3\left(\frac{\theta_m}{\gamma_m} - \frac{\mu_m}{\Gamma_m}\right) Ri, \tag{7.21}$$

which is also expressed as the sum of a constant and Ri-dependent component, namely the first and second terms respectively.

For Gaussian velocity and buoyancy profiles, which was shown in figure 5.5 to be a reasonable assumption in NBJs, we have that $\gamma_m = 4/3$, $\Gamma_m = 1$, $\theta_m = 2/(\lambda^2+1)$ and $\mu = 2/(2\lambda^2+2)$. In figure 5.6 it was shown that λ, and hence θ_m and μ_m, are not constant in negatively buoyant jets. However, their variation has little effect on the Ri term in α relations (2.23) and (7.21), and so may be approximated as constant with $\lambda \cong 1.46$ for this purpose. For the inner flow of a fountain, the profiles cannot be simply described by Gaussian functions, and so these profile coefficients must be numerically estimated from their integral definitions, (2.16) and (7.9). By assuming these are constant we obtain, by taking averages, $\theta_m \cong 0.68$ and $\mu_m \cong 0.36$ for $Fr_o = 30$, and $\theta_m \cong 0.65$ and $\mu_m \cong 0.34$ for $Fr_o = 15$. The data suggests that γ_m and Γ_m have a weak Ri dependence in fountains, with $1.27 \gtrsim \gamma_m \gtrsim 1.18$ and $0.90 \gtrsim \Gamma_m \gtrsim 0.76$ over $0 \lesssim -Ri \lesssim 0.5$. Since this variation is not very significant, these were approximated as constant using average values of $\gamma_m \cong 1.23$ and $\Gamma_m \cong 0.85$ for $Fr_o = 30$, and $\gamma_m \cong 1.23$ and $\Gamma_m \cong 0.84$ for $Fr_o = 15$. All four of these profile coefficients, θ_m, μ_m, γ_m and Γ_m, therefore have similar values for both fountains, with a negligible Fr_o dependence.

For a negatively buoyant jet, it was shown in §5.5 that δ_m is not constant, and instead varies linearly with Ri. The present data shows that an approximately linear relation also occurs in fountains. Additionally, the profile coefficient Δ_m, defined in (7.9) and related to the turbulent production, is also well described by a linear Ri relation. These can be expressed as,

$$\left.\begin{aligned} \delta_m &= \delta_o + \tilde{\delta} Ri, \\ \Delta_m &= \Delta_o + \tilde{\Delta} Ri, \end{aligned}\right\} \tag{7.22}$$

where δ_o and Δ_o represent the values at the source, and $\tilde{\delta}$ and $\tilde{\Delta}$ are additional ad hoc terms that capture the observed Ri dependence. The increasing $-\delta_m$ and $-\Delta_m$ with negative Ri is related to the behaviour of the $\overline{w'u'}$ profiles discussed in §6.2.2, where the turbulence did not decrease at the same rate as the mean flow in NBJs and fountains. A detailed analysis of the governing equations may shed light on the precise reason for this behaviour, which is left for potential future research. For the purposes of the present investigation, the observation of a linear trend and subsequent empirical expressions in (7.22) will be used.

By using these linear relations, the expression for α in (7.21) becomes,

$$\alpha = \underbrace{\frac{3}{2}\left(\frac{\delta_o}{\gamma_m} - \frac{4\Delta_o}{\Gamma_m}\right)}_{P_1} + \underbrace{3\left(\frac{\theta_m}{\gamma_m} - \frac{\mu_m}{\Gamma_m} + \frac{\tilde{\delta}}{2\gamma_m} - \frac{2\tilde{\Delta}}{\Gamma_m}\right) Ri}_{P_2}. \tag{7.23}$$

This expresses α as the sum of a constant and Ri-dependent component, P_1 and P_2, and is valid for both negatively buoyant jets and fountains. The following expression, which is valid for NBJs only, was originally presented in (5.9),

$$\alpha = \underbrace{-\frac{\delta_o}{2\gamma_m}}_{L_1} + \underbrace{\left(1 - \frac{\theta_m}{\gamma_m} - \frac{\tilde{\delta}}{2\gamma_m}\right) Ri}_{L_2}, \tag{7.24}$$

except here the subscript 'j' has been replaced with 'o' to correspond to the $Ri = 0$ intercept. This is for consistency with (7.23), and because we will not presume that the $Ri = 0$ value of δ_m and Δ_m in fully developed fountains correspond to the neutral jet values. Although both (7.23) and (7.24) are equally valid for negatively buoyant jets, (7.24) is simpler since it does not depend on Δ_m or Γ_m. Equation (7.24) will therefore be used for calculating α in negatively buoyant jets, while (7.23) will be used for fountains. It is then useful to attempt to unify the 'decomposed top-hat model' with the 'full model' by considering $\hat{\alpha} = \alpha$. Both (7.23) and (7.24) express α

in terms of constant and Ri-dependent components, which may then be compared individually to the components of $\hat{\alpha}$ defined in (7.20). We would then have,

$$\left.\begin{aligned} L_1 &= \alpha_e \\ L_2 &= -\frac{\hat{u}_{out}}{\hat{w}} \end{aligned}\right\} \text{NBJ} \tag{7.25}$$

$$\left.\begin{aligned} P_1 &= \alpha_e \\ P_2 &= -\frac{\hat{u}_{out}}{\hat{w}_{if}} \end{aligned}\right\} \text{Fountain} \tag{7.26}$$

for the negatively buoyant jet and fountains.

These different components and their summation are given in figure 7.8 for the $Fr_o = 30$ negatively buoyant jet, and in figure 7.9 for the $Fr_o = 30$ and $Fr_o = 15$ fountains. For the NBJ, figure 7.8(a) shows $L_1 = 0.075$ and $L_2 = 0.292Ri$ corresponding to (7.24), with the values originally obtained from the linear fits in (5.8). Although very good agreement is observed between α_e and L_1, the constant component of the entrainment coefficient, there is a discrepancy between the Ri-dependent terms, L_2 and $-\hat{u}_{out}/\hat{w}$. It was found that better agreement could be obtained by including the turbulence components of the profile coefficients, δ_f and γ_f originally defined in (2.16), in the expression for α. In this case, average values of $\delta_f \cong -0.044$ and $\gamma_f \cong 0.47$ were calculated using the present experimental data and assumed constant. This results in the following expression for α that can be used in place of (7.24),

$$\alpha = \underbrace{-\frac{\delta_o + \delta_f}{2\gamma_g}}_{L_1} + \underbrace{\left(1 - \frac{\theta_m}{\gamma_g} - \frac{\tilde{\delta}}{2\gamma_g}\right) Ri}_{L_2}, \tag{7.27}$$

where $\gamma_g = \gamma_m + \gamma_f$. Figure 7.8($b$) shows the same $\hat{\alpha}$ decomposition, but now with L_1 and L_2 calculated using (7.27). The constant terms, α_e and L_1, are not as close as in (a) but still reasonably agree, while the agreement between the Ri terms $-\hat{u}_{out}/\hat{w}$ and L_2, and the overall summations, $\hat{\alpha}$ and α have been significantly improved. Although this supports the validity of the 'decomposed top-hat' formulation, it raises questions as to whether the assumptions made in §5.5-5.7, where the turbulence components of the profile coefficients were ignored, are appropriate. Although the turbulence components do have an effect on the entrainment rate, the modelling of NBJs in §5.6 showed that reasonable $\overline{w}_c$ agreement could nevertheless be achieved without them. It is therefore argued that neglecting these higher order contributions is a reasonable simplification for the purposes of the present investigation. The

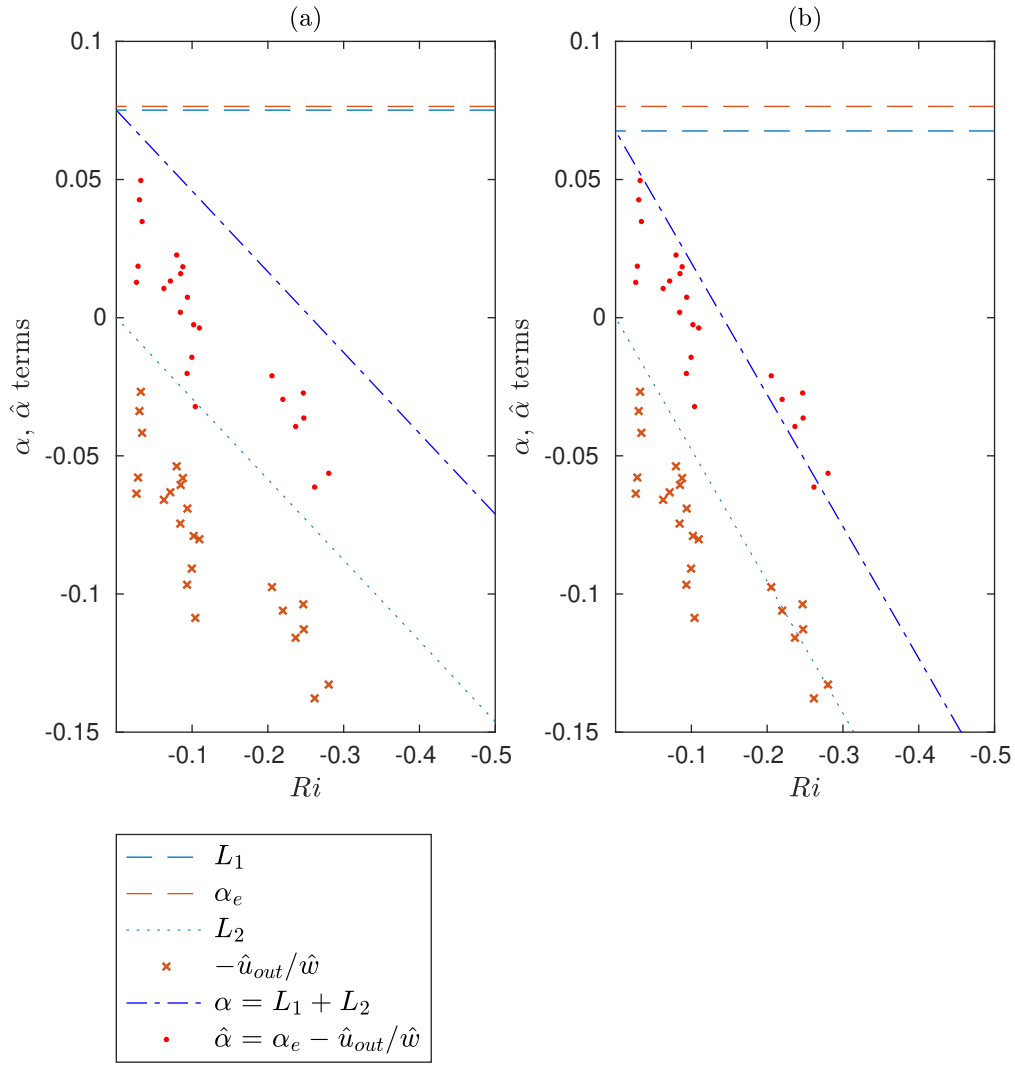

Figure 7.8: The constant and Ri-dependent components of the entrainment coefficient of a $Fr_o = 30$ negatively buoyant jet from both the decomposed top-hat model ($\hat{\alpha} = \alpha_e - \hat{u}_{out}/\hat{w}$), and the full model ($\alpha = L_1 + L_2$). Figure ($a$) shows the terms L_1 and L_2 as calculated using (7.24), while (b) uses (7.27). That is, (a) neglects the turbulence component of profile coefficients, δ_f and γ_f, while (b) includes them.

effect of including additional turbulence components, namely the subscript-f profile coefficients in (2.16), is left for potential future research.

The components of the entrainment coefficient for the fully developed fountain are given in figure 7.9(a) and (b) for $Fr_o = 30$ and 15 cases respectively. For both Fr_o cases, (7.23) has been used to calculate the α components, P_1 and P_2, with the turbulence profile coefficients neglected. Here the linear fits used to obtain $\delta_m = \delta_o + \tilde{\delta} Ri$ and $\Delta_m = \Delta_o + \tilde{\Delta} Ri$ have been obtained from the experimental data for each Fr_o fountain separately. The $Fr_o = 30$ case in (a) shows good agreement between both the constant and Ri-dependent components, with $\alpha_e \cong P_1$ and

$-\hat{u}_{out}/\hat{w}_{if} \cong P_2$, and subsequently $\alpha \cong \hat{\alpha}$. Although the agreement is more modest in the $Fr_o = 15$ case, the components and their summation are still broadly consistent.

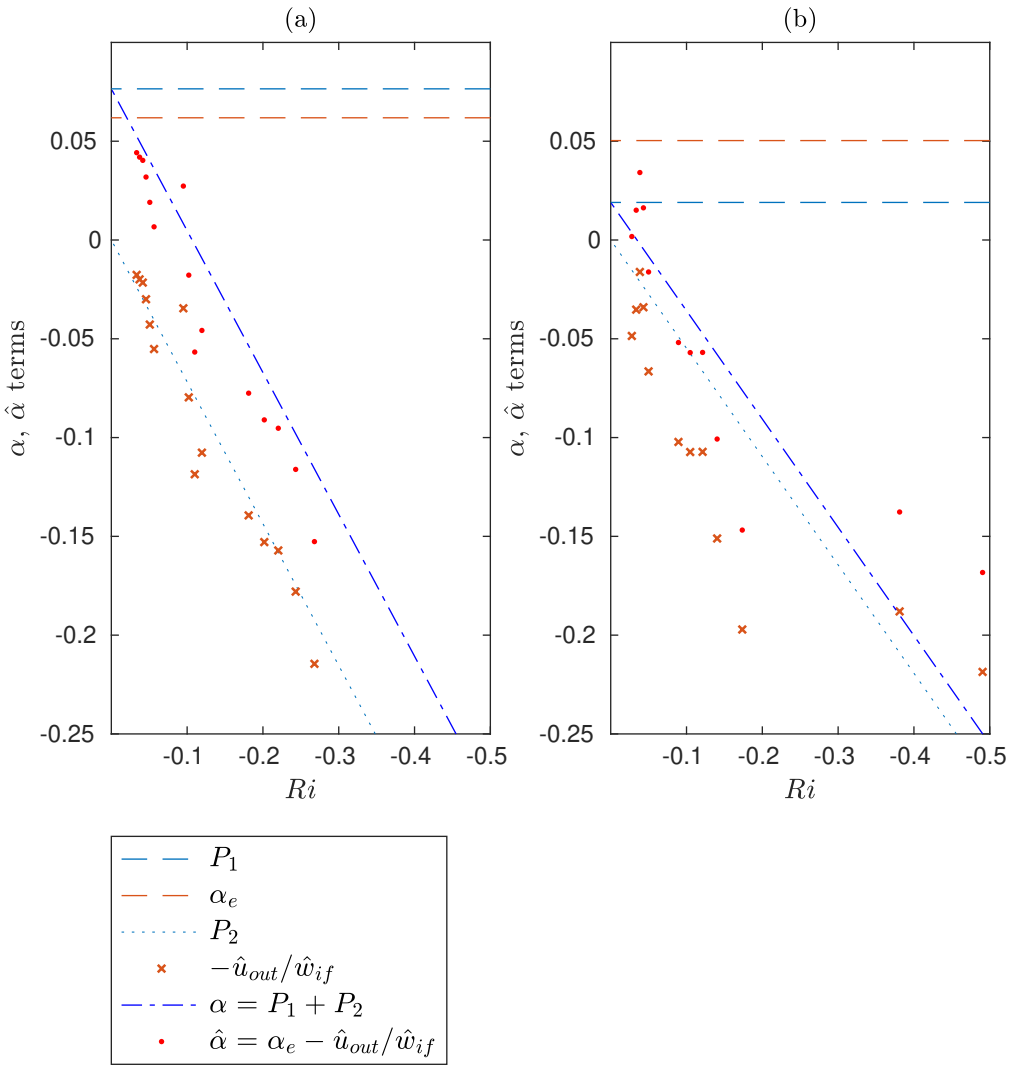

Figure 7.9: The constant and Ri-dependent components of the entrainment coefficient of a fully developed fountain from both the decomposed top-hat model ($\hat{\alpha} = \alpha_e - \hat{u}_{out}/\hat{w}$), and the full model ($\alpha = L_1 + L_2$). Results for the $Fr_o = 30$ fountain are shown in (a), and the $Fr_o = 15$ case shown in (b).

In the case of the negatively buoyant jet, the constant component corresponds to turbulent entrainment from ambient fluid into the NBJ. Near the source where $Ri \to 0$, this fully describes entrainment and may be interpreted as the 'neutral jet' value. This is supported by the present experimental data which give similar values of $\alpha = 0.071$ and $\alpha_e = 0.077$ for the neutral and negatively buoyant jets, respectively. For a fully developed fountain, the constant component can be interpreted as describing the 'turbulent entrainment' from the OF to the IF associated with the mean IF

velocity. In this case, the values are slightly lower than the neutral/negatively buoyant jets and also have a source Fr_o dependence, with $\alpha_e \cong 0.062$ and $\alpha_e \cong 0.050$ for the $Fr_o = 30$ and 15 cases, respectively. This difference may be attributed to the existence of a return flow, which will depend on Fr_o and is still present even at the source where $Ri = 0$. This effect can be seen in the full model through the profile coefficients δ_m and Δ_m, which will be discussed further in §7.4.

In describing the radial flow between the inner and outer flow regions of a fountain, the highly simplified 'decomposed top-hat' description of a fountain is consistent with the more general, 'full model', approach discussed in §7.2. These are also applicable to an NBJ, which can be thought of as fountain with a zero-velocity, zero-buoyancy, outer flow under the same top-hat formulation. This provides evidence that, despite fountains generally having a mean radial flow from the IF to OF (or into the ambient for an NBJ), they still 'entrain' fluid at a rate proportional to their characteristic axial velocity. This entrainment is captured by α_e in the top-hat model, and by terms L_1 and P_1 in the full model. This follows from equations (7.25) and (7.26), where L_1, P_1 and α_e are all positive and hence promote an inflow of fluid into the NBJ/fountain.

While buoyant jets and plumes are subject to an acceleration due to their positive buoyancy and $Ri > 0$, NBJs are instead decelerated as characterised by the increasingly negative Ri. This has implications for entrainment as captured by the $\hat{u}_{out}$ term in the decomposed formulation, and by L_2 and P_2 in the full model. In NBJs under the decomposed formulation, this has the effect of encouraging a radial outflow of fluid. In a physical flow, there will be instantaneous entrainment at some times and radial outflow at others. A mean radial outflow of fluid then occurs when the Ri-dependent term is larger in magnitude than the constant entrainment term, resulting in $\alpha < 0$. In addition to the present experiments, different regions of mean radial inflow and outflow have also been observed in other fountain investigations, such as by Williamson et al. (2011) and Cresswell and Szczepura (1993). The present decomposed top-hat model provides a consistent description of this observation, allowing it to be understood in a similar context to the classical entrainment relations originally applied to jets and plumes.

7.3.4 Special cases: pure jets/plumes

It is also useful to more closely consider the application of these models to neutral jets and plumes. Once fully developed, these idealised flows can be considered fully self-similar with constant profile coefficients. By additionally assuming that the

velocity and buoyancy/scalar profiles are Gaussian, then (7.5) and (7.10) become,

$$\alpha = -\frac{3}{8}\delta_m + \left(1 - \frac{3}{2(\lambda^2+1)}\right) Ri, \tag{7.28}$$

$$\alpha = \frac{3}{2}\left(\frac{3}{4}\delta_m - 4\Delta_m\right) + 3\left(\frac{3}{2(\lambda^2+1)} - \frac{2}{2\lambda^2+1}\right) Ri, \tag{7.29}$$

where λ, defined in (2.29), is the ratio of $1/e$ widths of the scalar and velocity profiles. For a neutral jet, $Ri = 0$, and so by equating (7.28) and (7.29) we find that $\delta_m = 4\Delta_m$. This is supported by the present experimental data for a neutral jet, where we find $\delta_m \cong 4\Delta_m \cong -0.20$.

If a self-similar buoyant jet or pure plume is now considered, with $0 < Ri \leq Ri_p$ and constant δ_m, then by equating the Ri components of (7.28) and (7.29) we obtain,

$$\frac{6}{\lambda^2+1} - \frac{6}{2\lambda^2+1} - 1 = 0. \tag{7.30}$$

That is, a non-linear equation restricting the possible values of λ to maintain consistency between (7.29) and (7.28), with positive solutions of $\lambda = 1$ and $\lambda = 1/\sqrt{2}$. Under these assumptions, we then have that λ can only take the values of 1 or $1/\sqrt{2}$ in order to maintain consistency with the conservation of mass, momentum and kinetic energy equations, (2.4)-(2.7), and the additionally derived $\overline{w}^3$ equation in (7.6). Although, to the best of this authors knowledge, there have been no studies to have reported a value as low as $\lambda = 1/\sqrt{2} \cong 0.707$ in buoyant jets or plumes, the prediction of $\lambda = 1$ is remarkably consistent with the existing plume literature (Papanicolaou and List 1988; Shabbir and George 1994; Wang and Law 2002; van Reeuwijk et al. 2016). This then provides a new theoretical justification of the commonly reported $\lambda = 1$ observation in pure plumes. It should be noted that although this consistency requirement exists for plumes/buoyant jets under these assumptions, there is no constraint here on λ in neutral jets ($Ri = 0$), which are typically reported to have $1.15 \lesssim \lambda \lesssim 1.30$ (Fischer et al. 1979; Wang and Law 2002; Ezzamel et al. 2015). If δ_m is not constant, such as in NBJs or near the source in positively buoyant jets (van Reeuwijk et al. 2016), then (7.30) is also not valid.

Consider now the application of the decomposed top-hat model to a Gaussian neutral jet by equating $\alpha = \hat{\alpha}$ from (7.28) and (7.20). Here the Ri-dependent term is zero and we have $\alpha_e = -3\delta_m/8$. That is, a constant turbulent entrainment coefficient α_e, and no outflow term. This is consistent with the classical description of a turbulent jet, which entrains ambient fluid at a rate proportional to its mean axial velocity, and is not subject to any 'mean radial outflow'.

For a buoyant jet with $\lambda = 1$ and constant δ_m, by setting $\alpha = \hat{\alpha}$ we obtain,

$$\alpha = \alpha_e - \frac{\hat{u}_{out}}{\hat{w}} = -\frac{3}{8}\delta_m + \frac{1}{4}Ri. \tag{7.31}$$

Equating the constant and Ri-dependent terms would then give $\alpha_e = -3\delta_m/8$ and $-\hat{u}_{out}/\hat{w} = Ri/4$. We then have $-\hat{u}_{out}/\hat{w} > 0$ and $\alpha_e > 0$, that is, both terms promoting entrainment from the ambient into the plume, rather than a balance of inflow and outflow as is the case in an NBJ. If applying the decomposed top-hat formulation to positively buoyant jets or plumes, it is therefore potentially misleading to refer to the Ri-dependent term as the 'outflow term', $\hat{u}_{out}$. Despite this, it is still a consistent description of the flow, and distinguishes between radial inflow associated with turbulent entrainment and with positive buoyancy. In these applications it may simply be preferable to use an alternative nomenclature, such as replacing $\hat{u}_{out}$ with $\hat{u}_b$, to indicate it is radial flow associated with buoyancy.

7.4 Effect of the OF on the IF

For fully developed fountains, α in the full model can be expressed by (7.21), and so depends on the profile coefficients, δ_m and Δ_m. In §7.3.3, these were both approximated as linear with Ri but with different coefficients for the $Fr_o = 30$ and $Fr_o = 15$ cases. Figure 7.10 shows δ_m and Δ_m for both Fr_o fountains, as well as for negatively buoyant jets with $Fr_o = 30$, 20 and 10. Both fountain cases are shown well approximated by the empirical linear δ_m and Δ_m relations,

$$\left.\begin{aligned}\delta_m &= -0.22 + 1.3Ri \\ \Delta_m &= -0.048 + 0.18Ri\end{aligned}\right\} Fr_o = 30, \tag{7.32}$$

$$\left.\begin{aligned}\delta_m &= -0.051 + 1.1Ri \\ \Delta_m &= -0.011 + 0.16Ri\end{aligned}\right\} Fr_o = 15, \tag{7.33}$$

and the $Fr_o = 30$ negatively buoyant jet by,

$$\left.\begin{aligned}\delta_m &= -0.20 + 0.60Ri \\ \Delta_m &= -0.041 + 0.089Ri\end{aligned}\right\} Fr_o = 30. \tag{7.34}$$

These may be written in the form $\delta_m = \delta_o + \tilde{\delta}Ri$ and $\Delta_m = \Delta_o + \tilde{\Delta}Ri$ as in (7.22). Although the corresponding Ri coefficients are quite similar for both Fr_o cases in the fully developed fountain, the constant terms are not. There is therefore clearly a source Fr_o effect on δ_m and Δ_m in fully developed fountains. Conversely, in the

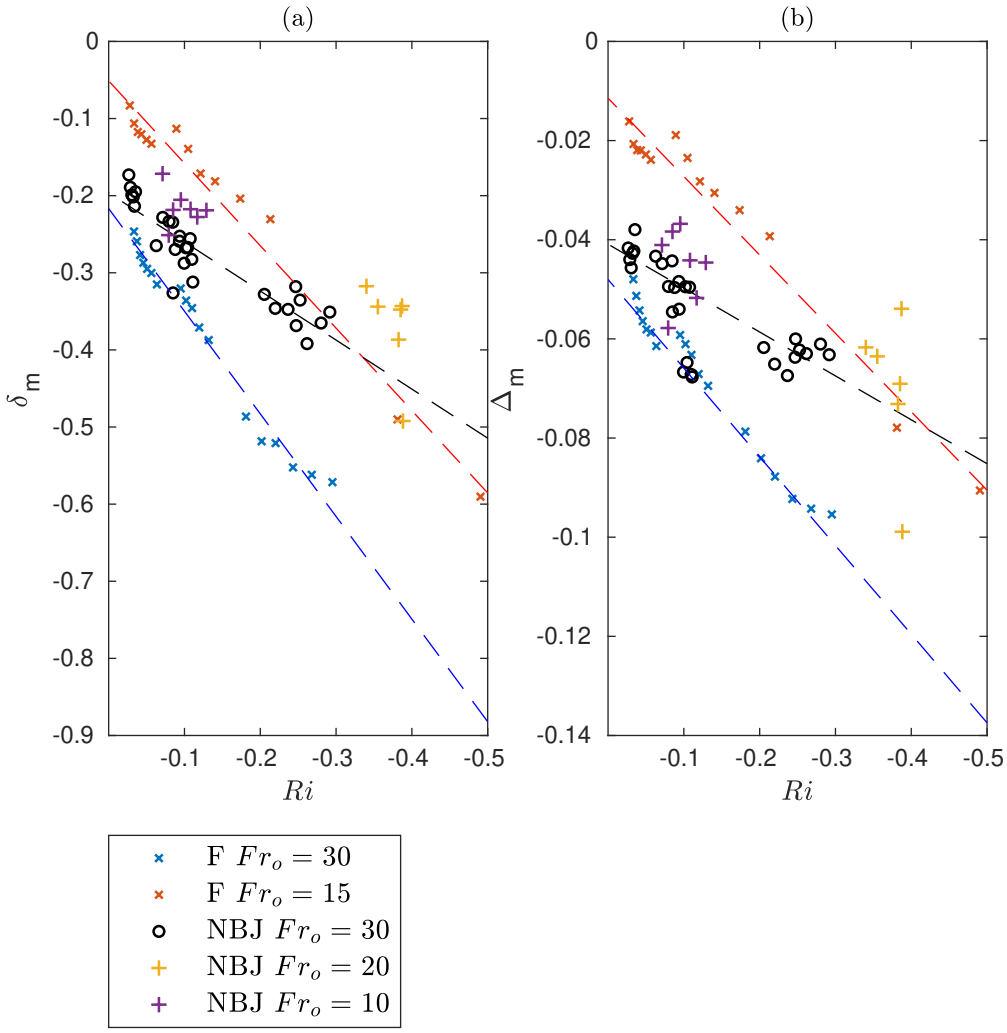

Figure 7.10: The profile coefficients, (a) δ_m, and (b) Δ_m, defined in (2.16) and (7.9), plotted with local Ri for fountains and negatively buoyant jets. Data is shown for $Fr_o = 30$ and 15 fountains, and $Fr_o = 30$, 20 and 10 negatively buoyant jets.

NBJ the $Fr_o = 10$ and $Fr_o = 30$ data are in good agreement at similar local Ri for both δ_m and Δ_m. The data is more scattered for the $Fr_o = 20$ case, but there is still reasonable agreement with the extrapolated line for both δ_m and Δ_m.

As $Ri \to 0$, a negatively buoyant jet becomes increasingly similar to a neutral jet, which has $Ri = 0$ everywhere. At $Ri = 0$, the values of δ_m and Δ_m should then correspond to the 'neutral jet values'. This was discussed in §5.5.2 for δ_m, and may also be seen in figure 7.10(a), where the Ri intercept of the fit is $\delta_o \cong -0.20$. This is the same as the average value from the present neutral jet experiments, $\delta_j \cong -0.20$, and is also in agreement with existing jet literature (Craske and van Reeuwijk 2015; Panchapakesan and Lumley 1993; Wang and Law 2002; Ezzamel et al. 2015). The present jet data gives an average value of $\Delta_j \cong -0.049$, which is somewhat higher but still in reasonable agreement with $\Delta_o \cong -0.041$ for the NBJ. Although the

inner flow of a fully developed fountain may become more similar to a jet or NBJ as $Ri \to 0$, it is still fundamentally different due to the presence of a return flow. Since this return flow still exists at $Ri = 0$, δ_o and Δ_o in fountains do not correspond to the neutral jet values. The presence of the outer flow is therefore likely the source of the Fr_o dependence of δ_m and Δ_m in fountains, which is not seen in NBJs. This manifests in term P_1 from (7.23), the entrainment coefficient in the full model, or equivalently α_e in the decomposed top-hat formulation.

In describing entrainment in fully developed fountains using either the full or decomposed top-hat models, knowledge of δ_m and Δ_m for the particular Fr_o is therefore required. This is not the case for an NBJ, which, from figure 7.10, appear independent of Fr_o. This is because there is no outer flow present and the local flow depends only on the local Ri. Predicting δ_m or Δ_m for arbitrary Fr_o fountains therefore likely requires further characterising the outer flow, and could be a useful topic for future investigations. One approach may be to replace w_m and r_m in the definitions of δ_m and Δ_m, with scales that include information about the OF. A preliminary attempt to use the relative velocity difference between the IF/OF, rather than the IF velocity only, did not eliminate the Fr_o dependence. Other potential approaches may be to include an additional turbulence velocity scale, possibly similar to w_f that was defined in (5.4) to collapse the turbulence profiles in an NBJ, although further research in required.

7.5 Conclusions

This chapter has investigated entrainment in negatively buoyant jets and fountains using two distinct approaches. The first approach, referred to as the 'full model', uses derived expressions for the entrainment coefficient, α, to describe radial flow between the IF/OF of a fountain, or between an NBJ and the ambient. Estimates for α in fountains and negatively buoyant jets using these expressions were presented in figure 7.1, which showed a strong Ri dependence on entrainment for all flows. For both fountains, $\alpha < 0$ over a large portion of their height, a finding consistent with previous studies by Williamson et al. (2011) ($Fr_o = 7$) and Cresswell and Szczepura (1993) ($Fr_o = 3.2$).

The second formulation of entrainment, the 'decomposed top-hat model', was introduced in §7.3, where radial flow between the IF/OF is split up into an inflow component proportional to the IF velocity scale, α_e, and an outflow component, $\hat{u}_{out}$. Using the present experimental data, these were estimated along the fountains and NBJ, finding that α_e was approximately constant whilst $\hat{u}_{out}$ varied with Ri.

This 'decomposed' formulation was shown to be broadly consistent with a simplified version of the 'full model' in §7.3.3, where entrainment can also be expressed as the sum of a constant and Ri-dependent component. Despite NBJs and fountains generally having a non-constant α, and $\alpha < 0$ after some axial distance, the decomposed top-hat formulation provides an interpretation of entrainment that is similar to the classical jet and plume description used by Morton et al. (1956). That is, that turbulent entrainment is proportional to a characteristic velocity at that height by a constant entrainment coefficient. However, for an NBJ or fountain IF, there is also an Ri-dependent radial outflow that is associated with the flows (negative) buoyancy.

The present study has found certain similarities between NBJs without a return flow and fully developed fountains, such as the approximately linear δ_m and Δ_m. In negatively buoyant jets, these profile coefficients do not appear to have a Fr_o dependence. In fully developed fountains, however, they do. This has implications for the entrainment coefficient, α in (7.23) and (7.24), describing radial flow across the IF/OF boundary. This Fr_o dependence in fountains, which likely arises due to differences in the outer flow, presents a challenge for accurately predicting entrainment in fountains with arbitrary Fr_o. Future research may seek to develop a description of the local, Ri-dependent, entrainment in fountains that can more easily be applied to different Fr_o cases. This could involve relating δ_m and Δ_m to the outer flow in a way that eliminates this Fr_o dependence. This could include mean velocity and length scales for the outer flow, or potentially an additional turbulence velocity scale that can capture the development of $\overline{w'u'}$. Such a study could benefit from extensive measurements estimating these profile coefficients along the fountain for a greater range of Fr_o.

The 'full model' description of the IF of a fountain captures all fundamental transfers in the flow through the profile coefficients. Some of which are approximately constant and independent of Fr_o, such as γ_m, Γ_m, θ_m and μ_m, while δ_m and Δ_m are not. Redefining δ_m and Δ_m so that they are constant and universal for all Fr_o fountains would therefore be useful in simplifying the application of this model. The present study has also focused primarily on entrainment between the IF/OF of a fountain, where future research may seek to investigate it between the ambient and OF, including at the cap region.

Chapter 8

Conclusion

8.1 Summary

This thesis has investigated negatively buoyant turbulent jets experimentally using combined PIV and PLIF measurements. Two distinct stages of the flow were considered, the initial 'negatively buoyant jet' stage, as well as the quasi-steady 'fully developed fountain' stage. Since the NBJ stage occurs before the opposing return flow is established, this could be analysed using some of the same tools often applied to neural and positively buoyant jets. Namely, the integral model approach originally developed by Morton et al. (1956) and Priestley and Ball (1955). This reveals some of the effects that negative buoyancy has on the development of jet-like flows. Eventually the mean velocity of an NBJ is reduced to zero due to its opposing buoyancy, after which it collapses back onto itself and a return flow starts to develop. Once the return flow has established the fully developed fountain stage is reached, where the flow consists of a negatively buoyant inner flow surrounded by an opposing outer flow. The IF of a fountain can then be considered a turbulent jet that is affected by both negative buoyancy and interactions with the OF. While comparing neutral and negatively buoyant jets reveals the effect of negative buoyancy on the flow, differences between NBJs and fountains helps identify the effect of the OF.

8.2 PIV and PLIF measurements

This investigation used combined 2D particle image velocimetry (PIV) and planar laser induced fluorescence (PLIF) to investigate NBJs and fountains. An experimental rig was designed to produce the flow in a 1000 L tank, and obtain images using 5 cameras operating simultaneously with a double pulsed 532 nm Nd:YAG laser. Four of these cameras were used to capture PIV/PLIF images of the flow in

the region of interest, with the images 'stitched' together to obtain a wider field of view. The fifth camera was used to obtain a measurement of the power profile of the laser pulses, which could then be used to correct each individual PLIF image for variations in laser power output. The PLIF algorithm and correction procedure was validated in §3.4.3, where it was found to reduce the error in scalar concentration measurements. This approach is important when using lasers that have a variable power profile shape, and when studying flows that may not be statistically stationary. The experimental set-up and image processing procedure was applied to a turbulent neutral jet in §4.4, where mean and turbulence statistics were obtained that were consistent with existing literature.

8.3 The physics of NBJs and fountains

8.3.1 Negatively buoyant jet stage

The initial negatively buoyant jet stage of the flow was investigated in chapter 5. Mean and turbulence profiles were presented for a $Fr_o = 30$ NBJ over a range of local Fr, with the mean velocity and scalar profiles found to take Gaussian shapes over the full range of Fr investigated. The relative widths of the scalar/velocity profiles, characterised by λ defined in (2.29), increased with axial distance from approximately $\lambda \cong 1.3$ to 1.5 for $20 \lesssim z/D \lesssim 35$. This is in contrast to pure jets and plumes, which are typically reported to have lower and approximately constant values of $\lambda \cong 1.2$ and 1.0, respectively, once they have reached a state of self-similarity (Fischer et al. 1979; Papanicolaou and List 1988; Wang and Law 2002; Ezzamel et al. 2015). New integral buoyancy and buoyancy-width scales, g_m and r_{mb}, were defined in (5.2) that scale with $\overline{b}$ independent of λ, and an analytical expression for $\mathrm{d}r_{mb}/\mathrm{d}z$ was derived in (5.23). This expression is valid for turbulent jets with arbitrary buoyancy and, when examined alongside $\mathrm{d}r_m/\mathrm{d}z$ in (5.14), assists in explaining the increasing λ observed in NBJs.

Pure jets and plumes have turbulence profiles that scale with the mean flow, such as $\overline{w'u'}/\overline{w}_c^2$ and $\overline{w'^2}/\overline{w}_c^2$, which collapse onto a single curve when plotted with a local width scale such as the velocity half-width (Hussein et al. 1994; Panchapakesan and Lumley 1993; Wang and Law 2002; Darisse et al. 2015). This was not observed in the present negatively buoyant jet data, which was shown in figure 5.10 where $\overline{w'u'}/\overline{w}_c^2$ and $\overline{w'^2}/\overline{w}_c^2$ increase with axial distance. This is primarily a result of the decelerating mean flow, characterised by a decreasing $\overline{w}_c$, rather than an increase in turbulence production. An additional turbulence velocity scale, w_f, was defined in (5.4) that is capable of collapsing the $\overline{w'u'}$ and $\overline{w'^2}$ profiles.

Entrainment in negatively buoyancy jets was investigated through the expression for α in (5.5), specifically applied to the case with Gaussian velocity/buoyancy profiles. The terms of this expression were plotted in figure 7.8 with Ri, which showed that despite the increasing *dimensionless* turbulence production, $-\delta_m$, the overall entrainment decreases with axial distance due to the increasingly negative Ri. Near the source, where $Ri \cong 0$ and the flow is dominated by momentum as opposed to negative buoyancy, α in the NBJ is similar to a neutral jet. Further along the NBJ, $Ri \to -\infty$ as $w_m \to 0$ and the flow becomes increasingly governed by negative buoyancy. This reduces entrainment in the NBJ and eventually results in $\alpha < 0$ for $Ri \lesssim -0.5$, indicating a net radial outflow from the NBJ to the ambient fluid. The development of α in the NBJ could be well approximated by a linear relationship with Ri, which was constructed by assuming a linear δ_m relation with Ri and a constant λ.

The integral model discussed in §2.4 and described by (2.19)-(2.21) was numerically solved for a negatively buoyant jet and compared to the present experimental data in figure 5.4. Different entrainment relations were used to model α, referred to as models 1 and 2 in §5.5.2, which correspond to a semi-empirical model based on a linear fit of δ_m and a constant $\lambda \cong 1.46$, and a constant $\delta_m \cong -0.22$ and $\lambda \cong 1.1$, respectively. Although both models give reasonable $w_o/\overline{w}_c$ predictions for $z/D \lesssim 30$, neither maintain accuracy over the full z/D range while simultaneously being consistent with the observed values of λ and δ_m. To the best of the authors knowledge, this was the first attempt to assess the local flow predictions of integral models to experimental data of an NBJ without a return flow.

8.3.2 Fully developed fountain stage

The fully developed fountain stage occurs after an NBJ has collapsed back onto itself and is oscillating around its steady stage height, z_{ss}. This was the main focus of chapter 6, which analysed data primarily from $Fr_o = 30$ and 15 fountains at a range of axial locations (and local Fr). Mean velocity and buoyancy profiles for a fountain were compared with an NBJ, both with $Fr_o = 30$, at a range of local Fr. Unlike the NBJ, the fountain profiles did not take similar Gaussian shapes along its height. Despite this, they were reasonable similar in the IF ($r \leq r_{io}$) when normalised by centreline value and their respective half-widths. Additionally, when the mean profiles of $Fr_o = 15$ and 30 fountains were compared at locations with similar local Fr (based on IF quantities), improved agreement was observed in the IF. Other profiles such as $\overline{w'u'}$ and $\overline{w'c'}$ were significantly different, even in the IF, between both Fr_o fountains and the NBJ. The difference between these profiles in

the two Fr_o fountains at similar Fr locations can be attributed to the presence of the return flow, which is different in the two cases and is not captured in the present definition of Fr.

The entrainment relation used in §5.5.2 to calculate α in an NBJ, (5.5), cannot be immediately applied to a fully developed fountain due to the presence of a return flow. By following a similar derivation procedure to that used in obtaining (5.5), but setting the integration limits to r_{io} (the IF/OF boundary) instead of infinity, a similar α expression given in (7.5) was derived. This is in the same form as (5.5) except now has a non-zero boundary condition term since $\overline{w'u'}$ does not go to zero at r_{io}. An alternative expression for α was derived in (7.10), which used an additional conservation equation that eliminated this boundary condition. Both expressions describe entrainment between the IF/OF regions of a fountain, and were referred to as the 'full model'. These were used to calculate α in $Fr_o = 15$ and 30 fully developed fountains based on experimental data across a range of Ri, and was presented in figure 7.1. The two expressions agreed with each other and gave α strongly decreasing with negative Ri, with $\alpha < 0$ for $Ri \lesssim -0.25$ in the $Fr_o = 30$ case and $Ri \lesssim -0.04$ in the $Fr_o = 15$ case.

The negative α indicates there is a net radial outflow of fluid from the IF to the OF, which has also been observed in previous numerical and experimental studies (Williamson et al. 2011; Cresswell and Szczepura 1993). This motivated the analysis of the 'decomposed top-hat' model, presented in §7.3, which separates radial flow between the IF/OF into and inflow and outflow components occurring simultaneously (McDougall 1981; Bloomfield and Kerr 2000; Hunt and Debugne 2016). The inflow was related to the IF velocity scale by an entrainment coefficient, α_e, while the radial outflow, $\hat{u}_{out}$, was left unconstrained. This could also be applied to an NBJ, which may be considered a fountain with a zero velocity, zero buoyancy, outer flow under this formulation. These were estimated using the present experimental data, and it was found that α_e was approximately constant for both Fr_o fountains and the NBJ, while $\hat{u}_{out}/\hat{w}_{if}$ increased with negative Ri. The constant α_e component could then be interpreted as the 'turbulent entrainment' coefficient from the OF to the IF, and is similar to the description of entrainment in pure jets and plumes, while the variable outflow component can be associated with negative buoyancy and the effect of the OF. Alternative body-force and entrainment formulations were also considered in the decomposed top-hat model (McDougall 1981; Bloomfield and Kerr 2000; Hunt and Debugne 2016), which all resulted in similar trends for α_e and $\hat{u}_{out}$ with Ri.

By taking empirical fits of the present experimental data, entrainment in the 'full

model' could also be expressed as the sum of constant and Ri-dependent components. This allowed the decomposed formulation to be compared to the full-model in §7.3.3, which were found to be in reasonable agreement. Despite this, a key issue that arises is that α differs between the $Fr_o = 15$ and 30 cases. This is driven by the profile coefficients δ_m and Δ_m, which relate to the dimensionless turbulent production in the IF and vary with Ri. The local Ri was defined based on integral velocity/buoyancy/length scales that are defined up to r_{io}, and so does not directly capture the OF. The effect of the outer flow at a particular Ri may differ for fountains with different Fr_o, which manifests as the apparent Fr_o dependence in δ_m, Δ_m and α, as well as the profiles presented in §6.3.

8.4 Future work

A notable finding of the study into negatively buoyant jets in chapter 5 was the increasing $-\delta_m$ with Ri. This arises due to the fact that $\overline{w'u'}$ does not decrease at the same rate as the mean flow, w_m, as discussed in §5.3.3. Future research may seek to better understand why this is, possibly through a detailed analysis of the governing equations and various turbulence/energy budgets applied specifically to NBJs. The increasing $-\delta_m$ was captured in the entrainment model 1, (5.9), through the ad hoc $\tilde{\delta}$ term estimated from an empirical fit of the data. An improved understanding of the increasing $-\delta_m$, and thus the origins of the $\tilde{\delta}$ term, may be useful in better modelling α in NBJs. Additionally, λ was shown to be higher in NBJs than plumes and jets, and increased with axial distance along the flow. This effect was neglected when solving the integral models for an NBJ, which assumed λ is constant. The precise influence of λ on the flow is complex since it appears in the expression for α as well as the definition of Ri, and future work may seek to solve the integral model without assuming a constant λ, possibly with the aid of the derived expression for $\mathrm{d}r_{mb}/\mathrm{d}z$ in (5.14).

The estimates of α_e and $\hat{u}_{out}$ in the decomposed top-hat model provided a new interpretation of entrainment in fully developed fountains. That is, that the radial flow can be characterised by an approximately constant 'turbulent entrainment' coefficient describing flow from the OF to IF, along with a radial outflow component that varies with the local Ri. There are, however, differences between entrainment in the $Fr_o = 15$ and 30 fountains that arise due to differences in the OF. The effect of the OF can be seen in the value of the profile coefficients δ_m and Δ_m in the full model, which were presented in figure 7.10 for $Fr_o = 15$ and $Fr_o = 30$ fountains. Future work may seek to develop a description of local entrainment in fountains that

more explicitly accounts for the effect of the return flow. This could be potentially be pursued by deriving an alternate 'full model' from the conservation equations that defines α and the profile coefficients to include information about the outer flow.

8.5 Final remarks

The present study has investigated the initial and quasi-steady stages of high Fr_o turbulent jets with negative buoyancy originating from a round inlet. The initial 'negatively buoyant jet' stage, which does not have a return flow, resembles a neutral or buoyant jet/plume except is subject to a buoyancy force that opposes its momentum. Studying this flow allowed fundamental questions of how negative buoyancy affects entrainment and the development of jet-like flows more generally to be investigated. This was the focus of chapter 5, where several key differences between neutral and negatively buoyancy jets were identified. In light of these differences, the classical integral models originally developed by Morton et al. (1956) and Priestley and Ball (1955) were solved and compared to the present experimental data. Although the models presented were incomplete, such as by neglecting higher order turbulence contributions and assuming a constant λ, reasonable agreement with the present experimental data was obtained for $z/D \lesssim 30$.

Fully developed flow, which consists of a turbulent NBJ surrounded by an opposing outer flow, is significantly more complex than an NBJ. This was the focus of chapter 6 and 7, where different approaches to describing mixing between the IF/OF regions were investigated. This was characterised through an entrainment coefficient, α, that described the radial flow across the IF/OF boundary. This process could also be interpreted as an inflow component occurring simultaneously with a radial outflow. Calculating entrainment using these approaches results in different estimates for different Fr_o fountains due to differences in the outer flow. An open question that remains is then how to best describe local entrainment in fountains more universally, for fountains with arbitrary Fr_o. Given the complexity of turbulent fountains, particularly with regard to the interactions between the IF/OF regions, there is still scope for additional research in this area. This may come in the form of theoretical, experimental, or numerically studies that seek to find the most complete description of local entrainment and mixing in forced fountains. Such work will not only assist in better modelling the countless real-world examples of negatively buoyant jets and fountains, but will contribute to a more fundamental understanding of the physics of complex shear flows.

Bibliography

G. Abraham. Jets with negative buoyancy in homogeneous fluid. *Journal of Hydraulic Research*, 5(4):235–248, 1967.

R. J. Adrian and J. Westerweel. *Particle image velocimetry*. Cambridge university press, 2011.

W. D. Baines, J. S. Turner, and I. H. Campbell. Turbulent fountains in an open chamber. *Journal of Fluid Mechanics*, 212:557–592, 1990.

N. Bartos. Laboratory investigations into displacement ventilation. Master's thesis, The University of Sydney, 2012.

H. Becker, H. Hottel, and G. Williams. The nozzle-fluid concentration field of the round, turbulent, free jet. *Journal of Fluid Mechanics*, 30(2):285–303, 1967.

A. Birch, D. Brown, M. Dodson, and J. Thomas. The turbulent concentration field of a methane jet. *Journal of Fluid Mechanics*, 88(3):431–449, 1978.

L. J. Bloomfield and R. C. Kerr. A theoretical model of a turbulent fountain. *Journal of Fluid Mechanics*, 424:197–216, 2000.

R. Budwig. Refractive index matching methods for liquid flow investigations. *Experiments in fluids*, 17(5):350–355, 1994.

H. C. Burridge and G. R. Hunt. The rise heights of low-and high-Froude-number turbulent axisymmetric fountains. *Journal of Fluid Mechanics*, 691:392–416, 2012.

H. C. Burridge and G. R. Hunt. Entrainment by turbulent fountains. *Journal of Fluid Mechanics*, 790:407–418, 2016.

I. H. Campbell and J. S. Turner. Fountains in magma chambers. *Journal of Petrology*, 30(4):885–923, 1989.

G. Carazzo, E. Kaminski, and S. Tait. The route to self-similarity in turbulent jets and plumes. *Journal of Fluid Mechanics*, 547:137–148, 2006.

G. Carazzo, E. Kaminski, and S. Tait. On the dynamics of volcanic columns: A comparison of field data with a new model of negatively buoyant jets. *Journal of Volcanology and Geothermal Research*, 178(1):94–103, 2008.

G. Carazzo, E. Kaminski, and S. Tait. The rise and fall of turbulent fountains: a new model for improved quantitative predictions. *Journal of Fluid Mechanics*, 657:265–284, 2010.

R. Chevray and N. Tutu. Intermittency and preferential transport of heat in a round jet. *Journal of Fluid Mechanics*, 88(1):133–160, 1978.

H. W. Coleman and W. G. Steele. *Experimentation, validation, and uncertainty analysis for engineers*. John Wiley & Sons, 2018.

J. Craske and M. van Reeuwijk. Energy dispersion in turbulent jets. part 1. direct simulation of steady and unsteady jets. *Journal of Fluid Mechanics*, 763:500–537, 2015.

J. Craske, P. Salizzoni, and M. van Reeuwijk. The turbulent Prandtl number in a pure plume is 3/5. *Journal of Fluid Mechanics*, 822:774–790, 2017.

R. Cresswell and R. Szczepura. Experimental investigation into a turbulent jet with negative buoyancy. *Physics of Fluids A: Fluid Dynamics*, 5(11):2865–2878, 1993.

J. Crimaldi. Planar laser induced fluorescence in aqueous flows. *Experiments in fluids*, 44(6):851–863, 2008.

A. Darisse, J. Lemay, and A. Benaïssa. Budgets of turbulent kinetic energy, Reynolds stresses, variance of temperature fluctuations and turbulent heat fluxes in a round jet. *Journal of Fluid Mechanics*, 774:95–142, 2015.

G. E. Elsinga, F. Scarano, B. Wieneke, and B. W. van Oudheusden. Tomographic particle image velocimetry. *Experiments in fluids*, 41(6):933–947, 2006.

A. Ezzamel, P. Salizzoni, and G. R. Hunt. Dynamical variability of axisymmetric buoyant plumes. *Journal of Fluid Mechanics*, 765:576–611, 2015.

A. Ferrier, D. Funk, and P. Roberts. Application of optical techniques to the study of plumes in stratified fluids. *Dynamics of Atmospheres and Oceans*, 20(1-2): 155–183, 1993.

H. B. Fischer, J. E. List, C. R. Koh, J. Imberger, and N. H. Brooks. *Mixing in inland and coastal waters*. Academic, 1979.

D. G. Fox. Forced plume in a stratified fluid. *Journal of Geophysical Research*, 75 (33):6818–6835, 1970.

E. Grandmaison, D. Rathgeber, and H. Becker. Some characteristics of concentration fluctuations in free turbulent jets. *The Canadian Journal of Chemical Engineering*, 60(2):212–219, 1982.

D. P. Hart. Piv error correction. *Experiments in fluids*, 29(1):13–22, 2000.

W. M. Haynes. *CRC handbook of chemistry and physics*. CRC press, 2014.

G. R. Hunt and H. C. Burridge. Fountains in industry and nature. *Annual Review of Fluid Mechanics*, 47:195–220, 2015.

G. R. Hunt and A. L. Debugne. Forced fountains. *Journal of Fluid Mechanics*, 802: 437–463, 2016.

H. J. Hussein, S. P. Capp, and W. K. George. Velocity measurements in a high-Reynolds-number, momentum-conserving, axisymmetric, turbulent jet. *Journal of Fluid Mechanics*, 258:31–75, 1994.

E. Kaminski, S. Tait, and G. Carazzo. Turbulent entrainment in jets with arbitrary buoyancy. *Journal of Fluid Mechanics*, 526:361–376, 2005.

N. B. Kaye and G. R. Hunt. Weak fountains. *Journal of Fluid Mechanics*, 558: 319–328, 2006.

R. D. Keane and R. J. Adrian. Theory of cross-correlation analysis of piv images. *Applied scientific research*, 49(3):191–215, 1992.

K. Kiser. Material and momentum transport in axisymmetric turbulent jets of water. *AIChE Journal*, 9(3):386–390, 1963.

M. Larson and L. Jönsson. Efficiency of mixing by a turbulent jet in a stably stratified fluid. *Dynamics of atmospheres and oceans*, 24(1-4):63–74, 1996.

J. H.-w. Lee and V. Chu. *Turbulent jets and plumes: a Lagrangian approach*. Springer Science & Business Media, 2012.

T. J. McDougall. Negatively buoyant vertical jets. *Tellus*, 33(3):313–320, 1981.

L. McGurk, N. Williamson, S. Armfield, and M. Kirkpatrick. Experimental investigation into turbulent negatively buoyant jets using combined piv and lif measurements. *Proceedings of the 21st Australasian Fluid Mechanics Conference*, 2018.

T. Medford, P. Danehy, S. Jones, N. Jiang, M. Webster, W. Lempert, J. Miller, and T. Meyer. Stereoscopic planar laser-induced fluorescence imaging at 500 khz. In *49th AIAA Aerospace Sciences Meeting including the New Horizons Forum and Aerospace Exposition*, page 985, 2011.

L. Milton-McGurk, N. Williamson, S. W. Arfmfield, M. P. Kirkpatrick, and K. M. Talluru. Entrainment and structure of negatively buoyant jets. *Journal of Fluid Mechanics (accepted)*, 2020a.

L. Milton-McGurk, N. Williamson, S. Armfield, and M. Kirkpatrick. Experimental investigation into turbulent negatively buoyant jets using combined PIV and PLIF measurements. *International Journal of Heat and Fluid Flow*, 82:108561, 2020b.

D. Mistry, J. Philip, J. R. Dawson, and I. Marusic. Entrainment at multi-scales across the turbulent/non-turbulent interface in an axisymmetric jet. *Journal of Fluid Mechanics*, 802:690–725, 2016.

T. Mizushina, F. Ogino, H. Takeuchi, and H. Ikawa. An experimental study of vertical turbulent jet with negative buoyancy. *Wärme-und Stoffübertragung*, 16 (1):15–21, 1982.

B. Morton. Coaxial turbulent jets. *International Journal of Heat and Mass Transfer*, 5(10):955–965, 1962.

B. R. Morton. Forced plumes. *Journal of Fluid Mechanics*, 5(1):151–163, 1959.

B. R. Morton, G. I. Taylor, and J. S. Turner. Turbulent gravitational convection from maintained and instantaneous sources. *Proceedings of the Royal Society of London. Series A. Mathematical and Physical Sciences*, 234(1196):1–23, 1956.

P. A. C. Okwuobi and R. Azad. Turbulence in a conical diffuser with fully developed flow at entry. *Journal of Fluid Mechanics*, 57(3):603–622, 1973.

E. Overmars, N. Warncke, C. Poelma, and J. Westerweel. Bias errors in piv: the pixel locking effect revisited. In *15th international symposium on applications of laser techniques to fluid mechanics, Lisbon, Portugal*, pages 5–8, 2010.

N. R. Panchapakesan and J. L. Lumley. Turbulence measurements in axisymmetric jets of air and helium. part 1. air jet. *Journal of Fluid Mechanics*, 246:197–223, 1993.

P. N. Papanicolaou and E. J. List. Investigations of round vertical turbulent buoyant jets. *Journal of Fluid Mechanics*, 195:341–391, 1988.

P. N. Papanicolaou, I. G. Papakonstantis, and G. C. Christodoulou. On the entrainment coefficient in negatively buoyant jets. *Journal of Fluid Mechanics*, 614: 447–470, 2008.

A. B. Pincince and E. J. List. Disposal of brine into an estuary. *Journal (Water Pollution Control Federation)*, pages 2335–2344, 1973.

C. H. B. Priestley and F. K. Ball. Continuous convection from an isolated source of heat. *Quarterly Journal of the Royal Meteorological Society*, 81(348):144–157, 1955.

P. J. W. Roberts, A. Ferrier, and G. Daviero. Mixing in inclined dense jets. *Journal of Hydraulic Engineering*, 123(8):693–699, 1997.

A. Shabbir and W. K. George. Experiments on a round turbulent buoyant plume. *Journal of Fluid Mechanics*, 275:1–32, 1994.

J. W. Shan, D. B. Lang, and P. E. Dimotakis. Scalar concentration measurements in liquid-phase flows with pulsed lasers. *Experiments in Fluids*, 36(2):268–273, 2004.

A. B. Shrinivas and G. R. Hunt. Unconfined turbulent entrainment across density interfaces. *Journal of fluid mechanics*, 757:573–598, 2014.

R. K. Singh and R. S. Azad. Structure of turbulence in an incipient-separating axisymmetric flow. *Journal of Fluids Engineering*, 117(3):433–438, 1995.

S. M. Soloff, R. J. Adrian, and Z.-C. Liu. Distortion compensation for generalized stereoscopic particle image velocimetry. *Measurement science and technology*, 8 (12):1441, 1997.

G. X. Y. Tan, M. Jamil, N. G. Z. Tee, L. Zhong, and C. H. Yap. 3d reconstruction of chick embryo vascular geometries using non-invasive high-frequency ultrasound for computational fluid dynamics studies. *Annals of biomedical engineering*, 43 (11):2780–2793, 2015.

J. Turner. Turbulent entrainment: the development of the entrainment assumption, and its application to geophysical flows. *Journal of Fluid Mechanics*, 173:431–471, 1986.

J. S. Turner. Jets and plumes with negative or reversing buoyancy. *Journal of Fluid Mechanics*, 26(4):779–792, 1966.

M. van Reeuwijk and J. Craske. Energy-consistent entrainment relations for jets and plumes. *Journal of Fluid Mechanics*, 782:333–355, 2015.

M. van Reeuwijk, P. Salizzoni, G. R. Hunt, and J. Craske. Turbulent transport and entrainment in jets and plumes: a DNS study. *Physical Review Fluids*, 1(7): 074301, 2016.

S. Vaux, R. Mehaddi, O. Vauquelin, and F. Candelier. Upward versus downward non-boussinesq turbulent fountains. *Journal of Fluid Mechanics*, 867:374–391, 2019.

J. Vejražka, M. Zedníková, and P. Stanovskỳ. Experiments on breakup of bubbles in a turbulent flow. *AIChE Journal*, 64(2):740–757, 2018.

H. Wang and A. W.-K. Law. Second-order integral model for a round turbulent buoyant jet. *Journal of Fluid Mechanics*, 459:397–428, 2002.

D. R. Webster, P. J. W. Roberts, and L. Ra'ad. Simultaneous DPTV/PLIF measurements of a turbulent jet. *Experiments in Fluids*, 30(1):65–72, 2001.

J. Weinkauff, P. Trunk, J. Frank, M. Dunn, A. Dreizler, and B. Böhm. Investigation of flame propagation in a partially premixed jet by high-speed-Stereo-PIV and acetone-PLIF. *Proceedings of the Combustion Institute*, 35(3):3773–3781, 2015.

J. Westerweel. Analysis of piv interrogation with low-pixel resolution. *Optical Diagnostics in Fluid and Thermal Flow*, 2005:624–635, 1993.

J. Westerweel. Efficient detection of spurious vectors in particle image velocimetry data. *Experiments in Fluids*, 16(3-4):236–247, 1994.

J. Westerweel, D. Dabiri, and M. Gharib. The effect of a discrete window offset on the accuracy of cross-correlation analysis of digital piv recordings. *Experiments in fluids*, 23(1):20–28, 1997.

C. Willert. Stereoscopic digital particle image velocimetry for application in wind tunnel flows. *Measurement science and technology*, 8(12):1465, 1997.

N. Williamson, S. W. Armfield, and W. Lin. Forced turbulent fountain flow behaviour. *Journal of Fluid Mechanics*, 671:535–558, 2011.

N. Williamson, M. Kirkpatrick, and S. Armfield. Entrainment across a sheared density interface in a cavity flow. *Journal of Fluid Mechanics*, 835:999–1021, 2018.

B. M. Wilson and B. L. Smith. Uncertainty on PIV mean and fluctuating velocity due to bias and random errors. *Measurement Science and Technology*, 24(3): 035302, 2013a.

B. M. Wilson and B. L. Smith. Taylor-series and Monte-Carlo-method uncertainty estimation of the width of a probability distribution based on varying bias and random error. *Measurement Science and Technology*, 24(3):035301, 2013b.

Y. Wu, W. Xu, Q. Lei, and L. Ma. Single-shot volumetric laser induced fluorescence (vlif) measurements in turbulent flows seeded with iodine. *Optics express*, 23(26): 33408–33418, 2015.

F. M. Zehentbauer, C. Moretto, R. Stephen, T. Thevar, J. R. Gilchrist, D. Pokrajac, K. L. Richard, and J. Kiefer. Fluorescence spectroscopy of rhodamine 6g: concentration and solvent effects. *Spectrochimica Acta Part A: Molecular and Biomolecular Spectroscopy*, 121:147–151, 2014.